

LA-6834-PR

Progress Report

UC-21

Issued: October 1977

C.3

**CIC-14 REPORT COLLECTION
REPRODUCTION
COPY**

Laser Fusion Program

COMPILED BY

E. STARK
F. SKOBERNE

October 1—December 31, 1976

LOS ALAMOS NATIONAL LABORATORY



3 9338 00387 1471

**Los Alamos
scientific laboratory**

of the University of California

LOS ALAMOS, NEW MEXICO 87545

An Affirmative Action/Equal Opportunity Employer

The four most recent reports in this series, unclassified, are LA-6050-PR, LA-6245-PR, LA-6510-PR, and LA-6616-PR.

This work was supported by the US Energy Research and Development Administration, Division of Laser Fusion.

Printed in the United States of America. Available from
National Technical Information Service
U.S. Department of Commerce
5285 Port Royal Road
Springfield, VA 22161
Price: Printed Copy \$6.50 Microfiche \$3.00

This report was prepared as an account of work sponsored by the United States Government. Neither the United States nor the United States Department of Energy, nor any of their employees, nor any of their contractors, subcontractors, or their employees, makes any warranty, express or implied, or assumes any legal liability or responsibility for the accuracy, completeness, or usefulness of any information, apparatus, product, or process disclosed, or represents that its use would not infringe privately owned rights.



CONTENTS

Abstract	1
Summary and Program Overview	2
I. CO ₂ Laser Program	7
Single-Beam System (SBS)	7
Two-Beam System (TBS)	8
Eight-Beam System (EBS)	10
High Energy Gas Laser Facility (HEGLF)	12
HEGLF Laser Design	17
HEGLF Building Design and Construction	23
Optical Subsystems	26
CO ₂ Laser Technology	27
II. New Laser Research and Development	42
Introduction	42
Oxygen and Other Group-VI Lasers	42
Excited State Potential Curves and Matrix Elements for Rare-Gas Oxides	46
Metal-Vapor Lasers	53
Optical Damage	56
III. Laser Fusion -- Theory, Experiments, and Target Design	62
Wavelength Scaling - Theoretical and Experimental Results	62
Target Experiments at 1.06 and 10.6 μm	63
Theoretical Studies of Laser Fusion	68
Target Design	77
IV. Laser Fusion Target Fabrication	83
Introduction	83
High-Pressure DT Gas-Filled Targets	83
Nondestructive Fuel Gas Analysis	90
Plastic Film Fabrication	91
Cryogenic Targets	92
V. Target Diagnostics	96
Introduction	96
Multiwave Picosecond Interferometry of CO ₂ Laser-Produced Plasmas	96
Target Alignment System for CO ₂ Laser Systems	98
X-Ray Microscope Development	98

	reflectance Measurements for 1-ns Laser Pulses at 10 μm	98
	Data Acquisition and Processing	99
VI.	Applications of Laser Fusion -- Feasibility and Systems Studies	101
	Laser Fusion Reactor Studies	101
	CAPITAL - A Fortran Program for Estimation of Capital Costs of Laser and Laser Fusion Experimental Facilities	107
	Commercial Application of Thermionic Conversion Using a Laser Fusion-Reactor Energy Source	109
VII.	Resources, Facilities, and Operational Safety	114
	Manpower Distribution	114
	Facilities	114
	Operational Safety	114
VII.	Patents, Presentations and Publications	115
	Patents	115
	Presentations	115
	Publications	116

Progress Report on the

LASL LASER FUSION PROGRAM

October 1 – December 31, 1976

by

Eugene Stark and the Staff of the Laser Research and Technology Division

Edited by

Frederick Skoberne

ABSTRACT

Progress in the development of high-energy short-pulse CO₂ laser systems for fusion research is reported. The Single-Beam System was used for target experimentation, and its optical train was improved. The initiation of two-beam target experiments on the Two-Beam System is described. Progress in construction checkout of the Eight-Beam System is continuing. The prototype program and HEGLF system design are discussed. Work in optical subsystem development, short-pulse amplification, and saturable absorbers is described.

Progress is reported in several areas of rare-gas oxide laser development and in the demonstration of damage-resistant reflectors. Heat-pipe metal vapor containment and work on dimeric mercury are described.

Significant new support for our previously outlined understanding of wavelength-scaling in laser-target interactions is presented. The theory and predicted performance of vacuum insulation for preheat control is discussed. Our design codes predict good performance of new conical and ion-driven implosion targets. Improved methods of characterizing and coating laser fusion targets are reported. Advances in x-ray microscope design, laser scattering measurements, and other diagnostics are discussed.

New results of our feasibility and systems studies are reported, including the effects of alternative pellet structural materials on pellet output and reactor wall sputtering, a cost-estimation code, and thermionic converters for reactor topping cycles.

SUMMARY AND PROGRAM OVERVIEW

CO₂ LASER PROGRAM

0.25 ns and a pulse duration of 0.87 ns FWHM.

Single-Beam System (SBS)

This system includes an oscillator and four electron-beam-controlled amplifiers. Three amplifiers were used in the first 10.6- μm laser target experiments early in 1973, delivering 10 J in a 1-ns pulse. Since then, the SBS has been upgraded to generate 250 J in 1-ns pulses and to deliver 180 J to a target with peak intensity of $7 \times 10^{14} \text{ W/cm}^2$. The SBS also serves as a developmental test bed for new laser-system components, e.g., oscillators, isolation schemes, and optical systems. Progress is summarized as follows:

- An upgrade of the optical train was begun to increase system stability, improve beam quality, and facilitate beam alignment.
- An atmospheric-spark retropulse isolator was installed on the oscillator table and functioned adequately.
- Several components to simplify beam alignment on structured targets were installed.

Two-Beam System (TBS)

The heart of this system is a dual-beam amplifier module in which two gain chambers share one cold-cathode electron-beam ionization gun. The oscillator pulse is split into two beams, each of which is amplified in three passes through a single gain chamber. The TBS was originally intended only as a prototype for the Eight-Beam System. However, when the need for additional laser capability at higher intensities became apparent, the TBS program was enlarged to include a target irradiation capability. The design point for the TBS is a total output of 2 to 4 TW, or $\sim 1.25 \text{ kJ}$ per beam in a 1-ns pulse. Specifically, the following progress was made:

- The first two-beam CO₂ target experiments were begun.
- Measurement of the output pulse with a 5-GHz oscilloscope revealed a risetime of

Eight-Beam System (EBS)

This system will include an oscillator, preamplifiers, and four dual-beam amplifiers, with a design-point performance of 10 to 20 TW in a 0.25- to 1-ns multiline pulse (maximum energy output, 10 kJ in 1 ns). This design point should be reached in March 1978, with target experiments to begin shortly thereafter. Progress is summarized as follows:

- The front end (oscillator and preamplifiers) has been fired from the main EBS control console for energy extraction measurements. At derated amplifier operation, single-beam output energies as high as 544 J were observed.
- Construction of the system continues on schedule.

High Energy Gas Laser Facility (HEGLF)

The HEGLF, planned for completion in 1982, represents a major step in laser fusion research. This system is expected to demonstrate scientific break-even (i.e., fusion yield equal to incident laser-pulse energy) and will serve as a major test bed for the study of a variety of target designs. It will be subsequently available for laser engineering-optimization studies for a prototype reactor. The power stage of this system will consist of six large annular amplifiers, which will yield 100 to 200 TW in a 1- to 0.25-ns pulse, respectively (maximum energy output, 100 kJ in 1 ns). The associated target irradiation facility will permit the symmetric irradiation of a fusion pellet by the six beams.

We feel that this program represents a least risk path to scientific break-even. The system represents a reasonable extrapolation of existing technology and engineering. Major subsystems will be evaluated in a prototype program. Progress is summarized as follows:

- The prototype program is proceeding with testing of the gridded electron gun,

construction of the prototype module, modification of the high-voltage test facility, and design work on the prototype pulser.

- A parametric design study was performed to optimize the integral design of the power supply, transmission cables, and power amplifier, given the beam size and amplification requirements.
- A prospective optical design was developed, treating each sector of each annular amplifier as a separate optical system. Forcing the beam through a spot focus inside the Power Amplifier Module (PAM) provides retropulse protection. In this design, only the final focusing mirror is parabolic; thus, alignment errors earlier in the train demand only pure beam steering for correction.
- Work began on the thermal and mechanical aspects of polishing NaCl flats for the PAM output windows. An annular-pitch polisher should provide the best control.

Optical Subsystems

The size of laser fusion targets and the length of laser systems impose severe requirements on optical subsystems. Alignment must be straightforward and quickly adjusted on a day-to-day basis. The systems should be stable against internal or environmental disturbances for several hours. These requirements have led to the assembly of a small task-force section responsible for the design, installation, and maintenance of optical subsystems and for system upgrades in our operating CO₂ laser systems. Highlights of our progress in this area follow:

- The Hartmann test alignment scheme has been completed on the TBS. The two focal spots have been aligned to coincide within 25 μm.
- A modified triple-pass optics system was installed on one beam of the EBS and eliminated the four-pass oscillation of the previous design.

CO₂ Laser Technology

Scientific support for our CO₂ system development program includes studies of short optical-pulse generation techniques, system isolation from parasitic oscillations, laser-system diagnostics, and other work to improve and optimize system performance. For example, oscillator pulses containing multiple rotational transitions will increase both pulse energy and peak intensity significantly and will reduce the risetime. Target deposition of only 50 μJ by parasitic oscillations or by laser precursor pulses can melt the target prior to the arrival of the main pulse; system isolation must prevent this unwanted energy deposition as well as alleviate the problem of optical damage by amplified reflections from the target. Extensive efforts in temporal and spatial beam diagnostics and in beam improvements are under way to achieve a small focused spot size. The following progress is significant:

- Calculation of multiline short-pulse amplification indicates that the TBS and EBS can produce 0.5-ns output pulses with only an oscillator retrofit.
- Studies of saturable absorption in p-type germanium have produced several important results. The absorption saturates inhomogeneously, and the spectral dependence of the saturation parameter is contrary to theory--dropping from 7 MW/cm² at 9.2 μm to 3.5 MW/cm² at 10.6 μm.
- Pulse-to-background contrast ratios have been enhanced by as much as 1000-fold by a 5-m low-pressure cell of CO₂ at 683 K.
- Complete characterization of the 5-GHz oscilloscope led to the conclusion that its bandwidth can be increased to 10 GHz by adding a compensating network.

NEW LASER RESEARCH

In the early years of laser fusion research, it was felt that the "ideal" short-pulse laser for fusion research had not yet been invented. Its desired characteristics included high efficiency,

visible or near-uv output, and a small-gain cross section coupled with high-density energy storage. However, recent experimental and theoretical results at CO₂ laser wavelengths may relax the projected requirement for a shorter wavelength.

Our efforts in new lasers are concentrated in three areas: fundamental investigations of kinetic processes and laser excitation methods, investigation of related technology areas, and establishment of a general experimental capability in electrical discharges and high-energy electron beams. Our major emphasis has been on Hg₂ and on rare-gas oxides. The following progress is noteworthy:

- Studies of the oxygen system progressed in several areas. Measurements of breakdown voltages for mixtures of argon and various oxygen donors, and estimates of the desired E/N for populating the upper laser level (1 to 2 x 10⁶ V cm²) support our optimism that stable discharge operation may be obtained at the desired E/N at 200 torr. Data on energy transfer to O₂ from several excited states of xenon and Xe₂ have been obtained and are being analyzed. Ab initio configuration interaction calculations, yielding potential energy and transition matrix elements, were performed.
- Studies of heat-pipe containment of metal vapors indicate that size and pressure scaling will require further heat-pipe research and development.
- Laser reflectors consisting of non-quarter wave multilayer dielectrics were designed and tested, and were found to have a significantly increased damage threshold.
- The discrepancy between published reports of gain on the 335-nm band of Hg₂ and our measurements of absorption have been analyzed, and a plausible explanation has been proposed.

LASER FUSION--THEORY, EXPERIMENTS, AND TARGET DESIGN

The laser fusion program is a coordinated effort in theory, experiment, and target design.

Because the interaction of high-intensity laser pulses with target plasmas represents a new regime of physics not previously studied in detail, there have been many uncertainties in modeling the relevant processes. Experimentally, we require precise spatial and temporal resolution, the spectra of emitted particles and radiation, as well as a complete characterization of the incident laser pulse. These experiments are conducted to test theoretical models and often lead to major modifications of theory. Theoretical efforts examine, for example, the various light-absorption mechanisms, hydrodynamic motion and instabilities, energy-transport mechanisms, and the deposition of nuclear reaction products. In turn, target design efforts must take account of our present theoretical understanding and of problems that may have arisen with previous designs. Significant progress was made in various areas.

- Continued studies of wavelength scaling in laser-target interactions indicate a weak ($\lambda^{0.5}$) wavelength dependence of suprathermal electron temperature at intensities of interest. Data from eight laboratories agree well with the scaling

$$T_h \sim (P_1 \lambda^2)^\delta,$$

where $\delta = 0.67$, for $P_1 \lambda^2 \leq 10^{15}$, and

$$\delta = 0.25 \text{ for } P_1 \lambda^2 > 10^{15} (\text{W } \mu\text{m}^2/\text{cm}^2).$$

Observations of the intensity dependence of K α radiation from layered targets confirm the $P_1^{0.25}$ scaling. Theoretically, we now understand this scaling to arise from steepening of the plasma density profile and from resonant absorption in the dominant absorption mechanism. These two factors imply a very short absorption scale length, and this explanation is supported by particle-in-cell simulations.

- Measurements on the Nd:glass system showed that the emitted x rays are polarized, indicating an anisotropic electron velocity distribution.

- Calculations of preheat control by vacuum insulation indicated that a vacuum gap of a few hundred micrometers decreases target fuel preheat by more than 1000-fold.
- Yield ratios of nearly 20 have been obtained for ion-driven implosion targets, which utilize symmetric laser irradiation only for ion production.
- A conical target in lead has been designed for our CO₂ laser systems. Two-dimensional calculations predict that 10⁷ neutrons should be produced if 10 J are absorbed by the cap on the conical region.

LASER FUSION TARGET FABRICATION

Fabrication and characterization of target pellets are important areas of supporting technology in our laser fusion program. Small, often complex, target pellets must be fabricated to strict specifications, e.g., filling a sphere to several hundred atmospheres with DT and depositing a uniform DT-ice layer on the inside of a microballoon. The characterization of completed pellets is also an important and challenging task. Our progress in this effort included the following:

- The code for interferogram calculation was extended to accommodate multiple shells of different refractive index. It can now be used to calculate interferograms of cryogenic targets of liquid or solid DT on the inside surface of a glass microballoon.
- Improvements to our chemical vapor deposition apparatus permit us to reproducibly deposit smooth, stress-free coatings of Mo₂C at least 6- μ m thick. Preliminary measurements indicate a strength of ~276 MPa (40 kpsi) and a hydrogen permeability ~4% that of molybdenum metal.
- We have fabricated targets consisting of a conical cavity in lead, filled with DT and

capped with a plastic film.

- Films of normal or deuterated polyethylene can now be fabricated in thicknesses from 200 nm to 500 μ m.
- We have developed several techniques for cutting laser entrance holes in spherical shells to produce microspherical blast-wave generators for some military applications experiments.
- Using the interferogram calculation code, we estimate that a thickness uniformity of \pm 20% has been achieved in DT-iceshells produced by our fast isothermal freezing technique.

TARGET DIAGNOSTICS

Measurements of laser-plasma interactions, which may last from 50 ps to 1 ns, impose severe constraints on the diagnostics, requiring much equipment to be designed in-house and pacing the state of the art in many areas. Progress in diagnostics development included the following:

- A system for multiwave picosecond interferometry is being developed for measuring the evolution of density gradients in CO₂ laser-produced plasmas. The system includes a modelocked Nd:glass laser that can be synchronized to a CO₂ laser oscillator. The 1- μ m pulses from the Nd:glass laser can be converted to 0.53 and 0.35 μ m with a KPD crystal. A double-grating interferometer provides the desired spatial resolution. The goals of this system are 5-ps temporal resolution and 1- μ m spatial resolution.
- An elliptical reflector has been built to measure the scattering from a flat target. This system should resolve the rather large discrepancy in reported reflectance measurements. Both integrated and time-resolved measurements will be possible.
- We have improved our x-ray microscope design. Choice of a simple test pattern permits calculation of the image of actual

x-ray sources with the design code XMIC, assuming perfect optics or optics with given surface errors or roughness. This technique was used successfully to evaluate a micromachined optical element.

APPLICATIONS OF LASER FUSION -- FEASIBILITY AND SYSTEMS STUDIES

Our feasibility and systems studies are performed to analyze the various commercial and military applications of laser fusion, and to identify technological problems requiring long-term development. Analysis, optimization, and tradeoff studies are performed on conceptual power-plant designs, and alternative applications of laser fusion are investigated. Progress was made in recent studies that have included the following:

- The computer codes CERES and LASNEX are being used to study the effects on fusion-pellet output of variations in structural materials in basic pellet designs. Methods have been developed for estimating trends in sputtering erosion for use in conjunction with pellet output

parametric studies, without the necessity of performing detailed sputtering calculations. With minor exceptions, these analyses indicate decreases in the total amount of sputtered material as the atomic weight of the pellet debris is increased.

- A first version of a FORTRAN computer program, CAPITAL, for use in estimating both direct and indirect capital costs at varying levels of sophistication for proposed laser and laser fusion experimental facilities has been written and tested.
- A preliminary assessment was made of the use of high-temperature thermionic converters as a topping cycle for laser fusion reactors. The topping cycle could be used to produce low-voltage direct current for electrochemical processing. For the design studied, energy deposited in the reactor cavity and heat rejected by the topping cycle are used in a conventional steam-turbine conversion cycle. Net conversion efficiencies of the combined cycles are high, and substantial reductions in production costs for the total electric output can be realized.

I. CO₂ LASER PROGRAM

The research and development programs on high-energy short-pulse CO₂ lasers were begun at LASL in 1969. Three large systems are now either operating or are being installed. The Single-Beam System (SBS), a four-stage prototype, was designed in 1971 and has been in operation since 1973 with an output energy of 250 J in a 1-ns pulse with an on-target intensity of 7.0×10^{14} W/cm². Target experimentation has begun on the Two-Beam System (TBS), which will ultimately generate pulses of 2 to 4 TW for target-irradiation experiments. Construction is under way on all subsystems of the Eight-Beam System (EBS), which is scheduled for completion in March 1978, and will begin target experiments at 10 to 20 TW shortly thereafter. A fourth system, the High Energy Gas Laser Facility (HEGLF), is in design and prototype stage. This system will generate laser pulses of 100 to 200 TW.

SINGLE-BEAM SYSTEM (SBS)

(G. Schappert, C. Landahl, K. Ware, K. Mitchell)

Introduction

The Single-Beam System (SBS) is operated both as a service facility for single-beam laser target-interaction experiments at 10.6 μ m with a 1.0-ns pulse as well as a developmental system for many aspects of operating and controlling high-energy CO₂ lasers systems for target experiments. The SBS consists of a gated oscillator and four electron-beam-sustained amplifiers. The system delivers on target a maximum intensity of 7×10^{14} W/cm² and yields new information for fusion-target design development.

In addition to using the SBS as a target-irradiation facility, we are continuing to upgrade the SBS to produce higher target irradiances. This upgrading involves reducing the problems of laser-pulse feedthrough, self-lasing and retroreflected pulses, and improving the beam quality.

During this quarter, we brought the SBS back on line for target experimentation and initiated a major upgrade of the whole optical train. Progress made and problems encountered are outlined below.

Electron Gun of Amplifier 4

After retrofitting the electron-gun filament support structure in Amplifier 4, the maximum electron-beam current was only 60% of the expected normal operating current. This reduced the pumping-chamber current, and hence the stored optical energy by ~22%. Despite this problem, the

system can deliver 100-J pulses, which is adequate for our present target experiments.

During the retrofit, we discovered an out-gassing problem, which was eventually traced to boron-nitride spacers used to insulate the individual filament support springs from the helper springs. A chemical analysis of these spacers indicated a gas content of 6% by weight. New spacers and filaments are being obtained, and the filaments may be overhauled again, depending on, e.g., energy demands and scheduling of target experiments.

Optical-Train Improvement

A complete upgrade of the SBS optical train was initiated. The configuration of the oscillator table is being changed and the beam-expansion optics between Amplifiers 2 and 3, the cells for the saturable-absorber gases, and the windows (Polytran NaCl) for all amplifiers will be replaced with new components.

We moved Amplifiers 1 and 2 closer to the oscillator and to each other. In this configuration we can connect the two pumping chambers, eliminating two windows. Further, the distance between Amplifiers 2 and 3 is now long enough so that a two-mirror beam-expansion telescope can be used. Previously four more mirrors were required to steer the beam through the appropriate telescope. Five new mirror stands have been installed.

These changes provide better beam stability, improved beam quality, and easier system alignment.

Temperature Problem

Daily temperature variations of 5 to 10 K make it difficult to keep the components on the oscillator table aligned. Four thermostatically controlled electric heaters have since been able to keep the temperature variations within ± 1.5 K, which solved the worst of our alignment problems.

Anticipating large temperature variations during the summer, we are investigating some simple but effective methods of temperature control for the oscillator environment.

Retropulse Isolation

Laser energy reflected from the target back through the amplifier chain (retropulse) is a serious problem because of the damage the converging beam can inflict with even a few joules of energy. We have installed on the oscillator table a simple coaxial spark gap of brass needle points (6-mm-diam rods) spaced ~ 10 mm apart, which effectively blocks the retropulse. The atmospheric spark gap is fired by a commercial pulse generator capable of a 70-kV, 50- Ω terminated pulse with a 1-ns risetime. The unit is fired by the oscillator discharge-voltage trigger with appropriate delays and intermediate triggering units to close the gap 40 to 100 ns after passage of the switched-out oscillator pulse. The setup may experience some jitter for a few nanoseconds, but in its present application does not require better control. The isolating spark has a diameter of ~ 1.5 mm, as indicated by burn patterns taken behind the spark channel, and probably has an effectively larger cross section that diffracts or scatters the laser beam. We monitored the spark channel with a photodiode to time the optical output relative to the switched-out oscillator pulse. With this diagnostic tool, we have optically verified that the light emitted by the retropulse is absorbed by the spark channel ~ 480 ns after the oscillator pulse had passed. This delay corresponds to a round-trip path length from oscillator to target and agrees with the physical distances of the beam path.

Beam Alignment on Structured Targets

The following installations have been completed:

- The motor-driven turning mirror in part of the target chamber is operational. The stepping motors and digital readouts are calibrated, permitting a controlled pointing of the beam.
- The mechanical target wheel with 12 stations is in position and is routinely used for target experiments.
- The pyroelectric quadrant detector, being a reference point on the target wheel, has been tested. These preliminary tests indicated that this system is not yet ready for routine implementation and may require better electronics.

Experience during this quarter has shown that the target-alignment procedure is still far from satisfactory. Furthermore, questions have arisen concerning the short-term beam-position stability. Full-system target experiments with ~ 100 -J pulses were conducted. The SBS is now ready for target experiments on a daily basis.

TWO-BEAM SYSTEM

(J. V. Parker)

Introduction

The two major functions of the Two-Beam System (TBS) are to serve as a developmental prototype for the dual-beam modules of the Eight-Beam Laser System (EBS), and to provide a facility for target irradiation experiments for military and laser fusion applications. This quarter marks the transition from a primary emphasis on prototype functions to a primary concern with target irradiation experiments.

During October and November 1976, we fired 85 single-beam target shots at a variety of foil targets. Output energies ranged from 20 to 385 J in 1-ns pulses. Target damage due to parasitic oscillations in the DBM continued to be an annoying problem when operating at the higher output energies. Of the 85 target shots fired, 48 were considered satisfactory (no prelasings, no data-collection problems), 27 were compromised by prelasings, and 10 were lost due to various malfunctions.

During December 1976, the TBS was made ready for two-beam operation. The Hartmann alignment system was brought into operation. The Hartmann test, performed at $10.6\ \mu\text{m}$ has been demonstrated to be a convenient means of achieving two-beam alignment on a common focal point with $< 50\text{-}\mu\text{m}$ error in pointing and $< 150\text{-}\mu\text{m}$ error in the focus direction.

The first two-beam target shot was fired successfully on December 23, 1976.

System Development (J. P. Carpenter, M. Nutter)

The changeover from prototype evaluation to target-irradiation experimentation significantly decreased both the amount and the type of development work performed on the TBS. During this quarter and in the future, most of the development effort will be directed toward refinements in the TBS and its operating system rather than toward major changes, with the exception of an optics retrofit.

An additional gas-pressure control panel was installed to provide independent adjustment of the spark-gap pressures for the two Marx generators. We found independent adjustment necessary because changes in spark-gap breakdown voltage with operating life are not consistent, even for physically identical gaps.

Our computerized data-logging programs have been expanded to handle an additional eight channels of fast analog data to accommodate two-beam operation.

Dual-Beam Module (J. P. Carpenter, A. Patrick)

We have modified the new optical system for the DBM to correct several design deficiencies. In particular, we added an access port to facilitate the adjustment or replacement of mirrors, and modified the input aperture to clear the incoming beam. The modified optical chambers have been reassembled for final testing prior to installation, and the remotely controlled mirror mounts have been wired and checked for proper operation.

The temporal behavior of the DBM output pulse was examined with a Laser Precision KT-1520 pyroelectric detector coupled through 50 ft of foam-flex cable to the 5-GHz scope. The measured rise-

time of a 200-J pulse was 250 ps. The pulse decayed exponentially with a 0.96-ns time constant resulting in a FWHM of 0.87 ns and an effective pulse width ($\equiv \frac{\text{Energy}}{\text{Peak Power}}$) of 1.18 ns.

Computer calculations predict that the risetime should be 100 ps for our present operating conditions; the observed risetime was much too long and might have been affected by the detector-cable combination. Pulse risetime will be measured with a faster detector.

On December 23, the first two-beam target shot was made successfully at a reduced energy of $\sim 85\ \text{J}$ per beam. Two-beam experiments at higher energies will continue into the next quarter.

Oscillator-Preamplifier System (J. Hayden)

In addition to its principal function of driving the DBM, the preamplifier-oscillator system is now used routinely to provide pulses for the Hartmann alignment apparatus. During this quarter, we examined the output-pulse characteristics of the oscillator-preamplifier system with a fast pyroelectric detector and with the 5-GHz oscilloscope. The overall pulse shape was of lower quality than expected. Pulse widths ranged from 1.8 to 2.5 ns, with the longer pulses showing distinct double peaks. This feature is attributed to poor modelocking and points out the inadequate stability of the present oscillator.

Fortuitously, the poor quality of the oscillator pulse is not important to the system operation, because the DBM output-pulse shape depends most strongly on the risetime of the input pulse. The measured risetime of the oscillator-preamplifier output pulse is 350 ps, controlled by the bleaching characteristics of the SF_6 cell located between Preamplifiers 1 and 2. The risetime decreases with SF_6 pressures until it reaches 350 ps at 8 torr cm. For higher pressures, the risetime remains constant.

In some target experiments, postpulse noise was a distinct problem. We have developed a technique for eliminating these postpulses and obtained encouraging results in preliminary tests. However, because implementation of this method requires substantial modifications to the system alignment, it will be postponed until the TBS is

shut down for installation of the new optical system.

EIGHT-BEAM LASER SYSTEM

Introduction (S. Singer)

The Eight-Beam Laser System (EBS) represents the next generation of high-power short-pulse CO₂ laser systems we will use to study the interaction of intense light beams with matter, with emphasis on investigating problems relating to laser fusion. This system is designed to deliver 10 to 20 TW to a target--10 kJ in a 1-ns pulse or 8 kJ in a 0.25-ns pulse. The EBS will consist of an oscillator-preamplifier system which generates a 0.25-ns multiline optical pulse at the several-hundred-megawatt level, and which will drive four DBMs clustered around a target chamber. Each of the eight 35-cm-diam beams will deliver ~ 650 to 1250 J (depending on pulse length) to the target chamber, which will contain an optical system to focus these beams onto a target.

The front end of this system is operational and is being used to support multiline energy-extraction and pulse-shape measurements on one side of the first DBM. Construction of the other DBMs is on schedule.

Front End (R. Carlson, J. Ladish)

We have assembled the front-end components for one beam of the Eight-Beam System and have fired the assembly from the control room in synchronization with the peaking of the gain in Module A of Amplifier 1. A multiline, 1-ns (FWHM) Gaussian pulse was propagated simultaneously from the front-end room through the triple-pass system for energy extraction measurements.

The present configuration of the front end was evaluated by measuring each component, identifying the shortcomings of each, and assessing the synergistic effect.

The single-beam output energy is typically 50 to 70 mJ, repeatable within $\pm 20\%$. The front-end pulse is Gaussian, of 1-ns duration (FWHM), and operates on at least three lines of the 10- μ m band [P(16), P(18), and P(20), with P(14) and P(22) intermittent]. Spatial filters, saturable absorbers, and repopulate isolators have been

incorporated into the front end. The p-doped germanium saturable absorber has contributed to pulse-shortening and has increased the extinction ratio from 3.5:1 to between 100 and 500:1. Timing of the system is via a Jorway clock and a delay generator, which can be triggered either locally by the front-end room or remotely by the control room. Timing accuracies between events can be set to within 100 ns. Emphasis will now be placed upon improving system beam quality, optical-component integrities, prepulse energy suppression, other TEA oscillator cavity configurations, and the use of gallium-doped germanium saturable absorbers.

Triple-Pass Amplifier Stability Studies (J. Ladish, M. Montgomery)

A series of measurements under varying conditions proved that the 38-cm (15-in)-diam mirror mounted in the pumping chamber actively participated in parasitic oscillations. The present configuration of the triple-pass power module is limited to a single-pass stable gain strength product of $g_0L \approx 5.5$ due to diffuse scattering within the chamber and subsequent coupling to the 38-cm mirror. Further studies will determine whether use of linear or nonlinear absorbers and/or baffles will raise the parasitic instability threshold.

The results of calculations performed to examine the effects of placing a linear or nonlinear absorber in front of the mirror are shown in Tables I and II, where E_i is the input energy to the triple-pass amplifier (TPA) in millijoules, E_o is the output-pulse energy in joules, I_p is the peak output intensity in terawatts, $\Delta\tau$ is the output-pulse width in nanoseconds, g_0 is the gain in % cm, and $2\alpha l$ is the absorption length product (two passes) of the absorber. The pressure was 1800 torr and the round-trip gain loss product was held constant at an assumed stable value of 5, i.e., $2g_0L - 2\alpha l = 10$. The input pulse width was 1.0 ns.

Energy Extraction Measurements

(R. Carlson, J. Ladish, M. Montgomery)

One of our major accomplishments this quarter has been the wedding of the single-beam front end to power-amplifier Module IA1 and the subsequent

TABLE I

PERFORMANCE OF P-DOPED GERMANIUM ABSORBER

E_i (mJ)	$2\alpha l = 0; g_0 = 2.5$			$2\alpha l = 4; g_0 = 3.5$			$2\alpha l = 6; g_0 = 4$		
	E_o	I_p	$\Delta\tau$	E_o	I_p	$\Delta\tau$	E_o	I_p	$\Delta\tau$
1	360	0.3	1.1	1070	1.2	0.7	1070	1.7	0.7
10	680	0.6	1.0	1230	1.4	0.7	1470	2.0	0.6
100	820	0.7	1.0	1300	1.6	0.6	1510	2.2	0.6

extraction of energy amounting to hundreds of joules per shot. The results of four separate sequences of measurements are summarized in Table III.

The input energy to the TPA (E_{in}) was measured by a pellicle-and-calorimeter assembly, whereas the output energy (E_{out}) was measured by dumping the output beam into a large-aperture calorimeter built at LASL. We used a CO_2 probe laser to monitor the small-signal gain-length product (g_0L) in the TPA during the energy extraction process. The relatively large uncertainty in g_0L ($\pm 10\%$) shown in Table III is due primarily to the gain distribution within the amplifier and not to the measurement itself.

Calculated output-energy values obtained with rate-equation code are given in Table IV for comparison.

The main differences (except where noted in Table III) between the four sequences of shots were in the attempt to improve TPA alignment through

Sequences (I-IV) and in the attempt to drive the TPA with a higher input energy.

Detailed temporal measurements will be conducted to verify predicted pulse-shortening effects expected in the multiline energy-extraction process.

TABLE III

ENERGY EXTRACTION DATA
(P = 1400 torr, FOUR-LINE EXTRACTION)

E_{in} (mJ)	E_{out} (J)	$g_0L (\pm 10\%)$	Sequence
2	74	4.8	I
3	109	4.8	I
5	138	4.8	I
8	258	3.8	II
14	460	4.5	II
6	265 (single-line extraction)	4.5	II
4	243	4.7	III
4	185 (1600 torr)	4.6	III
4	225 (1600 torr)	4.3	III
140	326	4.4	IV
130	516	4.5	IV
197	544	4.1	IV

TABLE II

PERFORMANCE OF LINEAR ABSORBER
($E_i = 100$ mJ)

	$2\alpha l$			
	0	4	6	8
g_0	2.5	3.5	4	4.5
E_o	680	815	850	880

TABLE IV

CALCULATED TPA ENERGY EXTRACTION OUTPUTS
(P = 1400 torr, FOUR-LINE EXTRACTION)

E_{in} (mJ)	E_{out}	g_0L
1	21	4.0
10	108	4.0
1	66	4.5
10	220	4.5
1	162	5.0
10	359	5.0

HIGH-ENERGY GAS LASER FACILITY

Introduction

The High-energy Gas Laser Facility (HEGLF) is a research tool to demonstrate the feasibility of laser fusion establishing scientific break-even conditions (where break-even is defined as the energy output being equal to the laser-energy input) for a deuterium-tritium fusion process. The facility requires the design and construction of a 100- to 200-TW CO₂ laser system (100 kJ in 1 ns or 50 kJ in a 0.25-ns pulse) and target facility.

Four test programs are presently being conducted to check out various considerations for the final design. These programs involve the gridded gun, the prototype module, the high-voltage test module, and the prototype pulser.

The gridded gun is complete and has been tested for the past few months. This device is used to test out a cold-cathode electron gun in cylindrical geometry with a grid control. The induced magnetic field strength is also being measured to determine the amount of pinching of the electron beam. Some results are reported below.

The prototype module is in the construction phase. Its purpose is first, to check out the gridded gun integrated with the discharge region and anode; second, to measure gain uniformity on the discharge region. Calculational results on gain uniformities are discussed below.

We are modifying the high-voltage test facility so that anode bushings as well as gun bushings may be tested.

Design work on the prototype pulser has been initiated. The pulser will be used to test the reliability of various components. The pulser consists of a bank of RLC circuits [single-mesh pulse-forming networks (PFNs)] connected by spark gaps in a Marx-generator configuration. Ultimately, there will be two pulser banks for the HEGLF system, one to drive the electron gun (known as the electron-gun pulser), and one to drive the anode (referred to as the gas pulser or pumping-chamber pulser.).

We are reporting herein on the ongoing theoretical parameter studies; on the status of electrical, mechanical, and optical designs of the

power-amplifier module (PAM); and on the target subsystem.

The HEGLF should operate, in a multiline mode, on 4 to 6 lines of the 10- μ m band, and at a gain-length product of 6. The power amplifier will have three or four sections of amplification to reduce the induced magnetic fields. Three systems are being analyzed for the optical design, differing mainly in the geometry of retro-pulse isolation. In all three, the retro-pulse is blocked by gas breakdown. In the first system to be discussed, breakdown is brought about by a ring focus; this design is very difficult to align and expensive to fabricate. The second, a point focus system, requires that an aberration imperfection be introduced in the optical system before the breakdown point and then removed after the focal point; this may be an acceptable design. In the third method, breakdown is attained by overlap of a narrow collimated beam that is folded back on itself by a mirror placed at an angle in the beam; this optical system is being analyzed.

The HEGLF system will be controlled by means of a central minicomputer, with microprocessors distributed throughout the facility, connected with fiber-optic cables.

The design of the buildings to house HEGLF is now at 30% of Title II and proceeding well. A preliminary safety-analysis report has been prepared for ERDA. Calculational estimates of neutron-dose rates have yielded design parameters for radiation shielding.

Preparations for procurement of the target-chamber vacuum system and of NaCl windows are proceeding on schedule.

Prototype Programs

Cold-Cathode Gridded Gun (W. Leland) Systems, Science and Software (S³) was engaged to design, build, and test a grid-controlled, cylindrical, cold-cathode gun with design-goal specifications appropriate to the anticipated requirements for a HEGLF power-amplifier module. Figure 1 shows a schematic of the gun, which has an active length of 280 cm and an anode diameter of 135 cm. The 53.4-cm-diam cathode is equipped with 12 emitting blades spaced equally around its

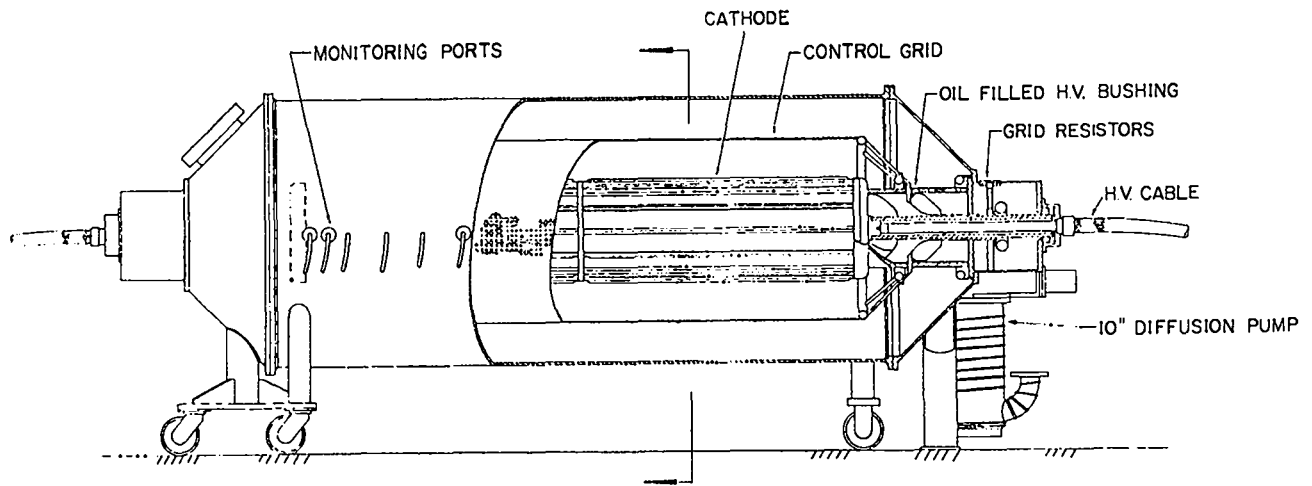


Fig. 1
Systems, Science and Software's gridded cold-cathode electron gun.

circumference and running the length of the cathode (280 cm). The grid consists of an 80%-open, perforated metal cylinder 280 cm long and 95.6 cm in diameter. The grid is supported at each end by a metal cone attached midway along the high-voltage bushing, which supports the cathode. Electrically, the design specifications called for operating voltages from 300 to 500 kV and an emission current density, variable by grid control, between 20 and 200 mA/cm² as measured at the anode. Emission pulse duration of up to 5 μs was specified. Our test program was designed to determine the degree to which design goals had been met, as well as to provide data on magnetic-field limitations inherent in such devices.

The design produced by S³ is based on the cathode-grid structure operating as a space-charge-limited cylindrical diode. The grid, being 80% open, would allow 80% of the current to continue to the outer shell or to the anode. An operating pulse of -300 to -500 kV is applied to the cathode by two high-voltage cables feeding the cathode ends. The grid, connected to ground via a resistance, intercepts a portion (20%) of the emission current and assumes a negative potential determined by the size of the grid resistor and gun geometry. By adjusting the size of the grid resistor the emission currents can, in effect, be adjusted to any desired value for a given cathode potential.

Test data relating measured emission current to grid resistance are presented in Fig. 2.

Agreement with prediction is well within experimental error. One can safely conclude, therefore, that grid control can be used to adjust the gun current to any value required for proper gas-discharge impedance.

Magnetic-field effects were diagnosed in the test program by measuring the longitudinal anode-current distribution for various values of total gun current. Typical data are shown in Fig. 3. In this instance the gun current is 5500 A for each half of the gun.

Clearly, magnetic effects must be considered in the design of these guns to meet a given set of requirements. To some extent, increased gun length

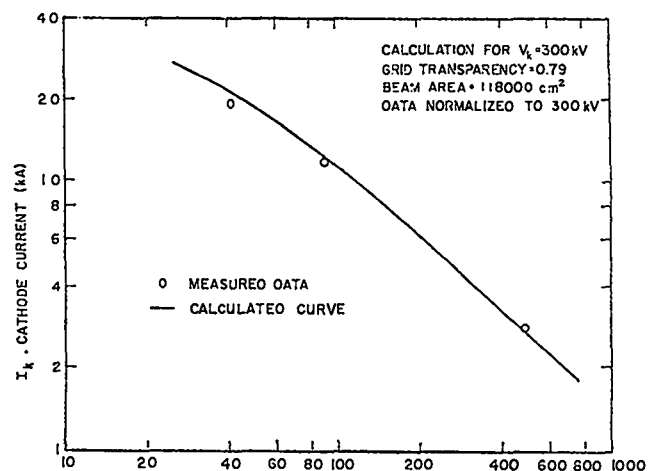


Fig. 2
Cathode current as a function of grid-resistance in cold-cathode electron gun.

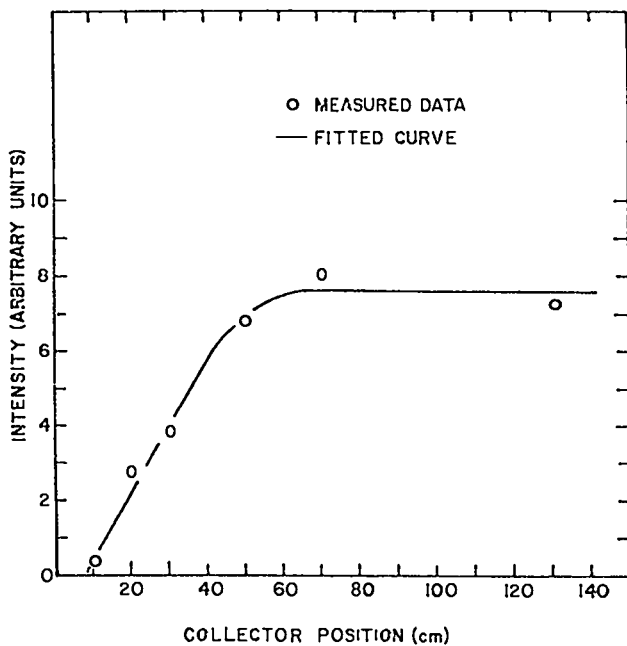


Fig. 3
Current intensity as a function of longitudinal position. Total current, 5500 A.

can compensate for end deficiencies caused by magnetic fields. In addition to the density of current arriving at the anode, both the angle of incidence and uniformity of ignition are of consequence. With the S^3 gun, uniformity appears to be within $\pm 15\%$ over areas not affected by magnetic fields, provided that operation is above 350 kV. At lower operating voltages, uniformity of cathode ignition poses some problems. Regarding the angle of incidence, the deviation from normal did not exceed 12° for the case shown in Fig. 3.

Prototype Module

Gain Uniformity Calculations (W. Leland, A. Kircher, U. Swanson, J. Comly)—The small-signal gain produced in CO_2 amplifier discharges can readily be calculated if the time histories of current density and electric field are known. However, for large-aperture electron-beam devices, the discharge may depart substantially from uniformity, and the time history of current density and electric field will vary with position in the discharge. The discharge nonuniformity results primarily from a nonuniform distribution of ionization from the primary beam and from geometry effects. Even after ascertaining the distribution of ionization from the primary beam, the nonlinear

character of the discharge creates a formidable calculational problem that must be solved to predict the spatial and temporal details of the discharge. When the discharge is powered by other than the idealized energy supplies and transmission systems, the nonlinearity of the discharge can materially affect the resulting waveforms of discharge current and voltage.

We have addressed these problems and have developed a calculational procedure for two-dimensional nonuniformities. The first step involves a Monte Carlo-type calculation capable of predicting the distribution of primary ionization with specified geometry and primary beam characteristics. Externally imposed electric and magnetic fields are also included. The next step involves calculating the time histories of current and electric field at various places in the discharge when powered by an actual energy supply and transmission line. The nonlinearity of some electrical-discharge characteristics is introduced via an experimentally measured property. For the range of interest, we assume a recombination-limited discharge. Thus $j = \sqrt{\frac{S}{\gamma}} ev$, where j is the current density, S is the primary ionization rate, γ is the recombination coefficient, e is the electronic charge, and v is the drift velocity. Nonlinearity results because $v/\sqrt{\gamma}$ is not proportional to the electric field. For a given gas mixture, $v/\sqrt{\gamma}$ is predicted and measured to be a universal function of the ratio E/N where E is the electric field and N the neutral gas number density. The measured functional dependence on E/N for the 0:1:4::He:N₂:CO₂ mixture is shown in Fig. 4, where $v/\sqrt{\gamma}$ is plotted as a function of E/N for a fixed value of S . This measured characteristic, the spatial distribution of S determined in Step 1, plus boundary conditions involving the geometry of electrodes and applied potentials are sufficient to uniquely determine the overall voltage-current characteristics of the discharge as well as the spatial variations of electric field and current density. Mathematically, the problem amounts to solving a nonlinear Poisson's equation subject to boundary conditions. Once the voltage-current characteristic of the discharge has been determined, the time history of the discharges can readily be

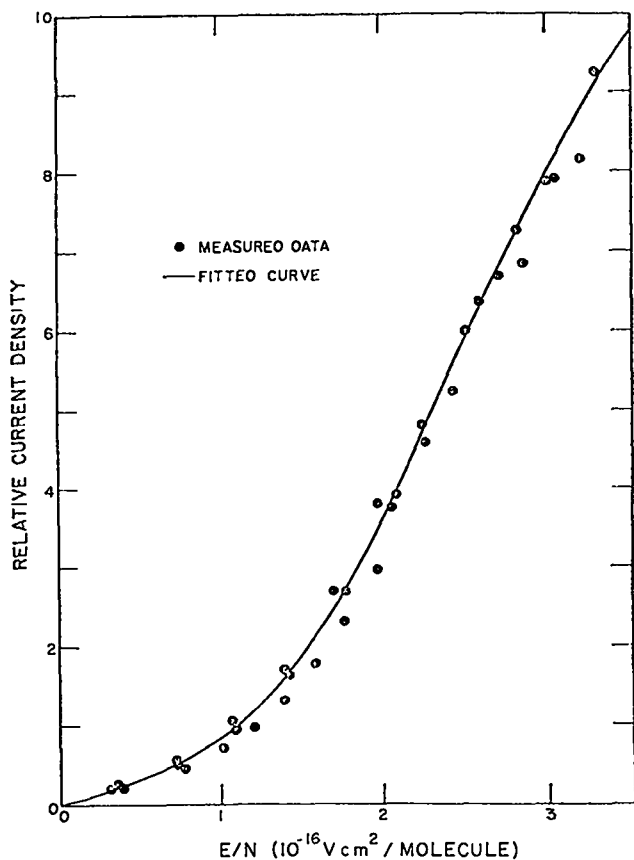


Fig. 4
Current Density as a function of E/N for 0:1:4::He:N₂:CO₂ gas mixture.

ascertained by combining this characteristic with those of the power-supply and transmission system.

The final step is the calculation of small-signal gain which, as mentioned earlier, is straightforward once the time histories of electric field and current density are known.

We have applied this calculational procedure to predict the gain distribution in an existing amplifier as well as in the prototype amplifier being built to verify several new features of the HEGLF power-amplifier design. The prototype and the HEGLF design incorporate a set of 12 discharges, arranged in cross section to form a nearly complete annular discharge. Primary electron beams generated inside the annulus are projected radially outward and enter the discharge regions as uniform beams penetrating the titanium window and the discharge cathodes. The calculated relative ionization produced by the primary beam is shown in Fig. 5. In this instance a 500-kV

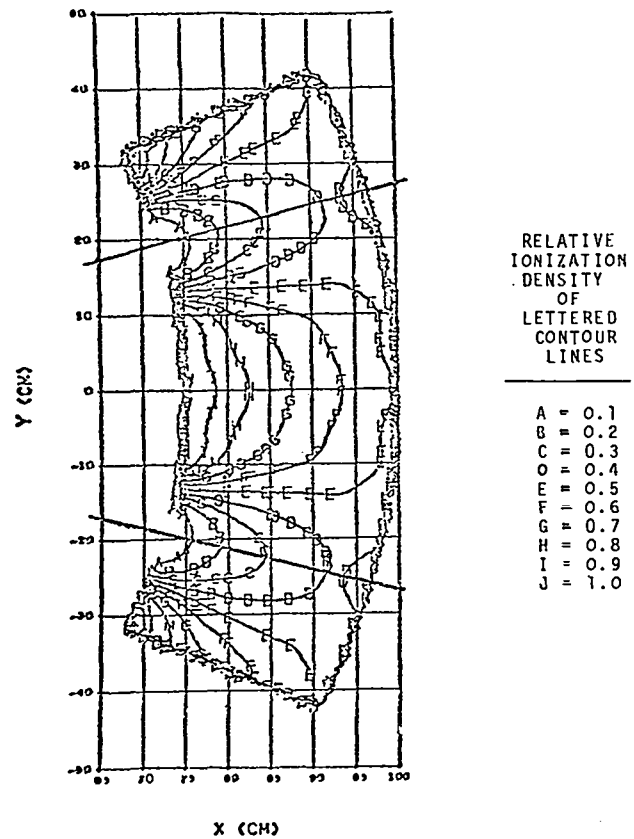


Fig. 5
Calculated symmetrical ionization density in CO₂ produced by primary electron-gun beam.

electron beam uniformly illuminates a 25-cm-wide entrance foil of 2-mil-thick titanium. An electric field of 18 kV/cm is assumed with a gas fill of 1800 torr of 0.1:4::He:N₂:CO₂ mixture. No magnetic field is assumed, corresponding to the condition at midlength. The geometry is cylindrical, with the inner and outer discharge boundaries at 75 and 100 cm, respectively. Only one of the 12 discharge regions is fully shown because all are alike.

By using the ionization distribution of Fig. 5, we calculated the expected performance of the prototype powered by a single-mesh PFN delivering power to the discharge via a coaxial cable with an overall propagation time of 0.2 μs. The resulting waveforms of current and voltage are shown in Fig. 6. The bump appearing on the voltage waveform at 0.4 μs is a consequence of the original mismatch of cable and discharge impedances at early times. Using these waveforms and the calculated distribution throughout the discharge, we

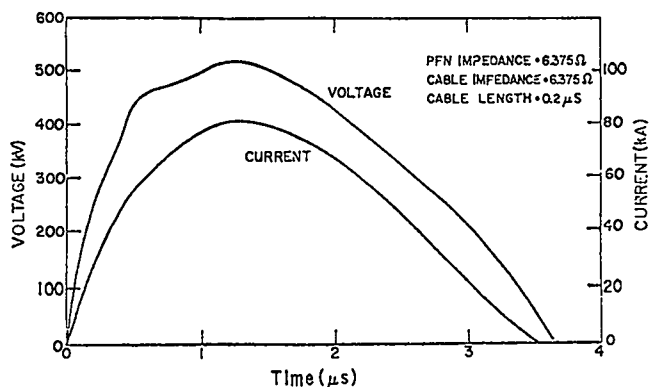


Fig. 6

Calculated current and voltage in prototype discharge supplied by one-mesh PFN connected with coaxial cable.

calculated small-signal gains for selected points throughout the discharge. Results for two configurations of electrodes are shown in Fig. 7. Small-signal gains on the P(20) line are listed at locations to which they apply. The lower set of numbers applies to a modification of the geometry, which simply involves placing an insulating barrier between anode and cathode at a position corresponding to the anode edge. This modification prevents fringing of the current and clearly improves the performance.

Prototype Module (W. Leland, T. Ganley, D. Swanson, E. Yavornik, W. Miller, K. Reipe)--Detailed design and procurement of components for the prototype amplifier module and auxiliary equipment is continuing. With a few exceptions, the design is complete. Delivery of all major module parts is scheduled for March 1977. Most building modifications have been completed. Much of the auxiliary equipment is on hand, and has been tested to the extent possible. The gun power supply has also been tested to 400 kV in air. Tests at the design voltage of 500 kV await delivery of the pressure vessel in which the module will be housed. The main discharge vessel has been assembled and check-out tests with a dummy load began in late December 1976. The gas supply system for the amplifier was also assembled and given preliminary tests. The unit utilizes sonic orifices to attain a proper mixture of CO₂ and N₂. In the first test we used bottled gas for both CO₂ and N₂, and obtained the specified mixture without difficulty. We will

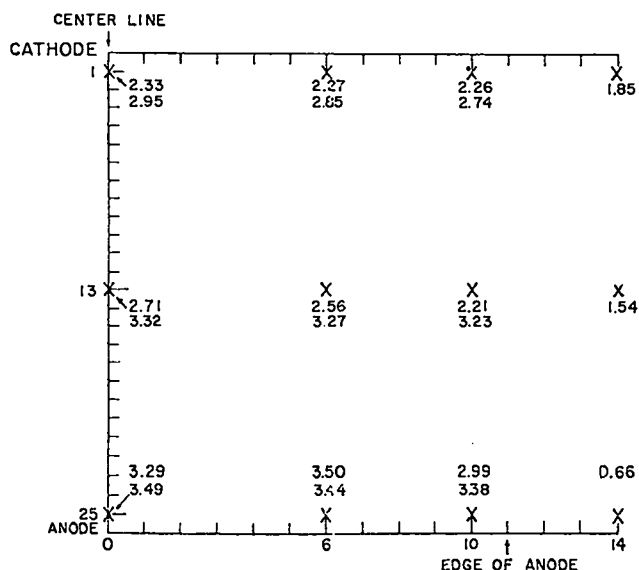


Fig. 7

Calculated gain uniformity in prototype module. Numbers represent calculated small-signal gain per meter at position marked X. Lower values are for the case of insulator between anode and cathode located at edge of anode. Upper values are for case without insulation.

continue our characterization efforts after receipt of the CO₂ supply system.

High-Voltage Test Module

(H. Jansen,

R. Lindstrand) -- A vacuum bushing test fixture enables us to test individual bushing sections so that we will not have to build and test complete assemblies during the development phase. Several electron-gun bushings and grading-ring configurations have been voltage-pulse tested, and testing continues.

The electron-gun side of the test module has been vacuum-tested and a graded-ring vacuum bushing was installed and tested for vacuum and structural integrity. An anode bushing and an anode have been assembled on the anode side of the test module to check the epoxy bushing material for mechanical creep.

The modifications to a megavolt Marx generator, which will permit high-voltage testing of the anode bushing, are near completion. The modifications will allow us to deliver a test pulse (10 to 90% risetime of 500 ns with less than 15% droop from peak voltage in 3 μs) that will simulate the anticipated operating pulse.

A control system to test the reliability of the gun bushing, anode bushing, and high-voltage

cables is being fabricated. The circuit design is finished and some of the logic boards have been built.

Prototype Pulser (K. Riepe) -- Design work on a prototype Marx generator (pulser) has begun. A low-voltage model was built and the inductance has been measured to be $2.7 \mu\text{H}$.

In support of the prototype pulser program, development and testing of reliable Marx components will be required. We will concentrate on high-energy-density capacitors and on high-current, low-prefire-rate spark gaps, but we will also evaluate high-voltage charging resistors, high-voltage relays, trigger systems, and other components and subsystems. Specifications for testing of capacitors and spark gaps have been prepared. Test plans for other components have been started.

HEGLF LASER DESIGN

Parameter Studies

Pulse Amplification (P. Wolfe, H. Volkin, J. Hafer) -- Recent experience with the Two-Beam System and the Eight-Beam System indicates that the gain-length product of 9 previously chosen and analytically verified for energy extraction in HEGLF is too high for stable operation. Our coherent-pulse propagation code was therefore extensively used to evaluate operating conditions in the neighborhood of a gain length product of 7 for the power amplifier's active regions ($g_0L = 6$ for the overall amplifier, including inactive region losses). Under these conditions, the 33% advantage of two-band over single-band operation is no longer attainable, because the HEGLF Power Amplifier Module is its own driver, i.e., the first of two passes provides the drive for the energy-extracting second pass, and the first-pass gain on the $9\text{-}\mu\text{m}$ band is now so low that impractically large inputs are needed to tap the reservoir of energy stored on that band. Thus, we are leaning toward single-band (but multiline) operation. Because the decision will now depend critically on the relationship between 9- and $10\text{-}\mu\text{m}$ gains, we are carefully reviewing the experimental and theoretical bases for the values used in our code,

Electromechanical and Discharge Studies (H. Jansen, K. Riepe) -- A parameter study was aimed at optimizing the design of the power-amplifier module, i.e., the power-amplifier proper, the transmission cables, and the capacitor-bank configuration for driving the anode. We were particularly interested in determining the number of amplifier sections, the active length of the amplifier, the pumping-current density, the required pumping energy, the number of pulsers, and the number and impedance of the cables. The following served as input: The given beam geometry; the computed and measured relationship between gain (g), time (t), and pumping current density (j), [where $g = g(j,t)$]: for two gain-length products ($g_0L = 9.0$ and 7.5). As a limiting parameter, we introduced the maximum permissible azimuthal magnetic field in the gas region.

Typical results for the $g_0L = 7.5$ case are plotted in Figs. 8, 9, and 10. Figure 8 shows how the number of amplifier sections and the maximum magnetic field determine the operating point in gain-vs-current density regime for pumping to peak gain and fractions thereof. Pumping to less than peak gain is proposed to save stored energy. Figure 9 shows the necessary active amplifier length and pulse time for the above conditions, and Fig. 10 shows the permissible pulser inductance per laser-beam sector for a single-mesh gas pulser. As an example, a three-section amplifier operating with a maximum magnetic field of 350 G would require a pumping current density of 5 A/cm^2 for pumping to $0.9 g_{\text{peak}}$. The active length would have to be 3.35 m and the allowed inductance per beam would be $11 \mu\text{H}$. If an inductance per pulser of $2.7 \mu\text{H}$ could be realized, we would be able to drive four beams with one pulser, resulting in a total need of only 18 pulsers. The stored electric energy per beam would be 78 kJ . The cable impedance per section would be 27Ω , which is achievable with one cable.

Electrical Design of Power Amplifier Module

(H. Jansen, K. Riepe) -- Design of a Marx generator which will be used as a single-mesh pulse-forming network to drive the pumping chamber has begun. The configuration is shown in Fig. 11. Although the design does not offer the lowest inductance, it

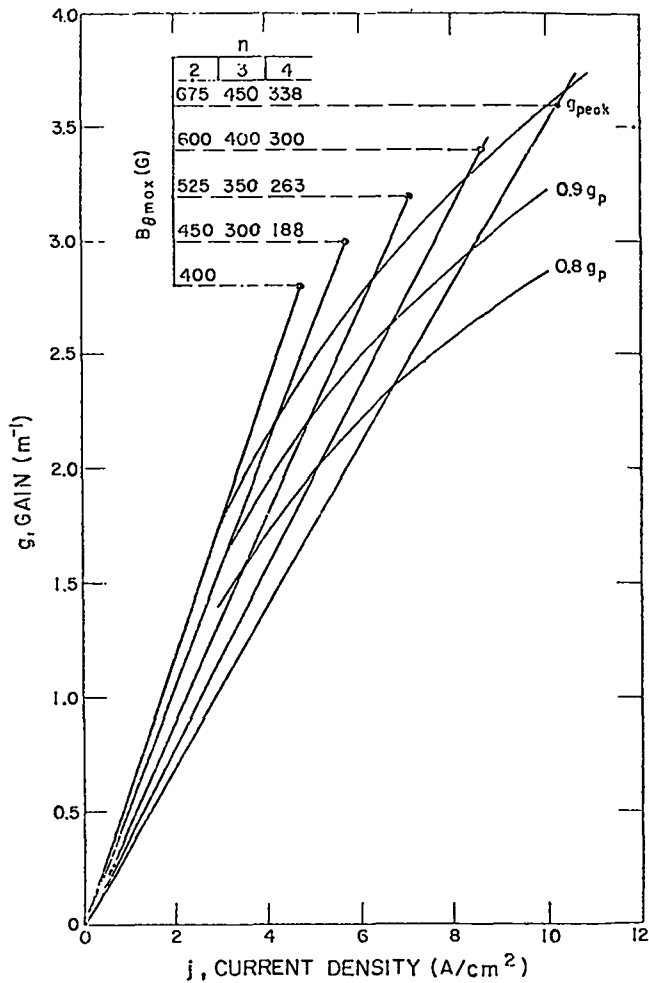


Fig. 8

Gain vs current density for pumping CO₂ power amplifier to 0.8 g, 0.9 g, and g_{peak}. Maximum azimuthal magnetic field, B, and number of axial anode sections (n) are used as parameters.

has been chosen for its mechanical simplicity and efficient use of space.

An electron-gun pulse circuit, using a pulse transformer inside the gun, was modeled, and a parameter study has been performed to determine the effects that a pulse transformer may have on the ignition characteristics of the gun. A gun-voltage rise rate at the moment of ignition of ~ 5 kV/ns seems to be desirable based on experience with other cold-cathode guns. Transformer designs that can achieve such a rate of rise have been evaluated. It seems that transformers can be designed without too much deviation from well-tested existing units.

Work on the preliminary design of the gun and of gas bushings for the power amplifier continued.

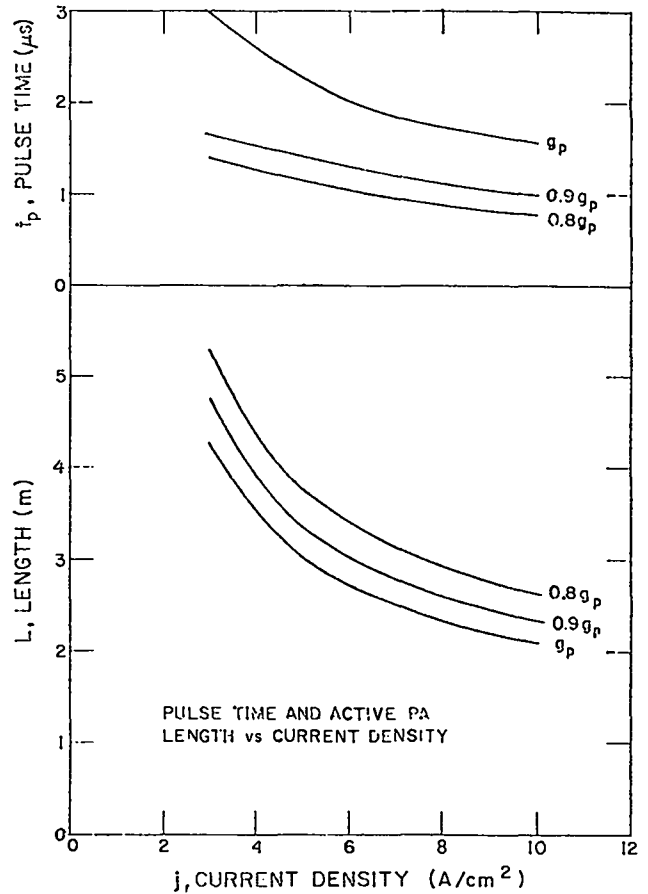


Fig. 9

Pulse time and active power-amplifier length as functions of current-density.

Mechanical Design of Power Amplifier Module

(V. Zeigler, H. Jansen)

A reference power-amplifier design has been selected utilizing three amplifier sections with a total length of 3.3 m. The design provides for vacuum pumping and power feeds to the electron guns at two stations: between the first and second, and between the second and third amplifier sections. Designs for other critical mechanical aspects of the power amplifier were selected. The basic concept is being reviewed prior to initiation of preliminary design work. Figures 12 through 14 show this reference design.

Optical Design and Analysis

Power Amplifier Baseline Systems

(J. Munroe, K. Jones, W. Reichelt)

General -- The optical design for the HEGLF power-amplifier module has evolved from the

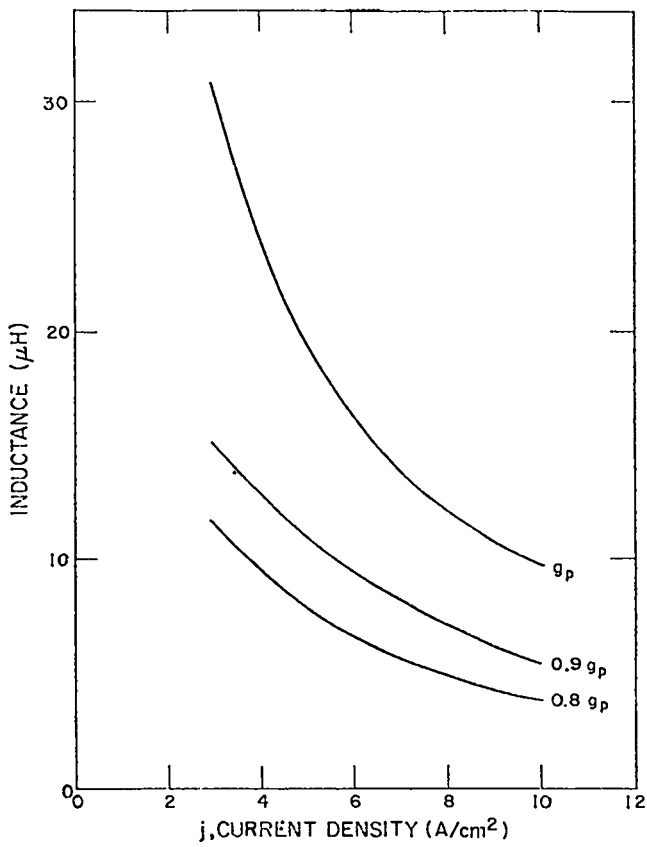


Fig. 10
Pulsar inductance per laser beam sector vs pump-current density.

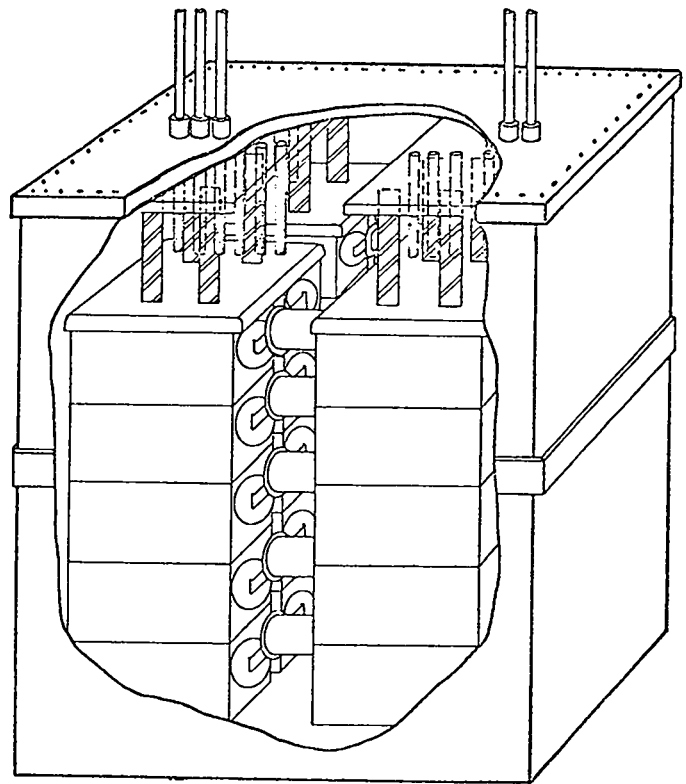


Fig. 11
Single-mesh, gas-pumping pulser for HEGLF power amplifier.

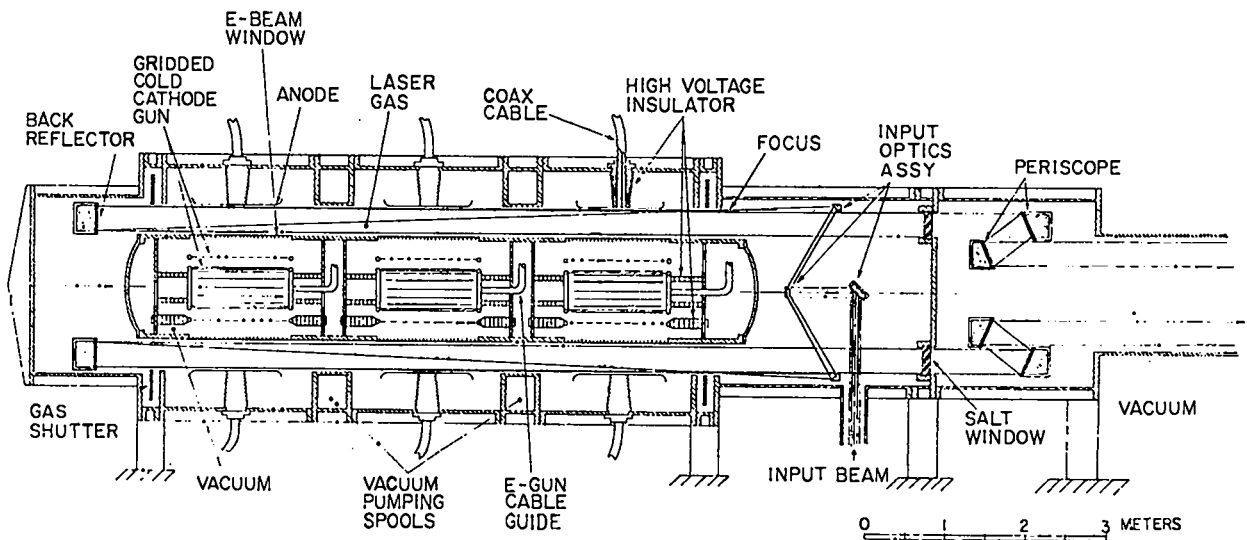


Fig. 12
Longitudinal section through HEGLF power amplifier.

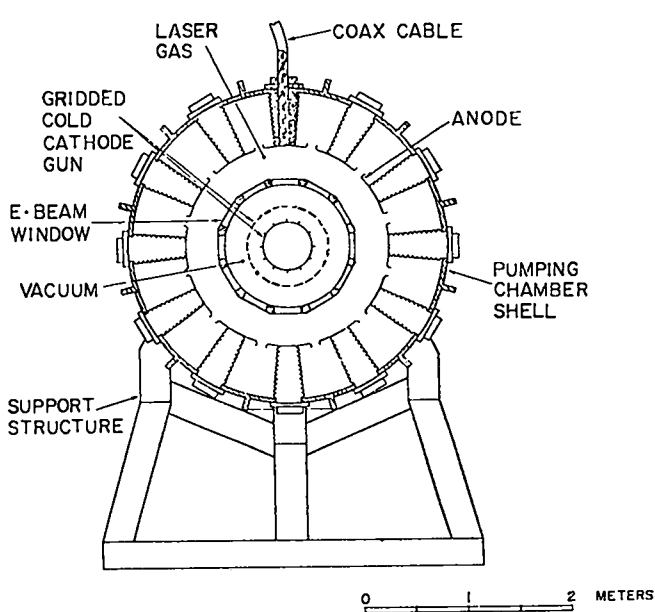


Fig. 13
Transverse section through anodes of HEGLF power amplifier.

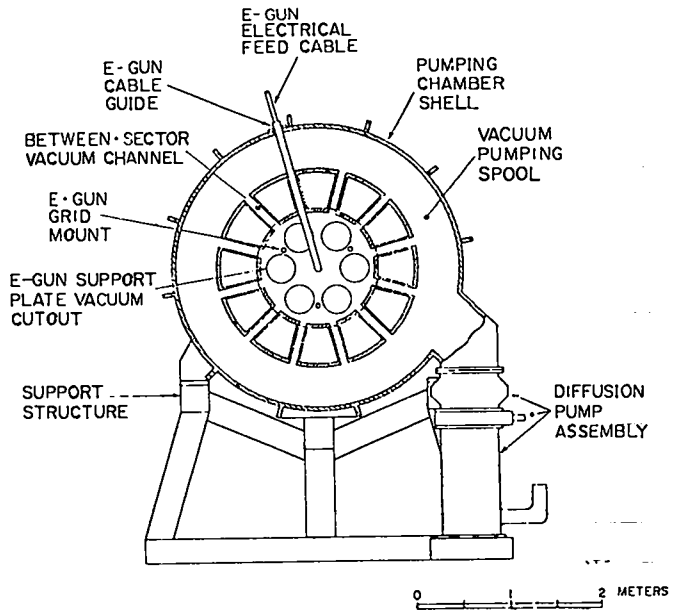


Fig. 14
Transverse section between anodes of HEGLF power amplifier.

following considerations when an annular amplifier configuration is assumed.

- The damage thresholds for copper and salt set a lower bound for the size of the beam at any point in the optical train.
- The maximum diameter of salt blanks, as limited by state-of-the-art fabrication, sets a practical upper bound on optical beam size and causes segmentation of the system because of unavoidable manufacturing variations in thickness and wedge angle.
- Passive retropulse protection requires that the beam pass through a constricted area between the front end and the actual power amplifier. The area of this region must be chosen so that the forward-moving pulse (from the front end) passes successfully, but that the backward-running pulse (e.g., reflection from the target) causes gas breakdown in the constricted area. This requirement can be fulfilled by several geometries: (1) ring-focus configurations, (2) spot-focus configurations, and (3) narrow-collimated-beam configurations.

In the ring-focus geometry, the flux passes through a line focus in the form of a circle concentric with the mechanical axis of the power amplifier. The effective area of the focus is controlled by the circumference of the circle and by the thickness of the beam waist. A ring-focus geometry requires axiconical optical elements and is unacceptable because of the resulting alignment sensitivity.

In a spot-focus geometry each sector is treated as a separate optical system. Each of the 12 sectors focuses the flux to a spot. The effective focused area is controlled by introducing aberration before the focus and removing it after the focus. The aberration can be introduced as astigmatism, by varying the angle of incidence to the first spherical mirror, and/or as spherical aberration, by varying the conic constant of the first mirror. The spot-focus system is quite insensitive to alignment errors, with the principal effect of misalignment being a pointing error. There is a practical limit to the amount of aberration that can realistically be introduced, which, in turn, limits the amount of energy that can be passed before gas breakdown occurs.

We have extensively modeled the ring-focus and spot-focus systems and are presently analyzing the collimated-beam configuration. In this configuration, retro-pulse protection depends on the effective termination of the collimated laser beam after reflection from a mirror. The phenomenon has been modeled, and experimental results have been obtained on the Two-Beam System.

System Design

The spot-focus system shown in Fig. 15 meets the above requirements. Each of the six amplifiers consists of 12 separate sectors that can be treated as independent optical systems. The collimated flux from the front end is divided into 12 beams (e.g., by a reflective polygon) and each of these beams is directed toward the first sphere of one of the sector optical trains. Two such trains are shown in Fig. 15.

A sector input beam is brought to a real focus by the last element of the input-optics assembly before entering the pumped region. This real focus protects the front end from a higher power retro-pulse by causing gas breakdown. The attainable cross-sectional area limits the energy throughput at this point. This real focus also permits efficient volume utilization: The beam expands from the internal focus and passes through the

pumped region; the back reflector collimates the beam and sends it back through the pumped region for a second pass; and two planar mirrors forming the periscope provide sufficient degrees of freedom to control both the location of the beam (up, down, left, right) and its direction of travel--the first mirror locates the beam and the second mirror points it.

The focusing paraboloid is the only element with a true axis: The beam must enter parallel to this axis to prevent aberration of the wavefront. The alignment system directs the beam into the focusing paraboloid so that the beam is not vignetted, and simultaneously points the beam to enter the paraboloid parallel to its axis.

Each paraboloid has a unique focal point (on its axis) which also must coincide with the target location. Depending on whether the focusing paraboloids are monolithic or sectored, target-chamber alignment will involve either 6 axes and 6 focal points or 72 axes and 72 focal points.

With the exception of the focusing paraboloid, misalignment of the elements constituting the optical train will introduce insignificant aberration. Misalignment will result in pure beam steering, not affecting the sharpness of focus. Corrections for misalignment amount to simply

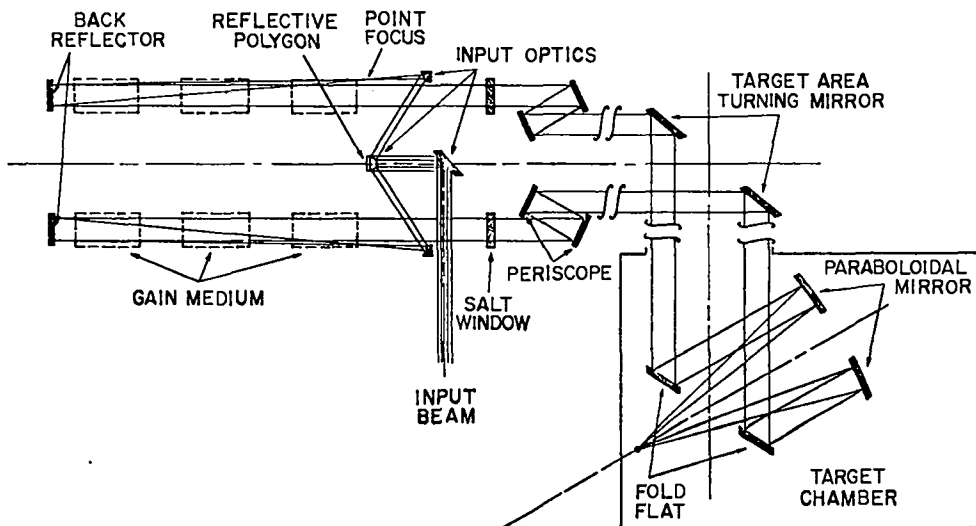


Fig. 15
Schematic of HEGLF large-beam optics. Two of 12 segments are shown.

positioning the beams, without vignetting and pointing, so that they arrive at the proper focusing paraboloid while traveling parallel to the axis of the paraboloid.

Misaligned focusing paraboloids will result in aberration as well as in pointing error. However, the tolerances on alignment are moderate (i.e., all focal points within 1 mm of target center) and achievable by good mechanical design. If these tolerances are satisfied, the result of misalignment of the paraboloids (or paraboloid sectors) can be considered as pure beam steering.

A sectored paraboloid offers the possibility of relaxing the optical-power (focal-length) specifications for the windows. If we examine window errors of quadratic and higher order phase terms (for power and irregularity, respectively), the quadratic terms result only in a focus shift while the higher order terms actually degrade lateral travel. The effects of power in the windows can be compensated for so that emphasis can be placed on minimizing the more serious irregularity.

Status of Computer Codes for Optical System Modeling

We are performing design and analysis studies by using several codes we recently acquired. ACCOS V is used for the bulk of our design and tolerancing effort. We will update this code soon, to correct a few known errors, and may compile a smaller version to improve turnaround time on less complex tasks. Another program, POLYPAGOS, has been installed and is in final testing. POLYPAGOS, will provide improved diffraction analysis; however, limitations in the tilt and aperture/obscuration routines may make it difficult to model a typical HEGLF segment or beam without program modification. Other codes are being installed or tested for specific analyses. The LASL code MAXWELL includes specific features to allow analysis of high-power CO₂ laser systems and will receive more attention in the future.

In addition to our computer-modeling efforts, we are performing laboratory diffraction experiments. This approach appears especially attractive for obtaining scaled near-field results by using visible-laser sources. Also, laboratory simulation may be more cost effective for some

problems than digital techniques and may provide a necessary check on digital results.

Target Subsystem (V. Zeigler, N. Wilson)

The new target-focusing system, using a turning mirror and an on-axis parabola, has been incorporated into a new space-frame system for support of the optical components. The space-frame concept has been defined in enough detail to start analyzing the dynamic characteristics of the structure. The calculational model has been completed for use with the SAP-IV (finite-element structural analysis) program and computer runs have begun.

Instrumentation and Controls

HEGLF Control-Computer Specifications

(J. Hong)

The specifications for procuring the HEGLF control minicomputer have been completed. Technical sections include requirements for hardware, compiler, and operating system.

The control computer will serve as the central supervisory computer for the HEGLF laser system. It will initially be used as a time-sharing computer aiding in the development of software for the Motorola M-6800 microprocessor. The computer will support a high-level language, a cross compiler, and a simulator for the M-6800 microprocessor.

Stepping-Motor Controller Development

(B. Strait, M. Thuot, W. Gutscher) -- A prototype stepping-motor controller system for positioning HEGLF laser mirrors has been designed and built. Several hundred stepping motors will be required to position and align the mirrors in the optical system.

The drive system must survive the extreme electromagnetic fields generated by the laser without loss of data or position. To combat these electromagnetic fields, the motor-controller electronics are contained in shielded boxes located near the mirror mounts, to reduce the length of the motor wiring. The boxes are connected to the central control system by fiber optics, which are immune to the effects of the electromagnetic fields. A diagram of such a system is shown in Fig. 16. The system includes motor controllers connected in a daisy chain with fiber-optic cables,

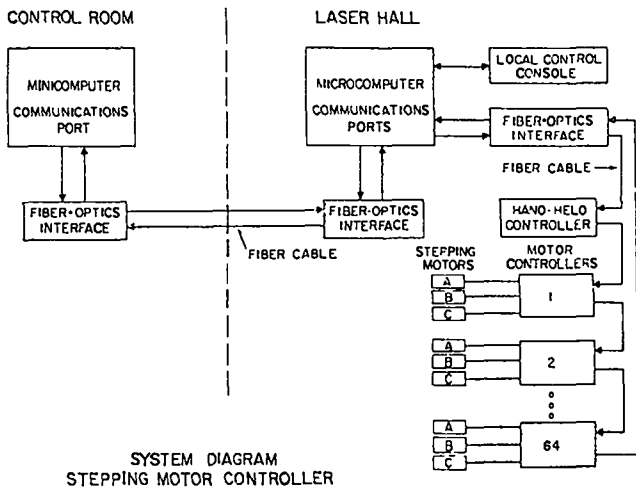


Fig. 16

System diagram for stepping-motor controller to be used in HEGLF.

a communications microcomputer, a local control console, a portable hand-held controller, and a high-speed serial communications system.

Fiber Optics for Analog Measurements

(M. Thuot)

We have begun the development of an analog fiber-optic link for current measurements at high potential. A schematic of the link is shown in Fig. 17. In this setup, a transformer generates a current proportional to the current in the high-voltage (550-kV) conductor; the transformer current drives the fiber-optic light-emitting diode transmitter so that the transmitter is self-powered and isolated from ground. A diode-amplifier circuit used as a receiver at the other end of the fiber-optic cable produces a voltage proportional to the light input and thus provides a voltage proportional to the current in the high-voltage conductor. The accuracy of measurements is about $\pm 5\%$.

HEGLF BUILDING DESIGN AND CONSTRUCTION

Introduction

The HEGLF and related activities will be housed in five major buildings: the laser building, the target building, a mechanical building, an office building, and a warehouse, as discussed in previous reports. The present status of the design effort is outlined below.

Architect-Engineer

(Norman Engineering Co., J. Allen)

A review of the Architect-Engineer's (A-E) design effort at the 30%-point of Title II was held in early December 1976. With the exception of electrical installations, design in all areas is progressing well, on schedule. The electrical effort will be increased. The A-E has divided the construction into four packages listed below. Package I - Laser Building, Mechanical Building, Passageways, and Warehouse; Package II - Target Building; Package III - Target Vacuum System (see below); Package IV - Office Building.

It is hoped that the availability of funds and the bid price will permit combining Packages I and IV into the first phase of construction. Funding constraints have forced us to postpone the letting of bids for Packages II and III until funds for FY 1978 are available. Bid Packages I and IV are being prepared ahead of Packages II and III.

Target-Vacuum System (TVS) (N. Wilson)

Preparation for target-vacuum system procurement continues. This system includes the vacuum beam lines, the turning-mirror chambers, the target chamber, and all vacuum pumping equipment. Procurement is directed toward contracting with a single industrial firm for engineering, fabrication, installation, and activation of the complete system. The following was accomplished:

- The intent to contract with a single firm to provide the TVS was reviewed with ERDA/LAAO, and agreement was reached to proceed with this plan.
- An Advance Notice of intent to negotiate a contract for engineering, fabrication, and erection of the TVS was submitted for publication to The Commerce Business Daily by ERDA/LAAO; statements of interest and capability were to be received by ERDA by January 7, 1977.
- Descriptions of required characteristics, configurations, and performance criteria are being prepared for incorporation by ERDA in a Request for Proposal (RFP) to build the TVS.

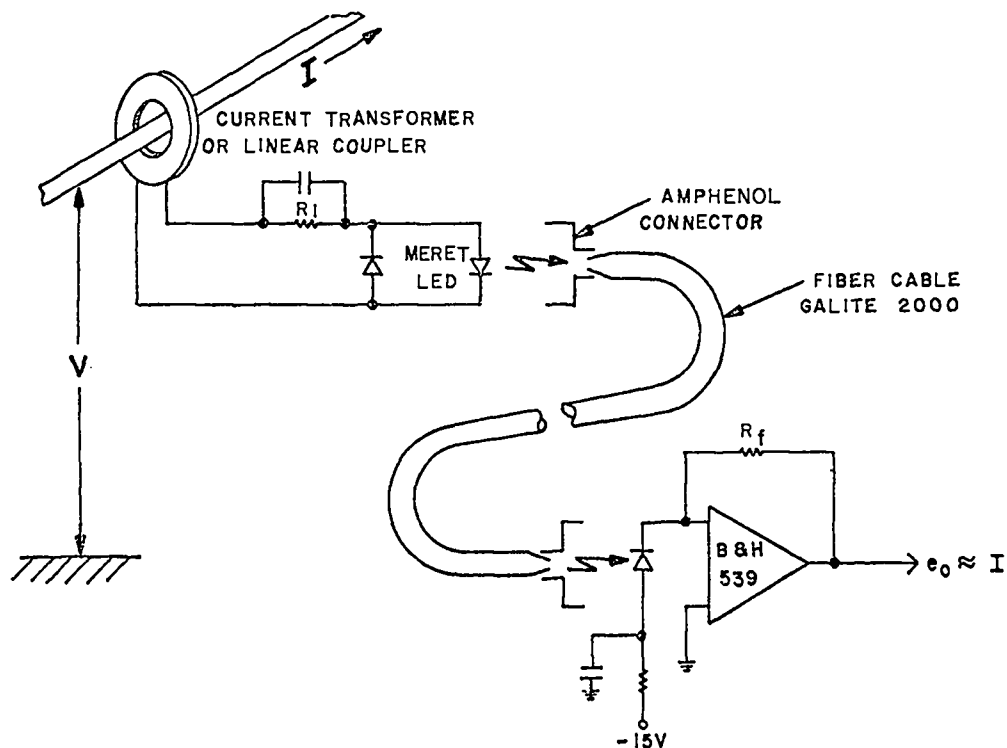


Fig. 17
Analog fiber-optic link for current measurement at high potential.

- The draft of a specification for the TVS prepared by the A-E for the 30% Title-II design review has been edited for completeness and accuracy. The final draft will be used in preparing the criteria to be incorporated into the RFP referred to above.
- Informative discussions with prospective TVS contractors continued. In addition to Pittsburgh-Des Moines Steel and High Vacuum Engineering Corp. who have stated their interest previously, expressions of interest were received from Leybold-Heraeus, Inc., Cryogenic Technology, Inc., Varian/NRC, and EG&G.
- The acquisition of an in-house capability is being continued to evaluate the characteristics of materials and apparatus under various vacuum conditions. The first apparatus needed, a vacuum materials evaluation system, is being designed. Existing equipment is being assembled for interim use, to study qualitatively the

characteristics of various wall materials to be used in vacuum.

Preliminary Safety Analysis Report (PSAR) (J. Graf, J. Hyder)

Since July 1971 LASL has been required to prepare Safety Analysis Reports for certain new facilities. This requirement has recently been formalized by ERDA in ERDA Manual, Chapter 0531, "Safety of Nonreactor Nuclear Facilities." The stated safety objective for nonreactor nuclear facilities is to ensure that environmental protection as well as health and safety matters are comprehensively addressed and receive an objective review with all identifiable risks reduced to a level as low as practical.

The HEGLF PSAR has been prepared to satisfy these objectives. All portions of the facility having safety-related features were described in detail. Step-by-step operation of major HEGLF components was also described. Hazards associated with equipment failures, electrical faults, lasers, fires, radiation, radioactive material, and natural disasters were examined. The major conclusions

reached in the PSAR were: (a) the health and safety of employees and of the general public will not be adversely affected by the construction and operation of the HEGLF, (b) the environment will not be significantly affected, and (c) any credible operational accident will result in limited property and programmatic losses.

A rough draft of the Preliminary Safety Analysis Report was assembled during the summer of 1976 and distributed for LASL internal review in September. Comments from this review were incorporated into the draft PSAR, which was sent to ERDA-ALO for review in October. The comments from the ERDA-ALO review were received in December, with LASL responses due in January 1977.

Radiation Shielding (M. Battat, W. Thompson)

Three sources of ionizing radiation must be considered in the Facility: bremsstrahlung from the power-amplifier electron guns, beta particles from tritium decay, and neutron and neutron-induced radiation as a result of deuterium-tritium fusion. A 23-cm (9-in.)-thick concrete wall separates the Laser Hall from occupied areas of the Laser Building. The Target Building has 1.83-m (6-ft)-thick walls and a 1.57-m (5-ft)-thick ceiling for neutron shielding.

Estimates of neutron-dose rates at selected locations in the control room were obtained by Monte Carlo methods. The primary sources specified were the neutrons that entered the Laser Hall after having traveled down the vacuum beam lines. Scattering in the laser amplifiers and in the room walls directs some of the neutrons toward the control room. The highest dose rate in the control room was computed to be ~5 mrem/yr.

Neutron dose rates were also calculated at 3 m outside the Laser Hall behind the PFN oil tanks. This radiation is due to neutrons escaping through the roof and walls of the Laser Hall. The dose rate was estimated to be ~40 mrem/yr. Contributions from air-scattered neutrons escaping through the roof of the Target Building were not considered.

Optical Development and Procurement

Polishing Development (R. Williamson) -- The individual exit apertures in the power-amplifier module are trapezoidal. Twelve apertures form an annular array through which the output beam passes.

We have initiated research into the thermal and mechanical aspect of polishing NaCl windows for these exit ports. The required combination of a 45-cm-diameter with a flatness to four fringes (at 633 nm) a 35-second wedge, and a high damage threshold has never been achieved in a single unit. In polishing, temperature gradients must be held to less than 0.03 K across the thickness to achieve flatness; and surface quality depends, in part, on lap fit. An annular pitch polish should provide best control of these problems.

We formulated the specifications for an annular pitch polisher, and have invited quotations. Consideration of the polishing parameters led to several innovations, e.g., to a diagnostic device for determining the effect of corrective adjustments; a closed-loop temperature-control system that interprets all machine-substrate interactions in real time; a modification to the tool restraint which precludes lap shear at any speed or friction; and a new machine adjustment mechanism which should have an early linear relation to, and control of, lap shape.

As a prelude to the polishing of these large polycrystalline NaCl windows, the Optical Sciences Center of the University of Arizona and the Development Optical Facility of the Air Force Weapons Laboratory will undertake a program of conventionally polishing large (4 to 11-in.; 10 to 28 cm-diam) polycrystalline NaCl. These studies will complement the development work to be done on the annular ring polisher when it arrives.

NaCl Window Procurement (W. Reichelt) -- A major critical path in the timely completion of the HEGLF program is the procurement of NaCl windows for the power amplifier. We have sent out a RFP to potential vendors who have demonstrated a technology base in alkali-halide production, obtained in both ERDA and DOD programs. In recent informal visits of potential vendors before submittal of their proposals, we discussed contractual and technological matters. The following information is reported.

- Crystal growth furnaces represent the most difficult design problem and require the longest time in the production plan.

- Conventional growth and fabrication technology seem adequate, although new technologies might result, ultimately, in a better, more cost-effective program.

Responses to the RFP are due by January 30, 1977. Window delivery dates are fixed by the anticipated phased completion dates for the power-amplifier Modules 1 through 6. Each of six deliveries will consist of 12 windows. The seventh delivery will consist of 16 units for system spares.

Optical Evaluation Facility (R. Williamson, J. Sollid, W. Reichelt, J. Allen) -- We will construct an optical evaluation and maintenance facility with General Plant Project (GPP) funds. The design criteria have been defined; Kruger, Lake, Hogue and Hutchinson of Albuquerque, NM, have been selected as the Architect-Engineer. Anticipated Scheduling dates are:

Title-I completion: February 20, 1977
 Title-II completion: June 15, 1977
 Building completion: May 31, 1978.

This facility, will be used in support of the entire Laser Fusion Program at LASL.

Diamond-Point Machining Program (W. Reichelt, D. Blevins) -- Diamond-point machining of optical components promises to provide a cost-and-time-effective method for producing the large number of components required for the HEGLF program. We are therefore supporting the diamond-point machining development program at the Y-12 Plant at Oak Ridge, Tenn. While the applicability of machining of small (11-in.) 28-cm-diam components has been proven in many programs the question has not been answered for large components (203-cm, 80-in. diam).

The focusing mirrors for the Eight-Beam System are parabolic off-axis mirrors ($f/2$). These mirrors are diamond-turned, six at one time, in a 152-cm (60in.)-diam parent fixture. Recent preliminary turning results indicate that interferograms can be obtained on the turned parts and that the surface value on large paraboloids is of the order of two fringes in the visible. The surface finish needs improving, and the program is now directed toward this problem. The ability to

optically machine surfaces on large diameters so that interferograms at visible light can be obtained immediately represents a major achievement in the program.

We are continuing our design analysis relating to the mounting and fixturing of components on the machines to obtain the best surfaces possible. The University of Tennessee, under contract to LASL, plays an active role in this effort and supports the Y-12 program. The fabrication of sectored annular mirrors has various implications for the machining program, e.g., machine burdens change, electroplating problems (for large diameters) vanish, and fixturing requirements change. The impact of such considerations on the program is under review.

OPTICAL SUBSYSTEMS (I. Liberman)

Single-Beam System

The redesign of the optical system was completed and has been partially implemented. Objectives of the redesign were the simplification of alignment, keeping the system in alignment longer, and improving the beam quality and energy entering the target chamber. Both optical stability and alignment time have improved considerably. No attempt was made to align the final focusing optics. Further improvements will be made when other optical components are installed in the near future. During the next phase of the upgrade we will design and install improved target-alignment equipment.

Two-Beam System

The target alignment system has been completed. The technique is based on a Hartmann test and has been proved to be a powerful alignment tool. Based on the known quality of the optics (primarily limited by the focusing paraboloids) the alignment procedure minimizes the focal spot (~150- μ m-diameter) and brings the two beams into coincidence at the focus to within ~25 μ m. Day-to-day realignment requires ~15 min or less per beam. This technique has the further advantage that the only alignment fixture within the

cluttered confines of the target chamber is a 2.5-cm-diam ball bearing.

Eight-Beam System

The modified triple-pass system has been installed and tested. The four-pass parasitic oscillation inherent in the previous design has been eliminated. However, a simple two-pass oscillation between the 38-cm (15-in.)-diam recollimating mirror at one end and the diffuse black paint on the other end still limits the useful gain of the amplifier. We will soon try to increase the oscillation threshold by two approaches: decrease the effective reflectivity of the black paint through the use of specular baffles and/or decrease the effective reflectivity of the mirror with linear or saturable absorbers.

CO₂ LASER TECHNOLOGY

Introduction

Each of our CO₂ laser systems described earlier represents a significant advance in the state of the art of reliable CO₂ laser subsystems, components, and diagnostics. The design, construction, and improvement of the systems require, therefore, basic support of CO₂ technology. Some important areas are: The development of short-pulse multifrequency oscillators, amplifier optimization, development of subsystems for the prevention of system self-oscillation and removal of prepulse energy, improvement of the transverse profile of the amplified laser pulses, and measurements of optical damage thresholds in system components.

Oscillator Development

General -- The HEGLF power-amplifier modules require an input energy of 1000 J. If presently available components were used, the system designed to provide this input would consist of many discrete amplifiers arranged in a single-pass configuration. We are studying a regenerative scheme which, we believe, will permit the attainment of such front-end design goals by a single amplifier unit and an injection oscillator. Construction of such a device is under way. We

also continued our measurements of passive pulse compression in p-type germanium, obtaining 0.3-ns pulses.

Regenerative Amplifier System -- Construction and subsystem testing on the regenerative amplifier facility continued. The planned layout is illustrated in Fig. 18.

The original regenerative amplifier scheme permits any finite number of passes through the amplifier medium after injection of the oscillation pulse.¹ In our modification of the Belanger scheme we choose only even numbers of passes, ensuring that the output and input will be oppositely directed. We then use a Faraday-rotator assembly to provide input-output isolation, and a germanium saturable absorber to provide adequate pulse-to-background energy contrast. The six-pass configuration is shown in Fig. 18. Such devices will be capable of nearly total energy extraction from an amplifier medium and will be particularly cost effective in large gain-volume devices.

In our preliminary tests, the multipass gain medium is the TBS preamplifier design (aperture, 3.5 cm; gain-length, 11.3 m), modified electrically to provide a gain-length product (g_0L) of 5.5 at 45 kV. With standard oscillators, two passes are sufficient for nearly total energy extraction from this device. To determine stability conditions and energy-extraction parameters for four- and six-pass geometries, a commercially available Lumonics 600 series amplifier will be employed in place of the TBS preamplifier. We thus expect to obtain scaling criteria for designing devices in the 200-J range.

The injection oscillator is an acoustically modelocked standard oscillator, operated helium-free. We will operate this device with a 1:1::N₂:CO₂ mixture for best multiline output.²

Passive Pulse Compression in Germanium -- As mentioned previously (see LA-6510-PR), p-type germanium is a high-power, broadband saturable absorber for the 10- μ m region, and is a nearly ideal passive pulse compressor for CO₂ signals with finite risetimes. For best results, it is important to maximize the product of absorber transmission and the first derivative dT/dI of transmission vs intensity at the chosen operating

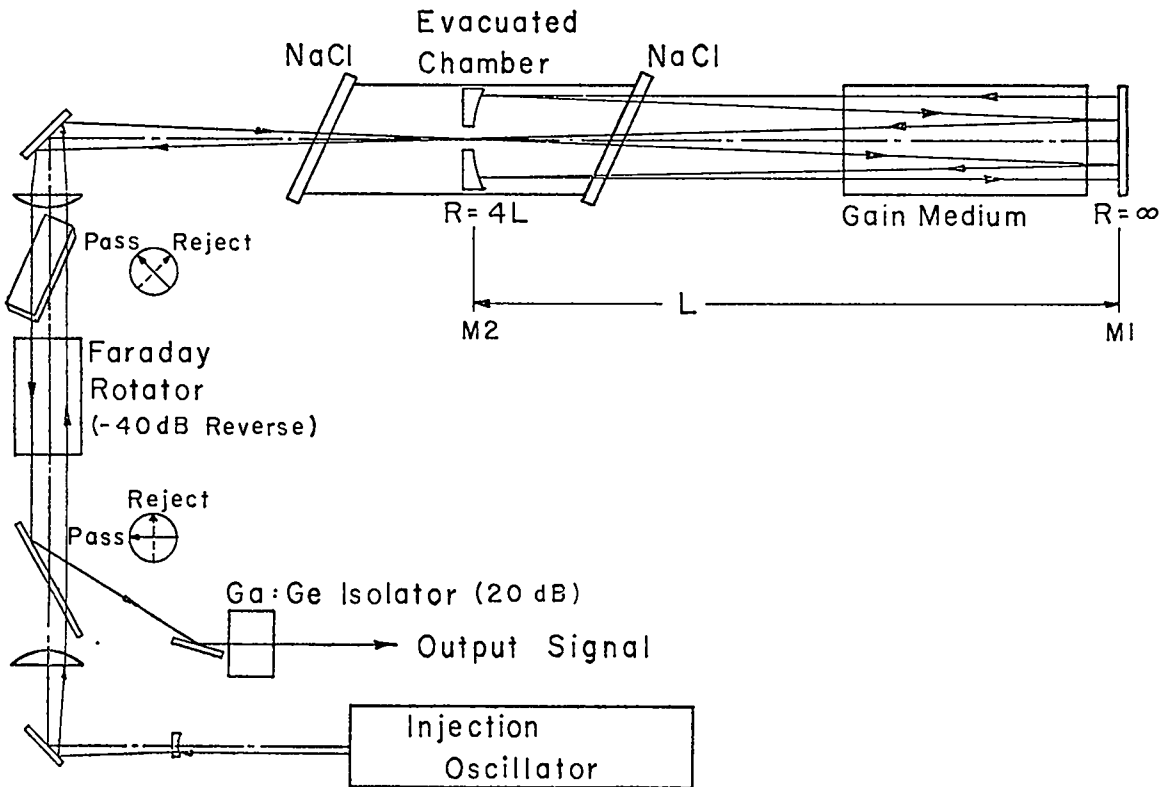


Fig. 18
Six-part configuration of regenerative oscillator under study. A germanium Faraday rotator is used for beam switchout.

point. The familiar gaseous saturable absorbers for the $10\text{-}\mu\text{m}$ region fail to meet expectations in this regard because of the complex vibrational absorption spectrum available to intense optical pulses in these molecules. In addition to a generally inadequate value of dT/dI for energy-efficient pulse compression, the reported absorber gases show strong structure in their transmission spectra, which makes them less useful for broadband work.

In contrast, our measurements show that p-type germanium displays nearly ideal bleaching characteristics of an inhomogeneously broadened, two-level system over the 9.2- to $10.7\text{-}\mu\text{m}$ wavelength range at intensities up to 0.3 GW/cm^2 . We have also determined that the saturation intensity for this material is essentially constant for a typical one-band multiline spectrum, as reported in the discussion of isolator development. As a final advantage, the energy relaxation time of p-type germanium is $\sim 2.6\text{ ps}$ in the $10\text{-}\mu\text{m}$ region,³ so that this absorber is equally effective in

compressing both the leading and the trailing edges of a 1-ns input pulse.

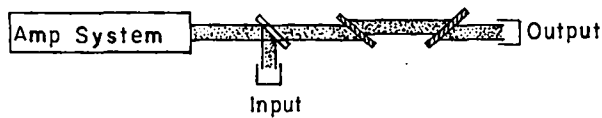
Fig. 19 shows the 300% compression obtained at $10.59\text{ }\mu\text{m}$ by using p-type germanium with a small-signal absorption coefficient of 9. Here, the energy transmission at the operating point was 2%. When the observed pulse compression ratio was plotted against input energy, the operating point for maximum compression agreed well with the maximum first derivative of the measured transmission-vs-intensity profile of the germanium sample.

Multiline Short-Pulse Amplification

(H. Volkin, J. Hafer)

We have modified a computer program,⁴ which is now in general use, for calculating short-pulse energy extraction in CO_2 laser amplifiers. Calculations are made by using the appropriate forms of: (1) Maxwell's equation for a plane-polarized unidirectional beam and (2) the equations of motion for the multilevel density matrix of the

Pulse Compression In Germanium



Parameters - $\alpha L = 9$
 $I_{in} \sim 200 \text{ MW/cm}^2$
 Energy Trans. $\sim 2\%$
 $\lambda = P(20), 10.59 \mu\text{m}$

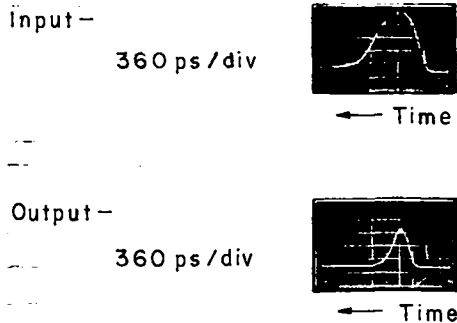


Fig. 19

Pulse compression in germanium. Compression factors of 3 are observed at input powers of 200 MW/cm^2 .

CO_2 molecules. The density matrix contains the population inversion and polarization between each pair of CO_2 energy levels whose transition line is contained in the input pulse. Diffraction effects are neglected due to the use of a single spatial dimension, but these effects are generally unimportant for pulse amplification. Otherwise, the only approximations introduced into the fundamental equations describing the pulse propagation are: (1) the neglect of conductivity in the amplifier gas, (2) the slowly varying envelope approximation for the polarization, and (3) a rotating-wave approximation in the polarization equation. The effects of the first two approximations are expected to be generally negligible for the conditions of interest in our work.

Accurate density-matrix theory is used rather than the simpler multilevel rate-equation theory, permitting inclusion of the coherence of the polarization. Coherence effects become significant when: (1) the pulse is sufficiently intense to saturate the transitions in a time comparable to

several dephasing collision times or less; or (2) the risetime of the pulse is comparable to, or less than, the collisional dephasing time of the transitions. The system of coupled first-order partial differential equations is integrated by a computer program based on a numerical algorithm, accurate to second order,⁵ adapted to multiline, multiband pulses.¹

Based on previous work,⁴ we have developed computer programs to calculate amplifier performance with double passes of the beam. During the first pass, the beam can be given any prescribed spatial variation of its cross-sectional area. Continuous change of beam area is represented by a series of matching cylinders, with the radius of each cylindrical section chosen so that its volume equals that of the actual volume swept out by the beam. The number of cylindrical sections can be made as large as desired and hence the model imposes no limitation on accuracy. Across the surface separating two cylinders, the intensity of the beam changes inversely with the area of the cylinder, so that energy flow is continuous. For the return pass, the beam is collimated and sweeps out a volume of gas that completely encloses the volume swept out in the first pass.

Any initial distribution of gain along the length of the amplifier can be specified. A uniform transverse gain profile is assumed. Each transition line in the pulse couples a rotational sublevel in the upper vibrational level (00^01) to one in the lower vibrational level (10^00 or 02^00). The populations in these rotational sublevels change as the result of radiative transitions induced by the incident pulse and rotational relaxation within the vibrational levels. For nanosecond pulse widths, relaxation between vibrational levels can be ignored.

Two versions of the computer program have been developed. The "exact" program stores the changed level populations existing after the first passage of the beam. On the return pass, the beam sees the new vibrational level inversions in the volume of gas swept out by the beam in the first pass and sees the initial inversions outside the irradiated volume. To save computer time, a second version of the computer program was prepared in which the returning beam sees a uniform inversion in the

transverse direction. At each position along the length of the amplifier, we used average populations weighted according to the area of radiated and unradiated gas in the transverse section at that position. However, this procedure is inaccurate and gives misleading results when the input pulse has an intensity high enough to cause significant changes in the level populations during the first pass. This result indicates the sensitivity of the energy extraction to the precise energy fluence and to the degree of saturation that exists in each spatial part of the beam. A more sophisticated averaging procedure, one that depends on the beam intensity in the first pass, is required if uniform transverse inversions are used in the return pass. A reexamination of the computing algorithm and programming used in the "exact" code to process the various parts of the beam in the return pass revealed significant inefficiency in the computations. Programming optimization will reduce the difference in computer time required for the two versions to about a factor of 2. This will make the "exact" version generally usable in further calculations.

A typical calculation is summarized in Table V. The data correspond to a single sector (one of 12) in one of the six annular amplifiers in the HEGLF. Along the length of the amplifier, each

sector has three gain sections with an absorbing region between each section and at each end. Initially the gain coefficient, g_0 , is 0.021/cm, the total gain length in a single pass, g_0L , is 7, the absorption coefficient, k_0 , is 0.0018/cm, and the total absorption length, k_0L , equals 0.72. The input pulse has a full width at half maximum of 1 ns and the energy is 1.2 J distributed equally in five lines in the 10- μ m band. The beam enters the sector with a cross-sectional area of 23 cm² and diverges uniformly to an exit area of 724 cm². The collimated return beam has a total area equal to the usable area of the sector, i.e., 819 cm². The diverging beam is modeled by seven cylindrical pieces, one in each of the seven gain-absorption sections. The first column in Table V identifies the various parts of the pulse. The cylindrical pieces of the final output pulse are numbered 1,2,...,8, in order of decreasing volumes of depleted gain seen on the return pass. The characteristics of the output pulse are also given.

It can be seen that the design point of 1390 kJ output energy per amplifier sector (100 kJ for HEGLF) in a 1-ns pulse is attained for this selection of operating conditions while keeping the peak energy fluence within the design limit of 2 J/cm². The times to reach 10 and 90% of total energy in the output pulse are 0.38 and 1.26 ns, respectively.

TABLE V
CALCULATED SHORT-PULSE ENERGY EXTRACTION
IN CO₂ LASER AMPLIFIERS

<u>Pulse Part</u>	<u>Time to Maximum Intensity (ns)</u>	<u>Maximum Intensity (GW/cm²)</u>	<u>Maximum Power (GW)</u>	<u>Total Energy (kJ)</u>	<u>Total Fluence (J/cm²)</u>
Pulse after First Pass of Amplification	0.9	0.2898	209.8	0.198	0.2735
1	0.5	2.1399	49.6	0.034	1.4653
2	0.5	2.1315	78.4	0.05	1.4610
3	0.5	2.3742	178.7	0.119	1.5847
4	0.5	2.3501	245.6	0.164	1.5736
5	0.4	2.7118	371.5	0.240	1.7514
6	0.4	2.6636	442.8	0.287	1.7294
7	0.4	3.3583	608.1	0.373	2.0605
8	0.4	3.2799	310.1	0.191	2.0249
Output Pulse	0.4	2.7573	2257.1	1.463	1.7877

Pulse Propagation in the TBS and EBS

Introduction-- an extensive series of modeling calculations were performed on pulse propagation through the TBS and EBS to aid in understanding their present performance and to evaluate the performance improvement to be expected by several proposed modifications to the existing systems. These modifications included installation of a modified triple-pass optical system (MTPA) to increase the gain-length product (g_0L) at which the system could operate without parasitic oscillations; installation of a four-line oscillator; and installation of a 0.5-ns multiline oscillator system.

Calculations

General--The system that was modeled is shown in Fig. 20. Conventional oscillators and preamplifiers were assumed. Preamplifier pressure was left as a variable for these calculations. Front-end isolation was provided by gallium-doped germanium. The Modified Triple-Pass Amplifier (MTPA) system included the option of a germanium isolator located at the end of Pass 1. No beam-transport losses other than germanium losses were included.

These calculations sought to address two possible operating regimes of the TBS and EBS systems and to determine the advantages of the proposed modifications. For operation with the present oscillator system producing 1-ns input pulses, we determined the advantages of multifrequency operation and increased g_0L in the

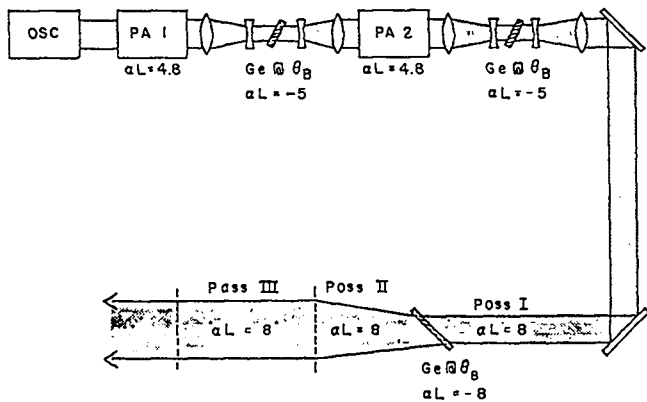


Fig. 20

Optical train for EBS and TBS pulse-propagation calculations.

MTPA. For a proposed upgrade to 0.5-ns input pulses, the same questions were investigated, in addition to the advantages of increasing the preamplifier bandwidth by increasing the operating pressure from 600 to 1800 torr.

One-Nanosecond Pulse Propagation -- The results of 1-ns pulse propagation for a variety of conditions are shown in Table VI. Several conclusions are apparent from examining this table. Increasing the g_0L from 6 to 8 leaves the pulse shape essentially unchanged but increases the energy by a factor of 2, causing the peak power per beam to increase by ~75%. For fixed g_0L an increase from one-line operation to four-line operation causes a small increase in the energy available (~25%), but causes a substantial reduction in the pulse width, resulting in an ~80 to 100% increase in peak power. Thus, if one is interested in increasing the peak-power performance, either modification will be successful and one should choose the simpler and more reliable of the two. However, if one requires a substantial increase in absolute energy available, the MTPA is the preferred option. If both options were pursued, power increases by factors of 3 to 4 can be expected with energy increases of 75 to 100%.

Half-Nanosecond Pulse Propagation -- By using the same power amplifier configurations as above, we calculated the propagation of 0.5-ns pulses in the MTPA. These calculations showed that multiline operation was essential for shorter pulse durations, with peak power increasing by a factor of 3 to 4 when going from one-line operation to four-line operation. The dependence on g_0L was similar to that noted in the 1-ns calculations. When g_0L was increased from 6 to 8 the output energy increased by 80 to 100%, the pulse shape remained nearly constant, and the output power doubled.

Another purpose in these calculations was to determine the bandwidth requirements for the front-end preamplifiers (PAs). Our devices presently operate at 600 torr. To determine whether increased pressure was required, we calculated the output of the MTPA with 0.5-ns pulses injected into the PA system and the PA pressure varied from 600 to 1800 torr. These

TABLE VI

PROPAGATION OF 1-ns PULSES IN THE DBS

Input Parameters

Pulse Duration, 1 ns (FWHM)
 Frequency Spectrum, one line or four lines
 (P-branch of 10- μ m band)
 Input Energy, 1.0 or 10.0 mJ
 Amplifier with Germanium at end of Pass 1 or
 without Germanium at end of Pass 1
 Amplifier Gain, 3 or 4%/cm

Amplifier Gain, 4%/cm

<u>Pulse Spectrum</u>	<u>Germanium</u>	<u>Input Energy(mJ)</u>	<u>Output Energy(J)</u>	<u>Peak Power(TW)</u>	<u>Pulse Risetime From 10-90% (ps)</u>	<u>Pulsewidth FWHM (ns)</u>
1 Line	No	1	1203	0.7	504	1.63
		10	1265	0.75	434	1.53
	Yes	1	672	0.57	500	1.14
		10	922	0.76	360	1.22
4 Lines	No	1	1520	1.25	430	1.04
		10	1561	1.50	364	0.940
	Yes	1	929	1.15	390	0.75
		10	1303	2.0	280	0.57

Amplifier Gain, 3%/cm

1 Line	No	1	640	0.4	540	1.56
		10	750	0.5	490	1.56
	Yes	1	35	0.04	560	0.85
		10	240	0.25	414	0.95
4 Lines	No	1	820	0.76	490	1.11
		10	975	0.92	420	0.98
	Yes	1	27	0.028	546	0.72
		10	373	0.56	343	0.64

results, displayed in Table VII, clearly show that the final performance of the MTPA is essentially independent of PA pressure for sufficient input drive energy. Thus, efficient 0.5-ns operation of the TBS and EBS can be achieved with no modifications to the existing front ends other than the installation of a short-pulse multiline oscillator.

Isolator Development

Introduction -- Interstage isolation is one of the major concerns in laser oscillator-amplifier systems used for target experiments. Amplifier systems with small-signal gain higher than 10^{10} are being considered. At such high gain, parasitic

oscillations can occur with only minor feedback present.

Isolation problems occur in three areas: prepulse amplification, parasitic oscillations, and amplification of target reflections.

- Prepulse amplification is a problem because a plastic laser-fusion target will melt if more than 50 μ J of light is focused upon it before the main pulse arrives. In our oscillator systems, the short pulse to be injected into the amplifier chain is electro-optically switched out of a longer smooth or modelocked pulse. When the electro-optic switch is opened, transmission is quite close to unity, but

TABLE VII

EBS AND TBS FRONT-END REQUIREMENTS

Conditions

<u>Input Pulse</u>	500 ps (FWHM) Gaussian Four-line Spectrum Plane Wave
<u>Power Amplifier</u>	gL = 8/pass, P(20)
<u>Parameters</u>	3:1/4:1::He:N ₂ :CO ₂ Mix Germanium at end of first pass, α1 = 8.

<u>Preamplifier Pressure (torr)</u>	<u>Input Energy (mJ)</u>	<u>Output Energy (J)</u>	<u>Pulse Width (ps)</u>	
			<u>At 50% Pulse Energy</u>	<u>At 90% Pulse Energy</u>
600	1	1091	240	430
600	10	1124	140	400
1800	1	1136	160	420
1800	10	1226	130	460

before the switch is "opened" it does not entirely block the beam: for a single-stage switch, about one-thousandth of the incident intensity is transmitted. It is this feedthrough that must be controlled. The low-intensity feedthrough experiences the peak of the amplifier's unsaturated gain and may grow to contain an appreciable fraction of the total energy output of the system.

- Parasitic oscillation must be avoided prior to amplification of the short pulse; it can melt the target, and it can deplete the gain of the amplifier system before the desired pulse arrives.
- Amplification of target reflections is a serious problem because of residual gain in the amplifiers after passage of the main pulse. As the target reflections are amplified and contracted in diameter, they will damage optical elements in the amplifier chain or in the oscillator.

Results of various attempts being made to solve these problems are discussed below.

Preliminary measurements on high-power transmission and pulse compression in gallium-doped

germanium are now complete. Germanium has been shown to function as a bleachable absorber over the wavelength range from 9 to 11 μm. Sulfur hexafluoride (SF₆) was demonstrated to provide efficient bleaching over the 10-μm P-branch from P(12) to P(24). Pulse reshaping in SF₆ was also investigated. Prepulse reduction using hot CO₂ was studied both theoretically and experimentally, and a program to evaluate potential ir Faraday rotator materials was initiated.

Bleachable Absorption in Germanium

Considerable progress has been made in our understanding of saturable absorption in p-type germanium, and the use of this phenomenon for interstage isolation in CO₂ systems. Recently, we have confirmed the predicted inhomogeneity of the broadening mechanism associated with the two-level heavy-to-light hole transition in germanium. We have also measured the spectral dependence of the saturation parameter, and found that its trend with wavelength is contrary to theory. Finally, we have observed a significant orientational dependence in the saturation intensity.

The large gain-bandwidth product and the necessity of highly saturated operation in large CO₂ laser systems require that an interstage saturable absorber for small-signal gain

suppression behave in wavelength-independent fashion. We have been successful in using the bleachable absorption arising from the heavy-to-light hole transition in p-type germanium for this purpose. Following a suggestion by Keilman,³ we reported the first direct evidence of inhomogeneous broadening of the responsible transition at high as well as low intensities,⁶ giving an intensity-dependent absorption coefficient α of

$$\alpha(I) = \frac{\alpha_0}{\sqrt{1 + I/I_s}}, \quad (1)$$

where α_0 is the low-power limit of the absorption coefficient, I_s is the saturation parameter in units of W/cm^2 , and I is the incident power. It has been thought that the absorption in p-type germanium was homogeneously broadened, giving a more rapid first-power dependence of $\alpha(I)$ on the quantity $(1 + I/I_s)$ in Eq.(1).⁷

The primary advantages of the p-type germanium interstage isolator relative to the gaseous absorbers are rapid relaxation and broadband performance. The latter is deduced mainly from the known homogeneity of the small-signal absorption coefficient over the range from 9.2 to 10.7 μm , which is of interest in CO_2 work.⁸ If, however I_s were found to be highly wavelength-dependent in this range, the broadband performance required for efficient subnanosecond energy extraction in CO_2 system could be compromised.

We have measured in detail the transmission of gallium-doped germanium as a function of incident intensity up to $1 \text{ GW}/\text{cm}^2$ at several wavelengths and two crystallographic orientations have been made. These data support the following claims:

- With minor departures just under the optical damage-threshold intensity, gallium-doped germanium bleaches like an inhomogeneously broadened, two-level system for wavelengths from 9.2 to 10.7 μm .
- This intensity exhibits a measurable crystallographic orientation dependence that can explain discrepancies between

previously reported saturation intensities in this material.

- The saturation intensity I_s decreases monotonically from $7 \text{ MW}/\text{cm}^2$ at 9.2 μm to $3.5 \text{ MW}/\text{cm}^2$ at 10.6 μm , contrary to theory.⁹

Typical experimental bleaching data for two different wavelengths, taken with the laser electric vector in the (111) plane, are shown in Fig. 21. The curves shown are calculated for a best fit to the data, taking into account the measured laser intensity distribution in space and time.

Conclusions from these measurements do not indicate that the broadband performance of the p-type germanium isolation device is impaired significantly.

Faraday Rotator Materials -- Development of efficient, scalable Faraday rotators is continuing, with work focusing on the development and testing of hot-pressed materials of the spinel family, which will be magnetically saturable, room-temperature rotators with a high figure of merit. Methods of improving interband rotators are also being studied.

The preferred solution to laser isolation problems is the Faraday rotation isolator.

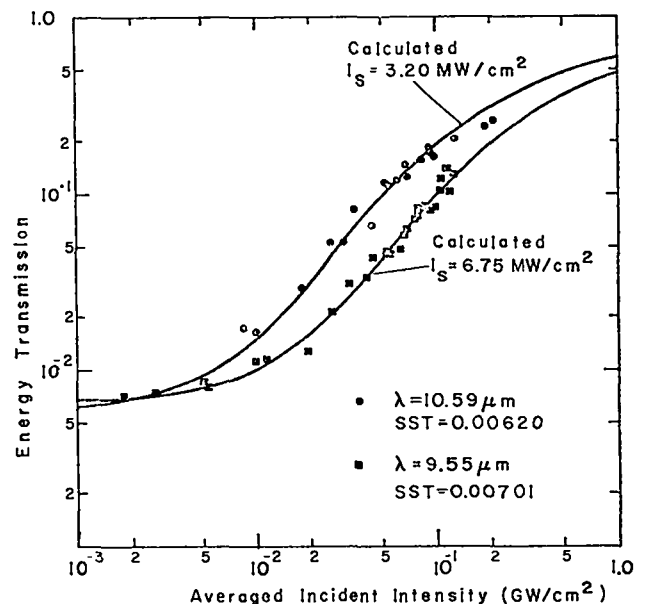


Fig. 21
High-power transmission of gallium-doped germanium for two CO_2 wavelengths.

Although germanium Faraday rotators have been made to work at CO₂ laser wavelengths,¹⁰ a working large-aperture rotator will certainly be expensive if it can be fabricated. Hot-pressed polycrystals of certain magnetic spinels have been shown¹¹ to have very favorable properties for Faraday isolator applications, and may offer several advantages over materials under consideration. First, the magnetic saturation of the Faraday effect in these materials reduces the magnetic-field uniformity requirements to very modest levels. Second, the large value of specific rotation in these materials reduces the quarter-wave thickness to less than 10 mm and the necessary field strength to a few thousand Gauss. This greatly reduces the cost associated with the field source as compared with germanium rotators. An optically short rotator will also be less likely to introduce unacceptable nonlinear optical effects. Third, the measured optical properties of one spinel, CdCr₂S₄, give a very acceptable isolator figure of merit of 28 deg/dB, about half that of germanium at 10-μm. Finally, the materials can be fabricated by hot-pressing and are therefore scalable in aperture.

A facility has been set up for the evaluation of Faraday rotator materials at various CO₂ laser wavelengths. We have constructed a cw laser with an output of 1 to 2 W on several lines in the R- and P-branches of the 10-μm band. The beam is steered through the bore of a superconducting solenoid containing the sample. Available solenoids include a 50-kG magnet (on loan from Eastman Kodak) with a 1.27-cm (0.5-in.) bore, and a 30-kG magnet with a 12.7-cm (0.5-in.) bore.

The signal-to-noise ratio of the measurement system permits us to resolve a rotation of 0.5 deg. For the 1-mm-thick samples to be studied, we expect rotations of 3 to 30 deg. Therefore, we are improving the signal processing to read ±0.1 deg rotations. Prior setups using this configuration have had sensitivities of millidegrees by using lock-in detection signal processing.

Several rotator materials that will be investigated are described below.

CoCr₂S₄ The magnetic spinel CoCr₂S₄ appears to be a very promising material for 10-μm isolation.¹² The saturated rotation at 10.6 μm is

320 deg/cm and hot-pressed samples with residual absorption as low as 7 cm⁻¹ have been made. The residual absorption appears to be impurity-related and intrinsic levels may be much less than 1 cm⁻¹.

We have begun a program to fabricate hot-pressed disks of magnetic spinel CoCr₂S₄, and are attempting to reduce the residual absorption to less than 1 cm⁻¹ in the 9- to 10-μm range by starting with electronics-grade materials. The first samples will be fabricated in early 1977.

CoRhFeO₄. This cobalt spinel has a transition temperature of 350 K and thus is a potential room-temperature Faraday rotator material. Computer analysis of the near-ir circular dichroism has predicted a Faraday rotation at 10-μm of ~75 deg/cm. In collaboration with the Naval Research Laboratory, we are investigating thin films of this material sputtered onto a transparent substrate. Initial efforts with a ZnSe substrate were unsuccessful due to decomposition of the ZnSe during film fabrication. Other ir-transparent substrates are being investigated so as to enable us to determine the residual absorption and the Verdet coefficient at 10.0 μm.

Hg_xCd_{1-x}Te -- A group from the Electrical Engineering Department at the University of New Mexico (UNM) has proposed the HgCdTe semiconductor series as an interband (nonmagnetic) Faraday rotator for 10 μm. Because the interband Verdet constant varies as E_g^{-7/2} far from the gap¹⁰ (where E_g is the band-gap energy) it can be enhanced by choosing a material with a smaller gap. The material, Hg_xCd_{1-x}Te, with x = 0.4 (E_g ≈ 0.5 eV) should have a Verdet constant of 1.2 deg/(kG cm), ~15 times that of germanium. Our preliminary measurements on a sample (x = 0.33 to 0.41, exact composition unknown) indicate a Verdet constant of 0.45 deg/(kG cm). The absorption coefficient of this sample was ~10 cm⁻¹ and therefore the figure of merit is small. The transparency of this material could presumably be improved. We are following up this measurement with more studies on samples provided by the UNM group.

Bleachable Absorption In SF₆ -- Although several gaseous absorbers exhibit bleaching behavior at 10.59 μm, none of the gases yet examined behaves like a classical two-level

absorber. No saturable absorber attains 100% transmission; and, even at incident intensities of $\sim 0.5 \text{ GW/cm}^2$, each exhibits some residual absorption.¹³ Sulfur hexafluoride has been shown to be the most efficient isolator for a laser operating on the CO_2 10- μm P(20) line,¹³ and has been employed successfully in the 1-ns, single-line pulse-generating systems presently in operation. We have now experimentally demonstrated that SF_6 is also a strong saturable absorber on each of the seven lines in the CO_2 10- μm P(12)-to-P(24) spectrum, thus indicating that SF_6 should be a very effective isolator for a multiline laser operating in the 10- μm P-branch.

Our GigaWatt Test Facility has been used to study the bleaching of SF_6 under irradiation by intense CO_2 laser pulses. Spatial filtering provided a well-characterized output pulse, whose space and time profiles were monitored with a pyroelectric array and with a fast 5-GHz oscilloscope. The transmission of a cell containing SF_6 was measured as a function of laser wavelength and input-pulse intensity. Surface-absorbing calorimeters were used to determine the incident and transmitted pulse energies. Typical results are shown in Fig. 22 for SF_6 transmission at P(12) and P(16), where the SF_6 pressure was adjusted to yield a small-signal transmission of 5×10^{-5} in each case. At an input intensity of $\sim 50 \text{ MW/cm}^2$, the P(12) transmission is

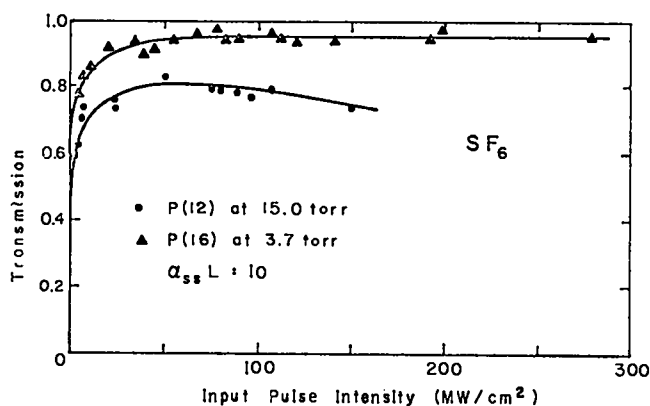


Fig. 22
High-intensity SF_6 transmission.

0.76 and the P(16) transmission is 0.87. Thus, SF_6 is seen to be an effective isolator with a large dynamic range of 10^4 , as given by the ratio of the high-intensity to the small-signal transmissions. Similar transmission data for all the P(12) to P(24) lines are given in Table VIII, demonstrating that SF_6 shows significant bleaching on each line. Of course, higher saturated transmissions could be obtained by operating at different intensities and pressures.

Experiments on the bleaching properties of SF_6 are continuing, and saturable absorbers for lines in the other CO_2 branches will be studied in greater detail.

Pulse Reshaping in SF_6 -- It is now well established that, when exposed to intense resonant laser radiation, polyatomic molecules such as SF_6 , are capable of absorbing many photons per molecule even in the absence of collisions. Such absorption has led to molecular dissociation¹⁴ and to anomalously high intensities necessary for bleaching.¹⁵ Much speculation has arisen concerning the nature of the absorption process. The role of the rotational distribution of the molecular states, the anharmonicity and splitting of the vibrational levels, the molecular coherence, and the molecular density of states have all been

TABLE VIII

PRELIMINARY HIGH-INTENSITY TRANSMISSION
OF SF_6 AT VARIOUS CO_2 10- μm P-BRANCH LASER LINES

Laser Line	Pressure (torr)	High-Intensity Transmission
P(12)	15.0	0.78
P(14)	9.0	0.79
P(16)	3.7	0.90
P(18)	5.8	0.67
P(20)	6.4	0.69
P(22)	10.9	0.33
P(24)	20.0	0.11

Note: The SF_6 pressure was chosen so that the small-signal transmission was $\sim 5 \times 10^{-5}$. Incident-pulse intensity was $\sim 100 \text{ MW/cm}^2$, and sample-cell length was 2.8 cm.

discussed and debated. Nevertheless, it is apparent that the process is of sufficient complexity that a definitive model cannot now be constructed.

To gain further insight into the absorption mechanism, we have undertaken a detailed study to directly observe the attenuation and reshaping of a short pulse after propagation through the polyatomic gas. Our earlier observations¹⁶ indicated that hot CO₂-induced ringing was reduced by as much as a factor of six when a nanosecond pulse was first allowed to saturate a cell of SF₆. The present set of measurements was performed on our GigaWatt Test Facility (GWTF) and involved studying the pulse-shape evolution of a nanosecond P(20) CO₂ laser pulse at 10.59 μm after collimated passage through a 2-cm² area of SF₆ in a 3.3-cm-long cell. Input pulse intensities up to 200 MW/cm² were used, and SF₆ pressures were varied from 0 to 30 torr. The pulse shape was monitored with a recently developed detector-oscillator combination with a combined risetime shorter than 100 ps.

A plot of representative data is shown in Fig. 23; the delay of the peak and the onset (5% of peak intensity) of the transmitted pulse with respect to the unattenuated pulse are both plotted against input intensity at each of three pressures. Note

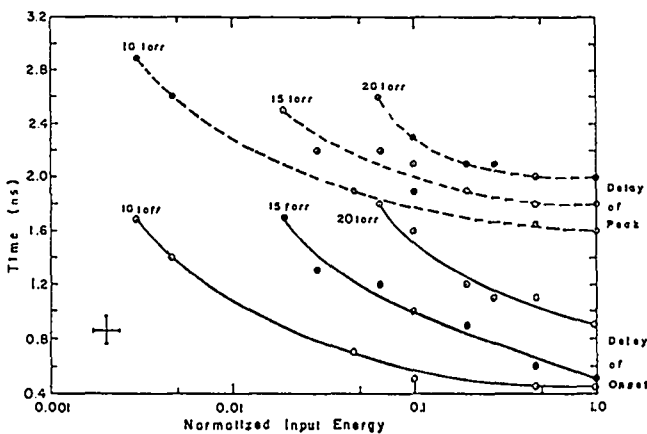


Fig. 23

Delay of pulse peak and delay of pulse onset as a function of input intensity; the value of unity corresponds to an input intensity of 200 MW/cm². Data are shown for sample cell pressures of 10, 15, and 20 torr. For clarity, the peak delay curves have been raised vertically by 1.2-ns.

that each curve falls off with increasing intensity and with decreasing pressure. In these experiments, risetime reduction factors as high as 2.5 were observed. At high input intensities, however, the duration was reduced with little change in risetime. In general, we find that at lower intensities the leading edge of the pulse is almost totally absorbed, while the tail is attenuated with little shape change.

Interpretation of these data is in progress. Our observations are consistent with a multiple-photon absorption process in which the cross section for absorption increases for a time after a given amount of energy has been absorbed. We find that the SF₆ molecule exhibits only partial saturation. The observation that the tail is attenuated with little shape modification is consistent with tail absorption occurring into the quasi-continuum. Experiments using CO₂ laser lines other than P(20) of the 10-μm branch are under way and will be similarly analyzed.

Pulse Contrast Enhancement with Hot CO₂ -- We have theoretically analyzed and experimentally verified a novel technique which significantly improves the contrast ratio (pulse-to-background intensity) of subnanosecond CO₂ laser pulses externally gated from a nearly bandwidth-limited 70-ns oscillator pulse.

In the contrast-ratio improvement scheme described here, the enhancement is obtained by passing the switched-out pulse through hot low-pressure CO₂ which, because of its narrow absorption lines, acts as a pulse-duration discriminator. By choosing the pressure of the hot CO₂ so that the absorbing bandwidth is intermediate between the narrow bandwidth of the long, smooth pulse and the broad bandwidth of the subnanosecond pulse, the long pulse is attenuated nearly in accordance with Beer's law, whereas the short pulse is transmitted with little attenuation. Hot CO₂ is especially suited for this task because of its strong absorption ($\approx 0.02/\text{cm}$ at 673 K) and its line-to-line frequency match with multifrequency oscillator systems.

To demonstrate this effect experimentally, we studied and compared the transmission of both 400-ns and 70-ps multiline CO₂ laser pulses through 5 m of CO₂ heated to 683 K. The subnanosecond

pulse was studied with a combined detector-oscilloscope system with a 100-ps risetime. Figure 24 shows the measured output pulse as a function of hot-CO₂ pressure; with increasing pressure the initial portion of the transmitted pulse loses amplitude and temporally narrows, and a ringing develops. In the transmitted pulse, the secondary ringing corresponds to an electric field that is 180 deg out of phase with the incident pulse; this is a manifestation of the evolution toward a zero-pulse. We have also measured the intensity attenuation of the long pulse. By comparing the short-pulse and long-pulse reductions, we find contrast-ratio improvement factors of 1, 21, 85, 552, 1211, 944, and 768 at pressures of 0, 5, 10, 15, 25, 40, 60, and 75 torr, respectively. Note that at 25 torr the ringing is only ~25% of the

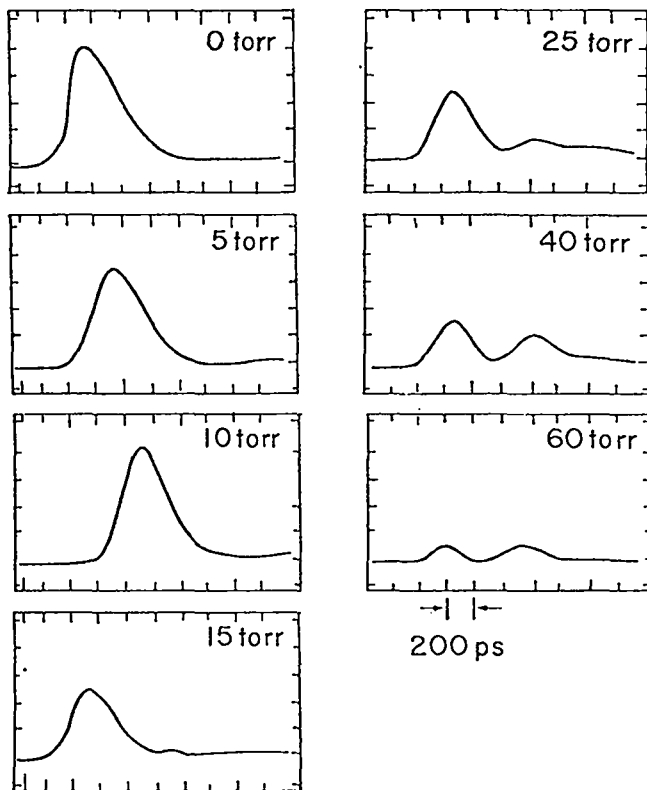


Fig. 24
Typical experimental results obtained with the ultra-fast oscilloscope. The hot-CO₂ pressures are indicated in the insets; the 0-torr pulse is the input pulse. All traces were taken with the same relative deflection, and the sweep speed is 200 ps/div. Note that with increasing pressure the main pulse loses intensity and becomes shorter, and that the ringing becomes more prominent.

peak amplitude and the contrast-ratio improvement is greater than 500:1.

In good agreement with the data, pulse-propagation modeling has been performed in both the linear and nonlinear regimes by appropriate CO₂ laser propagation codes.

Retropulse Isolator (R. F. Benjamin) -- The study of a retropulse isolator using a plasma produced at an aperture in vacuum was extended to higher energies. Because an isolator device would be useful between Amplifiers 3 and 4 in the Single-Beam System, it was necessary to test its effectiveness at the 5-J level. In these experiments, we used a green probe beam to monitor the plasma formed by the main CO₂ laser pulse. We found that a 260- μ m aperture allowed 70% of the incident CO₂ pulse to be transmitted before refraction attenuated the beam. The refracting plasma was rather dense, refracting the green light as well as the 10.6- μ m light. Most importantly, the green light was severely refracted for over 500 ns, indicating that the plasma is quite long-lived. We conclude that this retropulse isolator would be useful in a laser system where the target is as much as 75 m from the isolator.

Damage Studies

Damage studies have been performed on the Two-Beam System's oscillator-preamplifier system. An uncoated sample of NaCl polished by Air Force Weapons Laboratory (AFWL) was tested and found to exhibit no surface damage up to the flux at which bulk damage occurred (6.0 to 8.7 J/cm², 1.8-ns pulse). A sample of salt polished by Harshaw to its high-power laser finish exhibited surface damage at 3.5 J/cm² and bulk damage at 7.8 J/cm².

A sample of KCl polished by AFWL did not exhibit surface damage up to 6.0 J/cm². However, severe bulk damage occurred at 4.8 J/cm².

Several glass surfaces were irradiated to see if glass mirrors could be used as high-quality beam-sampler attenuators. Well-polished optical glass had a damage threshold of 1.8 J/cm², which would be satisfactory for use with the TBS and EBS at \leq 5% of full output.

Diagnostics Development

Introduction -- Laser fusion experiments

require well-characterized subnanosecond CO₂ laser pulses, demanding advancement in the state of the art in both short-pulse generation and fast diagnostics. A new electro-optical shutter and a solid-state plasma shutter are now in assembly and will extend our short-pulse generation capability to < 100 ps. Work is continuing on the ruby-laser-pumped parametric upconverter and on the streak camera-to-oscilloscope video system which, when complete, will extend our real-time CO₂ laser diagnostics capability to 1 ps. This diagnostic system will deliver the best time resolution possible. Because many experiments do not require this expensive, difficult diagnostic system, we need to develop a simpler system with reduced time resolution. This and other topics are discussed below.

Five-GigaHertz Oscilloscope -- We have completed a performance evaluation of the 5-GHz oscilloscope and from this evaluation have determined the feasibility of increasing its bandwidth to 10 GHz.

We constructed this device by using a TMC-4 cathode-ray tube purchased from R.T.C. La Radiotechnique-Compelec. This tube uses an integral microchannel-plate electron multiplier to obtain wide bandwidth and good sensitivity. Conventional circuitry is used in the construction except for the sweep, trigger, and gating, which use special avalanche transistor circuits designed by us. Performance characteristics of the oscilloscope are given in Table IX, and the scope response to a 20-ps risetime tunnel-diode pulser is shown in Fig. 25. The step-function response of Fig. 25 was used to calculate the frequency response in Table IX and in Figures 26 and 27. Figure 26 shows that the calculated phase distortion is not significant below 10 GHz, and Fig. 27 shows that the calculated amplitude roll-off is well behaved below 10 GHz. From these calculations we conclude that it is feasible to extend the oscilloscope bandwidth to 10 GHz by using a compensation network with a frequency response which, when convolved with Fig 27, gives a flat response up to 10 GHz. This extension will result in a loss in vertical sensitivity of ~20 dB. Our next goal will be the design of a compensation

TABLE IX

PERFORMANCE CHARACTERISTICS OF
5-GHZ OSCILLOSCOPE

Vertical Sensitivity	0.11 V/div (dc)
Line Width	0.4 mm (manufacturer's data).
Sweep Rates	0.1, 0.2, 0.5, 1.0, 2.0, 5.0, and 10.0 ns/div.
Sweep Voltages	200 V (0.1 ns/div), and 70 V (1.0 ns/div).
Frequency Response	-3 dB at 3.7 GHz; -5 dB at 5 GHz; -18 dB at 10 GHz.
Division Size	7 mm vertical by 7 mm horizontal.
Screen Size	6 divisions vertical by 10 divisions horizontal.
Input Impedance	50 Ω.

network with the proper amplitude and phase characteristics to extend the scope bandwidth to 10 GHz.

Subnanosecond Infrared Detectors

Evaluations of commercially available ir detectors have continued by using the Free-Induction Decay cell to generate short CO₂ laser pulses and the 5-GHz oscilloscope to record detector response. We have completed the evaluation of Santa Barbara Research Company's germanium:mercury liquid helium-cooled detector, of Laser Precision's 2- by

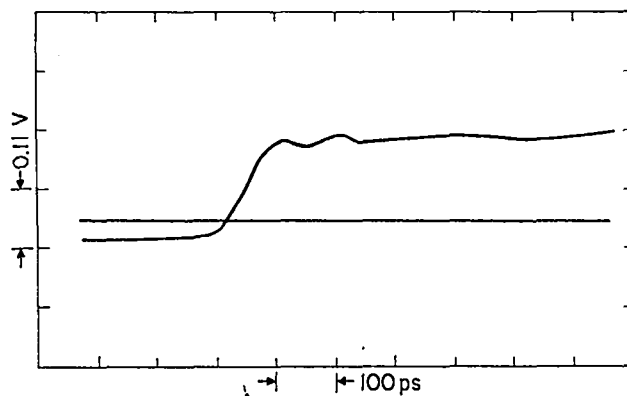


Fig. 25
Oscilloscope response to a 20-ps risetime step and a 10-GHz sine wave, with a horizontal alignment trace. (Scale: 100 ps/div horizontal, 0.11 V/div vertical).

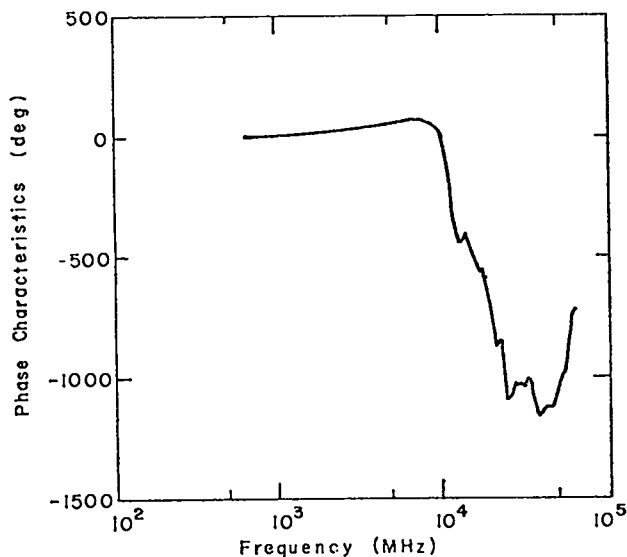


Fig. 26
Phase response of 5-GHz oscilloscope. Note that response is flat to 10 GHz.

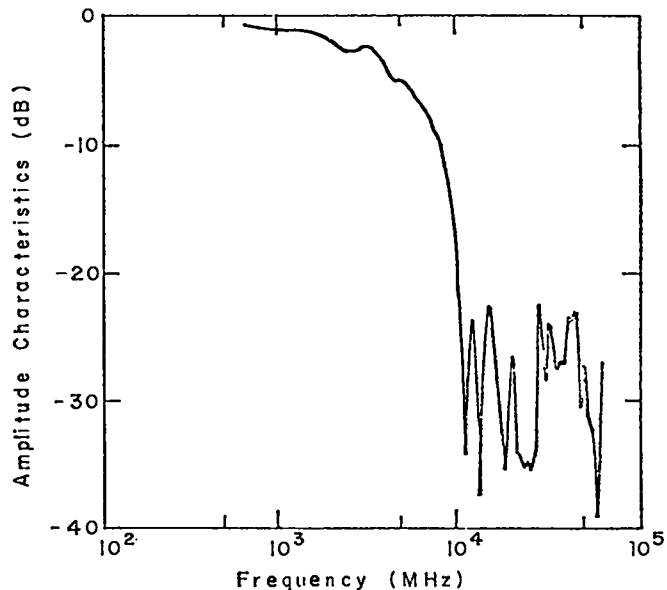


Fig. 27
Amplitude response of 5-GHz oscilloscope; rolloff of 3 db at 3.7 GHz.

2-mm, 4- by 4-mm, and 10- by 10-mm pyroelectric detectors, and of Rofin Limited Model-7425 photon-drag detector. The Rofin photon-drag detector has a FWHM response of 250 ps, as advertised, but ringing is evident when measuring short pulses. Amplitude and time response of Laser Precision's pyroelectric detectors show a linear decrease with increasing detector size. We conclude from the tests that an optimized pyroelectric detector for short pulses should be as small as possible. A 1- by 1-mm and a 0.5- by 0.5-mm Laser Precision detector will be tested and compared to the performance of the Molectron 1- by 1-mm pyroelectric detector, described in LA-6616-PR, to determine if a significant difference exists between manufacturers. In the preceding progress report (LA-6616-PR) we also presented Santa Barbara Research Company's germanium:mercury detector. Subsequent tests show that the detector risetime is 200 ps with a fall time in excess of 1 ns, as reported earlier, with the redesigned coupling network having no significant effect.

REFERENCES

1. Prof. P. Belanger, Universite Laval, Quebec, Canada, private communication (February 1976).
2. M. C. Richardson, *Appl. Phys. Lett.* 25, 31 (1974).
3. F. Keilmann, *IEEE J. Quant. Electron.* OE-12, 592 (1976).
4. B. J. Feldman, "Multiline Short Pulse Amplification and Compression in High Gain CO_2 Laser Amplifiers," *Opt. Comm.* 14 (May 1975) pp. 1316.
5. J. A. Fleck, Jr., "Ultrashort-Pulse Generation by Q-Switched Lasers," *Phys. Rev.* B1 (January 1970) pp. 84-100.
6. C. R. Phipps, Jr., S. J. Thomas, and J. F. Figueira, Paper WA6, OSA/IEEE Conf. on Laser and Electro-Optical Systems, San Diego, California (May 25-26, 1976).
7. A. F. Gibson, C. A. Rosito, C. A. Raffo, and M. F. Kimmitt, *Appl. Phys. Lett.* 21, 356 (1972).
8. H. B. Briggs and R. C. Fletcher, *Phys. Rev.* 91, 1342 (1953).
9. M. Sargent III, University of Arizona, to be published.

10. C. R. Phipps, Jr., and S. J. Thomas, J. Appl. Phys. 47, 204 (1976).
 11. R. Ahrenkiel and T. Coburn, IEEE Trans. on Magnetics 11, 1103 (1975).
 12. E. Carnall, D. Pearlman, T. J. Coburn, F. Moser, and T. W. Martin, Mat. Res. Bull. 7, 1361 (1972).
 13. E. Stark and F. Skoberne, Los Alamos Scientific Laboratory report LA-6510-PR (November 1976), pp. 47-49.
 14. R. V. Ambartzumian, V. S. Letokhov, E. A. Ryabov, and N. V. Chelakin, ZhETF Pis. Red. 20, 597 (1974) JETP Lett. 20, 273.
 15. E. Stark and F. Skoberne, Los Alamos Scientific Laboratory report LA-6245-PR (July 1976), p. 35.
 16. S. J. Czuchlewski, B. J. Feldman, R. A. Fisher, and A. V. Nowak, Bull. Am. Phys. Soc. 21, 1283 (1976).
-

II. NEW LASER RESEARCH AND DEVELOPMENT

New types of lasers must be developed to provide the desired energy per pulse, pulse length, pulse shape, wavelength, and efficiency for laser fusion applications. Our advanced laser research has focused on rare-gas oxides and on Hg₂ excimers.

INTRODUCTION

(O. Judd)

In our new laser research effort we emphasized three general areas:

- The production of O(¹S) by electrical-discharge techniques with application to the oxygen laser at a wavelength of 557 nm. This work represents an integrated effort consisting of electron-beam-controlled discharge experiments, kinetics measurements by means of short-pulse electron-beam-optical pumping techniques, theoretical modeling of electron and molecular kinetics for the discharge experiments, and ab initio calculations of excited-state potential curves and matrix elements for the rare-gas oxides.
- Metal-vapor laser research, which presently involves gain measurements on the 335-nm band of Hg₂* excited by an electrical discharge, and pressure and dimensional scaling studies of heat pipes for use with metal-vapor laser systems.
- The measurement and improvement of damage thresholds of optical components in the near-ir-through-uv wavelength region. New designs for multilayer dielectric films have increased the damage threshold, as verified by experimental comparison measurements at 1.06 μm. Multiwavelength damage comparison measurements have continued for refractory-oxide coatings.

These topics are discussed in greater detail in the following paragraphs.

OXYGEN AND OTHER GROUP-VI LASERS

Electron-Beam-Controlled Discharge Experiments

(J. McLeod, O. Judd)

General--The two key preconditions that must be met for efficient electrical discharge-production of O(¹S) at high storage densities are (1) a sufficiently high ratio of electric field vs particle number density E/N , and a sufficiently high current density under stable operating conditions for a discharge duration of 0.2 to 1.0 μs, and (2) an efficient collisional energy-transfer channel for the production of O(¹S) with minimum electron or molecular loss channels. These topics are discussed in greater detail in a special report.¹ Both areas are being addressed in our experiments as well as in other independent kinetics studies discussed later.

Results--The discharge operating regime for a gas mixture of argon and several oxygen donors (O₂, CO₂, N₂O) at various gas pressures and concentrations has been investigated experimentally. Electron-beam current densities were 1.0 and 0.04 A/cm². The experiments were carried out in our small electron-beam-controlled discharge devices; the area of the electron-beam window was 2.0 by 20.0 cm and the anode-cathode spacing was 1.3 cm; electron-beam energy was 230 keV. To determine the highest E/N value in the discharge under operating conditions, we measured the breakdown voltage for the grid cathode in the absence of the electron beam. Breakdown values for this particular discharge configuration were determined and correlated for several gas mixtures at different pressures. Higher breakdown values of E/N can, no doubt, be achieved with a better discharge-cathode design.

Maximum operating values of E/N are summarized in Fig. 28. In all cases the

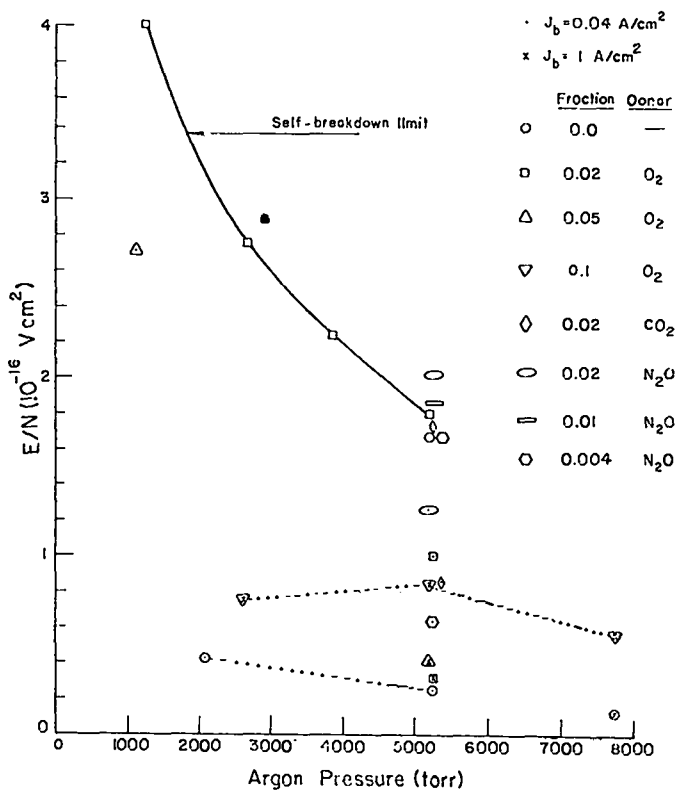


Fig 28

Maximum operating values of E/N as a function of gas pressure in electron-beam-controlled discharge experiments in mixtures of argon and various oxygen donors.

experimental geometry remained unchanged and the buffer gas was argon. Breakdown values of E/N in the absence of the electron beam are also plotted for comparison. Most of the initial data were obtained at 5200 torr, to simulate the high gas pressures required for laser action in rare-gas oxide molecules. However, because stimulated emission by the atomic transition is of equal interest, particularly for electrical-discharge pumping, we also carried out experimental measurements at lower pressure.

Theoretical calculations indicate that efficient power flow from the electrons in the discharge into the electronic states of argon requires that E/N be in the range $10^{-16} \leq E/N \leq (2 \times 10^{-16}) \text{ V cm}^{-2}$ for a gas mixture of argon and 0.1% O_2 (see Theory of Electron Kinetics, below). Although results for other (perhaps more desirable) oxygen donors are less certain, this range of E/N should be typical of that required in the discharge. The fractional concentration of

oxygen donors in most experiments significantly exceeded that dictated by excited-state laser kinetics. These high concentrations were necessary to minimize catastrophic instabilities in the discharge at the higher gas pressure. At lower pressures, stable discharge operation should be attainable with lower fractional concentrations of the oxygen donor; this behavior is attributed to the stabilizing action of electron attachment in the donor molecule. This process was discussed in detail in the preceding quarterly progress report (LA-6616-PR).

As indicated in Fig. 28, an E/N near $10^{-16} \text{ V cm}^{-2}$ could be achieved for several oxygen donors and fractional concentrations at the lower values of electron-beam current density. At higher densities of, e.g., 1.0 A/cm^2 , the stable operating values of E/N are lower due to higher plasma conductivity; this behavior is consistent with theoretical considerations. Because the measured values of E/N are typically half the self-breakdown limit, some future improvement could be expected. Our limited data obtained after reduction in total pressure from 5200 to 2000 torr, supports our expectation that stable discharge operation at values of E/N in the desired operating range can be achieved. Stable operation at both high-E/N and high-discharge current density, i.e., at high-power input to the discharge, is important for proper laser operation.

The strong oscillations in the discharge current and voltage that were reported previously (LA-6616-PR) and attributed to a dissociative attachment instability, were not observed at low gas pressures and electron-beam current densities. However, more data will be required to quantify these effects.

We have initiated fluorescence measurements at 558 nm to address the issues of energy-transfer channels for $O(^1S)$ production and loss. Simultaneously, we are measuring the rare-gas uv dimer emission; for argon, this band is centered at 125 nm. The goal of our measurements is to relate quantitatively the production of $O(^1S)$ to the energy input to the discharge. Our preliminary fluorescence measurements at 558 nm can be correlated with the field enhancement by

the discharge. This emission however, is broadband and is caused by the argon and not by the $O(^1S)$. These experiments will be continued in other discharge operating regimes and at lower fractional concentrations of the oxygen donor; kinetic considerations indicate that significant improvements in $O(^1S)$ population density can be achieved under these conditions.

Future efforts will concentrate on parametric discharge evaluation at low gas pressures and higher power. These measurements will require some modification of the present discharge-power supply. Improvements in the electron-beam power supply are also in progress. These modifications should permit more reliable experimentation over a wider operating range and should substantially reduce electromagnetic noise in the data-acquisition channels. Fluorescence measurements at 558 nm will continue over a broader range of discharge parameters; measurement of argon excimer emission at 125 nm should be possible in the near future.

Kinetics and Electron Beam

Optical Pumping Measurements (W. Hughes)

A temporary modification of the Cassandra electron-beam machine has been completed. We are now operating the device below design specification, at 1MV and 100 kA by using the peaking switch as an output switch. This alternative use of the peaking switch became necessary after the destruction of the original output switch during vendor installation and testing. The loss of the output switch has substantially slowed the anticipated experimental progress. We expect to receive a replacement output switch by mid-February; checkout and acceptance should be completed by mid-March 1977.

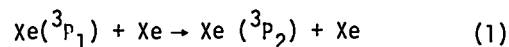
Our attempt to operate at reduced output has met with some success. Current risetimes of slightly less than 10 ns and voltage risetimes of ~5 ns have been realized. Cellophane dosimetry and carbon-black calorimetry have been used to diagnose the output beam. It appears that a beam with reasonable spatial uniformity is obtained from both the 50- and the 100-cm cathodes; however, only 50 and 30%, respectively, of the energy in the diode is delivered to a useful area.

The 1-m beam is spread out over an aperture of ~10 by 100 cm and is not well matched to our 1-m chamber. We will not try for a better spatial match because we expect a new output switch within a relatively short time. We will use the present beam for electrical checkout of our experimental detection system and for preliminary experimentation. The vendor is conducting three parallel efforts to provide a replacement--at full specification--of the output switch with either an acrylic, epoxy, or water body.

Safety precautions that have been incorporated are the removal of output-switch pressure immediately after each shot, visual inspection of the output switch after each shot, the installation of stand pipes on the transmission lines to relieve energy stored in the high-pressure gas in the event of mechanical failure of the output switch, and mechanical tiedown of the diode section to a reinforced concrete wall with a heavy steel bracket.

We have successfully prepared glued-and-welded titanium foil assemblies for our 1-m experimental chamber and have successfully pressure-checked the chamber system to 100 atm. Final pressure-checking with two chambers arranged in an optical pumping configuration will give us full certification for safe operation. Preliminary experimentation should start early in February 1977.

We have obtained more data on the kinetics of rare gases, either pure or mixed with other gases, by using our small optical pumping apparatus that was described in a previous report. A new kinetics code has been written which incorporates seven excited atomic and molecular states. This new code is primarily intended for treating data taken below 1.0 atm. Preliminary analysis of xenon data obtained with a krypton excimer light source promises to reveal many energy-transfer rates of interest. For example, the process



has a (preliminary) measured rate of $7 \times 10^{13} \text{ cm}^2 \text{ s}^{-1}$. A detailed kinetic model is being developed that will be valid for the full pressure range of the experiments, 10 torr to 3×10^4 torr. Data

to determine the energy-transfer rates to O_2 from $Xe(^3P_1)$, $Xe(^3P_2)$, $Xe_2(1_u^-:0_u^-)$ and $Xe_2(0_u^+)$, and from the same krypton states, have been obtained and are under analysis. For example, a preliminary analysis of the data for the process



yields a rate of $\sim 2.7 \times 10^{-10} \text{ cm}^3 \text{ s}^{-1}$.

Theory of Electron Kinetics (O. Judd)

A first consideration for electrical-discharge production of $O(^1S)$ is to determine the excitation efficiency for the various excited states by inelastic electron collisions. This information is obtained from numerical solutions of Boltzmann transport equation using as input the elastic and inelastic cross sections for the processes of interest. The system chosen for initial consideration is Ar- O_2 because most of the relevant inelastic cross sections for these two gases can be obtained from the literature. A more detailed description of this work is presented in LA-6710-PR.¹

A preliminary set of cross sections has been assembled elsewhere² and serves as the primary input to the computer code. The inelastic processes for O_2 include rotational excitation; vibrational excitation for transitions 0-1, 0-2, 0-3, and 0-4 and the resonant contributions for 0-1 and 0-2; several electronic-state processes; dissociative attachment; and ionization. The inelastic processes for argon include 13 electronic states; the cross-section data are derived from the semiempirical methods developed by Peterson and Allen³ and are modified to agree with the recent total electronic state scattering measurements.⁴

Rates for inelastic processes involving $O(^3P)$, $O(^1D)$, and $O(^1S)$ have also been estimated by using the cross sections derived in Ref. 5. A quantitative treatment of the atomic reactions requires a kinetic model that describes the dissociation rate and atomic concentration as a function of time. This result must then be coupled with the transport equation to obtain new values for the excitation rates. This procedure has not yet been carried out; consequently, the contribution from atomic reactions can only be

estimated. For purposes of this estimate, we will assume complete dissociation of the O_2 .

The results for argon containing 0.1% O_2 are shown in Fig. 29. Plotted is the fractional power transfer into the various inelastic processes of the gas as a function of the discharge parameter E/N . For $E/N \leq 6 \times 10^{-17} \text{ Vcm}^2$, the power flows predominantly into the electronic states of O_2 leading to O_2 dissociation and production of $O(^3P)$ and $O(^1D)$. The total loss to rotations, vibrations, and the ($a^1\Delta$) and ($b^1\Sigma$) electronic states is less than 6% for these values of E/N and decreases rapidly as E/N increases. The estimated contribution for the atom reaction $e + O(^3P) \rightarrow O(^1D) + e$, is shown as a dotted line in the figure. As indicated previously, this estimate should only be considered as an approximate upper bound for the process. The fractional power flow into the electronic states is somewhat lower than indicated due to the neglect of single and

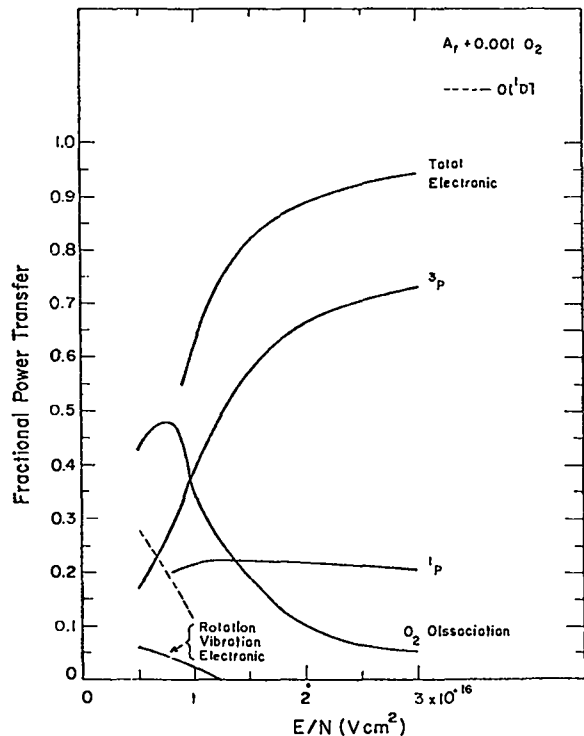


Fig. 29
Fractional power transfer from electrons into various inelastic processes in a mixture of argon and 0.1% O_2 as a function of the electrical-discharge parameter E/N .

multistep ionization processes. This reduction is typically 10 to 15%.

As E/N increases to values greater than 1×10^{-16} V cm², the dominant power flow is to the low-lying ³P levels in argon. For $E/N \geq 2 \times 10^{-17}$ V cm², the total fractional power flow directly into oxygen is less than 10%. The dominant production channels of O(¹S) in this range of E/N are photolysis, collisional dissociative excitation, and multistep excitation of the atom.

Although direct electron production of O(¹S) may occur at low values of E/N, efficient high-power operation of the electrical discharge only occurs for $E/N \geq 1 \times 10^{-16}$ V cm². In this range, the dominant power-flow channel is to the electronic states of argon, and production efficiencies of 80% for Ar* and Ar₂* energy-reservoir states seem to be indicated for $E/N \geq 2 \times 10^{-16}$ V cm².

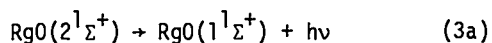
Excited State Potential Curves and Matrix Elements for Rare-Gas Oxides

(J. Dunning, P. Hay)

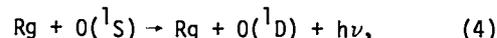
Low-Lying Electronic States of the Rare-Gas Oxides

General--The rare-gas monoxides have recently attracted considerable attention because lasing ⁶ (or gain) has been demonstrated on a perturbed O(¹S) → O(¹D) transition in argon, ^{7,8} krypton-, ⁹ and xenon-oxygen ¹⁰ mixtures, and because these monoxides offer some promise for laser fusion applications. ^{6, 9, 10} The laser transition has been assigned as a $2^1\Sigma^+ \rightarrow 1^1\Sigma^+$ transition of the corresponding rare-gas (Rg) monoxide.

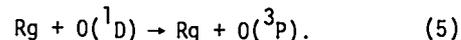
From the Rg(¹S) + O(³P, ¹D, ¹S) separated atom limits, six molecular states are obtained: a ³π and a ³Σ states from O(³P); $1^1\Sigma^+$, $1^1\Pi$, and $1^1\Delta$ states from O(¹D); and a $2^1\Sigma^+$ state from O(¹S).¹¹ Of particular relevance for the rare-gas monoxide laser systems are: the spectra of the perturbed O(¹S) → O(¹D) transition



the lifetime of the $2^1\Sigma^+$ state; the collision-induced emission rate coefficient for the O(¹S) state,



and the O(¹D) quenching rate



A theoretical description of these processes requires a knowledge of the potential-energy curves of all six states and of the transition moment coupling the $2^1\Sigma^+$ state arising from O(¹S) with the $1^1\Sigma^+$ and $1^1\Pi$ states from O(¹D). The latter process, Eq. (5), which is of importance in depleting the lower laser level, requires, in addition, a knowledge of the spin-orbit matrix element coupling the curves arising from O(¹D) with those from O(³P).

The lifetimes of the $2^1\Sigma^+$ states of ArO, KrO, and XeO have recently been determined and are six orders of magnitude shorter than the life time of the O(¹S) atomic state. This finding indicates a large enhancement in the transition moments that radiatively couple the $2^1\Sigma^+$ state with the $1^1\Sigma^+$ and $1^1\Pi$ states. The collision-induced O(¹S) → O(¹D) emission rate has also been determined for argon, krypton, and xenon. Again, a strong enhancement in the emission rate was observed.

We report here the results of ab initio configuration interaction calculations on the state of the rare-gas monoxides arising from the Rg(¹S) + O(³P, ¹D, ¹S) separated atom limits. The potential-energy curves for all six molecular states are reported, as are the dipole transition moments out of the $2^1\Sigma^+$ state.

Results and Discussion--The calculated potential-energy curves for the ³π, ³Σ⁻, $1^1\Sigma^+$, $1^1\Pi$, $1^1\Delta$, and $2^1\Sigma^+$ states of NeO, ArO, KrO, and XeO are plotted in Figs. 30 through 33, respectively. The curves arising from the Rg + O(¹D) and Rg + O(¹S) dissociation limits have been uniformly shifted downward by 0.30 and 0.69 eV, respectively, to correct for the errors in the atomic excitation energies. All subsequent discussion refers to the corrected curves.

All potential curves, with the exception of those for the $1^1\Sigma^+$ states of KrO and XeO, are unbound. Slight wells, not evident in the plots, are found for all the curves. The origin of these wells is not entirely understood; the calculations are not designed to account for van der Waals effects, although certain excitations contributing to the dispersion forces do appear in the polarization-configuration interaction (POL-CI) wavefunction. They may be due to basis set limitations and/or an artifact of the POL-CI method.

Potential Energy Curves for 3Π , $3\Sigma^-$, $2^1\Sigma^+$, 1Π , and 1Δ States--In Fig. 34 we compare the calculated potential-energy curves for the 3Π and $3\Sigma^-$ states with the potentials obtained by Foreman,

Lees, and Rol.¹² These potentials were derived from elastic-scattering data by assuming the potential to be of the form

$$V(R) = Ae^{-\alpha R}, \quad (6)$$

and adjusting A and α to best fit the measured differential cross sections. As noted in the introduction, this analysis unfortunately did not take account of the fact that two curves (3Π and $3\Sigma^-$) are needed to describe the interaction of a rare-gas atom with an oxygen atom in its ground state. In light of this, the close agreement between the calculated 3Π curves and the potentials derived by Foreman et al evident in Fig. 34 is

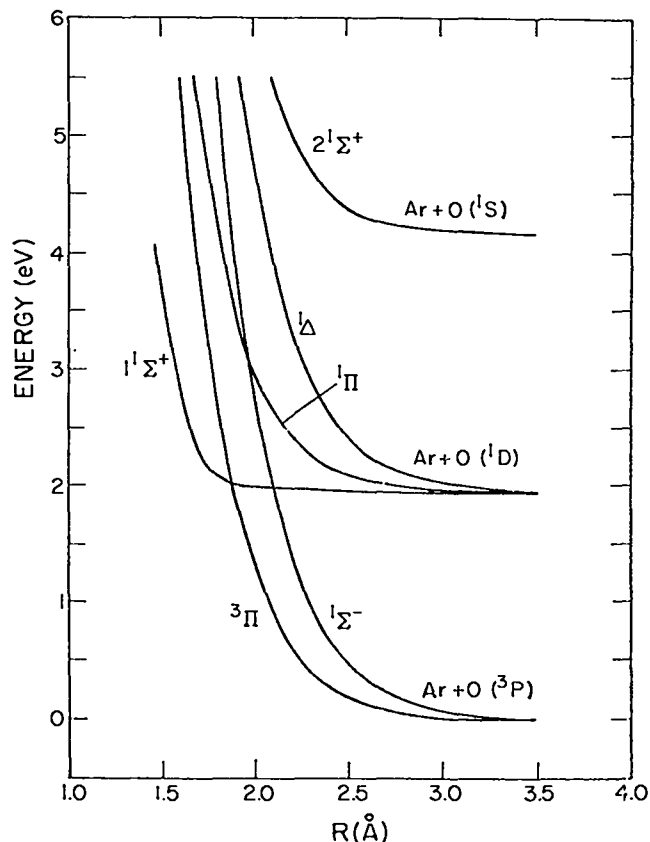
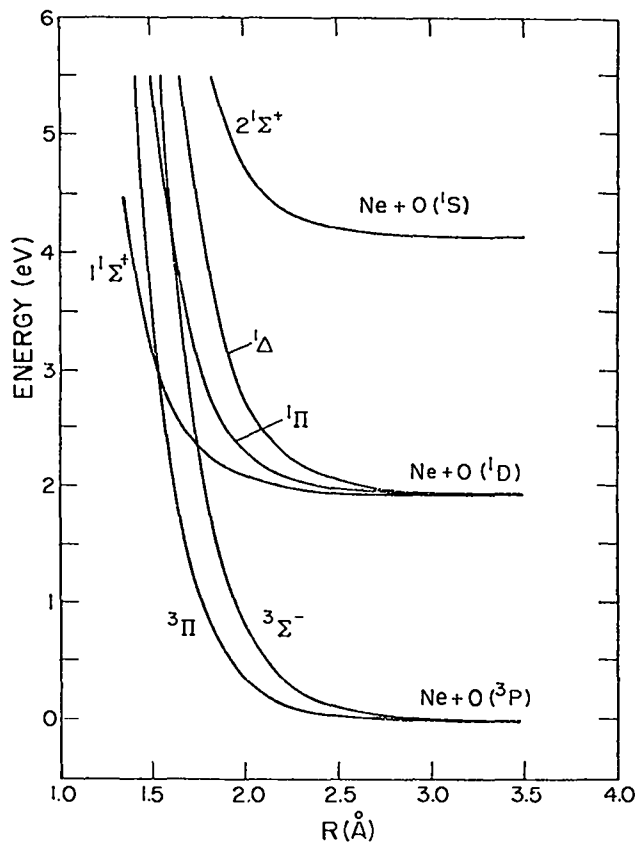


Fig. 30
Calculated potential-energy curves for the state of NeO arising from the $Ne(1S) + O(3P, 1D, 1S)$ separated atom limits. The curves have uniformly shifted to correct for the errors in the $O(1D-3P)$ excitation energies; see text.

Fig. 31
Calculated potential-energy curves for the states of ArO, arising from the $Ar(1S) + O(3P, 1D, 1S)$ separated atom limits. The curves have been uniformly shifted to correct for the error in the $O(1D-3P)$ and $O(1S-3P)$ excitation energies; see text.

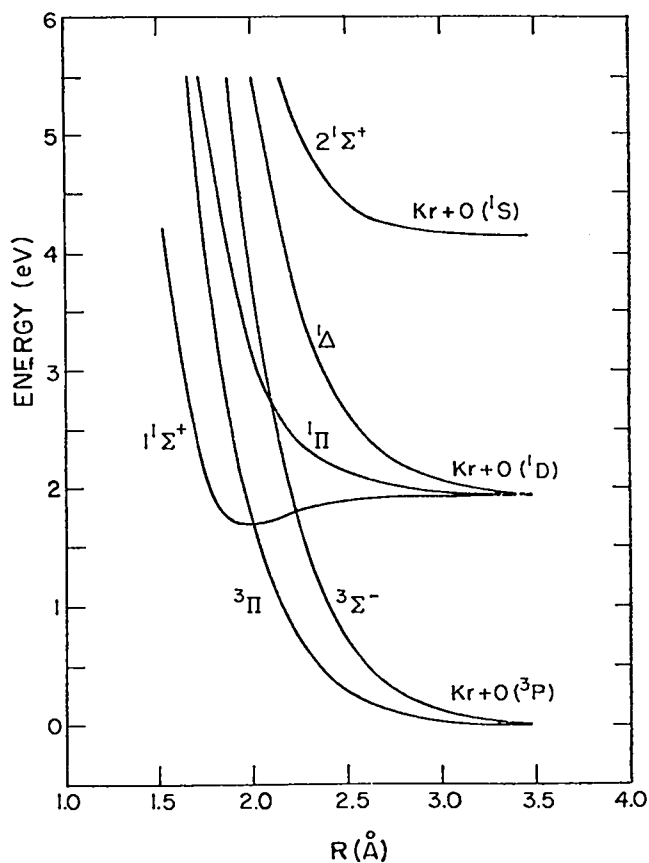


Fig. 32

Calculated potential-energy curves for the states of ${}^1\text{KrO}$ arising from the $\text{Kr}(^1\text{S}) + \text{O}(^3\text{P}, ^1\text{D}, ^1\text{S})$ separated atom limits. The curves have been uniformly shifted to correct for the errors in the $\text{O}(^1\text{D}-^3\text{P})$ and $\text{O}(^1\text{S}-^3\text{P})$ excitation energies; see text.

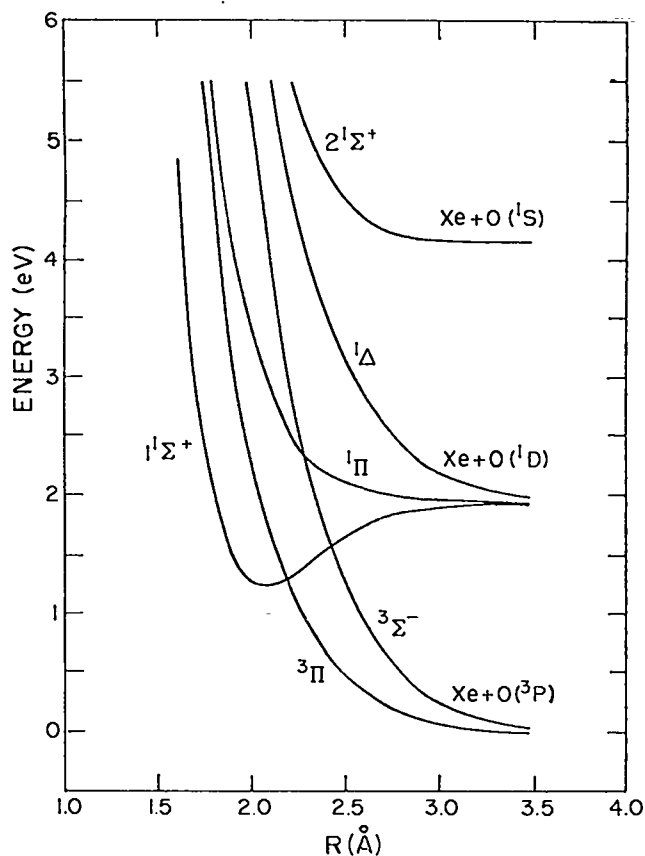


Fig. 33

Calculated potential-energy curves for the states of XeO arising from the $\text{Xe}(^1\text{S}) + \text{O}(^3\text{P}, ^1\text{D}, ^1\text{S})$ separated atom limits. The curves have been uniformly shifted to correct for the errors in the $\text{O}(^1\text{D}-^3\text{P})$ and $\text{O}(^1\text{S}-^3\text{P})$ excitation energies; see text.

certainly surprising and strongly encourages a more detailed analysis of the experimental data.

From an analysis of the major green band system of XeO (4800 to 5600 Å), Cooper, Cobb, and Tolnas¹³ obtained $D_e = 0.36$ eV and $\omega_e = 372$ cm^{-1} for the $1^1\Sigma^+$ state (see also Huestis *et al.*⁹). These values are to be compared with the calculated constants, $D_e = 0.70$ eV and $\omega_e = 470$ cm^{-1} . It is rather surprising that the calculated D_e is greater than the experimental D_e . Although one other such case is known, that of F_2 with which RgO is isoelectronic, the POL-CI method in general underestimates D_e . In F_2 the error is ~ 0.2 eV, comparable to that found here (0.34 eV). On the

other hand, the available experimental data are not sufficient to definitively establish the numbering of the observed vibrational bands; e.g., matrix isolation studies suggest that D_e should be larger by at least three vibrational quanta.

As noted above, the difference between the theoretical and experimental D_e values is 0.34 eV. Assuming an average vibrational spacing of 415 cm^{-1} (0.051 eV), this difference is equivalent to about seven vibrational levels; that is, the theoretical calculations suggest that the band assigned as the (0,0) band is, in fact, the (0,7) band. Further support for this assignment is given in Table X, which contains the calculated vibrational levels,

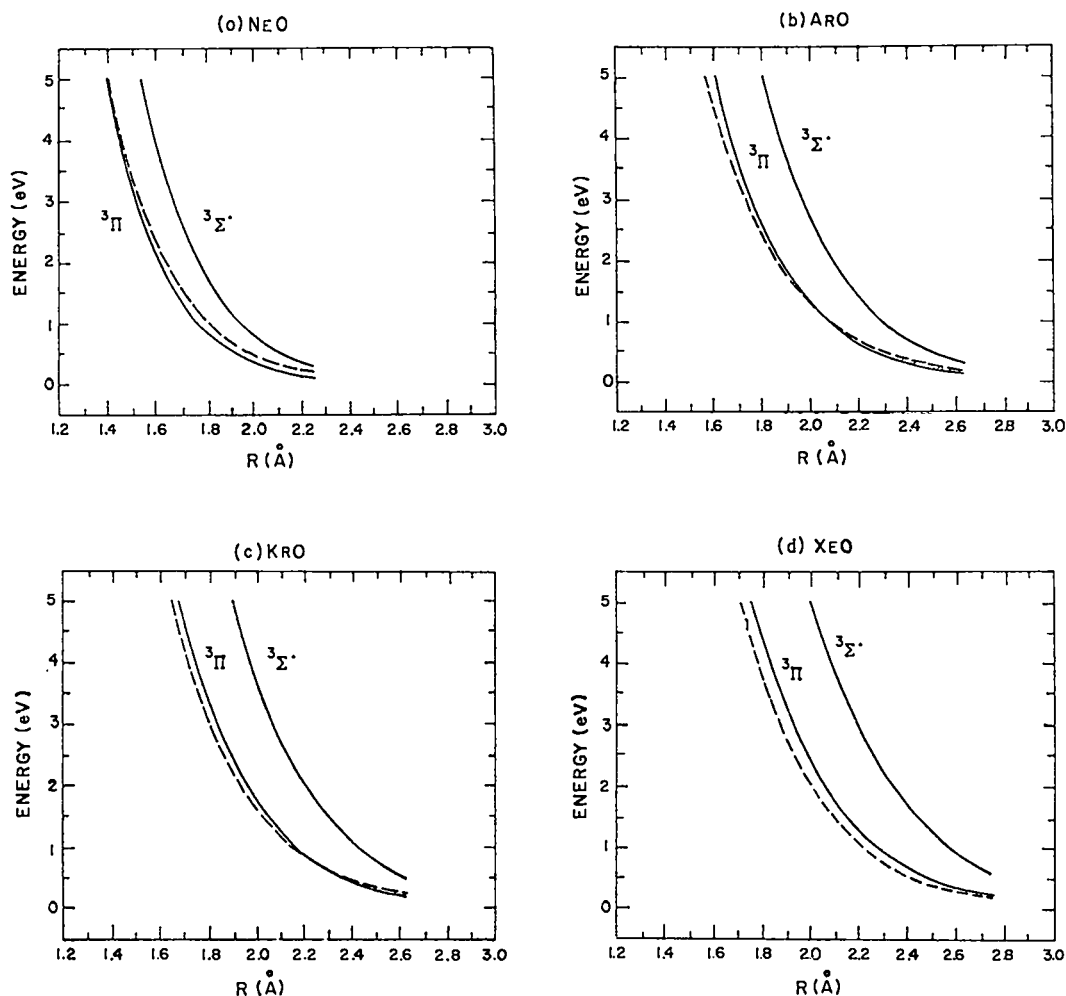


Fig. 34
Comparison of calculated potential-energy curves for the 3π and $3\Sigma^-$ states of RgO (solid lines) with the rare gas-oxygen interaction potentials determined by Foreman *et al.*¹² (dashed lines).

$G(v)$, and the calculated and observed vibrational spacings, $\Delta G(v + 1/2)$.¹³ From this information we find that the observed vibrational spacings are best fit if we assume that the vibrational numbering of the observed levels is shifted by seven. These arguments, of course, cannot establish the absolute vibrational numbering either; the probable errors in the theoretical calculations (± 0.3 eV) are too large to do that with confidence. Clearly, a more detailed study of the green-band system of XeO is needed, especially studies with pure isotopes of xenon, in order to establish the absolute vibrational numbering in the $1^1\Sigma^+$ state.

The disagreement between the calculated and experimental equilibrium separations (R_e) for the $1^1\Sigma^+$ state of XeO might also be noted. However, the experimental data are insufficient to determine the rotational parameters B_v . The "experimental" internuclear separation R_e^9 given in Table XI was obtained by positioning the potential curve for the $1^1\Sigma^+$ state relative to the semitheoretical curves of Abrahamson¹⁴ for Xe + O. It is, therefore, subject to a large uncertainty.

The rapidity of $O(^1D)$ quenching by the rare gases, Reaction (3), almost certainly requires a crossing of the curves arising from the $O(^1D)$ and

TABLE X

VIBRATIONAL LEVELS AND SPACINGS
FOR $1^1\Sigma^+$ STATE OF XeO

Vibrational Level	G(v) ^a (cm ⁻¹)	$\Delta G(v + 1/2)$ ^b	
		Calc. (cm ⁻¹)	Exp. (cm ⁻¹)
0	232	457	—
1	690	44	—
2	1134	431	—
3	-1565	416	—
4	1981	401	—
5	2382	385	—
6	2767	367	—
7	3134	349	347
8	3483	328	328
9	3811	306	302
10	4118	282	272
11	4400	256	252
12	4656	226	224
13	4882	193	201
14	5075	158	186
15 ^c	5233	—	—

^a Obtained by solving the vibrational ($J=0$)-Schroedinger equation with the calculated potential.

^b Reference 13.

^c Seven higher levels are omitted.

TABLE XI

CALCULATED CROSSING POINTS R_c AND ENERGIES ΔE_c FOR
 $1^1\Sigma^+ - 3^1\Pi$ AND $1^1\Sigma^+ - 3^1\Sigma^-$ CROSSINGS IN RARE-GAS MONOXIDES^a

Molecule	$1^1\Sigma^+ - 3^1\Pi$ ^b		$1^1\Sigma^+ - 3^1\Sigma^-$	
	R_c (Å)	ΔE_c (eV)	R_c (Å)	ΔE_c (eV)
NeO	1.53	0.92	1.74	0.39
ArO	1.87	0.068	2.09	0.028
KrO	2.00	-0.25	2.23	-0.16
XeO	2.19	-0.64	2.42	-0.37

^a Corrected for error in calculated $0(1D) - 0(3P)$ excitation energy; see text.

^b Relative to the $Rg(1S) + 0(1D)$ separated atom energy.

energies can be calculated is not known; in an earlier calculation on ArO in which the reference orbitals were taken for the $3^1\Sigma^-$ state, we obtained crossing points of 1.87 and 2.10 Å, and crossing energies of 0.051 and 0.015 eV for the $3^1\Pi$ and $3^1\Sigma^-$ states, respectively. The results for XeO are, however, consistent with the predissociation of the $1^1\Sigma^+$ state observed in the matrix-isolation studies.

In the past the dependence of the quenching-rate constant on the rare-gas species involved was attributed to spin-orbit effects, which would be larger, e.g., for xenon than for krypton. While this variation is still undoubtedly an important factor, especially in view of the variation in the ionic character of the $1^1\Sigma^+$ state noted earlier, the rather substantial variations in the crossing points and energies found here can also be expected to contribute to the observed trend in the quenching-rate constant. Isolating the factors that contribute to the observed variation quenching rate will in the end, of course, have to await detailed molecular dynamics calculations.

Transition Moments for $2^1\Sigma^+ - 1^1\Sigma^+$, $1^1\Pi$ Transitions--The dipole transition moments, μ_{ij} , coupling the $2^1\Sigma^+$ states of the rare-gas monoxides with the $1^1\Sigma^+$ and $1^1\Pi$ states are tabulated in Table XII and plotted in Fig. 35 for ArO, KrO, and XeO. As is evident, there is a considerable variation in μ_{ij} between

(1) the $2^1\Sigma^+ - 1^1\Sigma^+$ and $2^1\Sigma^+ - 1^1\Pi$ transitions, and

$0(3P)$ separated atom limits. As seen in Figs. 30 thru 33 this is indeed the case. The potential curves for the $1^1\Sigma^+$ states are crossed by both lower state curves in all the rare-gas oxides. Both the $3^1\Pi$ and $3^1\Sigma^-$ states can interact with the $1^1\Sigma^+$ state because all the states have an 0^+ component when spin-orbit coupling is included. A general trend in the crossing is obvious: The crossing points increase and the crossing energies decrease in going from NeO to XeO. In fact, for NeO the crossings occur so high on the repulsive wall of the $1^1\Sigma^+$ curve, at 0.92 eV for the $1^1\Sigma^+ - 3^1\Pi$ crossing and at 0.39 eV for the $1^1\Sigma^+ - 3^1\Sigma^-$ crossing, that neon should be only a poor quencher of $0(1D)$. In ArO only the $1^1\Sigma^+ - 3^1\Sigma^-$ crossing occurs in a thermally accessible region ($\Delta E_c = 0.028$ eV), whereas for KrO and XeO both crossings occur within the well of the $1^1\Sigma^+$ state. The values given in Table XI should be taken with caution because the accuracy with which the crossing points and

TABLE XII

CALCULATED DIPOLE TRANSITION MOMENTS, μ_{ij} , FOR $2^1\Sigma^+ - 1^1\Sigma^+$ AND $2^1\Sigma^+ - 1\Pi$ TRANSITIONS IN RARE-GAS MONOXIDES
 [Moments are in atomic units, internuclear spacings, R, in Bohr radii (a_0)]

R(a_0)	μ_{ij} in ArO		μ_{ij} in KrO		μ_{ij} in XeO	
	$2^1\Sigma^+ - 1^1\Sigma^+$	$2^1\Sigma^+ - 1\Pi$	$2^1\Sigma^+ - 1^1\Sigma^+$	$2^1\Sigma^+ - 1\Pi$	$2^1\Sigma^+ - 1^1\Sigma^+$	$2^1\Sigma^+ - 1\Pi$
2.75	0.0099	0.1273	—	—	—	—
3.00	0.1847	0.1062	—	—	—	—
3.25	—	—	0.2165	0.0835	—	—
3.50	0.3512	0.0819	0.3123	0.0894	0.2165	0.0584
4.00	0.3862	0.0598	0.4951	0.0880	0.4093	0.1211
4.50	0.2703	0.0391	0.4890	0.0704	0.6723	0.0822
4.75	—	—	0.4132	0.0590	—	—
5.00	0.1464	0.0236	0.3233	0.0480	0.7033	0.0468
5.50	0.0690	0.0142	0.1762	0.0305	0.4784	0.0253
6.00	0.0403	0.0089	0.0886	0.0196	0.2628	0.0146
6.50	—	—	—	0.0132	—	—
7.00	0.0043	0.0019	0.0287	—	0.0728	0.0063
8.50	0.0043	0.0019	0.0085	0.0041	0.0167	0.0027

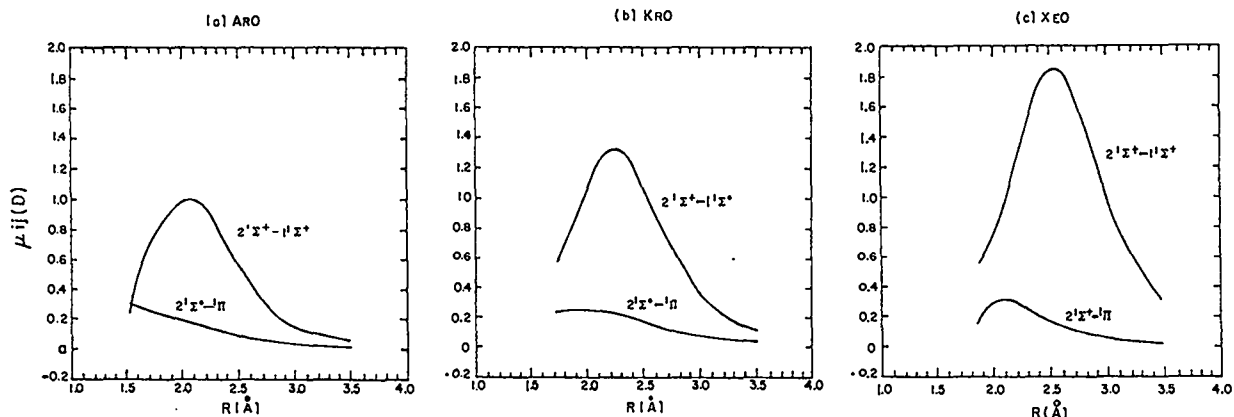


Fig. 35

Dipole transition moments for the $2^1\Sigma^+ - 1^1\Sigma^+$ and $2^1\Sigma^+ - 1\Pi$ transitions in ArO, KrO, and XeO.

(2) the $2^1\Sigma^+ - 1^1\Sigma^+$ transition in ArO, KrO, and XeO.

These variations are due to the same effect, namely, the incorporation of ionicity into the $1^1\Sigma^+$ state. The ionic contribution to the $1^1\Sigma^+$ state, which increases with decreasing R, leads to a strong enhancement in the $2^1\Sigma^+ - 1^1\Sigma^+$ transition moment upon molecular formation. The slight increase in the $2^1\Sigma^+ - 1\Pi$ moment, on the other hand, results only from the reduction in

symmetry from $1S - 1D$ and the associated small perturbations. The $2^1\Sigma^+ - 1^1\Sigma^+$ moment increases with the rare-gas atom in the sequence Ar<Kr<Xe because the ionic character in the $1^1\Sigma^+$ state increases in the same sequence, as noted earlier.

To quantify the effect of the variation in the transition moments, we have computed "pseudolifetimes (τ_p)" for the $2^1\Sigma^+$ states. The value of τ_p was calculated by

- determining the internuclear separation

which $E(R^*) - E(\infty) = 0.026$ eV (298 K) for the $2^1\Sigma^+$ state,

- interpolating $\Delta E(R^*)$ and $\mu_{ij}(R^*)$ for the $2^1\Sigma^+ - 1^1\Sigma^+$ and $2^1\Sigma^+ - 1^1\Pi$ transitions from the computed curves, and
- computing the pseudolifetime from

$$A_p = \tau_p^{-1} = 1.063 \times 10^6 \mu_{ij}^2 \Delta E^3 \text{ s}^{-1},$$

where μ_{ij} is given in atomic units and ΔE is in electron volts. The values of R^* , $\Delta E(R^*)$, $\mu_{ij}(R^*)$, A_p , and τ_p determined in this way are presented in Table XIII. A monotonic decrease in τ_p in the sequence ArO>KrO>XeO is predicted, in line with the increase in μ_{ij} in the sequence ArO<KrO<XeO noted above. This trend is in line with the measured collision-induced emission rate constants for argon, (Refs. 15, 16, 17) krypton, (Refs. 16, 17) and xenon. (Refs. 15, 16, 17.) In their studies of Reaction (2) Cunningham and Clark, (Ref. 17) found that

$$4 < \frac{k_{Xe}}{k_{Ar}} < 486, \quad (7)$$

where the lower limit refers to the green line emission and the upper limit to the green band emission. The ratio of the calculated pseudo-Einstein coefficients (A_p) for ArO and XeO

$$\frac{A_p(\text{XeO})}{A_p(\text{ArO})} = 74, \quad (8)$$

falls between these two limits. This trend is also in agreement with the reported experimental lifetimes for the $2^1\Sigma^+$ states of ArO [7 and 10 μs , Refs.(7, 11), and 7, respectively], KrO (1.6 μs , Ref. 17), XeO (0.17 and 0.29 μs , Refs. 17 and 16, respectively) and provide further evidence against the earlier measurement of the lifetime of XeO ($2^1\Sigma^+$) by Tisone¹⁸ (50 μs).

Quantitative studies of the collision-induced $0(^1S) - 0(^1D)$ emission in an argon-oxygen system have been reported by Julienne *et al.*¹⁹ (for a brief description of this calculation, see the

TABLE XIII

CALCULATED PSEUDOLIFETIMES FOR $2^1\Sigma^+$ STATES OF RARE-GAS OXIDES^a

Molecule	Transition	$R(\text{\AA})$	$\Delta E(R)(\text{eV})$ ^b	$\mu_z(R)$	$A(\text{s}^{-1})$	$\tau(\mu\text{s})$
ArO	$2^1\Sigma^+ - 1^1\Sigma^+$	2.97	2.26	0.0598	4.4×10^4	23.
	$-1^1\Pi$		2.22	0.0128	2.2×10^3	460.
KrO	$2^1\Sigma^+ - 1^1\Sigma^+$	3.02	2.27	0.134	2.2×10^5	4.5
	$-1^1\Pi$		2.22	0.0254	8.6×10^3	120.
XeO	$2^1\Sigma^+ - 1^1\Sigma^+$	2.89	2.32	0.496	3.3×10^6	.31
	$-1^1\Pi$		2.21	0.0264	8.0×10^3	125.

^a Lifetimes have been computed at the minimum internuclear spacing, R. Symbols denote the following:

ΔE = emission energy.

μ_z = transition moment, in atomic units.

A = Einstein A-coefficient.

τ = lifetime.

^b Corrected for the error in the calculated $0(^1S)-0(^1D)$ excitation energy; see the text.

introduction). They find good agreement between the calculated and observed emission-rate constant.

METAL-VAPOR LASERS

(C. York and O. Judd)

Introduction

Some promising new laser systems, for both fusion and isotope separation, use low-pressure corrosive-metal vapors as the active species. Among these species are "association" laser molecules in which the molecule exists in a bound excited state but has no stable ground state. The rare-gas dimers and rare-gas halides are examples of this type of molecule that have been made to lase. Among these metal vapors are the group IIB dimers (Zn_2 , Cd_2 , and Hg_2), the alkali group IIB excimers alkali-rare-gas excimers, and group IIIA rare-gas excimers (e.g., $Tl-Xe$). The alkali dimer molecules, in addition, offer the possibility of laser action due to the phenomenon of "displaced potential," which allows a strong population inversion, as in the case of bound-free radiation, and is the mechanism responsible for the lasing of H_2 molecules. Finally, optical pumping of discharge-produced alkali resonance levels can generate ir lasing at several discrete wavelengths.

We are investigating the most promising of these systems and are investigating the possibility of using the heat pipe for containing these vapors.

In our basic investigations, we are studying these systems with excitation provided by an electrical discharge. In almost all proposed metal-vapor lasers, the initial excited state, from which the laser upper level is generated (either by optical pumping or through intermolecular recombination), is a low-lying level of the metal atom (≈ 5 eV above the ground state). Such states, in general, have large cross sections for excitation by the low-energy electrons in electrical discharges. With appropriately chosen values of E/N (electric field/gas density), very large fractions of the input energy can be channeled into the states of interest. In the case of mercury, our calculations predict that the rates of electron production of the 3P_1 and 3P_0 states

which give rise to the molecular bands proposed for laser operation, can be four times higher than any other electron-production rate for values of $E/N \approx 2$ to 3×10^{-16} V cm^2 . Similar behavior is expected for the other metal vapors. Furthermore, the levels are very low relative to the ionization potentials of the rare gases. Thus, in an electric discharge in a mixture of metal vapor and rare gas, virtually all the energy will be deposited in the excited states of the metal atom. Very little energy will be channeled into the buffer-gas ions, even at very large density ratios of buffer gas to metal vapor. Optical pumping and relativistic electron-beam pumping offer special advantages in terms of interpreting the operative mechanisms (optical pumping) and in terms of coupling large amounts of energy into the gas (electron-beam pumping), but both techniques are severely limited as to achievable conversion efficiency. We feel, therefore, that discharge excitation offers the best hope of building a scalable, high-power, high-efficiency device.

Of all known discharge schemes, transverse-discharge pumping, either preionized or electron-beam-sustained, allows the greatest amount of energy to be deposited per unit volume.

Our studies aimed at the development of high-power metal-vapor excimer lasers have continued, with special emphasis on mercury. The results can be briefly summarized in two major conclusions:

- Detailed analysis of data from our extensive scaling studies indicate that heat pipes may be difficult to scale to the sizes and pressures required for laser fusion devices, without considerable further research into heat-pipe technology;
- Further experimentation at Los Alamos and/or other laboratories confirmed our initial discovery of energy absorption at 325 nm by excited mercury molecules although we have also shown certain conditions under which the degree of absorption can be decreased.

Recent results are summarized in the following paragraphs.

Heat-Pipe Technology

General--The heat-pipe development program has been directed toward determining the feasibility of using such devices to contain high-pressure corrosive gases at high temperatures while maintaining the medium at a homogeneity and optical quality adequate for propagation of a visible or near-uv light beam. We have built heat pipes ranging in diameter from 1.7 to 9.8 cm, which have been operated with working fluids of mercury, water, and sodium.

Experimental Results--The data and analyses pertaining to heat pipes have been compiled recently and the interested reader is referred to this report for detailed information.²⁰ The basic data and conclusions of this report are summarized as follows. Our initial tests regarding heat pipe scalability involved increasing the size for our initial 1.73-cm-diam four-armed device, which performed reasonably satisfactorily, to a double-ended device with heat-pipe sections on each end and a 7-cm-diam aperture. Operation of this device with mercury as a fluid was totally unsatisfactory for the following reasons: (1) mercury condensed on the windows during both startup and operation, even at buffer-gas pressures far in excess of the mercury saturation pressure; (2) heat-pipe action (Hg condensation) could not be obtained along the top of the tube due to the large differences in density between the hot mercury vapor and the heaviest available inert gas, xenon; this resulted in steeply sloped interface zones, which are unacceptable for laser purposes; and (3) strong turbulence and rain occurred under most conditions, even at moderately low pressures. In an attempt to determine whether the reason for this behavior was the lack of a buffer gas with a suitable density to match that of mercury, or insufficient wetting by the mercury, or simply a size problem, the heat-pipe fluid was changed to water with no other changes in physical parameters. Both heavier (neon) and lighter (helium) buffer gases produced results similar to those obtained with mercury (i.e., sloped interfaces, window condensation, and rain). However, we obtained

heat-pipe action with the mixture of helium and neon whose density matched that of the water vapor (a function of temperature); interfaces were relatively vertical and no vapor condensation on the windows occurred. Unfortunately, the mixture was very sensitive to small density changes and was unstable (as evidenced by pressure fluctuations) even when perfectly balanced; it produced heavy rain. Because the results seemed to point to a heat-pipe geometry problem rather than to specific difficulties with mercury, we reconverted the system to mercury use, but with an array of convection baffles in each heat-pipe end with a 9-cm-diam clear aperture. This system performed excellently, removing all previously observed difficulties. Good heat-pipe action with vertical interfaces without window condensation was obtained over a wide range of conditions. Further, no rain occurred until pressures exceeded 3 atm. Curiously, good performance was obtained with any inert gas, showing none of the strong density dependence observed previously. The aperture in the baffles has subsequently been increased to 3.8 cm with attendant degradation in performance. The larger apertures quickly caused the windows to be coated with condensate even though heat-pipe operation was observed (although at a greater deviation of the interface from vertical).

Our data suggest that a critical maximum diameter exists for effective (from an optical standpoint) heat-pipe operation. This diameter appears to be ~ 2 to 2.5 cm, but establishing a definitive value would require further study. Further large-aperture heat pipes seem to require some baffle structure with multiple holes. Research should continue both to investigate the operation of various heat-pipe configurations and to further elucidate the mechanisms responsible for this diameter limit.

Gain and Loss Measurement in Mercury Effort in this project has been directed toward improving the experimental apparatus and the diagnostics for high-pressure mercury discharge experiments. The apparatus has been modified so that the main discharge circuit now consists of a capacitor that is discharged across the volume through a floating, grounded-grid hydrogen thyatron switch. This arrangement permits us to operate the discharge in

either polarity and at repetition rates that are limited only by the available power supply current (presently, ~ 10 Hz). This higher repetition rate greatly facilitates the data acquisition and will allow the use of various signal-averaging techniques. The long electrode structure (5D cm) discussed in the previous report has been redesigned and successfully tested in a separate chamber. Uniform discharges have been obtained at pressures of up to ~ 2000 torr of pure helium. For the current data, however, the short electrodes (11.5 cm) have been retained because they provide less ambiguous data for the large optical attenuations observed in current experiments.

In the previous quarterly report, we presented preliminary data that indicated absorption at 325 nm of the He:Cd laser. These experiments have since been repeated with the following results. With a cell pressure and temperature of 30 psia and 693 K, respectively, the measured absorption coefficient was 0.11 cm^{-1} and the discharge-current density was 3.5 A/cm^2 . To verify that this effect was not due to refraction, the measurements were repeated at 632.8 nm, resulting in an absorption coefficient of $< 0.003 \text{ cm}^{-1}$.

In an attempt to determine more about the nature of this strong absorption, we have set up a tunable probe laser. This apparatus consists of a Molelectron UV-1000 nitrogen laser, which pumps a Molelectron DL-20D flowing-dye laser whose output is frequency-doubled by a lithium formate monohydrate (LFM) crystal with $\sim 1\%$ efficiency. Through the use of three dye solutions, we are able to cover the wavelength range from ~ 310 to 350 nm which effectively encompasses the Hg_2 uv band. The laser is now operational and generates 3-ns pulses with sufficient power (> 100 W) to produce detectable signals. The probe-laser pulse is, of course, much shorter than the ~ 2.5 - μs FWHM discharge pulse, and the gain (or loss) can therefore be probed as a function of time and wavelength by varying the temporal position of the probe signal relative to the discharge pulse. If the laser probe signal and the discharge current are simultaneously displayed on a dual-beam oscilloscope, a graphic representation of the loss can be observed by scanning the probe signal in time across the discharge duration. Typical results are shown in

Fig. 36 for two pressures and for two wavelengths (fundamental at 650 nm and doubled at 325 nm). The absorption indicated is significant and is consistent with previous results obtained with the He:Cd probe. The absorption at 6500 Å is believed to be an upper limit and is attributable to the amplitude fluctuations inherent in the dye laser which were not corrected in these data. Clearly, the observed attenuation is a function of discharge current, as shown in Fig. 37. It is also believed that the absorption should be a function of the degree of "superheat" (i.e., the degree to which Hg vapor temperature is above that corresponding to the equilibrium vapor pressure) at a given pressure because it has been previously shown²¹ that the states responsible for emission of the 335- and 485-nm Hg_2 bands are in thermal equilibrium. If the absorption is occurring from only one of these states, a population shift should effect a change in the absorption strength. However, experimental difficulties did not permit us to adequately decouple the mercury reservoir temperature from that of the cell so that we were unable to independently vary vapor temperature and pressure. Design modifications are nearly complete which will give independent temperature control and permit us to obtain absorption data with the degree of superheat as a parameter. In

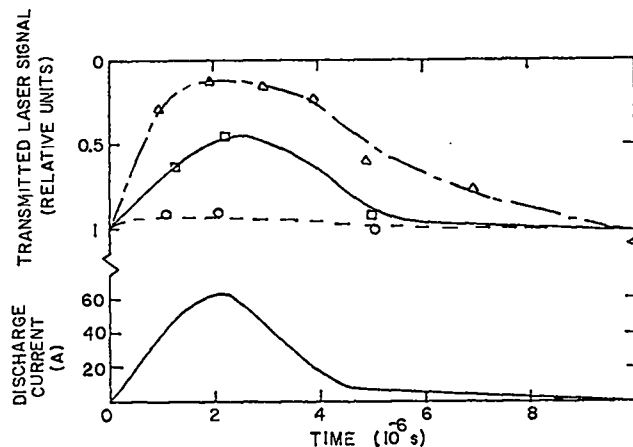


Fig. 36
Temporal behavior of discharge current and optical transmission of high-pressure Hg discharges.

25 psi, 325 nm;
35 psi, 325 nm;
35 psi, 650 nm.

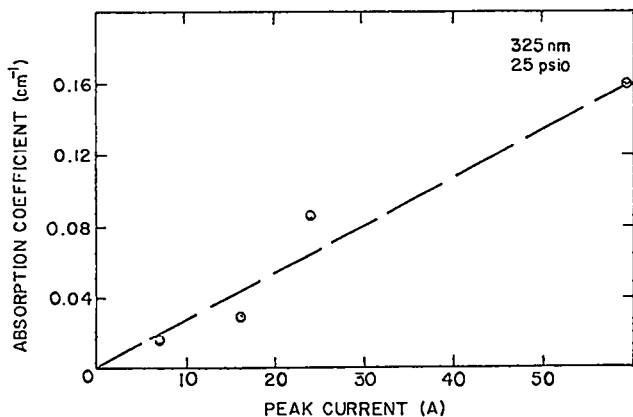


Fig. 37
Variation of peak absorption at 325 nm as a function of peak discharge current. Pressure, 25 psi. Discharge area, 17.25 cm².

In addition, modifications have been completed so that the fluctuations in the pulsed-laser amplitude can be averaged electronically to yield a more accurate measure of the absorption. Preliminary measurements of the wavelength dependence of the absorption performed from 322.5 to 330 nm show no variation to the limit of our accuracy. These experiments will also be repeated across the entire uv band with the improved apparatus.

The absorption we measured which has also been measured under optical-pumping conditions,²² is in apparent conflict with the previously published results of Schlie *et al.*²³ which indicated gain on the 335-nm band under electron-beam excitation. This discrepancy might be explained by the fact that, in the electron-beam experiment, most of the energy is deexcimers through dissociative recombination followed by radiative cascade and three-body formation. The other experiments, in contrast, produce mercury excimers through pumping from the ground state. The crucial difference is that the electron-beam experiments will probably produce a significant density of mercury excimer states higher than those connected to the 6³P manifold, whereas optical and discharge pumping will produce primarily the 6³P atomic states as well as dimers and trimers connected to those states. Electron-beam pumping can therefore establish a population inversion between the upper mercury dimers and the lower molecular states. If these upper states are placed correctly in energy

and at appropriate internuclear separation, they could produce gain for electron-beam excitation and absorption for the other excitation methods at the same wavelength. The observation of Schlie²³ of gain following the 335-nm emission profile would suggest that fortuitous, but perhaps not implausible, relative potential-energy curves might exist. We intend to investigate this possibility by two-photon pumping of the higher lying mercury levels with a tunable laser followed by observation of the subsequent emission. The strength and the spectral character of the fluorescence should provide the necessary data to determine whether the above hypothesis is correct. We hope that the combination of these two experiments (discharge and optical pumping) will provide the definitive answers within the next several months as to whether the observed absorption situation can be circumvented, reestablishing Hg₂ as a promising laser medium.

If the answer is encouraging, we will proceed with further development of the mercury laser. If, however, the data eliminate the Hg₂ molecule as a prospective laser medium, we will search for methods to apply the discharge techniques we developed for mercury (and which result in relatively high specific input-energy density) to other systems. In particular, our apparatus can easily be adapted to test for gain reported in the blue spectrum of HgCd exciplexes²⁴ under electrical-discharge excitation.

OPTICAL DAMAGE

Enhanced Damage Resistance of Laser Reflectors with Nonquarter-Wave Designs (D. Gill, B. Newnam, J. McLeod)

The damage resistance of multilayered dielectric laser reflectors has been increased substantially by using nonquarter-wave thickness designs for the top few layers. In principle we minimized in these designs the standing-wave (SW) electric field in the high-index layers, which are generally less damage-resistant than low-index layers. Algebraic equations were derived for optimum film thicknesses and for the resulting peak electric fields. Reflectors for 1.064- μ m light

were fabricated according to these designs, and their damage thresholds have been compared with the threshold of a similar reflector with all-quarter-wave (QW) thicknesses.

The standard dielectric reflector is composed of alternate layers of relatively high and low refractive indices, all of which are of QW optical thickness. In this design, the SW electric-field maxima occur at the layer interfaces and are largest in the top layers nearest the incident radiation (see Fig. 38a). Previous experiments²⁵⁻²⁷ have shown that the damage threshold of QW stacks of TiO₂ and SiO₂ is determined by the peak internal SW electric field in the high-index material (TiO₂). Thus, it is highly desirable to shift the position of the SW field maxima away from the film interfaces of the top layers of a reflector, into the low-index (stronger) layers. This is accomplished by use of non-QW thicknesses for the top layers.

To minimize the peak field in the high-index layers while maintaining maximum reflectance, the thicknesses of the top two layers are given by

$$\sin \theta_L = 1/N \quad (9)$$

and

$$\tan \theta_H = \frac{N}{\sqrt{N^2 - 1}}, \quad (10)$$

where the subscripts L and H refer to the first low- and high-index layers, where $N = n_H/n_L$, $\theta_i = 2\pi n_i d_i/\lambda$, and d = film thickness. Similar expressions have also been derived elsewhere.²⁸ For the thicknesses specified by Eqs. (9) and (10), the peak electric field in the first high-index layer is reduced by a factor of

$$\frac{N}{\sqrt{2N^2 - 1}}, \quad (11)$$

compared to the standard all-QW case. At the same time, the peak field in the first low-index layer is increased by a factor of

$$\frac{N^2}{\sqrt{2N^2 - 1}}. \quad (12)$$

The SW electric-field distribution in a two-layered modified reflector is shown in Fig. 38b. Note that the first peak has been displaced into the low-index layer, reducing the peak field in the high-index layer.

To lower the peak electric field in the high-index layer still further, one can modify the top four layers. For this case, the thicknesses of the top two layers are given by

$$\sin \theta_L = \frac{1}{\sqrt{2N^2 - 1}} \quad (13)$$

and

$$\tan \theta_H = \frac{N}{\sqrt{2(N^2 - 1)}}. \quad (14)$$

The thicknesses of the next two layers are still given by Eqs. (9) and (10). The SW electric-field distribution in a four-layer modified design is shown in Fig. 38 (c). The peak electric field in the first high-index layer is reduced by a factor of

$$\frac{N}{\sqrt{3N^2 - 2}}, \quad (15)$$

compared to the standard all-QW case, whereas the peak field in the first low-index layer is increased by a factor of

$$N \frac{2N^2 - 1}{\sqrt{3N^2 - 2}}. \quad (16)$$

These equations can be generalized for the modification of m pairs of layers. Let the layers be numbered outward, starting with the first modified layer next to the quarter-wave stack and ending with the top outermost layer next to the air. Then the thicknesses are given by

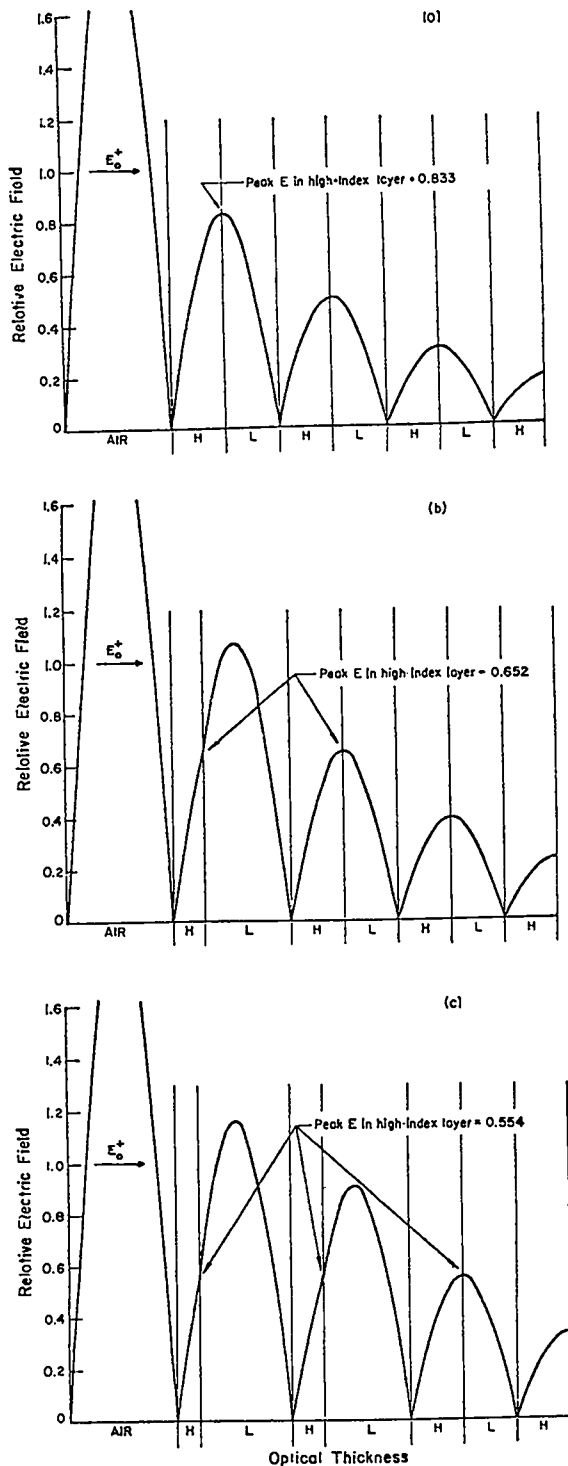


Fig. 38

Standing-wave electric-field distribution within a 15-layer reflector. Only the top seven layers are shown; remaining layers and substrate are off-scale to the right. Indices of refraction are 2.40 and 1.46. (a) Standard all-QW design; (b) two-layer-modified design using Eqs (1) and (2); and (c) four-layer modified design using Eqs. (1), (2), (5), and (6); see text.

$$\sin \theta_{2m-1} = \frac{1}{\sqrt{(m+1)^2 - (m-1)}} \quad (17)$$

and

$$\tan \theta_{2m} = \frac{N}{\sqrt{m(N^2-1)}} \quad (18)$$

The peak field occurring in a high-index layer, relative to the incident field in air, is given by

$$\frac{2}{n_L \sqrt{(m+1)N^2 - m}} \quad (19)$$

whereas the peak field in a low-index layer, relative to the incident field in air, is given by

$$\frac{2}{n_L} \sqrt{\frac{mn^2 - (m-1)}{(m+1)N^2 - m}} \quad (20)$$

Equations (19) and (20) can be used to form appropriate ratios to show the reduction or increase in fields for a particular case. All these designs result in thicknesses larger (smaller) than one QW for the low-index (high-index) material. Note that substitution of QW layers by non-QW layers specified by Eqs. (17) and (18) results in a small reduction in mirror reflectance (see Table XIV). However, addition of non-QW layers of these thicknesses to an existing all-QW stack will increase the reflectance.

Whether these modified designs will yield higher thresholds than the all-QW layer design depends on the ratio of the damage thresholds of the low- and high-index films. If $\rho \geq n$, then the two-layer modification is preferred over an all-QW design (at $\rho = N$, damage will occur simultaneously in the top low- and high-index films). Assuming $\rho > N$, a two-layer modification will allow the

TABLE XIV

REFLECTANCE AND DAMAGE THRESHOLD
VALUES FOR THREE REFLECTOR DESIGNS

Reflector Design	Reflectance at 1.064 μm (%)	Threshold Energy Density (J/cm^2)
A (15 QWs)	99.5	4.5-5.4
B (13 QWs + 2 non QWs)	99.3	4.5-8.0
C (11 QWs + 4 non-QWs)	98.7	4.5-6.4

external incident field to be increased by a factor of $\sqrt{2N^2 - 1}/N$, compared to the all-QW case, before damage occurs. If $\rho \geq \sqrt{2N^2 - 1}$, the four-layer modification is the better design and the field can be increased by a factor of $3N^2 - 2/N$, compared to the all-QW case before damage occurs. In general, if $\rho \geq \sqrt{mN^2 - (m-1)}$ then the 2m-layer modification is preferred and the incident field can be increased by a factor of $\sqrt{(m+1)N^2 - m}/N$ before damage occurs. For $\text{TiO}_2/\text{SiO}_2$ reflectors we have measured ρ to be 1.5 to 1.6 for 30-ps pulses at 1.064 μm . For most practical cases the value of ρ limits the useful designs to two- or four-layer modifications.

To properly evaluate the advantages of two- and four- layer modified designs over the all-QW design, reflectors of $\text{TiO}_2/\text{SiO}_2$ (index ratio $N = 1.64$) of each design were fabricated in a single coating run by appropriate shuttering and film-thickness monitoring techniques. Thus, except for the top two- or four-layers, the reflectors experienced identical conditions. Each reflector was exposed to a series (55) of single 30-ps pulses at 1.064 μm , and the thresholds are listed in Table XIV.

The upper end of the threshold range was defined as the maximum pulse energy for which damage was not detected and conversely for the lower end. It is seen that the lower values are identical, whereas the upper values vary significantly. The same value of 4.5 J/cm^2 for the low end is attributed to coating defects in the top TiO_2 film damaged by the first- pass traveling-wave field (at 4.3 MV/cm before a standing-wave pattern was established). The upper thresholds of Reflectors B and C were 48 and 18.5%, respectively,

higher than the threshold of Reflector A. Improvements of 58 and 102% would have been expected if high-index failure had occurred first. (These values do not exactly agree with the equations quoted earlier due to small errors in thickness of the modified layers. The values of 58% and 102% are correct for the reflectors actually made.) However, the respective electric fields in the top SiO_2 layers of Reflectors B and C at the threshold flux were 10.6 and 10.5 MV/cm, respectively. (These values approach the values of 13.5 MV/cm in a SiO_2 film and of 11.7 MV/cm in bulk SiO_2 previously reported by Apfel *et al.*²⁶ and by Smith *et al.*,²⁹ respectively.) We concluded that low-index failure determined the threshold for these designs, consistent with the theory because $\sqrt{2n^2 - 1} > \rho$ and N was also slightly larger than ρ . Thus, the two-layer modified design provided near-maximum improvement for these materials. The benefits of non-QW designs will be realized to a higher extent when films can be produced with fewer defects.

Radio-FrequencySputtering Techniques for Coating Deposition.

(B. Newnam, D. Gill)

The development of rf sputtering techniques for the deposition of damage-resistant films of TiO_2 and SiO_2 as laser coatings has been reported previously.^{30, 31, 32} For short pulses at 1.064 μm , the best of the coatings were superior to those produced by electron-gun deposition (EGD). The technology has recently been extended to produce coatings for use at visible and uv wavelengths. This work is also of direct interest for fusion laser systems, and we are therefore actively participating in it.

Battelle Pacific Northwest Laboratory has completed a three-month effort to produce refractive-oxide coatings for the ultraviolet. By using varied deposition parameters, 16 samples of single-layer coatings of HfO_2 and Y_2O_3 were deposited on Suprasil-2 substrates. We will damage test the samples at a wavelength of 0.355 μm .

Optical Coating Laboratory, Inc. (OCLI) is midway through a contract to sputter TiO_2 , ZrO_2 , and SiO_2 reflectors for visible and uv lasers under production conditions. With the previous results

and experience of Battelle as guidelines, OCLI is seeking to optimize the sputtering parameters for their equipment. We have received ten single-layer samples of TiO_2 and seven of ZrO_2 on Suprasil-2 substrates for damage-testing. Each of these samples has been irradiated at 40 different surface sites with single, 21-ps pulses at 532 nm having a spot-size radius of 0.13 mm. For the TiO_2 coatings, the peak internal electric field at the threshold of damage ranged between 4.4 and 5.4 MV/cm (corresponding to incident energy densities of 2.8 to 4.5 J/cm² incident) whereas the ZrO_2 thresholds ranged from 5.3 to 6.7 MV/cm (corresponding to 3.4 to 5.3 J/cm² incident). These thresholds are slightly higher than those of EGD coatings previously tested. Correlations of these damage thresholds with the deposition parameters provide guidance for further parameter optimization.

Several other properties of these sputtered films were compared to EGD films. First, the light scattering of the sputtered coatings was an order of magnitude lower. Second, the variation of the damage threshold from site to site on a given sputtered coating was generally less (about one-half). Both results indicated the presence of fewer coating defects. Third, the refractive indices of 2.65 for TiO_2 and 2.18 for ZrO_2 , at 0.532 μ m were considerably higher than those usually obtained for EGD coatings of TiO_2 (2.4) and ZrO_2 (2.05). Fourth, the damage thresholds of the zirconia coatings were 25% higher than those of titania at 532 nm for both coating processes.

The end product of this contract work will be rf-sputtered reflectors of TiO_2/SiO_2 and ZrO_2/SiO_2 for use at 0.532 and 0.355 μ m.

REFERENCES

- O. Judd, "Evaluation of Electrical-Discharge Pumping Technique for a High-Power Oxygen Laser," Los Alamos Scientific Laboratory Report LA-6710-PR (in preparation).
- A. V. Phelps, JILA, private communication, (1976).
- L. R. Peterson and J. E. Allen, J. Chem. Phys. 56, 6068 (1972).
- M. Schapper and H. Schreiber, Beitrage Zur Plasma Physik 9, 45 (1969).
- L. D. Thomas and R. K. Nesbet, Phys. Rev. A 11, 170 (1975).
- For a general discussion of rare gas-oxygen lasers, see S. Rockwood, Bull. Amer. Phys. Soc. 19, 151 (1974); S. Rockwood, "Mechanisms for Achieving Lasing on the 5577 A Line of Atomic Oxygen," Los Alamos Scientific Laboratory internal report (1973).
- W. M. Hughes, N. T. Olson, and R. Hunter, Appl. Phys. Lett. 28, 81 (1976).
- H. T. Powell, J. R. Murray, and C. K. Rhodes, Appl. Phys. Lett. 25, 730 (1975).
- D. L. Huestis, R. A. Gutcheck, R. M. Hill, M. V. McCusker, and D. C. Lorents, "Studies of E-Beam Pumped Molecular Lasers," Stanford Research Institute technical report MP 75-18, (1975).
- "Laser Program Annual Report - 1974," T. I. Davis and W. Clements, Eds, Lawrence Livermore Laboratory report (1975).
- G. Herzberg, Molecular Spectra and Structure I Spectra of Diatomic Molecules, (D. Van Nostrand Co., Inc., New York (1966), Chapter VI.
- P. B. Foreman, A. B. Lees, and P. K. Rol, Chem. Phys. 12, 213 (1976).
- (a) C. D. Cooper and M. Liochtenstein, Phys. Rev. 109, 2026 (1958); (b) C. D. Cooper, G. C. Cobb, and E. L. Tolnas, J. Molec. Spect. 7, 223 (1961).
- A. A. Abrahamson, Phys. Rev. 178, 76 (1969).
- D. L. Cunningham and K. C. Clark, J. Chem. Phys. 61, 1118 (1974).
- G. Black, R. L. Sharpless, and T. G. Slinger, J. Chem. Phys. 63, 4546 (1975).
- K. H. Welge and R. Atkinson, J. Chem. Phys. 64, 531 (1976).
- G. C. Tisone, J. Chem. Phys. 60, 3716 (1974).
- P. S. Julienne, M. Krauss, and W. Stevens, Chem. Phys. Lett. 38, 374 (1976).
- J. E. Deverall, "Gas-Interface Studies in Large Horizontal Heat Pipes," Los Alamos Scientific Laboratory report LA-6646-MS (January 1977).
- R. E. Drullinger, M. M. Hessel, and E. W. Smith, "Analysis of Optically Excited Mercury Molecules," NBS Monograph 143 (January 1975).
- R. L. Byer, Stanford University, private communication, and R. E. Drullinger NBS Boulder, Boulder, Colorado, private communication (1976).
- L. A. Schlie, B. D. Guenther, and R. D. Rathge, "Positive Gain Measurements on the 3350 A Continuum Band of Hg_2 ," Appl. Phys. Lett. 28, 393 (1976).

24. M. W. McGoch and G. R. Fournier, "Positive Gain Measurements on the 470 nm Continuum Band of CdHg," J. Appl. Phys (in print).
 25. B. E. Newnam and D. H. Gill, "Laser Damage Resistance and Standing-Wave Fields in Dielectric Coatings," OSA Asilomar Conference on Optical Interference Coatings, February 24-26, 1976. Abstract in J. Opt. Soc. Am. 66, 166 (1976).
 26. J. H. Apfel, J. S. Matteucci, B. E. Newnam, and D. H. Gill, "The Role of Electric Field Strength in Laser Damage of Dielectric Multilayers," 1976 Symposium on Damage in Laser Materials, Boulder, Colorado (July 1976).
 27. B. E. Newnam, D. H. Gill, and G. Faulkner, "Influence of Standing-Wave Fields on the Laser Damage Resistance of Dielectric Film," in Laser Induced Damage in Optical Materials; 1975, NBS Special Publication 435, pp 254-271.
 28. J. H. Apfel, "An Optical Coating Design with Reduced Electric Field Intensity," to be published.
 29. W. L. Smith, J. H. Bechtel, and N. Bloembergen, "Picosecond Breakdown Studies," op. cit., Ref.27, NBS Special Publication 435, pp. 321-330.
 30. E. Stark and F. Skoberne, Los Alamos Scientific Laboratory report LA-6245-PR (July 1976).
 31. D. H. Gill, B. E. Newnam, J. S. Hartmann, and W. J. Coleman, "Super-High Damage Thresholds for RF-Sputtered TiO₂ Films," OSA 1975 Annual Meeting, Boston, Massachusetts, October 1975. Abstract in J. Opt. Soc. Am. 66, 78 (1976).
 32. E. Stark and F. Skoberne, Los Alamos Scientific Laboratory report LA-6510-PR (November 1976).
-

III. LASER FUSION -- THEORY, EXPERIMENTS, AND TARGET DESIGN

In an integrated program of theory, target experiments, and target design, we are establishing a fundamental understanding of laser-target interactions, particularly of the relevant plasma physics and hydrodynamics. Both the experimental and the theoretical efforts have concentrated on studying the wavelength-dependence of laser-plasma interactions. The close coupling of theory and experiment has made it possible to eliminate theories that are not supported by experiment. In general, basic studies of laser-plasma interactions have shown that the design difficulties associated with long wavelengths are less severe than believed earlier, and that break-even target designs are attainable even in the presence of a hot-electron spectrum. These results have given us new confidence that significant yield can be obtained from more efficient, less expensive CO₂ lasers.

WAVELENGTH SCALING - THEORETICAL AND EXPERIMENTAL RESULTS

(D. V. Giovanielli)

Previous simplified calculations had suggested that suprathermal electrons might be considerably hotter and the critical-surface velocity much higher at long wavelengths than at short ones. However, our investigations of electron, ion, and x-ray emissions in target experiments with the Single-Beam CO₂ System (SBS) and the two-beam Nd:glass laser system indicate, at intensities of interest to laser fusion, that the hot-electron temperature differs at most by a factor of 3 between 1.06- and 10.6- μ m irradiation.^{1,2} This was suggested in our previous progress report³ in which we discussed the results of front- and backside ion emissions from thin flat targets. A compilation of data from several laboratories throughout the world is shown in Fig. 39. It can be seen that at high intensities the hot-electron temperature varies approximately as $(P_L \lambda^2)^{1/4}$, indicating a $\sqrt{\lambda}$ dependence (where P_L is laser intensity and λ is laser wavelength).

We have measured the dependence of laser-light transmission through thin foil targets on foil thickness and wavelength, and have found that the velocity of expansion of the critical density surface is similar for 1.06- and 10.6- μ m irradiation.¹ X-ray pinhole photographs confirm this conclusion.

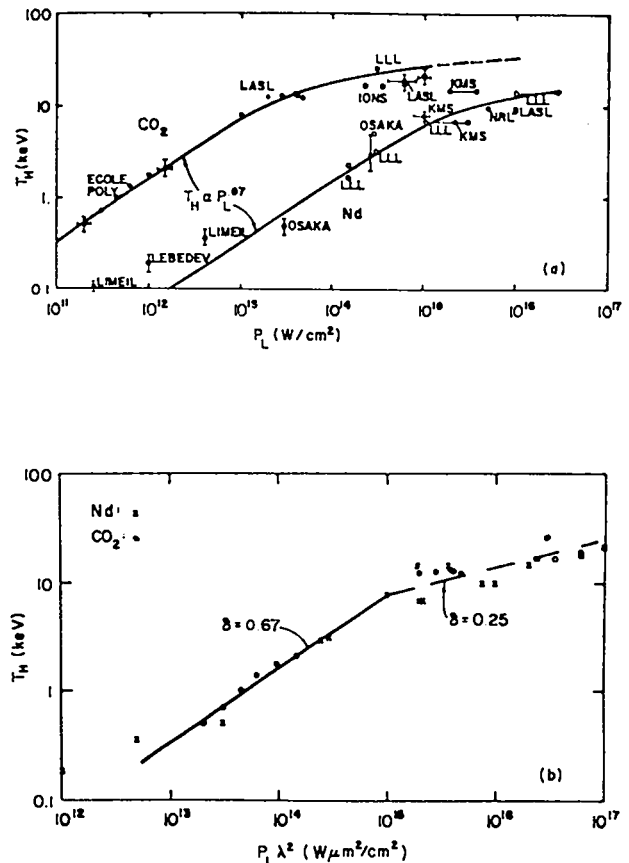


Fig. 39
Hot-electron temperature as a function of laser intensity and $P_L \lambda^2$. (Figures 39a, 39b, respectively. Data from many laboratories are included. The lower Curve in Fig. 39a contains the same data points as the curve in Fig. 39b.)

A theoretical explanation for this scaling, supported by particle-in-cell simulations, is given under Theoretical Studies of Laser Fusion.

TARGET EXPERIMENTS AT 1.06 AND 10.6 μm

Introduction

We have begun flat-foil target experiments with our Two-Beam CO_2 System. Both single-beam and two-beam illumination were used at energy levels up to 350 J per beam. Laser pulse width was 1.0 to 1.2 ns (FWHM). Spot diameters (80% included energy) of 150 to 175 μm provided peak intensities exceeding 10^{15} W/cm^2 .

The Single-Beam System was used to investigate x-ray emission from layered targets. Effects of laser "burnthrough" of the first layer were separated from those of high-energy electrons propagating into the substrate.

By using the Single-Beam System and the two-beam Nd:glass laser system, we studied the polarization of x rays generated by suprathermal electrons to determine average electron motion and integral energy distribution.

A new stereo-optical technique was developed and used to examine second-harmonic emission from a laser-produced plasma in an attempt to identify "flares" and other distortions of the critical-density region.

Ion Collector Studies (A. W. Ehler)

Eight ion collectors placed around the target chamber of the Two-Beam System indicated an operational environment substantially different from that of the Single-Beam System. The electromagnetic pulse (EMP) noise level was higher, as expected, and a 0.2- μs soft x-ray pulse was present which obscured the ion signal. Proper shielding reduced the EMP noise to tolerable levels. A thin (0.5- μm) nickel foil placed over an ion collector reduced the x-ray signal by a factor of 10^8 or more, but allowed ions of energy greater than 85 keV to penetrate. At a laser-pulse energy of 300 J, we observed ion energies of 660 keV. This is as expected for a laser intensity of $\sim 10^{15} \text{ W/cm}^2$. We are revising the ion-collector design to improve the reliability of our measurements.

Ion Distributions From Thomson Parabola With Plastic Track Detector (F. Young)

In attempting to understand the physics of coupling laser energy into the plasma formed by ablation of a target surface, we irradiated targets with 1.0-ns pulses of $\sim 10^{14} \text{ W/cm}^2$ intensity at 10.6- μm and measured ion distributions as a function of energy and charge-to-mass ratio.

A Thomson-parabola mass analyzer,⁴ which employs a cellulose-nitrate nuclear-track detector⁵ for recording ions, was used to analyze and record the energy and number of ions emitted from the laser-produced plasmas. This mass analyzer with its parallel, homogeneous electrostatic and magnetostatic fields simultaneously resolved a multicomponent ion beam into a series of parabolas, each characterized by a charge-to-mass ratio $\frac{Z}{A}$ and by its energy. Because the energy analysis was performed by means of the Thomson parabola, Kodak-Pathé nitrocellulose CA 80.15 film⁶ was used only as a particle counter, as discussed below.

Figure 40 shows ion data recorded from a multicomponent plasma containing a mixture of hydrogen, carbon, oxygen, nitrogen, chlorine, and lead atoms. Parabola geometries were determined by adjusting the magnetic and electric fields to 380 G and 900 V, respectively, for constant drift-tube, aperture (500 μm), and electrode settings. These data were taken with the Two-Beam System.

After the cellulose-nitrate film was exposed to a plasma, the film was chemically treated in a 10% NaOH solution at a temperature of 60° C (333 K). The lowest parabola in Fig. 40 represents the proton energy and number distribution.

A nuclear-track data-reduction program to construct $\frac{dN}{dv}$ distributions (number of protons per unit velocity interval) was begun, and some preliminary results were obtained. They show that the Kodak-Pathé nitrocellulose CA 80.15 film can be used with an energy analyzer for quantitative measurements of the energy and number of protons emitted from laser-produced plasmas. The threshold for proton-track registration was measured to be $\sim 0.800 \text{ MeV/mg cm}^2$.

The sources of error in the Thomson parabola used in these experiments will be discussed in a future report. These sources of error include (1)



Fig. 40
Thomson-parabola ion distribution recorded with plastic detectors.

space-charge expansion, (2) Debye shielding, and (3) recombination and charge exchange.

Future work will be directed toward (1) experimental analysis of range-energy relations of protons and heavy ions in cellulose nitrate; (2) the study of response characteristics of cellulose nitrate and other dielectric track detectors to low-energy heavy ions and fast-energy neutrons; (3) further analysis of measured proton and heavy-ion velocity distributions to determine whether they agree with isothermal or adiabatic expansion distributions; and (4) analysis of other features of the ion data of Fig. 40.

X-Ray Pinhole Camera Results on the Two-Beam System

(D. B. vanHulsteyn and D. E. Bannerman)

Pinhole cameras were installed in the target chamber of the Two-Beam System for most of the shots taken to date, mainly to obtain information on the size and structure of the portion of laser-induced plasmas that emit x rays. In addition, pinhole cameras placed both in front of and behind planar targets indicate the type of x rays which produce the images and, hence, the mechanisms that give rise to these x rays. For example, if a relatively thick target (~1 mil) produces an image on the beam side which differs

from that on the reverse side, we can determine the portions produced by line radiation and those that arise from the higher-energy continuum. This latter information, of course, is limited by the film response to the various x-ray energies.

The cameras were oriented 45° from the vertical in a plane normal to the target surfaces. The film in the front camera was Kodak RAR 2490 in each case. On the earlier shots, this film was also used in the back camera, but because it is insensitive to high-energy x rays, we switched to medical no-screen film.

On the first series of shots, the pinholes located 1.5 cm from the target were blown out. This problem was solved by placing a brass protector with a 4-mil aperture in front of the pinhole. We then observed extensive pitting of the brass protector. The cause of this damage has not been determined, but it may be due to a capacitive discharge between the target and the conducting pinhole-camera snout. A high-Z ceramic (ZrO_2) camera is being fabricated and will be used to see whether this destruction persists.

On a series of shots involving metal targets, a layer of metal was deposited onto the brass protector. X-ray absorption measurements indicated a nonuniform thickness of $< 0.1 \mu\text{m}$. About 10^{16}

atoms were transported from the target to the pinhole over a distance of 1.5 cm and were deposited on a disk whose diameter is 0.3 cm. Because the solid angle subtended is very small, this result indicates that the ions may take a preferred path toward the pinhole. We will determine whether this deposition was caused by sputtering, vapor deposition, or discharge. The insulated camera should help resolve this question.

On one series of shots, the cameras were removed. Data obtained from ion and x-ray detectors appeared to be unaffected, indicating that a discharge if present, does not significantly affect the gross features of the plasma.

The earliest shots on CH_2 yielded no detectable images, consistent with previous work with the Single-Beam System. The absence of lines is due to filtering by the beryllium light protector. The fact that no continuous signals were observed may be ascribed to the insensitivity of the RAR 2490 film to high-energy x rays.

Later shots onto Mylar targets were more revealing, due to the presence of oxygen. In one series, for example, the images were all $\sim 400 \mu\text{m}$ in diameter. However, the higher energy shots also showed definite hot spots of $\sim 100\text{-}\mu\text{m}$ diameter. This effect was also observed on the back pinholes, but to a much lesser extent, indicating either that a prepulse may form a small local plasma which, in turn, is heated by the main pulse, or that this effect may be a result of beam structure.

As a final, encouraging note, we were able to obtain strong signals by using $20\text{-}\mu\text{m}$ pinholes, a result we had not achieved with the Single-Beam System. In the next series of shots, we will install a $10\text{-}\mu\text{m}$ pinhole, which will provide good resolution if the signal is strong enough. Subsequently, we will install an array of four pinholes in one substrate. By appropriate selection of filters, this setup will yield information not only on the structure of the laser target interaction region but on the x-ray energies as well.

plasmas originates in cold material surrounding the plasma and is excited by fast electrons. In a recent experiment we used layered targets of evaporated aluminum varying in thickness from 50 \AA to $20 \mu\text{m}$ on a SiO_2 substrate. The emission of the silicon $K\alpha$ radiation decreased exponentially as the thickness of the aluminum layer increased. From the attenuation of the silicon $K\alpha$ radiation, we estimated that the maximum electron energy was 18 keV for a 10-J laser pulse.

The attenuation of the silicon $K\alpha$ line by aluminum as a function of energy on target is shown in Fig. 41. The ratio of the intensity of the silicon $K\alpha$ line to that of the $\text{Al}(1s^2p-1s^2)$ line is lower by a factor of 10 for 100 J on target than for 10 J. However, the intensity of the silicon $K\alpha$

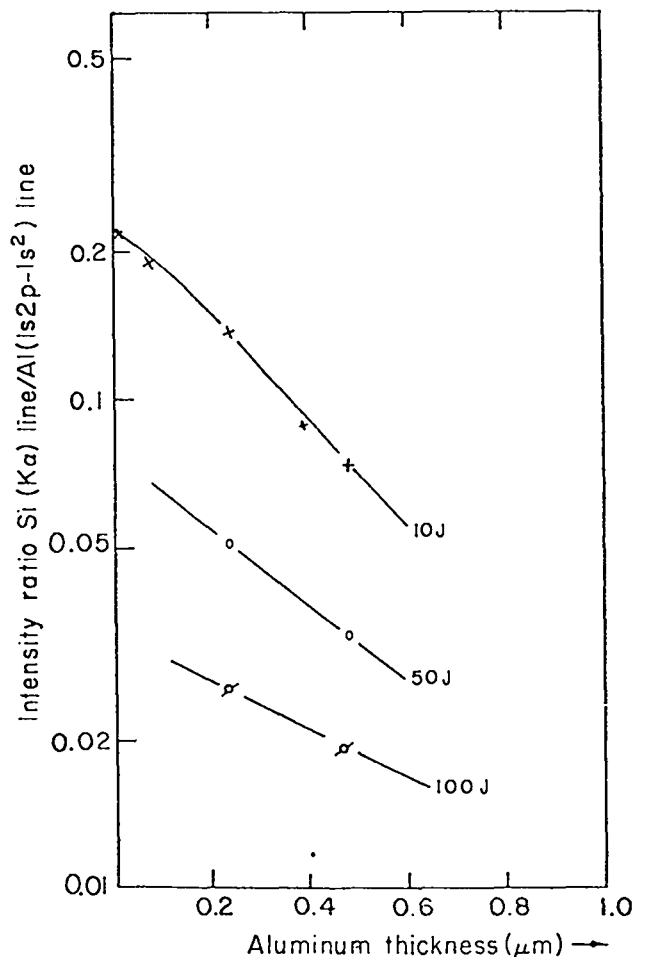


Fig. 41
Normalized silicon K intensities from slab targets of evaporated aluminum on SiO_2 for laser energies of 10, 50, and 100 J.

X-Ray Measurements From Layered Targets (K.B.Mitchell)

Previously ³ we had shown that the $K\alpha$ radiation observed in x-ray spectra from $10\text{-}\mu\text{m}$

line is nearly constant with increase in laser energy; hence, we conclude that the total energy in electrons is nearly independent of laser energy. The increase of electron energies or electron temperature is proportional to $E^{0.25}$, where E is the laser energy. The slopes of these curves imply only slight increase of electron energies with increase of laser-pulse energy.

We intend to repeat this experiment with a high-Z substrate to obtain greater electron absorption and conversion to x rays. If we can correctly measure the effect of electrons of higher energy, measurements of the $K\alpha$ radiation from layered targets could be a valuable diagnostic tool for investigating the problem of preheat.

Polarization of X Rays From Laser-Produced Plasmas

(J. L. Shohet, D. B. vanHulsteyn, S. J. Gitomer)

The single-beam Nd:glass laser system was used to show that x rays from laser-produced plasmas are polarized. This is significant because it indicates an anisotropic velocity distribution of electrons produced by the interaction of laser pulses with matter.

The purpose of this investigation is to obtain a quantitative relationship between the degree of polarization and the anisotropy, which will allow us to determine such important parameters as hot-electron temperature and direction of electron streaming.

The polarization detectors used in these experiments consisted of four photomultiplier tubes with NaI scintillators. These tubes were mounted at right angles to each other about a CH_2 scattering center to detect x rays from the target which were Compton-scattered by the CH_2 through 90° . One pair of opposing photomultiplier tubes, therefore, recorded x rays of opposite polarization from the x rays recorded by the other pair of tubes. (Fig. 42).

The x-ray polarization observed was strongly affected by the angle between the polarimeter axis and the target surface, that is, by the angle at which the x rays left the target with respect to the target surface. This effect was most striking when the polarimeter was aimed nearly parallel to the flat target surface. Laser-plasma researchers currently believe that electrons stream from the

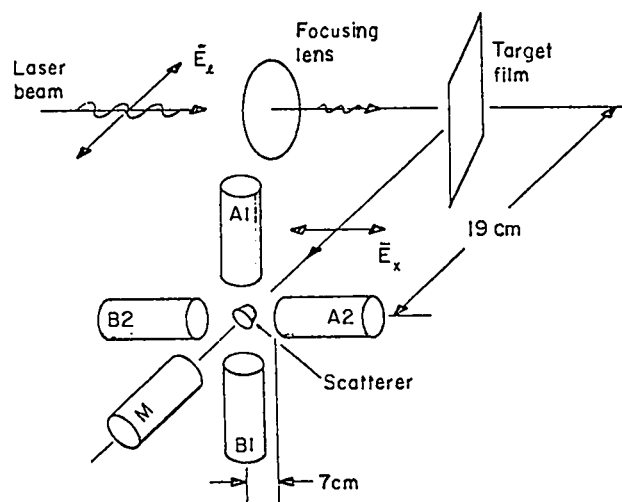


Fig. 42

Schematic of experiment to measure polarization of x rays from laser-induced plasma; A1, A2, B1, B2, and M are photomultiplier tubes.

plasma in directions approximately normal to the target surface. Using classical bremsstrahlung analysis⁷ small-angle scattering should yield x rays polarized vertically, that is, perpendicularly to the plane formed by the target normal and the polarimeter axis. However, we observed that the x rays scattered at small angles were polarized horizontally. This indicates that the bremsstrahlung scattering mechanism must apply to large-angle scattering and not to small-angle scattering as we had anticipated.

As a result of these findings, we are performing a theoretical calculation to relate the degree of polarization to an anisotropic Maxwellian electron distribution. We hope that we will thus be able to relate the polarization to the perpendicular and parallel electron temperatures.

Another series of shots was taken with the polarimeter aimed normal to the target surface. Because this is the principal direction in which electrons are supposed to stream from the target, we did not expect to see significant polarization. None was observed.

Polarized Stereoscopic Camera for Harmonic Emission

(D. R. Kohler)

In previous work⁸ on interferometry of

laser-produced plasmas, it was noted that the plasma image showed flare-like structures. It was also recently reported that the angular distribution of electrons emitted from laser-produced plasmas can be quite nonuniform.⁹ The stereoscopic polarization camera, described in an earlier report,³ was designed to take stereoscopic photographs of the second harmonic light emitted from a plasma.

Such photographs would allow us to correlate the flares with the nonuniform emission of electrons. Provision was made to obtain the stereoscopic photographs in two orthogonal polarizations, because we expect the generation of the second harmonic light near the critical plasma density to be affected by the directions of density gradients and local fields.

A schematic of the stereoscopic polarization camera is shown in Fig. 43. It is a simple relay-lens system to which a biprism (BP) and a Wollaston prism (WP) have been added. The biprism produces two images separated in viewing angle by 6° , which is common for stereoscopic viewing. The Wollaston prism produces a similar separation for vertically (upper images) and horizontally (lower images) polarized light. The interference filter for $0.53\text{-}\mu\text{m}$ light, which was placed near the plane IP, is not shown; L3 is a combination of microscope and microscope camera.

The camera has been used in a Nd:glass laser system. The laser produced a 50-ps pulse of

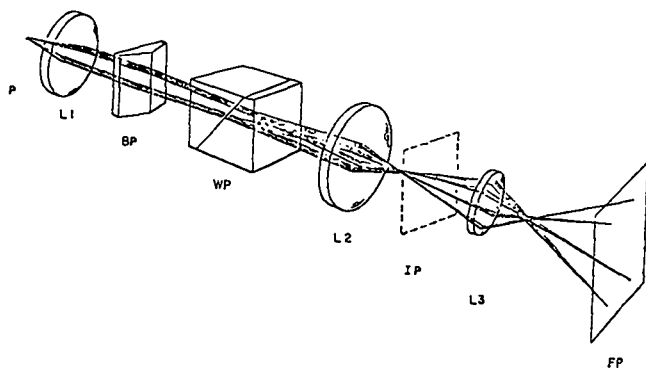


Fig. 43

Schematic of stereoscopic-polarization camera. P = plasma; L1, L2, L3 = lenses; BP = biprism; WP = Wollaston prisms; IP = intermediate image plane; FP = film plane.

$1.06\text{-}\mu\text{m}$ light containing (typically) 4 ± 2 J of energy. The light was focused by an aspheric single lens in an $f/2.5$ cone to a spot ~ 80 to $100\ \mu\text{m}$ in diameter (80% encircled energy). The light entering the target chamber was horizontally polarized. The camera was placed in a port 67.5° from the incident beam in the horizontal plane.

The target used for Fig. 44 was a flat polyethylene sheet with its normal at 22° to the incident beam (45.5° to the camera). The plasma was $\sim 100\ \mu\text{m}$ in diameter. Although the image shows structure, it does not show the same kind of flare-like structures seen before.⁴ We have not yet obtained enough information on the distribution of emitted electrons to be correlated with the stereoscopic photographs.

Note that there is no obvious polarization of the light. This observation conflicts with results obtained by other researchers and indicates that more work may need to be done.

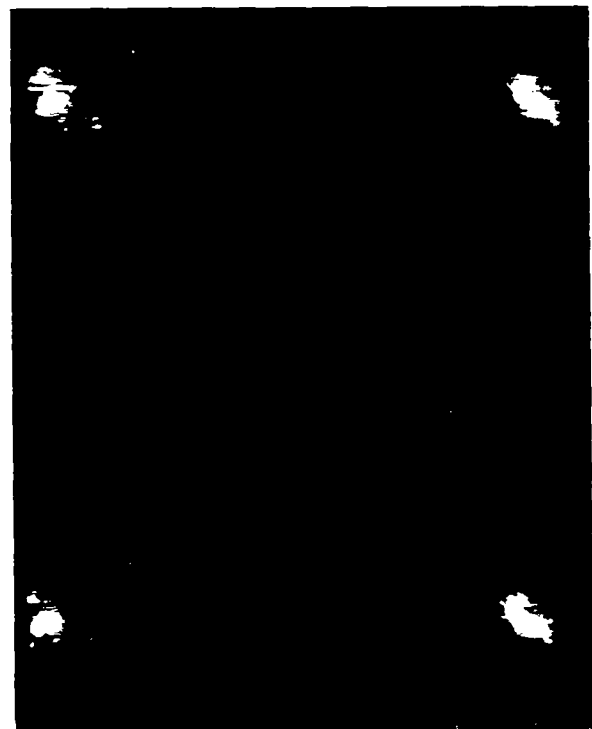


Fig. 44

Photograph of plasma in its second-harmonic light ($0.53\ \mu\text{m}$); top row, vertically polarized; bottom row, horizontally polarized. Targets illuminated from the right with $1.06\text{-}\mu\text{m}$ light polarized perpendicularly to the image plane.

THEORETICAL STUDIES OF LASER FUSION

Hot-Electron Modeling

(D. W. Forslund, J. M. Kindel, K. Lee)

In our last report (LA-6616-PR) we described progress in understanding the hot-electron spectra in laser-plasma experiments. Since then, we have refined our theoretical models to the point where we believe we understand the experimental data from a variety of laboratories, both qualitatively and quantitatively. In particular, we believe we are able to explain why the hot-electron temperature in laser-produced plasmas at high-incident laser intensity scales weakly with both laser wavelength and laser intensity. Careful two-dimensional plasma simulations show that, at high laser power, the self-consistent steepening of the plasma density profile makes resonant absorption the dominant absorption mechanism; while, at the same time, the electron-heating mechanism of resonant absorption allows the steepened profile to persist. The model, which is described below, predicts that the characteristic hot-electron energy, T_H , is given approximately by

$$T_H(\text{keV}) \approx 20(\lambda^2)^{1/4} T_c^{1/2}, \quad (1)$$

where I is the laser intensity in units of 10^{16} W/cm^2 , λ is the laser wavelength in micrometers, and T_c is the background electron temperature in kiloelectron volts at the critical density. Because of a limited number of costly simulation points, the exponents in the above equation are uncertain to a $1/6$ TW power.

In this new regime, in which the laser pressure balances the plasma pressure, it is important to determine the amount of absorption and the electron spectrum arising from the absorption. To determine the relevant physical processes, we have carried out a number of particle-in-cell simulations with the two-dimensional relativistic simulation code WAVE. These calculations differ from earlier ones,¹⁰ because they consider, for a given plasma temperature, a plasma-density profile that leads to an approximate pressure balance. We are thus able to determine more rapidly the equilibrium electron spectrum and the stability

properties of the equilibrium. Previous calculations have suffered from the fact that plasma and laser light were out of equilibrium during most of the simulation. In our latest calculations we have varied the oscillating velocity v_0 by a factor of 4. This variation is accomplished physically by either varying the incident electric field E_0 (proportionally to $I^{1/2}$) or varying the wavelength λ . Within the limits of collisionless absorption these two ways of varying v_0 are indistinguishable. For a laser intensity of 10^{16} W/cm^2 with polarization in the plane of incidence, the wave vector of the laser at 20° to the density gradient, and a background electron temperature of 2.5 keV, we have carried out four simulations at $\lambda = 0.7, 1.6, 2.0,$ and $3.0 \mu\text{m}$. Note that, in comparison to the last quarterly report, we have deleted the simulation at $4 \mu\text{m}$ because of its numerical problems, and have added simulations at 0.7 and $3.0 \mu\text{m}$. In each case the upper equilibrium density is $2.5 \times 10^{21} \text{cm}^{-3}$ corresponding to 1.25, 2.5, 10, and 23 times the respective critical densities.

Results of these simulations are summarized in Fig. 45. In each case the absorption coefficient is 30%. There is no evidence of parametric instability; the absorption is essentially resonant. The self-consistent profile adjusts itself until the density jumps from underdense to highly overdense in less than 10 Debye lengths at

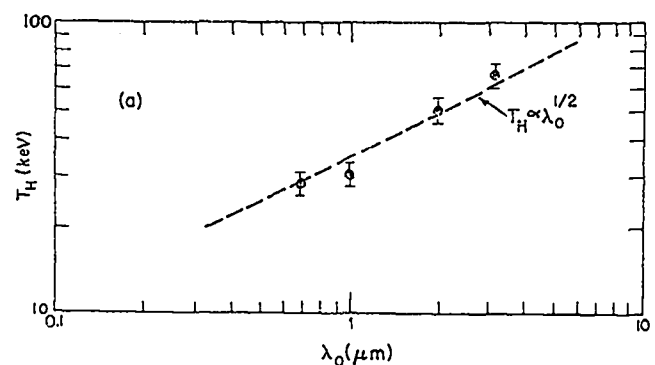


Fig. 45
Measured hot-electron temperature as a function of laser wavelength for simulations with intensity of 10^{16} W/cm^2 ; background electron temperature $T_c = 2.5$ keV. The incident light wave impinges at 20° to the density gradient and is polarized in the plane of incidence; the ion-to-electron mass ratio is 100. Typically, 250 000 simulation particles were used and $\Delta x \sim v_e/\omega_{p0}$.

the critical density. The locally generated plasma wave in the steep density gradient is observed to deposit the absorbed laser energy into a high-energy tail in the electron distribution. The observed hot-electron energy is plotted in Fig. 45 as a function of wavelength. Because the distributions are now Maxwellian, we define the characteristic hot-electron energy T_H as that energy below which half the absorbed laser energy is transported into the plasma. We see from Fig. 45 that T_H scales approximately as $(P_L \lambda^2)^{1/4}$.

We have also varied the background electron temperature (and consequently, the equilibrium density) at an intensity of 10^{16} W/cm² and a wavelength of 1.0 μ m. The results are shown in Fig. 46. The curve shown is essentially the same as that reproduced in LA-6616-PR, except that we have added a point (which required 25 h of computer time). The simulations appear consistent with T_H varying as $T_C^{1/2-1/3}$. Combining the results of Figs. 45 and 46 we obtain the result of Eq. (1).

To explain the scaling law given by Eq. (1), one can appeal to the following heuristic argument. For the case of a fixed-density profile, we have performed a large number of simulations and have found that $T_H \sim eEL$, where E is the magnitude of the local plasma-wave electric field and L is its scale length (Ref. 10). This can be understood simply as the energy gained by a resonant electron falling through the localized wave potential $\Delta \ell \sim EL$. At high laser intensities where the density gradient is very steep, as just mentioned, the

plasma-wave electric field is essentially equal to the incident laser electric field. This is true for a wide range of angles of incidence and is consistent with the 30% absorption mentioned above. The determination of T_H then reduces to the determination of the length L .

In the absence of profile steepening we might imagine L to be determined by some large hydrodynamic scale length; this would result in a very large electron energy. In the steepened density gradient there are three scale lengths to which L might correspond: v_e/ω , the Debye length at critical density; c/w_{p0} , the skin depth of the incident light wave using the upper shelf density; and v_e/w_{p0} , the upper-density Debye length. Because the excited plasma wave is inherently a phenomenon associated with the critical density, one might expect the v_e/ω dependence to dominate. This would cause T_H to scale as λ , as we described in the last quarter. By using the Debye length at the upper density, we find that T_H would depend only on T_C and be independent of laser power or wavelength. From the observed dependences of T_H it appears that the scale length L is the geometric mean of the Debye length at the critical density and the electromagnetic skin depth,

$$L \propto \left(\frac{v_e c}{\omega w_{p0}} \right). \quad (2)$$

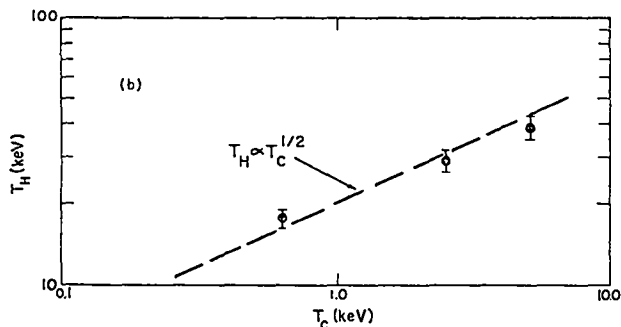


Fig. 46

Measured hot-electron temperature as a function of background temperature for simulations with the parameters of Fig. 45 except that $\lambda = 1.0 \mu$ m.

Thus, we believe that we now understand the weak scaling of T_H with wavelength and intensity.

Experiments at Los Alamos Scientific Laboratory¹¹ with CO₂ and Nd:glass laser systems at nearly the same intensity have indicated hot-electron temperatures that depend very weakly on laser wavelength, consistent with the observations in simulations of scaling as $\lambda^{1/2}$. We have plotted^{11,12} the hot-electron temperature determined from x-ray and ion data from CO₂ and Nd:glass lasers at various intensities from laboratories throughout the world. A portion of this graph is shown in Fig. 47 as T_H versus $P_L \lambda^2$. The triangles represent 1.06- μ m x-ray data; the dots, 10.6- μ m x-ray data; and the squares, 10.6- μ m ion data. Note that the weak dependence of T_H on

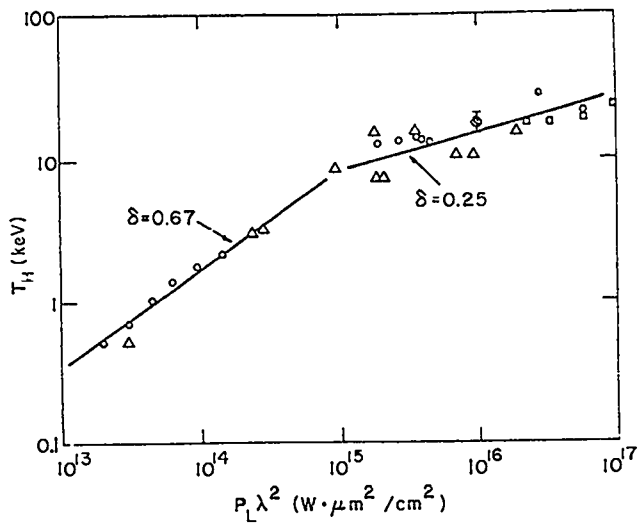


Fig. 47
Experimentally measured hot-electron temperature as a function of $P_L \lambda^2$. The bar corresponds to a simulation shown for comparison.

wavelength and intensity observed in the simulations also seems to appear in these data. The large dot represents the hot-electron temperature obtained from a WAVE simulation for $\lambda = 1.0 \mu\text{m}$, $I = 10^{16} \text{ W/cm}^2$, and $T_c = 625 \text{ eV}$. Although resonant absorption may explain the hot-electron energy, it should be mentioned that experiments at the Naval Research Laboratory show significantly higher absorption than simple resonant absorption would suggest. 13, 14

Because the background temperature of 500 eV observed in the experiments is almost completely independent of laser power and wavelength, the region of strong profile steepening ($v_0/v_e \sim 1$) begins at $P_L \lambda^2$ of $10^{15} \text{ W}\mu\text{m}^2/\text{cm}^2$. Below this power the hot-electron temperature should be determined by other processes. Indeed, the dependence of the hot-electron energy on laser power and wavelength is different in this lower power regime. The dependency may, in fact, be more in line with simple flux-limiting arguments, as mentioned earlier.

One might expect that the sharp gradient equilibrium discussed above might be highly unstable. Indeed, for polarization perpendicular to the plane of incidence, such an equilibrium is quite unstable.¹⁵ However, for polarization even

only partially in the plane of incidence, rippling of the surface tends to stabilize at a finite amplitude so that the integrity of the sharp interface is maintained. More details of this effect will be discussed in the next report.

Magnetic-Field Generation in Resonant Absorption of Light (B. Bezzerides, D. F. DuBois, D. W. Forslund, E. L. Lindman)

We have derived a simple formula for the static magnetic field generated by resonant absorption of light in an inhomogeneous plasma. It is shown that this field evolves adiabatically in time with the high-frequency wave amplitudes, and that steady state is achieved by a balance between radiation-induced stresses and frictional or convective losses, the latter effects having been neglected in all previous work on this subject. Computer simulations and experimental results are compared.

From Ampere's law and the steady-state current induced by the high-frequency-radiation electric field $E_H(x,t) = E(x) \exp[-l(\omega t - k_y y)] + \text{c.c.}$ we find the z-component of the quasi-static magnetic field to be

$$\langle B_z \rangle / mc = 2[\omega_p^2(x)/\omega] \text{Im}[u_x(x)u_y^*(x)]c^{-2}. \quad (3)$$

Here $u(x) = eE(x)(i\omega)^{-1}$ is the amplitude of the local jitter velocity of an electron in the high-frequency field and $\omega_p^2(x) = 4\pi\langle n(x) \rangle e^2/m$ where $\langle n(x) \rangle$ is the local time-averaged electron density. The density gradient is in the x direction and the high-frequency radiation is polarized in the x-y plane with angle of incidence θ . We will show that Eq.(3) is in excellent agreement with computer-simulation results and with some preliminary experiments. (Here we use brackets $\langle \rangle$ to denote quantities time-averaged over a light-wave period).

Previous work^{16, 17} has focused on calculating $\partial_t \langle B_z \rangle$ using Faraday's law. In Ref. 17 a static solenoidal electric field $\langle E_y \rangle$ was calculated from $\langle T_{ij} \rangle$ the total stress tensor, $\langle E_y \rangle = (e \langle n \rangle)^{-1} (\partial_i \langle T_{iy} \rangle)$ (summation over repeated vector indices). The field $\langle E_y \rangle$ develops in

response to the radiation-induced force $\partial_i \langle T_{iy} \rangle$. Faraday's law then gives

$$\partial_t \langle B_z \rangle = -c \partial_x \langle E_y \rangle = c(e \langle n \rangle)^{-1} \partial_x \partial_i \langle T_{iy} \rangle. \quad (4)$$

To proceed with Eq.(4) one requires an accurate expression for the force, or for the time-averaged tensor $\langle T_{iy} \rangle$ if the stress-tensor formalism is used. The total stress tensor is the sum of the familiar electromagnetic and particle stress tensors. An approximate formula was used for the electron stress tensor,

$$\langle T_{ij}^e \rangle = \langle P_{ij}^e \rangle - m \langle n \rangle (1 + v^2/\omega^2)^{-1} \langle u_i u_j \rangle, \quad (5)$$

where $\langle P_{ij}^e \rangle$ is the particle thermal pressure, which is independent of fields, and ν is a phenomenological collision frequency.¹⁷ However, this expression for the stress is deficient because it does not result in a force that includes the effect of the time-averaged drag force $\nu_m \langle J_y \rangle e^{-1}$. With this drag force included Eq. (4) should read

$$\partial_t \langle B_z \rangle = -c \partial_x \langle E_y \rangle = c(e \langle n \rangle)^{-1} \partial_x [\partial_i \langle T_{iy} \rangle + \nu(m/e) \langle J_y \rangle]. \quad (4')$$

Of course, Eq. (4') follows directly from the electron equation of motion with the drag and Lorentz forces. In steady state where $\partial_t \langle B_z \rangle = 0$ and $\partial_t \langle E_y \rangle = 0$ we obtain the quasi-static current

$$\langle J_y \rangle = -(e/m\nu) \partial_i \langle T_{iy} \rangle. \quad (6)$$

With explicit use of Eq. (5) and of the Maxwell stress, Eq. (6) becomes:

$$\langle J_y \rangle = -2(e \langle n \rangle) / \omega [\partial_x \text{Im}(u_x u_y^*) + k_0 \sin \theta (u_i u_i^*)]. \quad (7)$$

Finally, using Ampere's law, we find Eq. (3) if we neglect the term proportional to the incident-light wave number k_0 and the relatively slow spatial variation of $\langle n \rangle$. These terms are numerically negligible for the cases considered. Thus we find a localized, static current resulting in a magnetic field from the balance of the drag force with the induced electromagnetic stress forces.

It is simple to obtain the complete time dependence of $\langle B_z \rangle$. From Ampere's law we expect $\langle B_z \rangle$ to develop on the same time scale as $\langle J_y \rangle$, which in turn derives its time dependence from the high-frequency field amplitudes. Thus we conclude that

$$\langle B \rangle^{-1} \partial_t \langle B \rangle \approx \langle E \rangle^{-1} \partial_t \langle E \rangle, \quad (8)$$

where $\langle E \rangle$ is the envelope of the electric-field component which grows at the slower rate. As a confirmation of Eq. (8), consider Fig. 48 where the time history of $\langle B_z \rangle$ is shown. (The maximum value at a given time is plotted). From the figure we find $\partial_t \langle B_z \rangle / \langle B_z \rangle \equiv \nu_B \sim 3 \times 10^{-2} \omega$. This value for ν_B should be compared with $\partial_t \langle E_x \rangle / \langle E_x \rangle \sim 1 \times 10^{-2} \omega$, which is of the same order of magnitude as $(\nu_e / \omega L)^{2/3}$ -- the relevant time scale for the growth

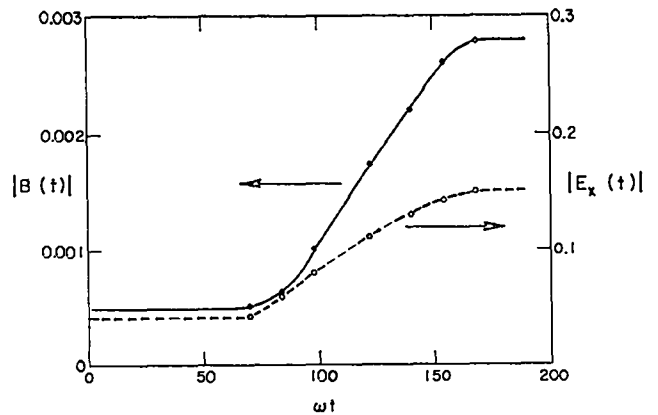


Fig. 48
Maximum amplitude of E_x and $\langle B_z \rangle$ as a function of time from simulation. Simulation results are for $k_0 L = 12.5$; $v_0/c = 0.05$; $\sin \theta = 0.4$, and incident intensity $E_0 \equiv 0.025$. All fields are expressed in units of $mc\omega/e$.

of E_x , when plasma-wave convection out of the critical region with density scale length L is responsible for the absorption rate.

In Fig. 49a we have plotted Eq. (3) for $\langle B_z \rangle$ by using the steady-state fields $\langle E_x \rangle$ and $\langle E_y \rangle$ as obtained from the electromagnetic PIC (particle-in-cell) code WAVE.¹⁸ For the sake of comparison we also show the same quantity in Fig. 49 (b) as obtained directly from the simulation. As can be seen the agreement is good, the spatial profile, peak magnitudes, phases, and small secondary peaks being quite similar.

Equation (3) also agrees with the general spatial shape and parity observed in a recent experiment.¹⁹ This experiment showed that, for example, if $k_y \rightarrow -k_y$ then $E_y \rightarrow E_y$, $E_x \rightarrow -E_x$ (in our notation) and $\langle B_z \rangle \rightarrow -\langle B_z \rangle$. We see from Eq. (3) that these parity relations are obeyed.

Equation (3) was derived by assuming a local collision frequency ν . Yet it gives excellent agreement for the collisionless regime of plasma simulation of laser fusion where wave convection or nonlocal wave damping dominates. It can be shown that Eq. (3) is still valid under these conditions.

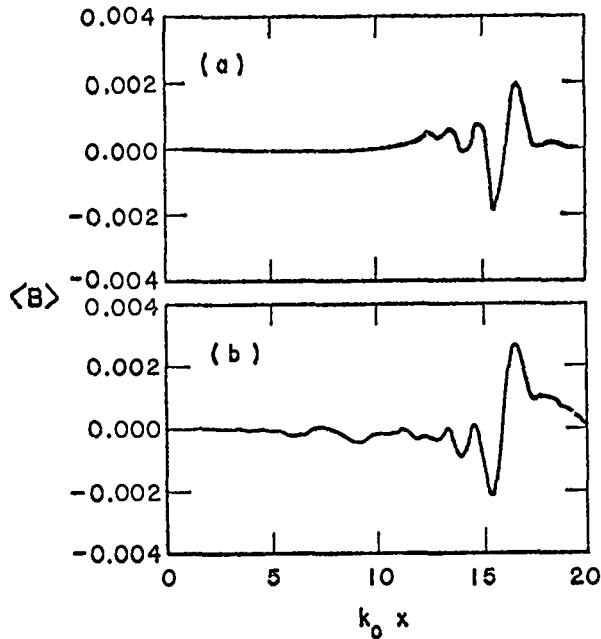


Fig. 49
Predicted magnetic fields; (a) Magnetic field $\langle B_z \rangle$ predicted by theory using the simulation field; (b) magnetic field $\langle B_z \rangle$ entirely from simulation.

We introduce the transformation of the electron distribution function^{20, 21}

$$f^e(\vec{r}, \vec{v}, t) = F(\vec{r}, \vec{v} - \vec{u}_H, t), \quad (9)$$

where $\vec{u}_H(\vec{r}, t)$ is the time-dependent jitter velocity and $\vec{u}_H = -e/mE_H$. It is useful to isolate the time-averaged part of F in the local oscillating velocity frame by writing

$$F(\vec{r}, \vec{v}, t) = F_L(\vec{r}, \vec{v}, t) + F_H(\vec{r}, \vec{v}, t); F_L = \langle F \rangle. \quad (9a)$$

In general, the current is given by

$$\langle J_y \rangle = -e \int d^3v v_y f^e(\vec{r}, \vec{v}, t); \quad (10)$$

by using the transformation, Eq. (8) we can write

$$\langle J_y \rangle = -e \langle n_H u_H \rangle + \delta \langle J_y \rangle \quad (11)$$

$$\delta \langle J_y \rangle = -e \int d^3v v_y F_L(\vec{r}, \vec{v}, t); n_H = \int d^3v F_H.$$

Thus, in addition to the obvious fluid-like contribution to the current we find a low-frequency current $\langle J_y \rangle$ resulting from a low-frequency modification of the distribution function. To calculate F_L , a consistent kinetic theory is required. Such a kinetic theory was formulated in Ref. 21 and is generalized to three dimensions in Ref. 20.

Omitting the details in determining F_L we find for example,

$$\delta \langle J_y \rangle = -e \langle n \rangle \omega^{-2} [\partial_x (\partial_t u_{Hx}) \langle u_{Hy} \rangle - k_y \omega \langle u_{Hy}^2 \rangle]. \quad (12)$$

With Eq. (11) we can easily recover the first and dominant term in Eq. (7). It should be stressed that this simple expression for the

steady-state magnetic field is valid only in a localized region around the critical surface. For example, additional contributions from the high-frequency distribution become important when the phase velocity of the plasma wave has decreased to the point at which wave damping is significant.

Vacuum Insulation to Prevent Hot-Electron Preheat of Targets (D. W. Forslund, S. J. Gitomer, J. M. Kindel, E. L. Lindman)

In general suprathermal electrons produced in laser light absorption, can adversely affect target performance by preheating the fuel and/or degrading pusher action. As known, shielding the fuel by high-Z material can add too much mass for good target performance. We therefore suggested that a vacuum can be a more efficient insulator (see Report LA-6616-PR).

As known, suprathermal electrons move to high-density regions, simultaneously causing return current of cold electrons to maintain charge neutrality. It has been suggested that the suprathermal electrons may be stopped by the electric field that is generated as the cold return-current electrons move through a resistive medium. The resistance can be either classical or can be due to an ion acoustic turbulence. As pointed out previously we cannot depend on a mechanism in which the return-current resistance will shield the hot electrons because the resistive medium is reduced in effectiveness by rapid energy deposition. If Q is the absorbed-energy flux carried by hot electrons, and if these hot electrons are turned around in a distance L , resistive heating will cause an energy flux of nearly Q to be deposited into the background plasma. In fact, if we compare the usual classical electron range for energy deposition with the return-current resistance turnaround length L , it is easily shown that a small amount of heating will make classical electron scattering the more important mechanism for turning the electrons around.

We may, therefore, state in general that a mass penalty is incurred if hot electrons are to be shielded.

Let us consider the use of a vacuum between two spherical shells to stop the bulk of the hot

electrons (see LA-6510-PR, p. 85). The laser energy is absorbed on the outer shell which comes into thermal contact with the inner shell as soon as the ions traverse the intervening space. Assume that the two foils shown in Fig. 50 are sections of concentric spherical shells. Obviously, most of the volume used to stop the hot electrons is vacuum. Because the only mass added is that of the outer shell, the mass penalty in a target design is not severe. The hot electrons are turned around in the vacuum and, therefore, cannot burn out the resistive medium. Most importantly, the vacuum insulation lengthens the time scale for hot-electron preheat from an electron streaming or conduction time to an ion time scale.

We can, in rather heuristic fashion, describe how vacuum insulation works. Laser light is absorbed in the exposed front layer of the shell by electrons, which form a sheath at the front and rear of the outer foil. As in any sheath, a few electrons escape and set up an electric field that turns the bulk of the electrons back. However, in our case, the sheath is modified by the presence of a second foil as discussed later.

A heuristic argument may illustrate the salient features of the scaling law that describes the flux of escaping electrons hitting the second foil in the presence of fixed ions. The energy flux Q may be expressed by

$$Q = (n_e T_H) v_H, \quad (13)$$

where n_e is the electron density at the second

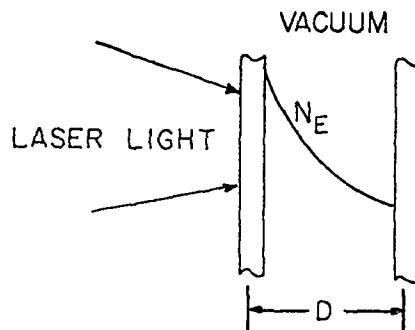


Fig. 50
Schematic of vacuum insulation concept where laser light impinges from the left; the separation distance between the foils and N_e is the electron density.

foil, T_H is the hot-electron temperature at the first foil, and v_H is the characteristic hot-electron velocity. The electron density is determined by equating the hot-electron Debye length $\lambda_{D,H}$ to the separation between the foils D ; thus, the density n_e is proportional to T_H/D^2 . By using this proportionality in the above flux equation, we obtain

$$Q = 10^9 \frac{T_H^{5/2} (\text{keV})}{D^2 (\mu\text{m})} \quad (14)$$

This is the Langmuir-Child's law for a space-charge-limited diode, in which we have considered the energy flux, rather than the current that varies as $T_H^{3/2}$.

If we allow the plasma to move, it is critical to know how long the vacuum insulation can be maintained. For a given gap width D , the problem reduces to determining the velocity of the expanding density profile when it equals the hot-electron density. If during the laser pulse, the density at the second foil reaches the hot-electron density, then the insulation will have shorted out, because hot electrons can now stream across the intervening space.

There are two limits to vacuum insulation. First, the suprathermal electrons dissipate most of their energy by expansion of the ions and do not deposit much energy in the background plasma. In this case, the shorting velocity must be the ion acoustic velocity at the hot-electron temperature. The ion expansion is isothermal. Experiments with very thin foils fall into this category, because fast ions will carry the energy from one foil to another. Second, collisional energy of the hot electrons is lost in the background plasma of the first foil leading to the so-called exploding-pusher limit. The shorting velocity is less than in the first case, but exactly how much less is still under investigation.

For the first case, a number of turnarounds per electron, if equal to $\sqrt{m_i/m_e}$ per electron, is required for the hot-electron energy to be transferred to ions. Fewer turnarounds lead to a heating of the background plasma.

For the double-foil experiments, which are discussed elsewhere, we have carried out some

tentative one-dimensional modeling with LASNEX. From some representative calculations (Fig. 51) at intensities of $5 \times 10^{14} \text{ W/cm}^2$ at $10.6 \mu\text{m}$, we can plot the insulation time for double foils made of plastic as a function of foil separation distance. As a rule of thumb for smaller foil separations, we may state that $1.0 \mu\text{m}$ of separation distance is required per picosecond of pulse duration or that the shorting velocity is 10^8 cm/s . The suprathermal electron temperature in these experiments was 20 keV.

Sheath Physics in Vacuum Insulation

(K. Lee, E. L. Lindman)

The conceptual idea of vacuum insulation has been discussed above. Consideration of the physics involved has permitted us to formulate a scaling law for the effectiveness of vacuum insulation as a function of hot-electron temperature and vacuum space gap. We are presenting below calculations and numerical results on the suppression of heat flux due to a vacuum gap, obtained by generalizing Langmuir's work on thermionic current between parallel, plane electrodes. The hydrodynamic closure of the vacuum gap and the decreasing effectiveness of hot-electron heat flux suppression is estimated from an isothermal rarefaction model.

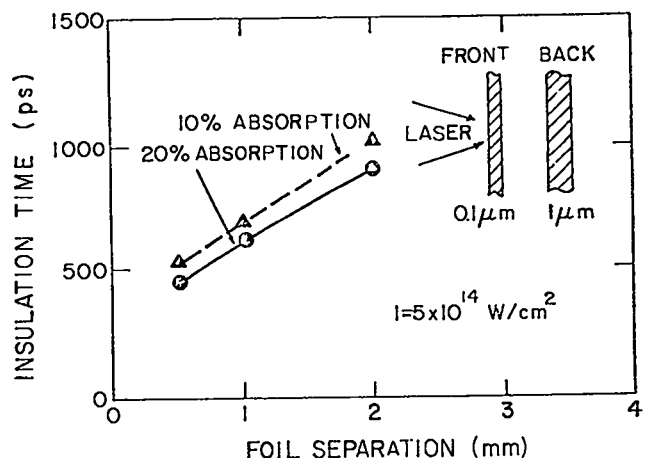


Fig. 51 Preliminary LASNEX modeling of our vacuum insulation experiments. The CO_2 laser intensity is $5 \times 10^{14} \text{ W/cm}^2$; foils used in the experiments are sketched in the insert.

To model vacuum insulation in plane geometry, consider a vacuum gap separating two plane boundaries. At one boundary the energetic electrons are maintained at a temperature T_H with a density n_H . At the other boundary, the cold electrons are maintained at a temperature T_C with a density n_C . The heat flux Q from the hot boundary to the cold boundary is related

$$Q = JT_H [1 - T_C/T_H \ln(J \sqrt{\frac{2\pi m_e}{T_C}} / en_C)]. \quad (15)$$

The hot-electron current is given by the maximum drop, φ_m , in electrical potential across the vacuum gap

$$J = en_H \sqrt{\frac{T_H}{2\pi m_e}} e^{-\frac{e\varphi_m}{T_H}}. \quad (16)$$

For a given hot current J , the required vacuum gap D in units of hot-electron Debye length is given by

$$D = n_+ - n_-, \quad (17)$$

where

$$n_{\mp} = \mp (J^*)^{-1/2} \int_0^{b_{\mp}} \left\{ [e^x (1 \pm S(\sqrt{x})) - 1 \mp \frac{2\sqrt{x}}{\sqrt{\pi}}] \right. \\ \left. + \frac{1}{\alpha} [e^{\alpha^2 x} (1 \mp S(\alpha\sqrt{x})) - 1 \pm 2 \frac{\alpha\sqrt{x}}{\sqrt{\pi}}] \right\}^{-1/2} dx,$$

$$b_- = - \ln J^*,$$

$$b_+ = - \frac{T_C}{T_H} \ln \left(\frac{n_H}{n_C} \sqrt{\frac{T_H}{T_C}} J^* \right),$$

$$J^* = \frac{J}{en_H} \sqrt{\frac{2\pi m_e}{T_H}}, \text{ and}$$

$$S(t) = \frac{2}{\sqrt{\pi}} \int_0^t e^{-x^2} dx.$$

Figure 52 shows the vacuum-gap distance as a function of percentage of energetic electron current transmitted, defined as $100 J^*$. The two curves are obtained for the indicated temperature and density ratios at $T_H = 30$ keV and $n_H = 10^{18} \text{ cm}^{-3}$. The curves show that the results are insensitive to large variations in density and temperature ratio and that the transmitted current scales inversely with the square of the vacuum-gap distance, as was derived heuristically in the preceding section. Except for a small correction, the heat flux across the vacuum gap scales directly as the hot-electron current. For the indicated parameters, Fig. 52 shows that a small vacuum gap of $175 \mu\text{m}$ can reduce the hot-electron heat flux by more than three orders of magnitude.

Although a small vacuum gap can initially suppress the hot-electron heat flux very effectively, the narrowing of the vacuum gap due to hydrodynamic expansion of the hot boundary decreases its effectiveness very rapidly. The closure rate and the increase in heat flux as a function of time can be estimated from an isothermal rarefaction model of the hydrodynamic expansion. With the exception of the fast-ion leading edge of the expansion, the isothermal rarefaction model is accurately described by the

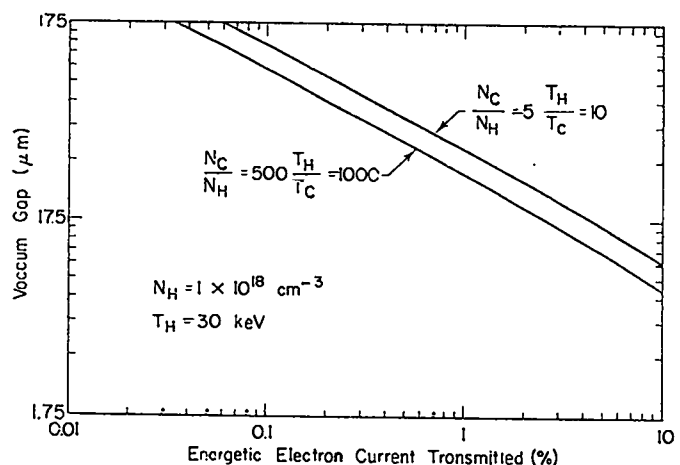


Fig. 52
Vacuum-gap requirement as a function of transmitted energetic-electron current percentage.

similarity solution given by Landau and Lifshitz in their text on fluid mechanics.²² At the front of the expansion, the local density scale length equals the local Debye length and does not admit a similarity solution. By imposing the condition that the local density scale length be equal to the local Debye length and that the solution be connected to the similarity solution, we obtain the velocity of the low-density foot

$$V_m = 2C_s \ln \omega_{pi} t, \quad (18)$$

where V_m is the velocity of the leading edge, c_s is the ion sound speed at the hot-electron temperature, and ω_{pi} is the ion plasma frequency corresponding to n_H . This estimate is in excellent agreement with numerical calculations.²³ From the isothermal rarefaction model, the electrical potential φ is given by

$$\frac{e\varphi}{T_H} = -\frac{x}{tc_s} - 1 = -v/c_s. \quad (19)$$

Because the velocity of the fast ions is known, the shorting time due to the fast-ion foot can be calculated, and the fraction of energetic electron current at the time of shorting is given by

$$J^* = e \frac{e^{\varphi_m/T_H}}{e^{-v_m/c_s}}. \quad (20)$$

For a density $n_H = 10^{18} \text{ cm}^{-3}$ and a temperature $T_H = 30 \text{ keV}$, the fast-ion shorting time and the percentage of energetic-electron current transmitted when the vacuum shorts out as a function of vacuum gap are shown in Fig. 53. Note that the percentage of fast-electron current transmitted is small, e.g., only 1% for a vacuum

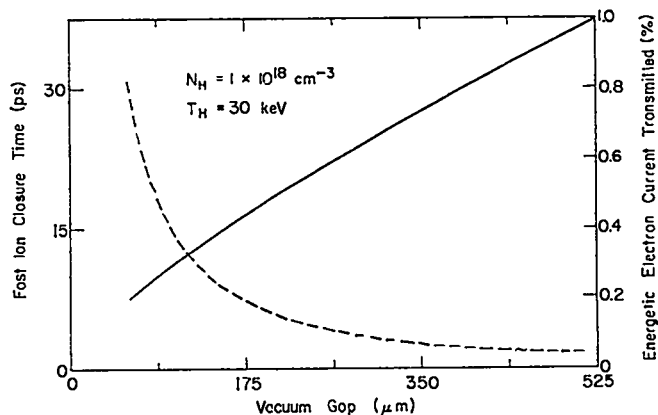


Fig. 53
Vacuum-gap closure by fast ions and energetic-electron current transmitted at closure.

gap of reasonable size. Thus, shorting by fast ions does not represent a problem; shorting is rather due to the expanding bulk plasma. Assuming that the isothermal-rarefaction solution is still valid after the initial fast-ion pulse hits the second foil, the percentage of transmitted current then increases as a function of time

$$J^* = e^{-\frac{D}{tc_s} - 1}, \quad (21)$$

where D is the initial vacuum gap.

Preliminary simulation results indicate that this expression is an overestimation because it does not include the presence of a cold-boundary sheath which decreases the maximum potential drop across the two boundaries from that given by the rarefaction model. More simulations will be carried out, and comparisons with the above model will be presented in the next report.

In conclusion, vacuum insulation represents a viable means of preventing fuel preheat in fusion targets. A reasonable vacuum gap of a few hundred micrometers decreases preheat by more than three orders of magnitude. Vacuum-gap shorting is due to the bulk of hot plasma expanding at the hot-ion acoustic speed. The requirement of support structure to separate the target shells at a defined vacuum-gap distance and its effect remain to be investigated.

TARGET DESIGN

Introduction

Although most of our target design work is classified, we can mention some of our developmental efforts and some unclassified design calculations. The codes being used and being improved are LASNEX, a two-dimensional Lagrangian code acquired from Lawrence Livermore Laboratory; MCRAD, a LASL-developed two-dimensional Lagrangian code; and CERES, a LASL-developed one-dimensional Lagrangian code.

The multigroup radiation treatment in LASNEX is being improved so that more accurate opacities can be used. Several changes have been made to allow quite accurate three-temperature (3T) calculations including operation with a laser ray-trace code. Because none of our design codes uses a Monte Carlo treatment to describe suprathreshold electrons, we have included hot electrons in CERES by a Monte Carlo routine. This inclusion should permit some comparison with the multigroup treatment in LASNEX. The beam-disposition package in LASNEX is being used to study ion-beam implosions, whose energetic ions are created by the laser: an outer low-Z shell receiving spherically symmetric laser illumination explodes, and fast ions emitted from the inside of the shell are used to drive an implosion of an inner DT shell.

Compression and Burn by Fast Ions

(J. M. Kindel, E. L. Lindman)

Laser light at high intensities has been shown to produce copious amounts of fast ions at energies exceeding 100 keV. Our experiments, in which the laser irradiates a foil that is thinner than the range of an energetic electron, have shown large numbers of fast ions streaming from the rear of the foil. In fact, hot electrons bouncing back and forth inside the foil should accelerate roughly equal amounts of fast ions off the front and the back, a phenomenon we intend to utilize in our target design.²⁴⁻²⁷ We have therefore considered illuminating a shell uniformly (4π) and using the fast ions streaming off the inside of this shell to drive an implosion of an inner target consisting of a DT shell with a high-Z layer. This

scheme is shown schematically in Fig. 54. In our last report (LA-6616-PR), we discussed calculations in which yield ratios of 10 to 20% were achieved. With some change in structure we have obtained yield ratios of nearly 20. These high-yield ratios are rather insensitive to changes in both energy and pulse shape over a fairly wide parameter range. The advantages of this approach may be summarized as follows.

- High conversion efficiency of absorbed energy to fast-ion energy.
- No Rayleigh-Taylor instabilities during fast-ion generation.
- No hot electrons (or fast ions) generated at pellet surface.
- Vacuum insulation of hot electrons generated elsewhere.
- Improved spherical symmetry from hot-electron energy transport.
- All fast-ion energy impinging on pellet is absorbed.
- Energy delivered to pellet is transformed into bulk heating of electrons (and ions).

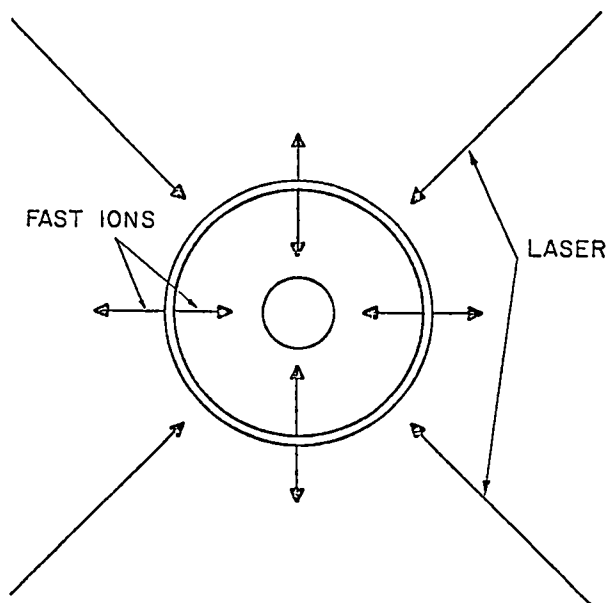


Fig. 54
Schematic of target using laser-produced fast ions to drive an implosion.

Disadvantages are:

- Fabrication difficulties;
- Low absorption of laser light;
- The character of the blowoff plasma, which allows the more energetic, more deeply penetrating ions to be absorbed early in the implosion.

The best pellet design, according to the LASNEX calculations, is shown in Fig. 55. We assume that beryllium ions with a range of $0.75 \times 10^{-3} \text{ g/cm}^2$ are incident on the low-Z ablator material LiD. We have 58 μg of LiD, 27 μg of CHOW (a high-Z impregnated plastic), and 2.6 μg of DT fuel frozen onto the inside of the plastic. The time dependence of the ion-energy pulse is shown in Fig. 56. For input energies ranging from 15 to 30 kJ, the peak power ranges from 15 to 30 TW. The figure shows a two-straight-lines approximation to the energy delivered by an expanding plasma.

The yield ratios obtained for the one-dimensional spherically symmetric calculations with input energies between 15 and 30 kJ are shown in Fig. 57. Three-temperature calculations with LASNEX indicate yield ratios above 14 for input energies ranging from 15 to 30 kJ. By using multigroup radiation transport we obtained a much narrower energy range for reasonable output. The

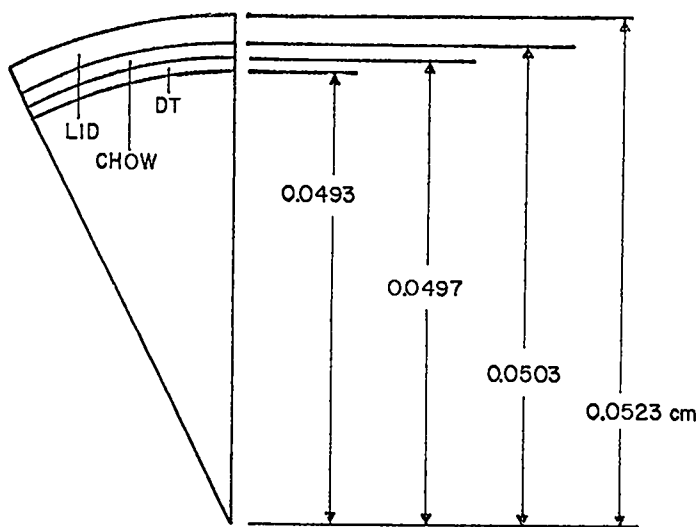


Fig. 55
Pellet structure of high-yield fast-ion target.

peak yield ratio in this case is 14 at an energy input of 18 kJ. Thus, if 20% of a 100-kJ pulse can be deposited in the pellet in the form of fast ions, 250 kJ is obtained for an overall yield ratio of 2.5.

Further work will include calculations of a more realistic curve of energy vs time and its incorporation into similar calculations. Two-dimensional calculations are also needed.

Conical Target for Near-Term CO_2 Experiments

(R. Mason)

The exploding-pusher mode of present-day laser targets yields high neutron counts most readily; however, at low energies the 1-ns CO_2 pulse is generally too long for the collapse times of small, low-mass microballoons to be imploded. We are therefore developing a conical target for near-term CO_2 experiments that is better suited to the energy output characteristics of our lasers.

The output pulse from our Single-Beam CO_2 System can currently be focused to a 200- μm -diam spot, containing 83% of the energy (70 J). In foil experiments, 10 to 20 J of this energy is absorbed, and the rest of the light is refracted or reflected. A 50- μm -diam microballoon, typical of KMSF and LLL experiments intercepts in this beam only 6% of its energy, and with refraction only 0.5 to 1 J. Because its collapse time in the exploding-pusher mode is typically 80 ps,²⁸ only 0.08 J would be absorbed during the implosion. The mass of the microballoon is 27 ng. To create kilovolt temperatures in the fuel, an energy of 0.1 J/ng must be absorbed, which means that our microballoon will be too cold by at least a factor

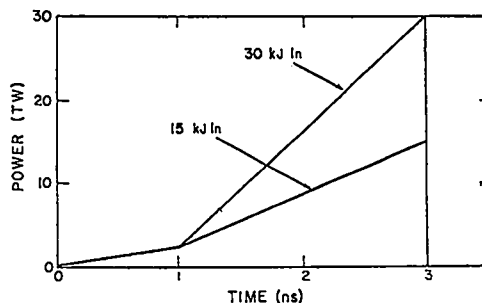


Fig. 56
Time dependence of ion-power transmittal into target described in Fig. 55.

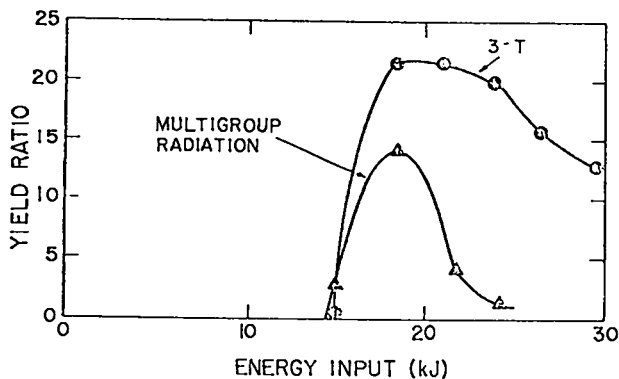


Fig. 57
Yield ratio versus input energy for the design shown in Fig. 54.

of 30. Below 1 keV, the thermonuclear burn rate varies as the temperature to the sixth power. Although $\sim 10^7$ neutrons have been produced with 50- μm -diam, 80-ps, 25-J Nd:glass beams, we can expect only few neutrons from this microballon under CO_2 illumination with its larger spot size and longer pulse.

This neutron yield increases somewhat if we use larger microballoons of, e. g., 200- μm diameter; however, with a fixed shell thickness the increase in the subtended beam energy is offset by an equal increase in target mass. The matching of target and CO_2 pulse improves because the shell takes longer to implode. As an exploding pusher, the larger microballoon takes 320 ps to implode, and the absorbed energy would therefore be too low by only a factor of 7. We expect that two-beam symmetrical illumination at doubled energy input will produce copious amounts of neutrons. Our Two-Beam System is now available for such microballoon experiments; but in parallel it is reasonable to proceed to designs that can be illuminated differently than uniformly (4π). The simplest procedure is to implode a sector of a spherical microballoon. This can be accomplished by embedding a conical DT region in the face of a high-Z slab (of lead, for example) and covering the cone with a spherical cap, as shown in Fig. 58. The laser light is then applied directly and normally onto the face of the cap.

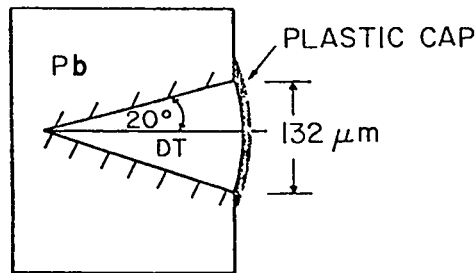


Fig. 58
Schematic of near-term conical target. The cone imbedded in the lead is filled with 1 atm of DT gas and is closed with a 3- μm CH_2 cap.

The target works as an exploding pusher. If an energy of ≈ 0.1 J/ng is delivered to the cap, the cap is heated to kilovolt temperatures and explodes. It expands into the DT region and compresses the fuel to burn conditions. Typically, we assume a flat, 1-ns, 80- to 130-J laser pulse incident on the target.

The advantages of the conical design are:

- It lengthens the implosion time by locating the plastic mass at a much larger radius than an equal mass in a sphere.
- It simulates a much more massive sphere imploded by a much larger laser system. The mass in a 20° half-angle cone corresponds to a full microballoon 29 times more massive. Thus, illumination with 70 J corresponds to illumination over a full sphere by a 2-kJ pulse.
- Illumination of the cap is reliably more uniform (avoiding the equatorial intensity deficiencies) and less subject to refraction than for microballoons.

The chief disadvantage of the design is caused by the fact that cooling of the cap near the conical wall during the implosion results in a drag, which leads to weaker compression of the fuel near the walls than on the conical axis, while conduction of energy out of the fuel to the walls results in burn at lower temperature and reduced neutron output.

For our Single-Beam CO₂ System, the target is determined somewhat uniquely. Because the beam is nearly uniform over an inner 140- μm -diam spot, the radius should be $\sim 66 \mu\text{m}$. Foil experiments indicate that the range of suprathreshold electrons in the plastic is 17 μm , so that at a cap thickness of 3 μm we can be reasonably sure that the CO₂ energy will be deposited with near uniformity throughout the pusher. Simulations show that the collapse time for a 5° half-angle cone is 1.1 ns, but such a cone is probably too narrow, with excessive drag and conduction losses. At 20° the collapse time with 4.3 J absorbed is 430 ps, which wastes some of the pulse energy, but two-dimensional simulations show that the wall losses are acceptable, as shown below.

We have conducted one- and two-dimensional simulations of this conical target with our MCRAD code. This is a 3-temperature, two-dimensional Lagrangian hydrodynamic-burn code with interactive light-pen rezoning capability. This capability was crucial to managing the many requisite rezones along the conical wall containing the fuel.

Figure 59 summarizes our one-dimensional calculations. It shows that 10^9 neutrons are predicted by these calculations for 8 J delivered to the plastic cap over 1 ns. Figure 60 shows that only about half, $\sim 4 \text{ J}$, is absorbed up to the time of maximum fuel compression. About 10^6 neutrons are predicted for 1 J delivered; nearly 10^{10} are predicted for the full 70 J.

Figure 60 shows that the ion temperature in the fuel rises from $\sim 2 \text{ keV}$ with 1 J delivered, to 9 keV with the 8-J deposition. The maximum DT density ranges between 0.2 and 0.3 g/cm^3 , which is typical of an exploding pusher target.¹ The DT fill density is $2.5 \times 10^{-4} \text{ g/cm}^3$ (1 atm).

Within a one-dimensional framework we have also examined the sensitivity of our results to a variation in parameters. For example, as we vary the fill pressure, we find a flat neutron output down to 0.5 atm, and then a further decrease by 50% for a fill pressure as low as 1/8 atm. The maximum fuel density stays near 0.3 g/cm^3 for all these fills. Decreases in foil thickness to 1.5 μm do not change performance, but at 0.75 μm , performance is altered considerably. Variations in cone angle

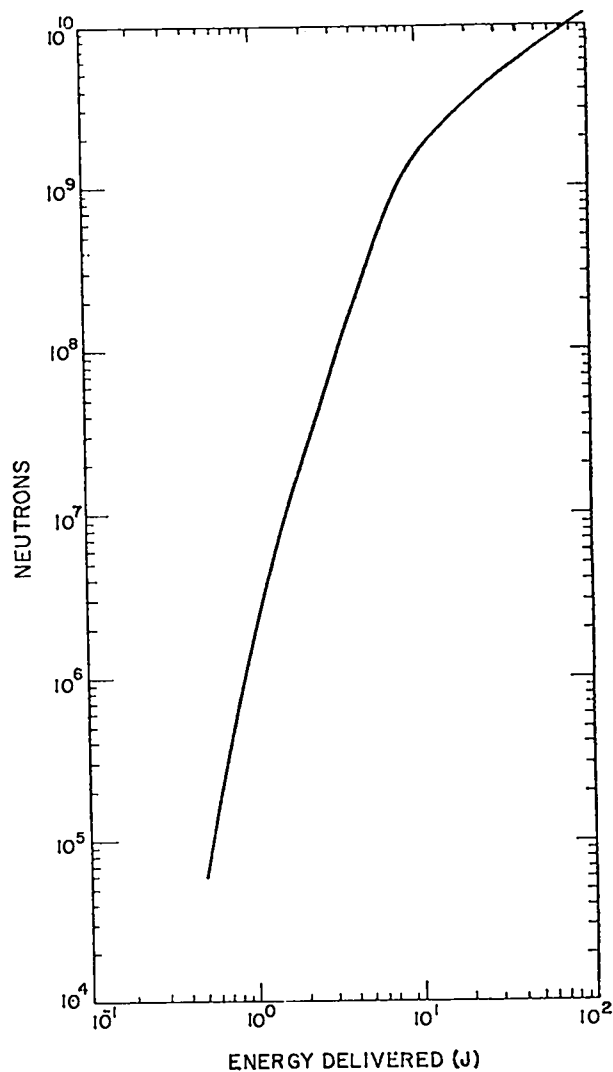


Fig. 59
Number of neutrons produced in conical target as a function of absorbed energy.

reveal that a 5° half-angle cone is best, predicting 10^{10} neutrons with 10 J supplied. Over the full range of cone angles (with the cap radius fixed at 66 μm) the peak fuel temperature remains near 10 keV, and the maximum fuel density is 0.3 g/cm^3 . Lastly, we have also varied the CH₂ cap dimensions. As the cap size increases the specific-energy deposition drops and collapse takes longer. A cap radius of 82 μm yields more neutrons, but would require defocusing of the CO₂ beam.

We have also carried out two-dimensional calculations with the 20° half-cone target. A

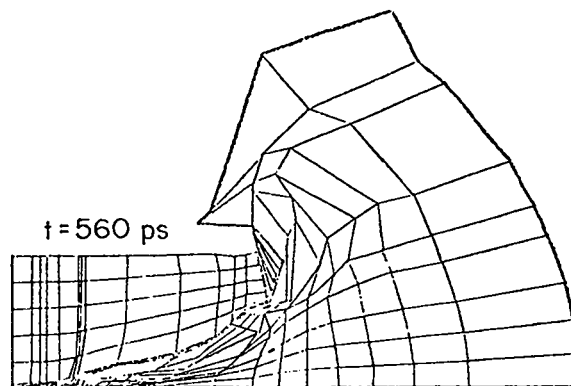
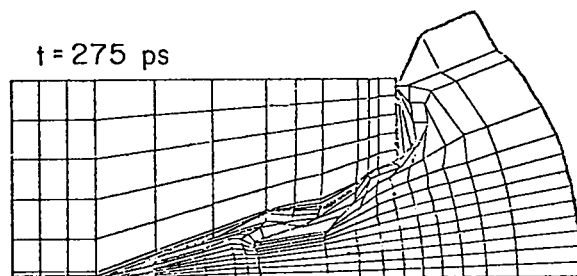
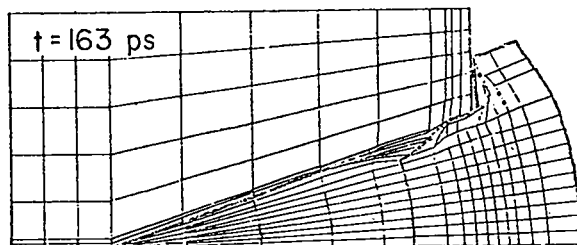
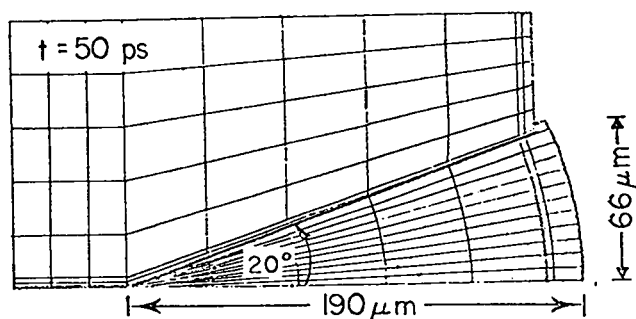
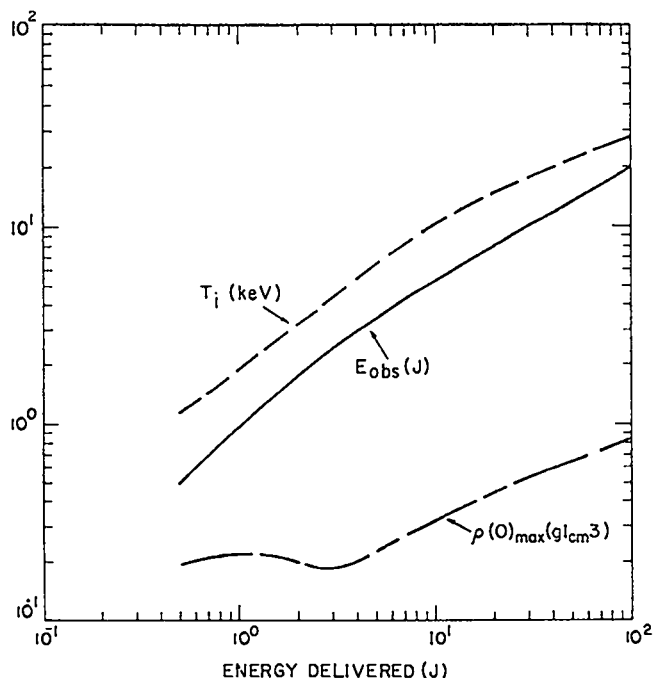


Fig. 61
Two-dimensional calculations for 20° half-angle cone; see text.

Fig. 60
Indicated parameters plotted as a function of absorbed energy for a cap radius of 66 μ m, a DT fill pressure of 1 atm, and a cap thickness of 3 μ m.

representative calculation is shown in Fig. 61. Numerous rezonings must be done with the MCRAD interactive light-pen rezoner, (mostly horizontal lines in the lead). The sequence shown is for 10 J delivered over 1 ns. By 163 ps, plastic is running vertically up the face of the lead (causing incidentally, a need for numerous rezones at the vertical interface), and some cooling has occurred in the plastic adjacent to the conical wall. Thus, plastic at the wall has advanced only half as far against the DT as plastic on the conical axis. A shock in the lead has caused its heating near the wall and some bulging by the lead into the conical region.

In the two-dimensional calculations, we find that the fuel on the axis is compressed first and reaches a maximum temperature of ~ 1.5 keV. The axial fuel density reaches a higher value than in the one-dimensional prediction, ~ 2 g/cm³. These maxima are achieved at ~ 370 ps, earlier than in the one-dimensional prediction. Burn at the center is aided somewhat by an expansion of the lead near the vertex into the cone region at ~ 350

ps. The two-dimensional yield prediction is 10^7 neutrons, roughly two orders of magnitude below the one-dimensional prediction, which is consistent with the reduced fuel temperature from conduction losses. However, the reduction, we proceed to two dimensions, may have been overstated as a result of calculational error introduced by the many rezonings needed to manage the slip surface along the cone. At late times (at ~ 500 ps) the off-axis

plastic reaches the conical vertex region and pushes back on the lead following the cooling phase after reexpansion of the CH₂ and DT.

REFERENCES

1. D. V. Giovanielli, Los Alamos Scientific Laboratory internal report.
2. Additional data points proved by J. Martineau, Centr d'Etudes de Limeil, for CO₂ experiments; and by H. Ahlstrom, R. A. Hass, K. R. Manes, E. K. Storm, D. W. Phillion, V. C. Rupert, and M. J. Boyle, Bull. Am. Phys. Soc. 21, 1046 (1976), for neodymium experiments also fit well on these curves.
3. E. Stark and F. Skoberne, Los Alamos Scientific Laboratory report LA-6616-PR (May 1977).
4. J. N. Olsen, G. W. Kuswa, and E. D. Jones, J. Appl. Phys. 44, No. 5, 2275 (1973).
5. R. L. Fleischer, P. B. Price, and R. M. Walker, Nuclear Tracks in Solids; Principles and Applications (University of California Press, 1975).
6. Film available from Eastman Kodak Company, Scientific Photography, 343 State Street, Rochester, New York.
7. J. D. Jackson, Classical Electrodynamics (John Wiley & Sons, Inc., New York, London, Sydney, 1966).
8. D. R. Kohler, D. V. Giovanielli, R. P. Godwin, G. H. McCall, and M. M. Mueller, Bull. Amer. Phys. Soc. 19, 854 (1974).
9. D. V. Giovanielli, J. F. Kephart, and A. H. Williams, J. Appl. Phys. 47, 2907-10 (1976).
10. D. W. Forslund, J. M. Kindel, K. Lee, E. L. Lindman, and R. L. Morse, Phys. Rev. A 11, 679 (1975); K. G. Estabrook, E. J. Valeo, and W. L. Kruer, Phys. Fluids 18, 1151 (1975).
11. D. V. Giovanielli and G. H. McCall, submitted to Phys. Rev. Letters, 1977, and references therein; D. V. Giovanielli, J. F. Kephart, and G. H. McCall, 1976 IEEE Int'l Conf. on Plasma Science, Austin, Texas (May 24-25, 1976); Tai Ho Tan, D. V. Giovanielli, G. H. McCall, and A. H. Williams, 1976 IEEE Int'l Conf. on Plasma Science, Austin, Texas (May 24-25, 1976).
12. E. K. Storm, Bull. Am. Phys. Soc. 21, 1173 (1976); H. G. Ahlstrom, J. F. Holzrichter, R. A. Hass, E. K. Storm, K. R. Manes, D. W. Phillion, V. C. Rupert, M. J. Boyle, and K. M. Brooks, Proc. Europ. Conf. on Laser Interaction with Matter, Palaiseau, France (October 1976).
13. B. H. Ripin, P. G. Burkhalter, F. C. Young, J. M. McMahon, D. G. Colombant, S. E. Bodner, R. R. Whitlock, D. J. Nagel, D. J. Johnson, N. K. Winsor, C. M. Dozier, R. D. Bleach, J. A. Stamper, and E. A. McLean, "Laser Fusion Studies at NRL," NRL report 3315, pp. 100-177 (August 1976).
14. B. H. Ripin, Appl. Phys. Lett., (to appear February 1977)
15. R. Z. Sagdeev, Plasma Phys. Probl. Controlled Thermonucl. Reactions III, p. 406. Leontovich Ed., English transl. (Pergamon, Oxford, 1959); and D. W. Forslund, J. M. Kindel, K. Lee, and E. L. Lindman (to be published).
16. J. A. Stamper, Phys. Fluids 19, 758 (1976).
17. J. J. Thomson, C. E. Max, and K. Estabrook, Phys. Rev. Lett. 35, 663 (1975).
18. D. W. Forslund, J. M. Kindel, K. Lee, E. L. Lindman, and R. L. Morse, Phys. Rev. II, 679 (1975).
19. W. F. DiVergilio, TRW Systems, Redondo Beach, Calif., (1976).
20. B. Bezzerides, D. F. DuBois, and D. W. Forslund, "Magnetic Field Generation by Resonance Absorption of Light," submitted to Phys. Rev.
21. B. Bezzerides and D. F. Dubois, Phys. Rev. Lett. 34, 1381 (1975).
22. L. D. Landau and E. M. Lifshitz, Fluid Mechanics, (Pergamon Press, London 1959).
23. J. E. Crow, P. L. Auer, and J. E. Allen, J. of Plasma Phys. 14, pp. 65-77, (1976).
24. J. Nuckolls, Presentation to Laser Fusion Coordinating Committee, Livermore, Calif. (January 1973).
25. D. Giovanielli and E. L. Lindman, Patent Disclosure S-45, 308, Los Alamos Scientific Laboratory (February 1974).
26. S. A. Goldstein and J. Guillory, Phys. Rev. Lett. 35, 1160-1163 (1975).
27. J. M. Kindel and E. L. Lindman, Patent Disclosure S-46, 646, Los Alamos Scientific Laboratory (February 1976).
28. G. S. Fraley and R. J. Mason, Phys. Rev. Lett. 35, 520 (1975).

IV. LASER FUSION TARGET FABRICATION

Our pellet fabrication effort, supported by extensive theoretical investigations, supplies the thermonuclear fuel in packaged form suitable for laser-driven compressional heating experiments. These targets range from simple deuterated-tritiated plastic films to frozen DT pellets to complex DT gas-filled hollow microballoons, mounted on ultrathin supports and coated with various metals and/or plastics. Numerous quality-control and nondestructive testing techniques for characterizing the finished pellets are being developed.

INTRODUCTION

(R. J. Fries)

In our target fabrication effort, we are developing techniques and methods to fabricate spherical targets containing DT fuel in a variety of chemical and physical forms. High-pressure DT gas has been used extensively as the fuel because it can be conveniently packaged in glass or metal microballoons for use as laser fusion targets. However, the designers and experimentalists would prefer a higher density of DT fuel than can be obtained conveniently in gaseous form. In addition, significantly better yields are predicted if the fuel can be formed as a high-density shell surrounding either a vacuum or a low-pressure spherical core, because it is then unnecessary to work against the high pressure of the inner fuel core during the compression of the spherical fuel shell. These considerations have led to our development of methods to condense layers of cryogenic DT, either liquid or solid, onto the inside surfaces of microballoons. In addition, we are developing techniques to prepare room-temperature solids containing fuel atoms at high density (e.g., polyethylene, lithium hydride, and ammonia borane, in each of which the hydrogen has been replaced by an equiatomic mixture of deuterium and tritium) and to form these into microspheres and/or microballoons. The non-fuel atoms in these room-temperature solids (carbon, lithium, nitrogen, and boron) must also be

compressed and heated to fusion conditions along with the deuterium and the tritium, but because they do not participate in the fusion reaction, they act as diluents of the fuel. As a result, targets fueled with these room-temperature solids are not expected to perform as well as those with cryogenic DT fuel shells. However, the fuels that are solid at room temperature are considerably easier to work with both in target fabrication and in laser-target interaction experiments; they also enlarge the parameter space available for exploration in our interaction experiments.

Along with the development of techniques to fabricate the fuel pellets, we also are developing methods to apply a wide variety of coatings to the fuel pellet and to support the pellets for irradiation by the laser beam using thin plastic films or glass fibers so as to introduce a minimum of extraneous material into the system. Finally, we are continuously developing techniques to select, characterize, and measure the various pieces of the target both prior to and after assembly.

HIGH-PRESSURE DT GAS-FILLED TARGETS

(R. J. Fries)

General

We have continued the development of techniques and methods to fabricate hollow, multilayered spherical targets to be filled with high-pressure DT fuel gas. These generally consist of a high-Z, high-density metal pusher shell

overcoated with a low-Z, low-density absorber-ablator layer. This outer layer absorbs energy from the incident laser, heats, vaporizes, and streams away from the pusher shell causing the pusher shell to implode via the rocket reaction forces. The pusher shell can be deposited onto a nonremovable mandrel (e.g., a glass or metal microballoon), but improved performance might be obtained if the pusher shell is fabricated directly as a freestanding metal microballoon. In either case, high-strength pusher shells are desired so that a high DT pressure can be used, minimizing the additional compression required to attain a fusion burn.

Nonremovable Mandrels

Many of our current targets use bare glass microballoons as pusher shells, filled with high-pressure DT gas to serve as the fuel. Therefore, we continued our development of methods for quality selection and characterization of these bare glass microballoons. Many of these techniques should also be applicable to metal microballoon targets, and should be useful in selecting and characterizing microballoons for use as mandrels for structured, multilayered targets.

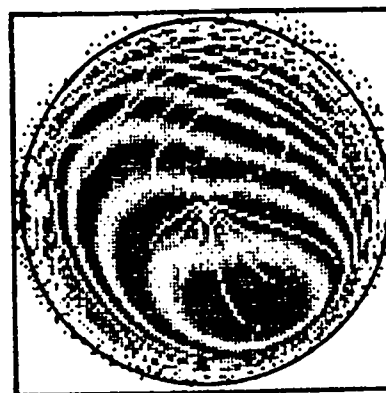
Measurement of Microballoons

Interferometry

(B. Newberger, S. Hall) -- We continued the development and evaluation of our computer code to calculate interferograms.¹ The current version will generate interferograms for up to six adjacent shells of different refractive indices, each interface being an ellipsoid of revolution having arbitrary orientation. All internally reflected rays, except those internally reflected at the outermost surface, are now included in the calculation. As one example of the usefulness of this program, we calculated an interferogram to agree with a rather asymmetric pattern observed for a glass microballoon (GMB) as shown in Fig. 62. The calculated interferogram is for a single-layer GMB whose inner and outer surfaces are ellipsoids of revolution having a common center with minor axes of 90 and 94 μm and major axes of 92 and 96 μm , respectively. The major axes of the two ellipsoids are separated by an angle of 70.5°, and



(a)



(b)

Fig. 62
Measured (a) and calculated (b) interferograms for an asymmetric glass microballoon.

the optical axis is at an angle of 45° to the plane containing the major axes.

Another illustration of the usefulness of this program is the calculation of interferograms to be expected when a layer of DT ice is frozen onto the inside surface of a GMB. This is described below under cryogenic targets.

Microradiography (D. Stupin, M. Winkler) -- Our assessment of the resolution capabilities of our geometric microradiography technique was continued. We are trying to fabricate a multiwire resolution test target from 0.25- μm -diam platinum/rhodium wire, but have been unsuccessful thus far because of the extreme fragility of this wire. The as-received wire is coated with silver, which must be dissolved with acid to uncover the platinum/rhodium core. Microradiographs were obtained of a single strand of this wire, but obvious thickness variations were apparent along its length, making interpretation very difficult.

We will next try to obtain corresponding scanning-electron micrographs and microradiographs to aid in this interpretation.

Pusher-Shell Deposition (D. F. Catlett)

General -- We have continued the development of methods to deposit uniform layers of high-Z metals onto various types of mandrels for use as pusher shells. Our primary objectives are high-strength coatings with useful deuterium-tritium permeability. As described previously, we have developed electroless and electroplating techniques for depositing a wide range of metals and alloys onto microsphere substrates.² In addition, we are developing chemical vapor deposition (CVD), physical vapor deposition (PVD), and sputtering to offer us the widest possible choice of metals and alloys for use in coating target microspheres. Emphasis during this reporting period was on CVD, on electro- and electroless-plating small batches of mandrels and high-strength alloys, and on sputtering.

Chemical Vapor Deposition

(W. McCreary) -- The CVD process involves the chemical or thermal reduction of a metal-containing compound at the surface of a substrate. The method has been useful for coating microsphere substrates in a gas-fluidized-bed coating apparatus, which mixes the substrates well and allows us to apply useful metal coatings to these otherwise difficult-to-handle structures.

Molybdenum from Molybdenum Carbonyl, Mo(CO)₆

(W. McCreary) -- Very strong tungsten/rhenium alloys have been deposited by CVD.³ This result has suggested that molybdenum/rhenium alloys might also form strong CVD coatings, but at a better strength-to-mass ratio because molybdenum has a density half that of tungsten (~10 vs ~20 g/cm³). Therefore, we have been developing techniques to deposit molybdenum and molybdenum/rhenium alloys by CVD techniques.

Initially, we tried to deposit molybdenum metal from molybdenum carbonyl, Mo(CO)₆. However, chemical analyses and x-ray diffraction measurements indicated that the coatings consist of dimolybdenum carbide (Mo₂C), regardless of experimental conditions.⁴ Because this Mo₂C could also be a useful coating material for laser target

applications, we have continued the Mo(CO)₆ work. Our previous CVD experience with Mo(CO)₆ has shown that frequently our coatings are either cracked because of residual stresses, or have rough surfaces because of gas-phase nucleation problems. Because the coatings of laser targets must be both stress-free and smooth, we have continued coater development and improved our control of process variables to allow good coatings to be obtained reproducibly. Primary emphasis was placed on measuring the fluid-bed temperature and temperature gradient and on evaluating the sensitivity of coating quality to operating parameters.

Three different coatiers were used, Pyrex I, Pyrex II, and graphite. Pyrex I is the coater used previously,⁵ which had a temperature gradient (ΔT) of ~200 K along the 6- to 7-cm length of the fluidized bed. Pyrex II is a new coater designed for smaller ΔT , measured to be ~125 K. Graphite was heated inductively (in contrast to the resistance-heated clamshell furnace used with the Pyrex coatiers) and had the smallest ΔT , namely ~15 K.

Six runs were made in Pyrex I at the same furnace temperature (625 K) and at flow conditions varying around values that previously resulted in good (i.e., smooth and stress-free) coatings at least some of the time.⁵ All runs produced stress-free coatings but the surfaces were no better than Class 2 (as defined previously⁵).

Four runs were made in Pyrex II at flow conditions chosen to give fluid-bed motion similar to that observed in Pyrex I and at a bed temperature of 575 K (equivalent to the average bed temperature existing at the 625 K furnace temperature used previously⁵). Significantly, all these runs yielded very good coatings at thicknesses of 6 μ m or less, one of which is illustrated in Fig. 63; the large speck in Fig. 63 (c) is 150 nm in diameter, the rounded bumps are ~50 nm, and the average surface smoothness is ~20 nm.

Temperature-control problems were experienced in all runs with graphite, and all these coatings had rough surfaces. However, we will continue our development of this coater to evaluate the effects on coating quality of a fluid bed with very small temperature gradient.

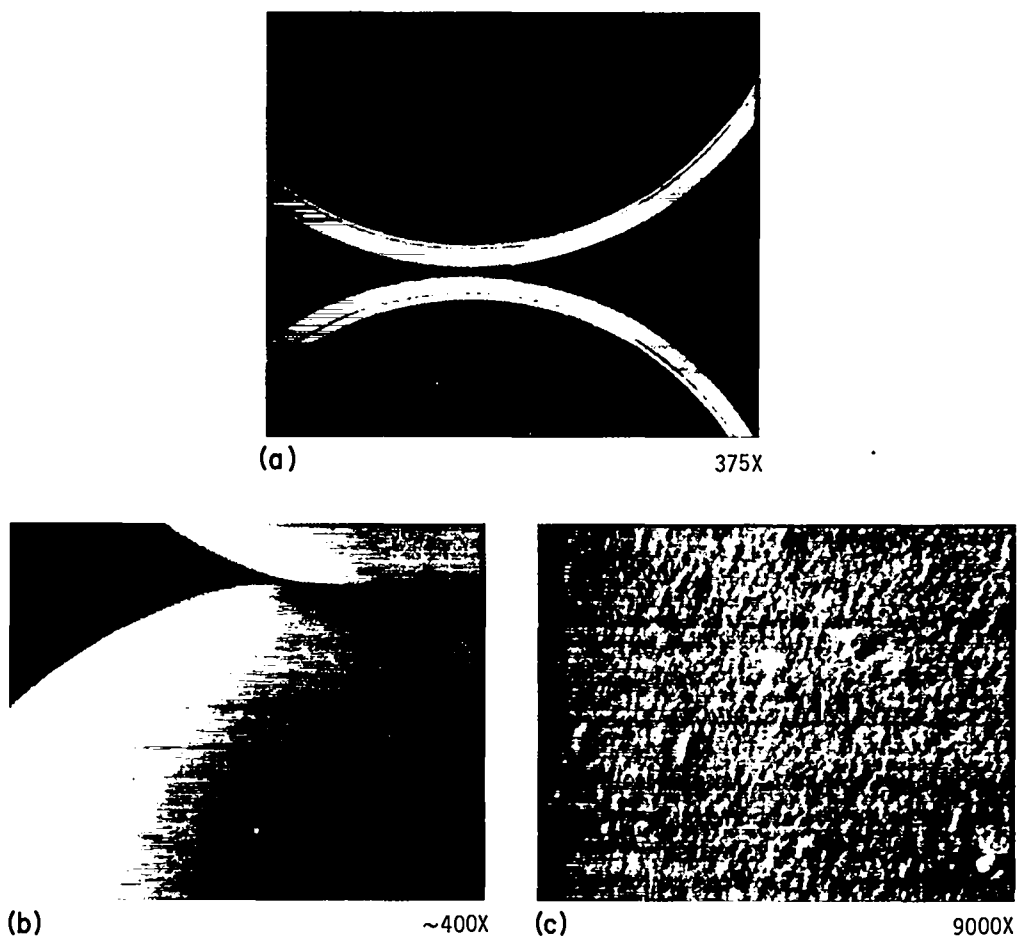


Fig. 63
Metallographic cross section (a), and scanning-electron micrographs (b) and (c), of high-quality Mo_2C coatings applied by CVD.

Molybdenum from Molybdenum Hexafluoride MoF_6
(W. McCreary, D. Carroll) We are evaluating CVD molybdenum from the hydrogen reduction of MoF_6 to obtain coatings of molybdenum metal rather than the Mo_2C obtained from the carbonyl as discussed.

We continued our development of the new coater described previously;⁶ fourteen coating runs were made, exploring the effects of operating parameters and coater modifications on coating quality. As illustrated in Fig. 64, we do get very good molybdenum coatings in some runs, but reproducibility is still poor.

Tungsten from Tungsten Hexafluoride, WF_6
(W. McCreary, D. Carroll) -- Seven coating runs were made by using hydrogen reduction of WF_6 in the apparatus discussed above to coat Solacel substrates with tungsten. The tungsten deposition

process is much more reproducible than that for molybdenum, and good to excellent coatings were obtained in six of the seven runs. An example of one of the excellent tungsten coatings is shown in Fig. 65.

Electro- and Electroless Plating

(A. Mayer, P. Kieffer)

Our efforts to develop techniques to electroplate or electroless-plate small batches of glass or metal mandrels (i.e., 50 to 100 microsphere mandrels per run) were continued. We attempted to electroplate gold onto ~50 high-quality beryllium/copper microspheres mixed with a larger volume of different size microspheres (referred to as the carrier) in our pulse plater described previously.² The gold coatings were



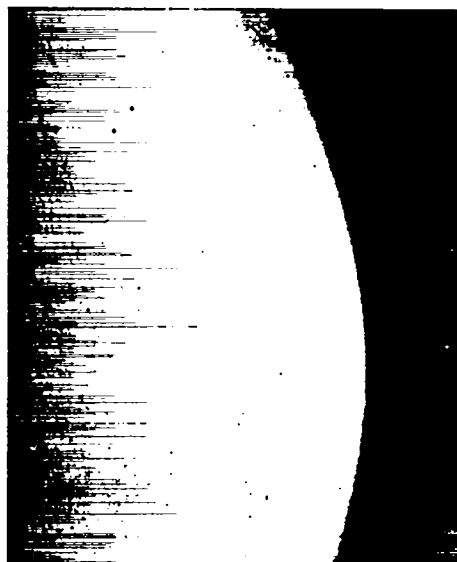
(a)

75X



(b)

60X



(c)

225X

Fig. 64

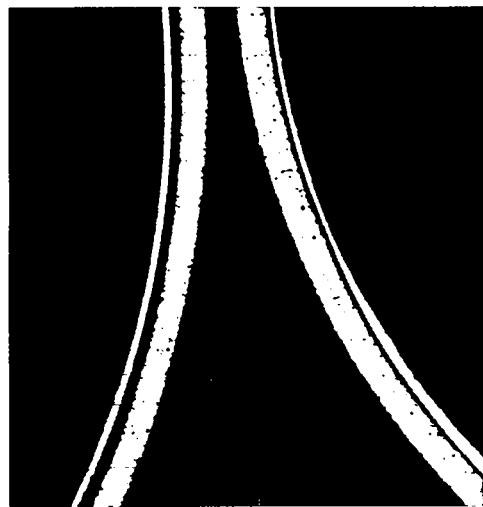
Metallographic cross section (a), and scanning-electron micrographs (b) and (c), of high-quality molybdenum coatings applied by CVD.

rough and of nonuniform thickness, both features presumably a result of inadequate random motion of the particles during plating; other sizes and types of carriers will be evaluated next.

We continued our effort to electroless nickel plate onto batches of 50 to 100 preselected glass microballoons that are first metallized either by CVD or by PVD.⁶ Poor-quality coatings and poor recovery rates continue to be a problem. A modified apparatus is being fabricated to solve these problems; in addition, we will investigate the relationship between the conditions employed in

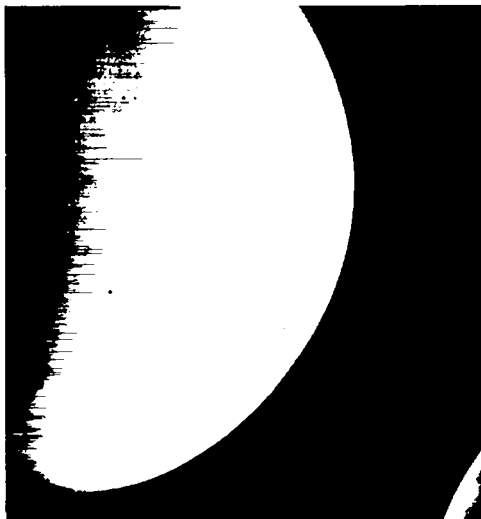
the precoating process and the quality obtained in the electroless plating step.

We made a series of initial electroplating runs to evaluate the properties of nickel/iron alloy coatings deposited from a commercial plating bath (NIRON from Udylyte Corp.). The deposit composition was 65Ni-33Fe-1.3Cu plus several trace elements (< 1000 ppm). Mechanical properties of our deposit are summarized in Table XV; the hardness was 550 DPH.



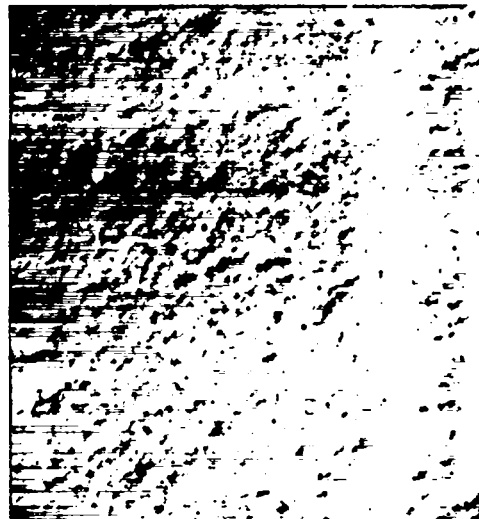
(a)

375X



(b)

~250X



(c)

9000X

Fig. 55

Metallographic cross sections (a), and scanning-electron micrographs (b) and (c), of high-quality tungsten coatings applied by CVD.

The high strength of this alloy makes it a very interesting pusher material for high-pressure gas-filled laser fusion targets. We are now conducting experiments to determine whether the strength of this nickel/iron alloy is significantly decreased by diffusing hydrogen into the alloy to the level that would be in equilibrium with the high-pressure fuel gas. In addition spherical pressure vessels are being electroformed from the alloy and pressure/rupture tests will also be run. If the alloy still seems promising after these

tests, we will develop techniques to electroplate high-quality coatings of the alloy onto microballoon substrates.

Sputtering

(A. Lowe)

Our development of a sputtering technique to coat microspheres with a uniform layer of metals and/or oxides was continued, further exploring the use of combined electromechanical and plasma agitation of the microsphere substrates. We estab-

TABLE XV

MECHANICAL PROPERTIES OF ELECTROPLATED NICKEL/IRON ALLOY^a

Sample No.	Tensile Strength		Yield Strength ^(b)		Elongation For Various Gage Lengths (%)			Poisson's Ratio	Young's Modulus ^(c)	
	MPa	(kpsi)	MPa	(kpsi)	6.7 mm	12.7 mm	25.4 mm		GPa	Mpsi
1	1830	265	1330	194	—	5	4	0.281	157	22.8
2	1740	253	1290	187	4	2	2	0.263	157	22.8
3	—	—	—	—	—	—	—	0.246	155	22.5

^a Rectangular specimen cross section, 0.5 by 9.5 mm.

^b Based on 0.2% offset from the modulus.

^c Based on the best straight line near the origin of a curve traced from stress values and from the average of two opposite strain gages.

lished that the tendency of the coated microspheres to stick to the support plate after extended coating times occurs because of increased temperature of the microsphere/support-plate system rather than because of increased coating thickness per se. Thus, the problem can be avoided by interrupting extended coating runs to allow the system to cool. In addition, we have obtained, and are installing, a second sputtering unit that should minimize substrate heating.

To date, we have coated titanium, gold, aluminum, or nickel onto microsphere substrates including glass microballoons, Solacels, beryllium/copper microspheres, and steel microspheres. Good adherence was obtained in all cases, but coating thicknesses varied by a factor of two, at best. We have obtained a new electromechanical vibrator whose vibration frequency and waveform are adjustable; in addition, we have modified the coater to provide an improved view of the bouncing microspheres. With these improvements, we soon expect to determine system operating parameters that will result in uniform coatings.

Strength and Permeability of Pusher Shells

(H. Maltrud, E. Redemann)

Preliminary measurements were made of the strength and hydrogen permeability of some Solacels coated with ~ 10 μm of dimolybdenum carbide (Mo₂C) by CVD from Mo(CO)₆. Our measurements indicate a hydrogen permeability at 675 K-- only 4% that

reported for molybdenum metal. Microballoons having an aspect ratio (radius/wall thickness) of ~ 8 could not be burst by filling to 685 atm; therefore, the tensile strength of these shells is in excess of 276 MPa (40 kpsi). These measurements will be continued and extended to other coating materials.

Lead Cone Targets

(E. Farnum, B. Cranfill, J. Feuerherd)

We have developed techniques to fabricate the lead-cone targets recently described by Mason⁷ and illustrated in Fig. 66. A rod of Pb-5Sn alloy was machined into cylinders and the conical hole was formed by pressing a highly polished tool steel point into one end of the cylinder. A small rim, formed by this method around the edge of the hole, was not deemed objectionable. Microscopic inspection verified that the surface finish and tip radius of the steel point were accurately replicated in the lead. The radius at the apex of the cone was estimated from the area of uniform focus to be less than 5 μm.

A polyvinyl alcohol (PVA) film was chosen to cover the mouth of the cone because literature data indicated PVA to have one of the lowest hydrogen permeation rates of any of the plastic film formers.⁸ Several methods of providing this target with a gas-fill tube were proposed and judged likely to succeed. However, consideration of gas permeation rates through the 3-μm-thick plastic films used to cover the mouths of the cones

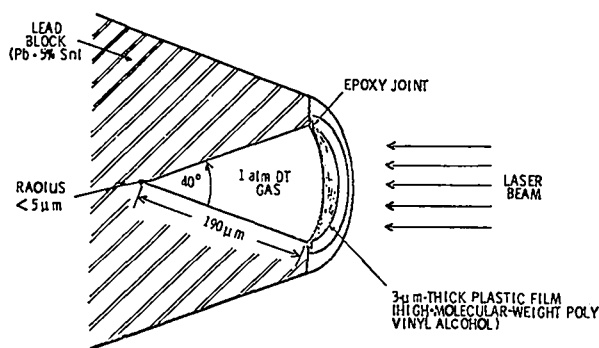


Fig. 66
Schematic of lead-cone target.

suggested that the cones could be both emptied of the assembly-environment gas and filled with the desired DT fuel gas by permeation through the plastic film (especially if the target were assembled in a helium-filled glovebag rather than in air). The PVA films are glued to the lead with epoxy.

Initial targets were covered with films made from a medium-molecular-weight PVA. These targets were then filled with fuel by soaking in 1.2 atm of DT gas for 7.2 h at 325 K. The tritium loss rate of these targets was measured by using our optical photon-counting technique discussed below. After subtracting a nearly constant background activity (believed to be tritium contamination of the plastic and/or lead used in the target) the loss rate of the tritium gas was found to have a half-life of ~ 5 h. Since then we have obtained some high-molecular-weight PVA that is reported to have a lower hydrogen permeation rate,⁹ have learned to make films from it, and are currently measuring its helium and hydrogen permeation rates prior to using it in laser targets. In addition, we are improving the surface finish and are trying to put a sharper point on our steel indenter by hand-polishing with a 1-μm diamond lap.

NONDESTRUCTIVE FUEL GAS ANALYSIS

(V. Cottles, M. Mueller)

We continued our development of the optical photon-counting technique for nondestructive assay of the tritium content of glass-microballoon

targets. Application of this technique to targets over a wide range of diameters and gas-fill pressures requires that we know the fraction of emitted beta energy absorbed by the gas and by the glass microballoon (GMB) wall as a function of target parameters. (The number of photons emitted should be proportional to the beta energy absorbed by the gas or the glass.) We modified and extended an existing computer code¹⁰ to calculate fractional beta absorption in the gas as a function of the product of gas density and target diameter. These calculations indicated that photon production in the gas should vary as $\sim \rho R^{4.3}$, whereas that in the GMB wall should vary as $\sim \rho R^{2.6}$. (In addition, a new code was written to calculate beta absorption as a function of depth in the GMB wall, but only preliminary results are yet available.)

We have measured the total photon production, at wavelengths from 200 to 600 nm, for several sets of commercial GMBs (3M Type B18A) covering a range of diameters and gas densities as shown in Fig. 67. (All these count-rate data are normalized to 100% tritium.) The photon output can be represented as

$$N = 3.2 \times 10^4 \rho^{0.8} R^{2.8},$$

where N is the photon count rate (normalized to 100% tritium), ρ is the gas density in amagats, and R is the GMB radius in micrometers.

The R -dependence of these data indicates that most of the photons from this set of GMBs are generated in the glass wall, a process that will depend on the efficiency of the particular glass-wall material as a scintillator. We previously measured the photon production rate for a series of 3M Type-B40A GMBs,⁵ for which the count rate was proportional to $R^{3.7}$, indicating that the wall material of these B40A GMBs is a less efficient scintillator than that of the B18As. Thus, in the B40As, a larger fraction of the photons originates in the gas phase.

We recently measured the spectrum of the photons generated in Type B18A-GMBs, covering wavelengths from 190 to 690 nm. The raw data are shown in Fig. 68, and the net data, after unfolding spectrometer and detector responses, are presented in Fig. 69. The unfolded spectrum exhibits a peak at ~ 350 nm and a broad hump at ~ 480 nm, which we

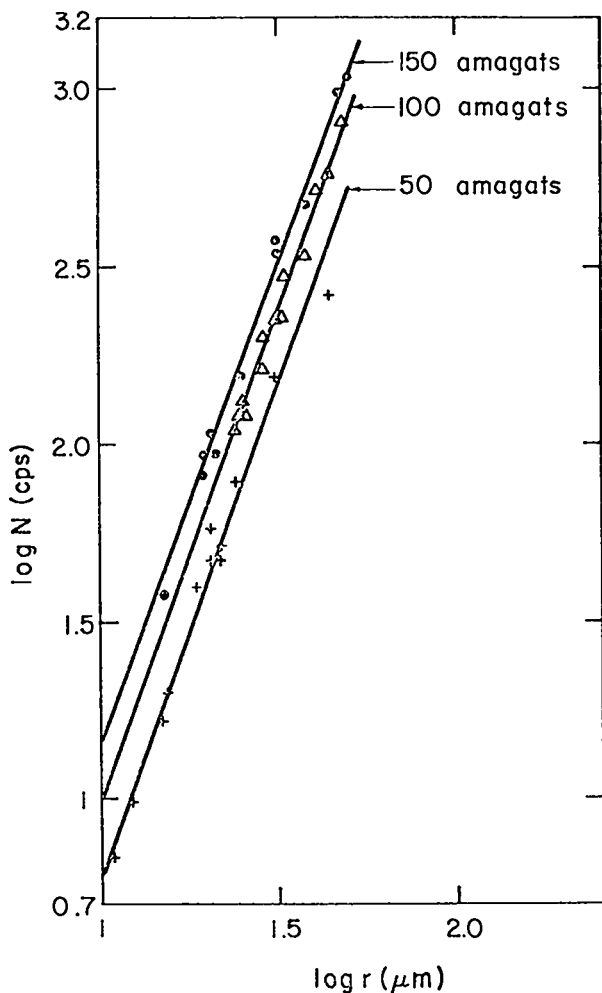


Fig. 67

Photon count-rate data for DT- and T_2 -filled glass microballons.

attribute to scintillation of the glass wall of the microballoon. In addition, at our 200-nm short-wavelength cutoff, the count rate is rising with decreasing wavelength, probably either due to fluorescence in the glass excited by the Lyman alpha radiation of the hydrogen gas or due to beta interaction with the nitrogen in the air outside the GMB.

PLASTIC FILM FABRICATION

(B. Cranfill)

We have continued our development of techniques for producing thin films of normal or

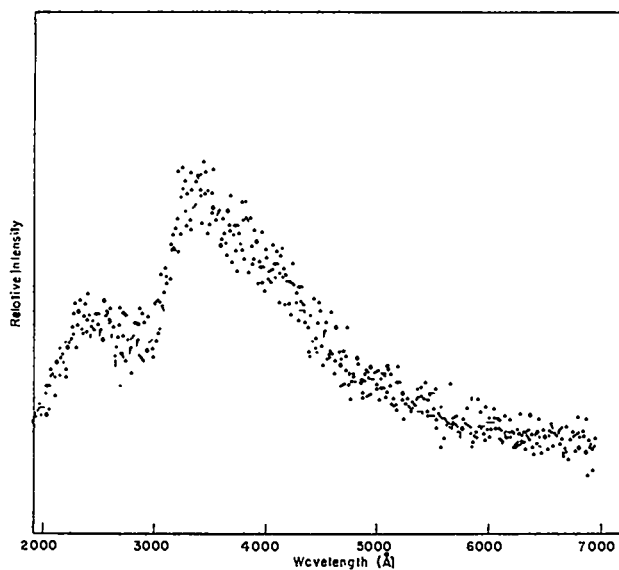


Fig. 68

Photon spectrum from T_2 -filled glass microballons (as measured).

deuterated polyethylene. We extended the usefulness of our technique (described previously^{1,5}) of dipping glass microscope slides in

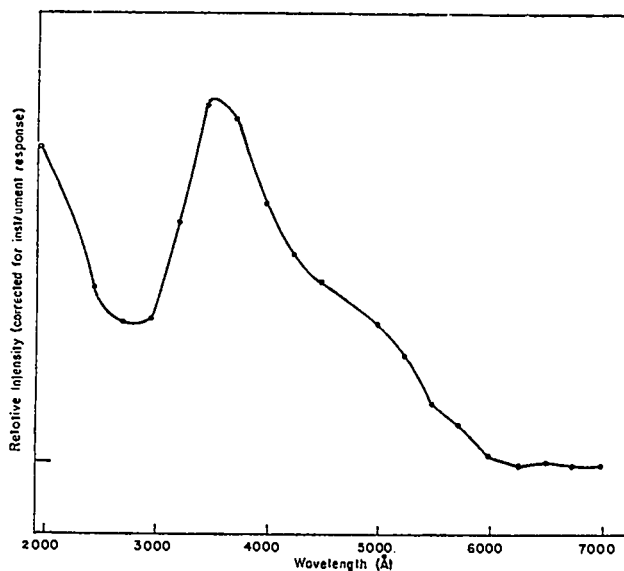


Fig. 69

Photon spectrum from T_2 -filled glass microballoon after correcting for² spectrometer and detector responses.

hot polyethylene solutions to obtain a thin coating of solution on the slide, after which the solvent is allowed to evaporate leaving behind a plastic film coating that can be removed from the slide by floatation onto a water surface. We tried xylene as the solvent because it has a higher boiling point than the toluene used previously. This allows the use of higher solution temperatures, which, in turn, allows more concentrated polyethylene solutions to be prepared and, consequently, thicker films to be obtained. Thus, 8 wt% solutions of polyethylene in xylene at 405 K produce 2- μm -thick polyethylene films. A summary of our data is presented in Fig. 70.

Note that the type of polyethylene markedly affects the results obtained. The technique was developed by using Dow Microthene FN510, which is a low-density, low-molecular-weight polyethylene. We have also used this method successfully to prepare deuterated polyethylene films from a low-density, low-molecular-weight deuterated polyethylene (CD_2). Using toluene solutions at 405 K, the CD_2 films were ~12% thinner than the Microthene FN510 normal polyethylene films obtained under the same conditions, enumerated in Fig. 70. However, attempts to use this technique with high-density, high-molecular-weight deuterated polyethylene were unsuccessful because of its considerably lower solubility.

We also developed a rapid, convenient technique of making thicker polyethylene films by

pouring hot polyethylene solution into a mold prepared by laying wire around the edge of a glass slide. As an example, 50- μm -thick deuterated polyethylene films were prepared by filling a mold made from 500- μm -diam wire with a 10% polyethylene solution. The solution is either allowed to overflow the edges of the mold or else is leveled by scraping a straight edge along the top of the wire. Evaporation of the solvent leaves behind a polyethylene film of appropriate thickness; however, if the solution is cooled too rapidly, a white powdery film is formed. This technique is suitable for both high-density and low-density polyethylene.

CRYOGENIC TARGETS

(R. J. Fries)

Introduction

Laser fusion targets fueled with cryogenic liquid or solid DT offer the advantage of high initial fuel density without the disadvantage of diluent atoms that are present in room-temperature solids having a high hydrogen density [such as, lithium in Li(D,T) or carbon in $(-\text{CDT})_n$]. Calculations indicate that the yields from targets fueled with liquid- or solid-density DT can be considerably higher than those from targets of the same design, but fueled with high-pressure DT gas. As a result, we are actively pursuing the development of cryogenic targets despite the significant experimental complications encountered in the fabrication of such targets and in their use in laser target interaction experiments.

Spherical Geometries

The cryogenic target receiving highest emphasis is a uniform, hollow shell of solid or liquid DT condensed onto the inside surface of a glass or metal microballoon container that serves as the pusher shell. We are concentrating our efforts on glass microballoons, simultaneously developing techniques (a) to condense the DT into a uniformly thick layer on the inside surface of the glass and (b) to measure the thickness uniformity of the DT shell. Two general approaches are being examined. In one case, we deliberately impose a

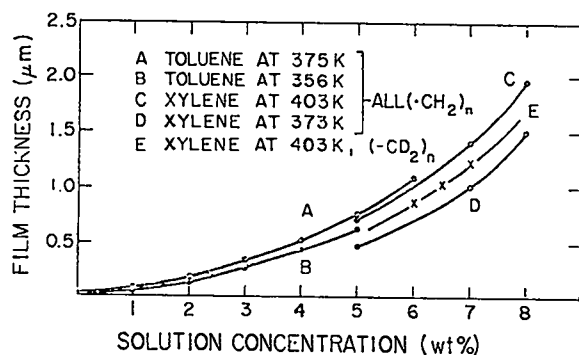


Fig. 70
Film thicknesses of normal and deuterated polyethylene deposited onto glass slides from solutions of various concentration.

temperature gradient by blowing a jet of cold helium onto the top of the target in an attempt to counteract the effect of gravitational forces; in the other, we surround the target with an isothermal environment and try to freeze the DT uniformly onto the surface. Most of our effort during this quarter was devoted to the latter technique.

Fast Isothermal Freezing (FIF) Techniques

(J. Miller)

We continued our development of the FIF technique (described in detail in the last report⁵) in which we rapidly condense and freeze the DT fuel gas in a glass microballoon (GMB) to form a uniformly thick layer of solid DT on the inside surface of the GMB. We first vaporize the DT by shining a focused helium-neon laser beam onto a GMB supported by a thin glass stalk in a ~ 4 K copper cell filled with low-pressure helium gas that serves as a heat-exchange fluid. When we shutter the laser beam, the helium gas rapidly cools the GMB, the DT condenses and freezes into a uniformly thick layer of solid DT.

As reported previously,⁵ we obtain solid DT layers of highest uniformity by using the most rapid condensation and freezing rates, at the highest exchange gas pressure. The upper limit of the heat-exchange gas pressure is established by the power available in the heating laser; if the pressure is too high we cannot completely vaporize the DT fuel. We previously used a 2-mW heating laser which allowed heat-exchange gas pressures up to ~ 7.3 Pa (55 mtorr). Recently, we used a more powerful heating laser (50 mW) and measured freezing time as a function of gas pressure up to 60 Pa (450 mtorr), as illustrated in Fig. 71. As the gas pressure is increased, the freezing time first decreases and then becomes constant at ~ 0.2 s for pressures of 21 Pa (160 mtorr) and above. This behavior follows directly from the pressure-dependence of the thermal conductivity of gaseous helium.

Our computer code to calculate interferograms was modified to accommodate shells with multiple layers of differing refractive indices. Although the layer thickness of the solid DT fuel is comparable to the wall thickness of the glass

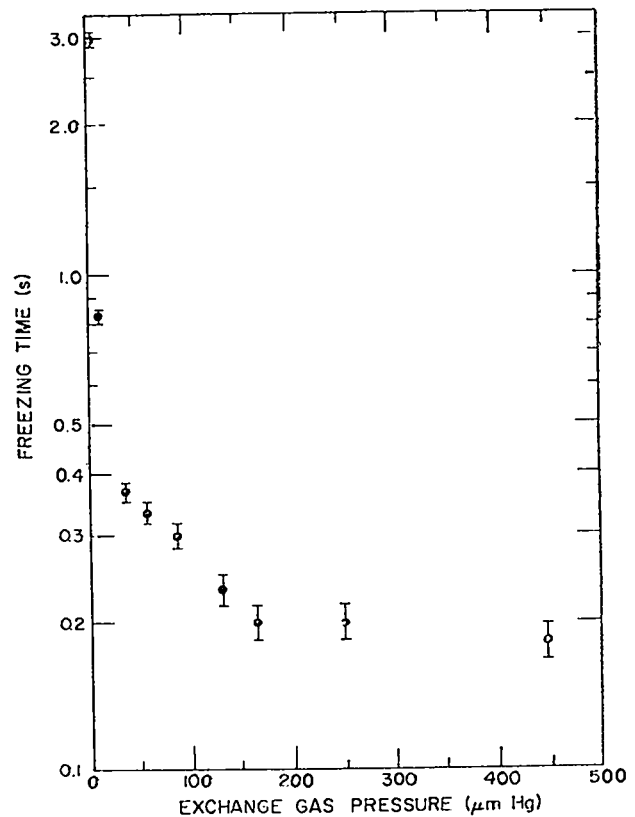


Fig. 71

Freezing rates observed for our fast isothermal freezing (FIF) technique at various heat-exchange gas pressures.

microballoon, the refractive indices differ substantially ($n \approx 1.17$ for solid DT and $n \approx 1.5$ for glass). However, the computer-generated interferograms show a high sensitivity to the geometry of the DT shell, as shown in Fig. 72. The calculations are for a ~ 100 - μm -diam GMB (0.65 - μm wall), filled with 10 ng of fuel (average DT solid layer thickness, ~ 1.3 μm). Here, the glass microballoon was assumed perfect and the inner surface of the solid DT layer was assumed spherical. The center of the DT layer is shifted by various distances to the right from the microballoon's center, and the DT-layer thickness uniformity is characterized by a parameter Q , defined as the ratio of minimum DT-layer thickness to average DT-layer thickness.

The most noticeable change in the interferograms in Fig. 72 occurs in the positions

of the central interference fringes. With $Q = 0.92$, the central fringe is displayed from the

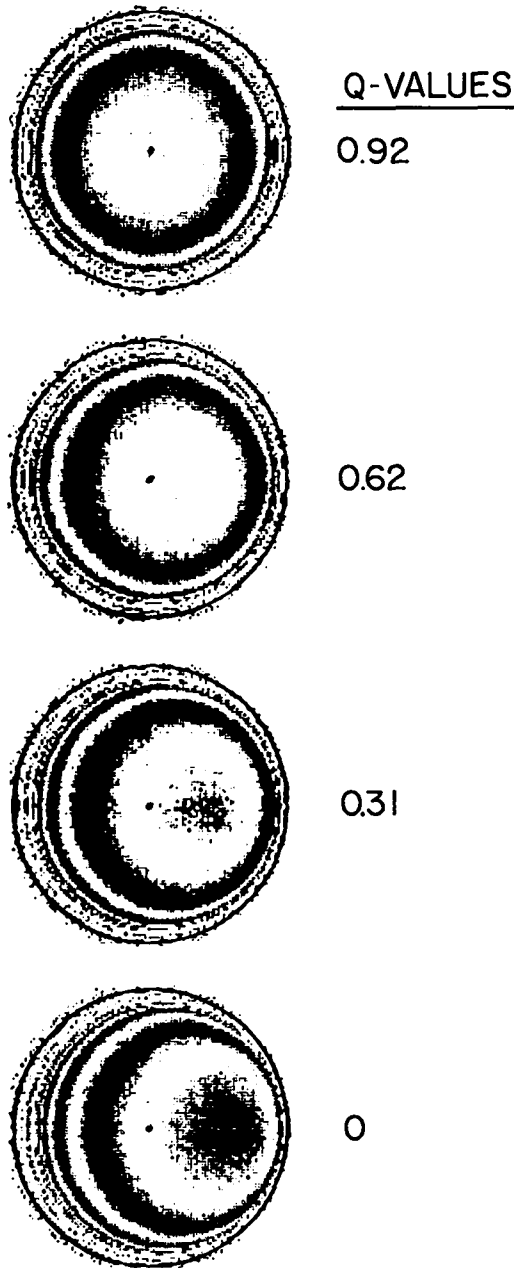


Fig. 72

Computer-generated interferograms for a series of solid DT shells frozen onto the inside surface of a perfect glass microballoon. The quality index, Q , is defined as the minimum DT-layer thickness divided by the average DT-layer thickness.

microballoon center by $\sim 1/40$ th of the microballoon diameter. A DT layer that has a zero thickness at one point ($Q = 0$) produces a displacement of the central fringe by a quarter of the microballoon diameter. The displacement of the central interference fringe from the GMB center is plotted against Q in Fig. 73.

By comparing experimental interferograms (obtained with a wedge interferometer) of a cryogenic target produced by the FIF technique with the results shown in Fig. 73, the DT layer's uniformity can be quantitatively determined. The sequence of photographs in Fig. 74 shows interferograms of a freezing target taken at intervals of 0.033 s. In the first photograph with the DT fuel still gaseous, the quality of the GMB is measured. As the FIF freezing process proceeds, the number of fringes increases as the DT is condensed and frozen onto the inner surface of the microballoon. In the last photograph, the DT is a solid layer with a uniformity of at least $Q = 0.9$ in the plane perpendicular to the viewing axis. Solid DT layers of this uniformity are reproducibly and consistently made by using the fast isothermal freezing technique.

Work in progress includes obtaining interferograms of frozen targets along a second direction. A new heating laser, operating at $3.39 \mu\text{m}$, will be tried in an attempt to improve energy coupling to the target. We are also in the process of building a prototype FIF apparatus suitable for

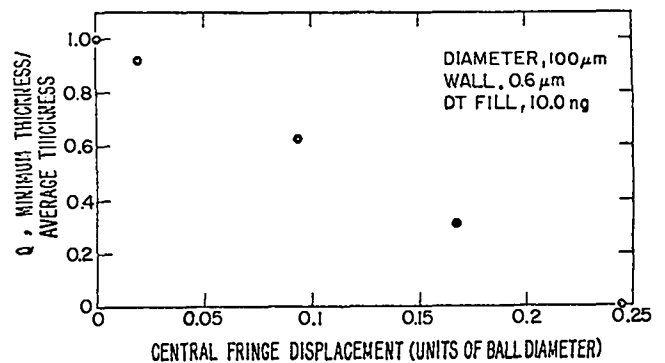


Fig. 73

Central interference fringe shift versus quality index, Q , for a series of solid DT layers frozen onto the inside surface of a perfect glass microballoon.

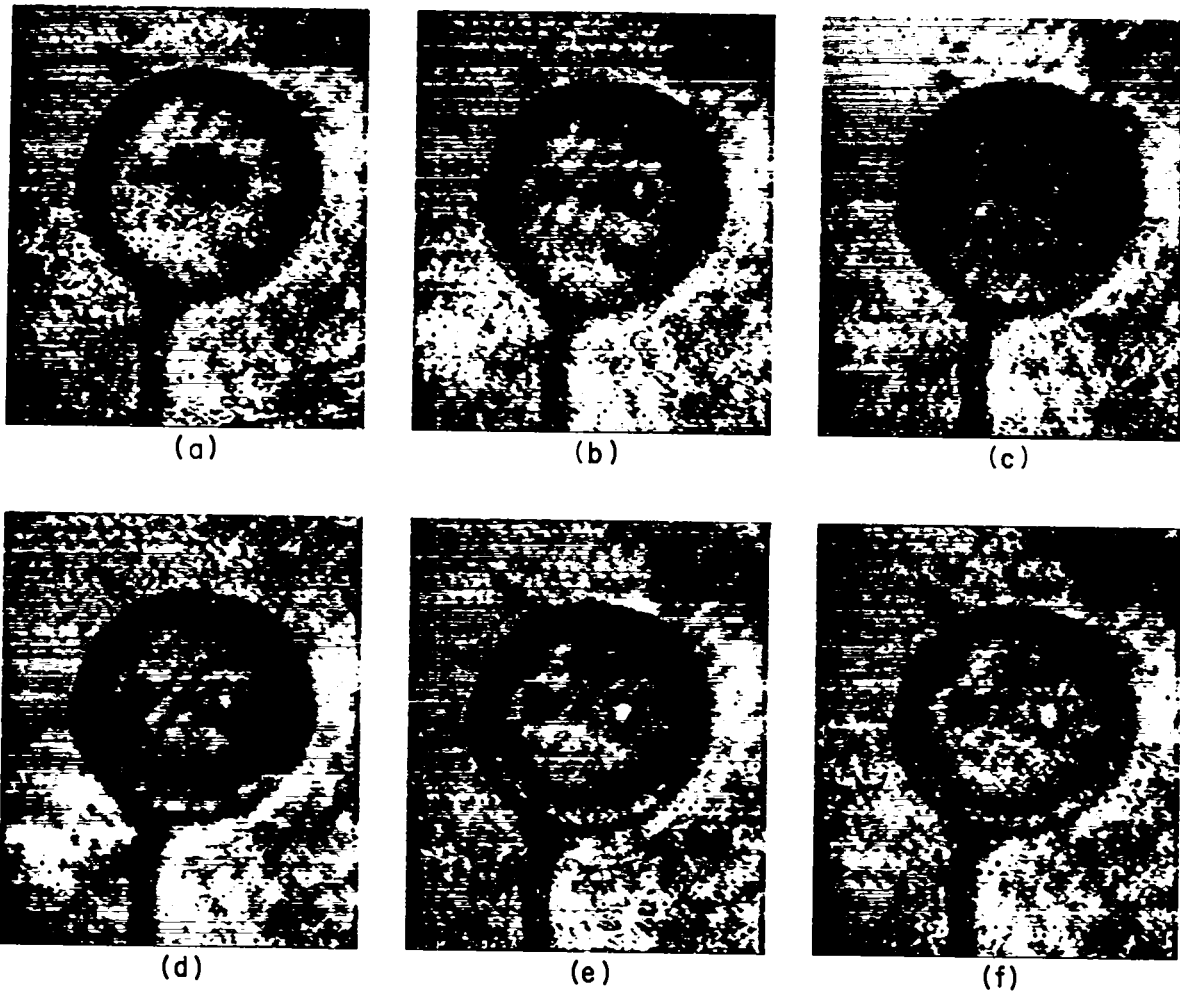


Fig. 74

Experimental interferograms for a freezing target obtained at 33 ms intervals: (a) DT is all gas; (b) through (e) shows the developing DT shell; (f) all of the DT is frozen into the shell with a uniformity of at least $Q = 0.9$.

the target chamber of the Two-Beam System. Considerable cryogenic engineering is required for this project because the frozen target must be accurately located and the freezing cell must be rapidly withdrawn prior to the laser shot.

REFERENCES

1. E. Stark and F. Skoberne, Los Alamos Scientific Laboratory report LA-6510-PR (November 1976) pp. 94-95.
2. E. Stark and F. Skoberne, Los Alamos Scientific Laboratory report LA-6245-PR (July 1976) pp. 80-82.
3. W. R. Holman and F. J. Huegel, Proc. 2nd Conf. on Chemical Vapor Deposition, Electrochemical Society, Los Angeles, California (1970) p. 171.
4. op. cit. Ref. 1, pp. 96-97.
5. E. Stark and F. Skoberne, Los Alamos Scientific Laboratory report LA-6616-PR (May 1977) Sec. IV.
6. op. cit. Ref. 1, p. 97.
7. R. J. Mason, D. V. Brockway, and E. L. Lindman, Bull Am Phys. Soc. 21, 1153 (1976).
8. Guide to Plastics - Properties and Specification Charts, by the Editors of Modern Plastics Encyclopedia (McGraw Hill Book Co., 1975).
9. R. Nolan, KMS Fusion, Ann Arbor, Michigan, private communication (December 1976).
10. M. M. Mueller, Bull. Am. Phys. Soc. 20, 1257 (1975).

V. TARGET DIAGNOSTICS

The tiny volume and brief duration involved in the laser-fusion process create needs for new diagnostic techniques having spatial and temporal resolutions in the submicrometer and 1- to 100-ps regime, respectively. These needs are being met with a vigorous program of diagnostics in such areas as laser calorimetry, charged particle and neutron detection, x-ray spectrometry, and subnanosecond streak-camera development.

INTRODUCTION

The short duration and minute spatial extent of laser fusion experiments impose demands on instrumentation that cannot, in general, be satisfied by existing devices. Therefore, our diagnostics development program concentrates on advancing the state of the art in high-speed, high-resolution instrumentation. The development of time-resolved imaging systems in the visible and x-ray spectrum is of special interest.

Because of recent theoretical and experimental results, measuring the density gradient near the critical surface of a plasma has become an important task for determining wavelength-scaling effects.

We have developed a multiwavelength, picosecond-resolution interferometer for diagnosing density profiles and the motion of plasmas generated by short-pulse CO₂ lasers. Operation of this device will require the synchronization of a visible or near-infrared laser pulse with the CO₂ pulse. A resolution of 2 μm has been demonstrated for the interferometer.

Because sensitive, rapid-viewing image systems with a large dynamic range for 10.6-μm light are still in development, we have built an optical alignment and focusing system for the Two-Beam CO₂ System.

X-ray microscopes have been designed, fabricated (by micromachining and replication), and tested. The first devices have a resolution of ~25 μm with a collection efficiency more than 1000 times that of an equivalent pinhole camera.

An ellipsoidal reflector has been designed, built, and calibrated to collect scattered CO₂ laser light from a target. Backscattered laser-pulse energy can be measured and the total absorbed laser energy can be deduced simultaneously. Either time- or space-resolved scattered-light measurements can also be made, for either the incident wavelength or its harmonics.

MULTIWAVE PICOSECOND INTERFEROMETRY OF CO₂ LASER-PRODUCED PLASMAS

(R. L. Carman, A. G. Engelhardt, N. Clabo)

General

We are engaged in experiments to determine interferometrically the evolution of density gradients and profile modifications in CO₂-laser-produced plasmas. A temporal resolution better than 5 ps and a spatial resolution of ~1.0 μm appear necessary based on previous work¹ at LASL and elsewhere. We have demonstrated technical feasibility of subpicosecond, high-spatial-resolution laser interferometry, and have developed a very stable CO₂ laser oscillator. We have thus reached the final design stages of the hardware that critically affects reproducibility of performance. Adequate time-synchronization of the Nd:glass laser with the CO₂ laser remains to be demonstrated.

Interferometer

Beginning with the double-grating interferometer^{1,2} (DGI), we established the possibility of spatial resolution of >316 line pairs/mm corresponding to 1.6-μm resolution when

illuminated by a helium:neon laser (Fig. 75). Because the glass-laser source to be used has a pulse bandwidth of 200 cm^{-1} , we studied the broadband source response. It must be remembered that the spectral bandpass of the DGI for a given fringe contrast is determined by the number of grooves per mm of the gratings; too few grooves degrade the contrast and the clarity of background fringes.

By reducing the source bandwidth to 500 cm^{-1} , we obtained clear diffracted first-order stalk images, and at 250 cm^{-1} clearly defined fringes in both the zeroth and first-order images (Fig. 75). We find that a bandwidth of 200 cm^{-1} is consistent with pulses as short as 0.88 ps; also, we have already successfully compressed³ our Nd:glass laser pulses to 0.3 ps. We therefore conclude that subpicosecond interferometry with a spatial resolution of $\sim 2 \mu\text{m}$ is feasible with the DGI.

Laser System

Recently we operated successfully the duplicate of a Nd: glass laser built elsewhere.^{1,4} Its modelocked pulse train of $\sim 100 \text{ ps}$ had a total energy of $\sim 0.35 \text{ J}$ and consisted of 5-ps pulses with energies of 3 to 5 mJ. The spectral bandwidth was 200 cm^{-1} and the divergence $170 \mu\text{rad}$.

By utilizing a 2.0-mm-thick phase-matched KDP crystal, we achieved a 24% conversion efficiency to $0.53 \mu\text{m}$. We used a second phase-matched, 25-mm-long KDP mixing crystal to convert 20% of this $0.53\text{-}\mu\text{m}$ radiation to $0.35\text{-}\mu\text{m}$ near-uv radiation. This result represents an overall efficiency of $\sim 5\%$. Recent work at NRL clearly indicates that much shorter crystals would greatly increase our efficiencies. However, at present, we have enough light for illumination of the DGI for both green ($0.53 \mu\text{m}$) and uv light ($0.35 \mu\text{m}$).

We are designing more stable mirror mounts and lens holders, a flowing-dye cell, and an enclosure that will minimize dust and exposure of the modelocking dye to room light. Also, because rod cooling limits the repetition rate to 12 pulses/h, we are modifying the rod-cooling technique for better and quicker removal of Δn , where n is the index of refraction.

We constructed a pulsed CO_2 oscillator utilizing an old concept⁵ for the design of a stable CO_2 laser cavity. The cavity contains a LASL-designed, high-pressure TEA laser and a low-pressure smoothing tube. It produces amplitude-smoothed pulses of 30-to 150-ns duration and $\sim 500 \text{ mJ}$ in energy. Operating the 1-m smoothing tube continuously with a current of 10 mA

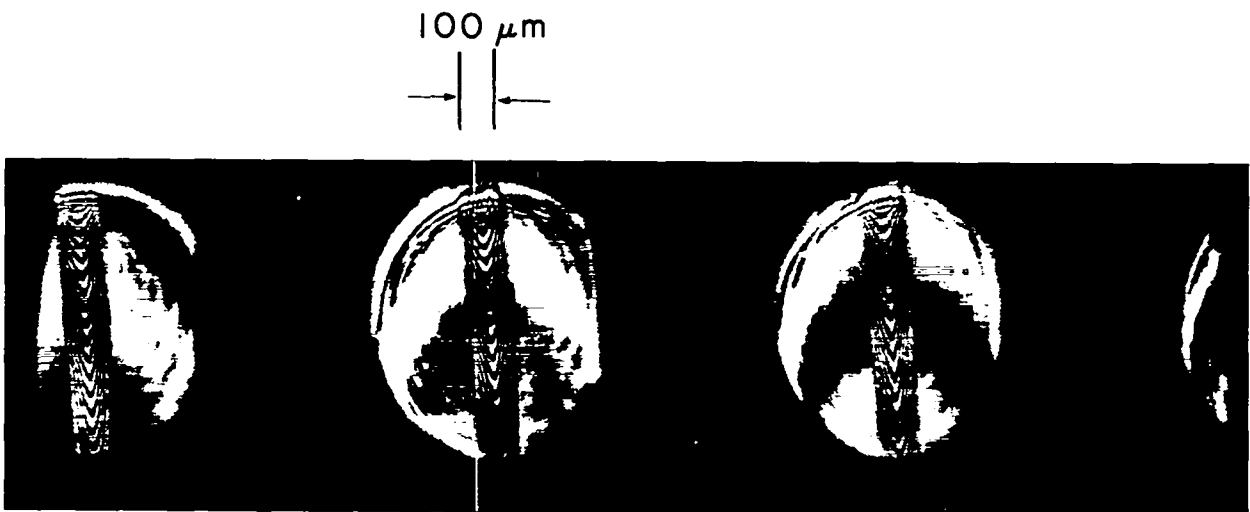


Fig. 75
Interferogram of a $100\text{-}\mu\text{m}$ -diameter glass stalk taken with the DGI illuminated by He-Ne laser light.

leads to a very stable output of 4- to 6-W multimode, and to 0.5 W in the TEM₀₀ mode. We measured the stability with a chart-recorder calorimeter and a pyroelectric detector and found it to be constant for more than 6 h. No drifts were observed in the alignment over several weeks. We conclude, therefore, that this oscillator when combined with a well-designed pulse clipper, should provide a very stable and reproducible source of subnanosecond pulses.

In summary, we feel that we have all the technology well in hand to demonstrate the feasibility of multiwave picosecond interferometry for plasma diagnostics, and to apply these techniques to large-scale laser fusion experiments in using the Two-Beam System.

TARGET ALIGNMENT SYSTEM FOR CO₂ LASER SYSTEMS

(D. R. Kohler)

An optical system was used to locate the center of a spherical surrogate target and to place a target within 2 μm of that location. The surrogate is the ball that is used in the mask test to align the beams of the Two-Beam System onto the target position.⁶ The targets must be mounted on an indexing target wheel so that they are brought to the same location as the center of the ball.

In this scheme, the center of the ball is found optically by the use of a sensitive autocollimation technique. The same optical system is then used as an imaging system to adjust the targets to come to the same location as the center of the ball.

X-RAY MICROSCOPE DEVELOPMENT

(G. H. McCall)

The optical element for the x-ray microscope described in the last progress report² was fabricated at the Union Carbide Y-12 plant by diamond-point machining and replication. No special care was taken to obtain a surface better than that routinely produced, because this first element was intended as a baseline for design-code and fabrication testing. Figure 76 shows an x-ray image of two 6-μm-diam holes with center-to-center spacing of 100 μm punched in a copper foil, which



Fig. 76
X-ray image of two 6-μm holes 100 μm apart.

was illuminated from behind by an aluminum-anode Henke tube. The resolution obtained was ~ 25 μm.

The configuration of this test pattern was chosen because it was a simple matter to modify the design code, XMIC, for calculating the image of an extended source of this type. This modification is a significant improvement over standard design techniques because it makes it possible to calculate an experimental case directly rather than inferring the response from a point-source calculation. We can now examine directly the effect of surface errors and surface roughness on the image of an actual source and study the distortion of an image as a result of misalignment. Figure 77 (a) shows the calculated image of Fig. 76 for a perfect optical element, and Fig. 77 (b) shows the image assuming a 300-μrad random slope error.

The surface roughness derived from these measurements was about ten times the roughness of a diamond-point-machined surface that was tested by American Science and Engineering. New elements are being fabricated at Y-12 under improved control techniques, and other optical designs are being investigated.

REFLECTANCE MEASUREMENTS FOR 1-ns LASER PULSES AT 10μm

(V. M. Cottles)

When a high-power laser pulse interacts with the surface of a target in vacuum, a fraction of

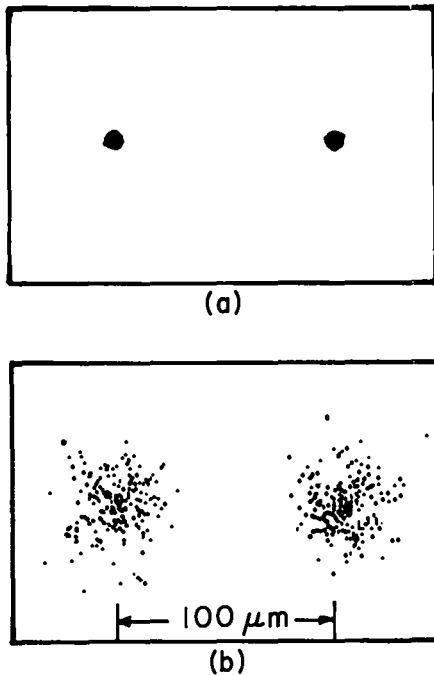


Fig. 77

Calculated image of Fig. 76: (a), for perfect optical element, (b), assuming 300- μm random slope error.

the incident beam is scattered by various processes, resulting in specular and diffuse reflection. For realistic laser fusion target modeling, it is important to know empirically the amount of scattering that occurs for 10- μm laser pulses of ~ 1 -ns duration as a function of incident power density. Scattering measurements at other laboratories⁷ indicate that the integrated reflectance may be between 60 and 80% at intensities of 10^{12} W/cm^2 . With long pulses (40 to 50 ns) at power densities from 10^{11} to 10^{13} W/cm^2 reflectance values ranging from 8 to 90% have been reported.^{8, 9}

We are developing a laser-pulse energy-balance measuring system for use with the Single-Beam System to obtain reflectance data for short pulses and intensities of 10^{14} W/cm^2 . The optics of the system are shown in Fig. 78 undergoing a

quality test with a helium:neon laser. The laser beam, representing the focused CO_2 laser pulse, enters from the left, passes through an $f/2$ hole in an elliptical brass mirror and strikes a plane-slab, optically thick target at the first focus of the mirror. Light that scatters from the target and strikes the mirror is reflected to the second focus, where a pyroelectric detector or a calorimeter aperture is placed to measure the total amount of light scattered by the target into the mirror. The light scattered back through the $f/2$ aperture is separated from the incident beam by a NaCl beam splitter and is monitored by either a pyroelectric detector or a calorimeter.

Because none of the light passes through the target and because the elliptical mirror surface extends to the latus rectum of the first focus, the system monitors light scattered into 2π which, in this geometry, is all the scattered light.

Initial experiments will be performed with calorimeters to obtain time-integrated reflectance measurements for 1-ns pulses with intensities ranging from 10^{11} to 10^{14} W/cm^2 for CH_2 slab targets. Later experiments will use fast pyroelectric detectors to provide time-resolved reflectance data.

DATA ACQUISITION AND PROCESSING

(R. Peck)

A CAMAC serial highway was assembled for use with the new DEC PDP 11/70 computer which will be delivered in early 1977. This highway will enable centralized acquisition of data from several lasers.

The serial highway was first used to interface the Nd:glass laser with a Nova-840 computer. This allowed testing the CAMAC hardware components and the development of some software. The highway will be used next to interface the Two-Beam CO_2 System with another Nova-840 until the new DEC computer is operational. Programs that have been written and tested include structured-data organization, acquisition and retrieval modules, and an instructive operation dialogue.

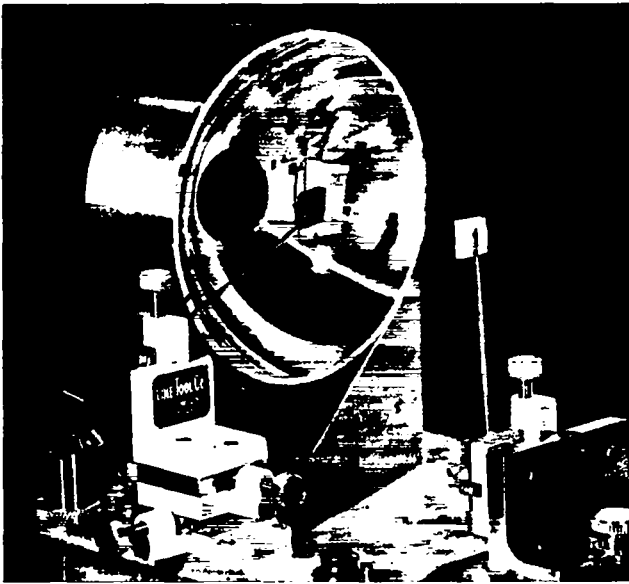


Fig. 78

Laser-pulse energy-balance measuring system undergoing quality test with He:Ne laser.

REFERENCES

1. R. L. Carman, A. G. Engelhardt, and N. Clabo, Proceedings of the Fourth Workshop in Laser Interaction and Related Plasma Phenomena, H. Schwartz and H. Hora, Eds. (Plenum Press, New York, 1977).
2. E. Stark and F. Skoberne, Los Alamos Scientific Laboratory report LA-6510-PR (November 1976).
3. J. Reintjes, R. L. Carman, and F. Shimizu, *Phys. Rev.* 8A, 3, 1480 (September 1973).
4. J. Reintjes and R. C. Eckardt, *Appl. Lett.* 30, 2, 91 (1977).
5. C. Freed, MIT-Lincoln Laboratory, private communication (1976).
6. E. Stark and F. Skoberne, Los Alamos Scientific Laboratory report LA-6510-PR (November 1976).
7. J. Martineau, P. Paranthoen, M. Rabeau, and C. Patou, "Energy Balance Measurements on a Nanosecond CO₂ Laser Created Plasma," *Optics Communications* 15, 3 (November-December 1975).
8. T. P. Donaldson, M. Hubbard, and I. J. Spalding, *Phys. Rev. Lett.* 37, 20 (November 1976).
9. E. Fabre, C. Garban, C. Popovics, A. Poquerusse, C. Stenz, and J. Virmont, "Experimental Investigation of Plasmas Created by CO₂ Laser Irradiation of Plane Targets," Int. Atomic Energy Agency Report CN-35/G.

VI. APPLICATIONS OF LASER FUSION -- FEASIBILITY AND SYSTEMS STUDIES

Our feasibility and systems studies are being performed to analyze the technical feasibility and economic aspects of various commercial and military applications of laser fusion. The direct production of electricity in central-station power plants is of major concern. The general objectives of these studies are: the conceptualization and preliminary engineering assessment of laser fusion reactors and generating stations; the development of parametric computer models of power-plant subsystems for economic and technology tradeoff and comparison studies; and the identification of problems requiring long-term development efforts. Applications of laser fusion in the production of fuel for fission reactors, the production of synthetic fuels such as hydrogen, and as a source of high-temperature process heat are also being investigated.

LASER FUSION REACTOR STUDIES

Laser Fusion-Pellet Output Studies (J. J. Devaney, R. N. Griego)

We have acquired the computer codes LACER and LASNEX for calculating fusion-pellet output characteristics. These codes are being used in parametric studies of the effects that variations in structural materials in our basic pellet designs have on pellet output. We expect that most of our needs will be satisfied by LACER, which is more economical to run than LASNEX, and we have written a computer program to process the output of LACER into a form convenient for reactor-cavity analysis.

The results of our pellet output calculations will be used in reactor design and system tradeoff studies to select acceptable pellet designs for commercial applications. In addition to having acceptable output characteristics, pellet designs will be selected that are economical to fabricate, i.e., pellets that are made from cheap and abundant materials and for which restrictions on manufacturing tolerances are minimal.

Pellet-output parametric studies will also be used to select pellet designs for military applications. Initial studies of pellets for military applications will emphasize the use of the HEGLF and/or of an upgrade of the HEGLF.

Ion Motion In Laser Fusion Reactor Vessels

Analysis Code

(J. C. Goldstein, D. O. Dickman) -- Viable designs of laser fusion reactor vessels must minimize damage to cavity walls from pellet debris. Previous studies^{1,2} indicated that wall erosion due to the impact of charged-particle debris can be controlled by a background magnetic field. We have extended these studies by means of a considerably refined and modified version of an earlier simulation code.^{3,4} The new code,^{5,6} LIFE (Laser Initiated Fusion Explosion), treats debris plasma motion (after completion of pellet-compression and thermonuclear-burn phases) in an axially symmetric magnetically protected reactor cavity by the particle-in-cell (PIC) method.³ The motion of the debris plasma is followed spatially and temporally until a substantial fraction of the original pellet mass has left the cavity interior. Extensive data pertaining to the intersection of particle trajectories with the reactor cavity components constitute the primary output of the code. This information is recorded for subsequent analysis by other codes, which calculate the erosion of surfaces by sputtering due to the impact of pellet debris. The configuration of the background magnetic field is selected to shield some of the cavity walls while simultaneously directing the charged particle debris onto other especially designed heat-sink surfaces. Thus, LIFE is used to determine the effects of varying both the cavity

geometry and the configuration of the magnetic field until - for a particular pellet microexplosion - wall erosion decreases to an acceptable level. Several assumptions were made to simplify the general problem:

- Only an axially symmetric cavity is considered; the cross-sectional area of the cavity may be a function of axial position and may be circular, annular, or vary from circular to annular.
- The cavity is reflection-symmetric about the midplane $z = 0$.
- Only the motion of positive ions is explicitly calculated; local charge neutrality of the plasma temperature that is in effect zero (thermal energy of pellet compression and thermonuclear burn are converted to radial expansion).
- No electric fields are included due to end-shortings.
- Plasma number density always remains axisymmetric as well as reflection symmetric about the midplane $z = 0$.
- Plasma ions interact with the magnetic field via the Lorentz force $\vec{F} = (8/c) \vec{V} \times \vec{B}$.
- Although all three particle velocity components are calculated, the assumed symmetries imply that the only significant current is that in the azimuthal direction. This current, J_e , is the source term for a Poisson equation for one component of the vector potential, A_θ , from which the magnetic field components B_r and B_z are obtained.
- The cavity walls are made of materials that are good electrical conductors.

The particular capabilities of LIFE include:

- General axisymmetric geometry, as defined above.
- Choice of initial background magnetic field as a superposition of (a) a uniform field in the z -direction and (b) fields generated by up to five pairs of single-turn configuration calculated from given boundary

values of the vector potential A_θ .

- Up to 100 different (charge, mass) plasma ion species can be accommodated.
- The simulation ratio (number of real particles per simulation particle) can be different for each species.

The results of a LIFE calculation include recording of the following data.

- Type and kinetic energy of particle species at impact with a cavity component.
- Time and location of each particle impact with walls.
- Angle of impact with respect to the inward-pointing normal to the boundary surface.

These results are used in subsequent material sputtering calculations. The motion of the plasma within the reactor cavity can be displayed as a color motion picture.^{5,6}

Cavity Design

(J. C. Goldstein, D. O. Dickman, I. O. Bohachevsky)

We recently completed a cavity design⁶ based on theoretical pellet microexplosion data. Figure 79 shows a schematic of the reactor; Fig. 80 the actual computing region in the LIFE calculation; and Fig. 81, the distribution of energy and particle number along the upper boundary of the cavity. Note that almost all the debris has hit the heat-sink surface and that the distribution of

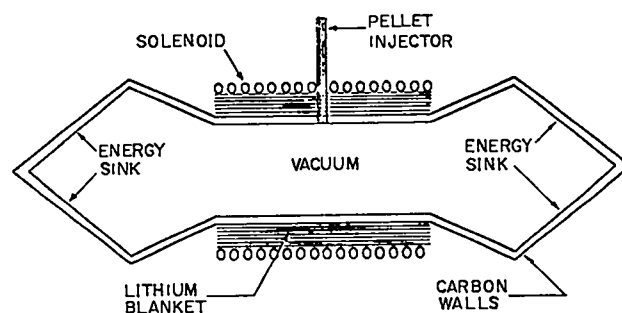


Fig. 79
Reactor-cavity schematic (plane section of a figure of revolution).



Fig. 80
Reactor-cavity region in numerical computation.

impacts on that surface is reasonably uniform. Figure 82 shows the angle to the inward-pointing normal made by the impacts as divided into four equal bins between 0 and $\pi/2$.

Dependence of Sputtering Erosion On Fusion-Pellet Output Characteristics

(I. O. Bohachevsky, J. Hafer)

Introduction -- The initiation of parametric studies of fusion-pellet output characteristics during the previous quarter generated a need for a method to estimate trends in sputtering erosion of laser fusion reactor-cavity walls without performing detailed sputtering calculations. We are interested in defining the dependence of total amount of eroded wall material on the atomic number of projectile ions (pellet debris), on total pellet mass, and on pellet yield. This knowledge will be helpful in the selection of materials for structural shells of fusion pellets.

To determine the dependence of sputtering erosion on these parameters, we constructed a

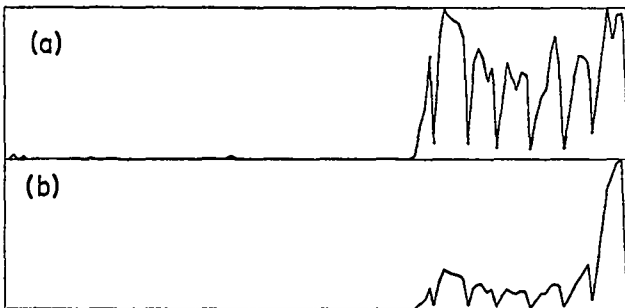


Fig. 81
Energy loss (a) and particle-number loss (b) through cavity boundary as a function of longitudinal position z.

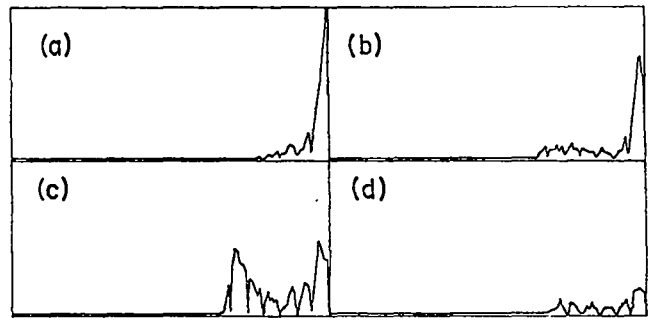


Fig. 82
Number of particles whose polar angle of impact, with respect to local inward-pointing normal to cavity surface, lies in a particular range vs longitudinal position z:

- (a) $0 \leq \theta \leq \pi/8$, (c) $\pi/4 < \theta < 3\pi/8$
- (b) $\pi/8 < \theta < \pi/4$, (d) $3\pi/8 < \theta < \pi/2$.

simple sputtering model and calculated the erosion explicitly.

The Sputtering Model -- The sputtering model consists of two parts: (a) the dependence of the sputtering coefficient S on projectile ion energy E, and (b) the dependence of ion fluence N on fuel-pellet mass M and its other characteristics.

Sputtering Coefficient, S(E) -- We postulate that the sputtering coefficient depends on ion energy in the following manner.

- S(E) increases linearly from zero at $E = 0$ to S_m at E_m where S_m is the maximum value of S and E_m is the ion energy at which sputtering reaches its maximum;
- S(E) remains constant in the region $E_m \leq E \leq rE_m$ where $r \geq e$ is an arbitrary constant (the restriction on r is not essential and will be explained later);
- S(E) decreases as $\epsilon^{-1} \ln \epsilon$ for $E \geq rE_m$ where $\epsilon = E/E_m$ is the nondimensional ion energy.

The behavior described above is represented schematically in Fig. 83; it is a reasonable approximation to the theoretically and experimentally determined functional dependence of S(E).^{7,8} We have assumed that the threshold energy for sputtering is zero; this approximation is satisfactory for this analysis because the threshold energy is usually less than 10 eV and is

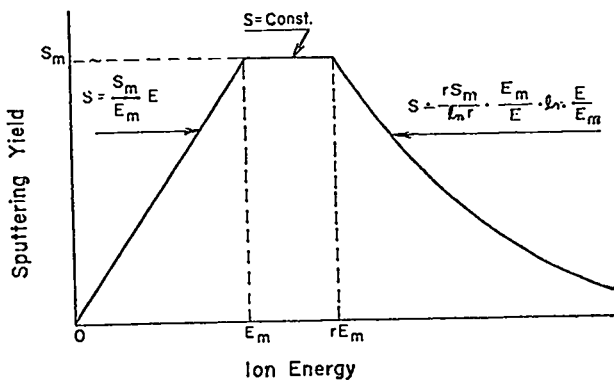


Fig. 83
Model defining dependence of sputtering coefficient on ion energy.

therefore negligible in comparison to E_m , which is generally tens or hundreds of keV.

The physical quantities E_m and S_m are characteristic of the ion material and depend on its atomic number Z ; we use Sigmund's theory⁹ to calculate that dependence. The results for molybdenum and carbon (cavity walls) are shown in Figs 84, 85, 86, and 87; they indicate the $E_m(Z)$ is nearly quadratic and $S_m(Z)$ is nearly linear in Z . Accordingly, we set:

$$E_m = KZ^2 \quad (1)$$

$$S_m = C_1 + C_2Z \quad (2)$$

where the constants K , C_1 , and C_2 are obtained by matching Eqs. (1) and (2) with theoretically or experimentally obtained dependencies $E_m(Z)$ and $S_m(Z)$. For example, in the case of molybdenum target (cavity wall), Figs. 84 and 85 indicate $K \approx 9000$, $C_1 \approx 2.0$, and $C_2 \approx 0.2$

Consistent with the approximations inherent in Eqs. (1) and (2), we also approximate the atomic weight by

$$a = 2Z + \delta Z^2, \quad (3)$$

where δ is a small number.

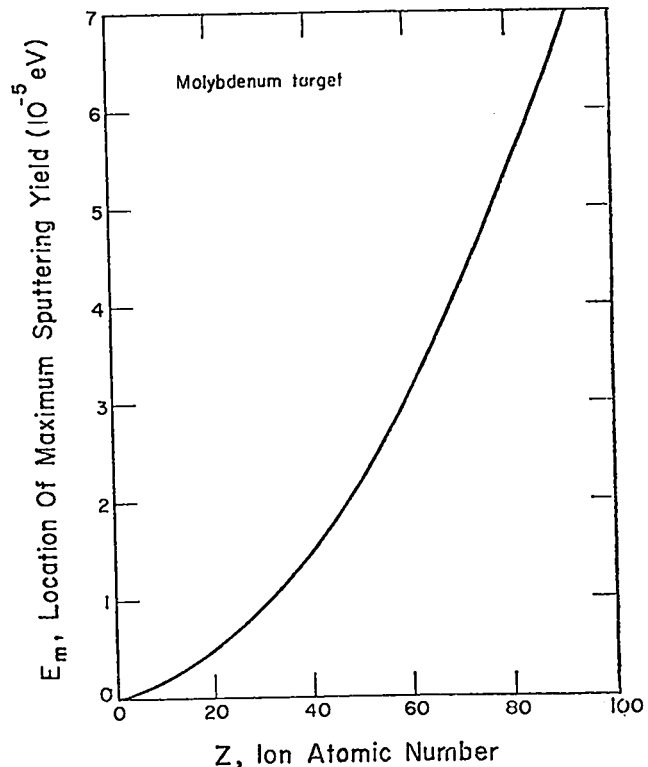


Fig. 84
Ion energy at which the sputtering coefficient reaches a maximum for molybdenum target.

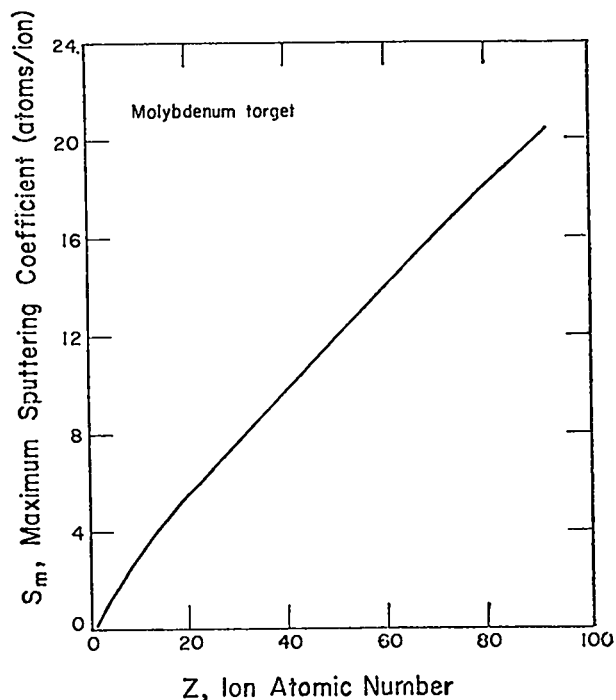


Fig. 85
Maximum sputtering coefficient for a molybdenum target.

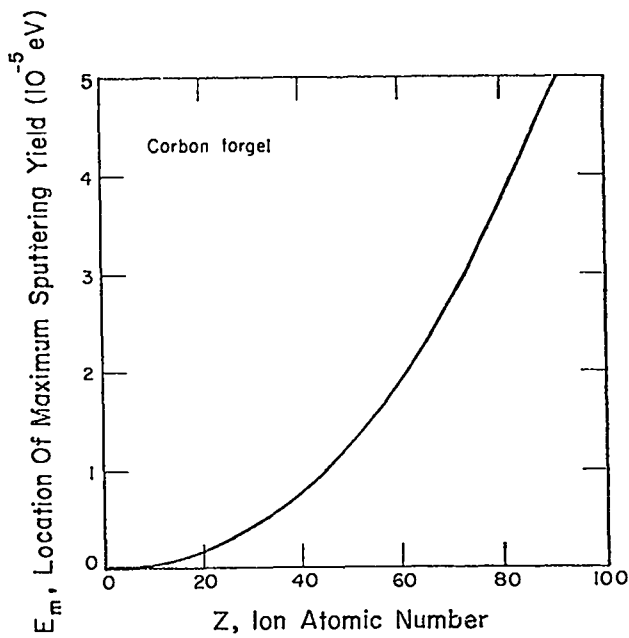


Fig. 86

Ion energy at which the sputtering coefficient reaches a maximum for a carbon target.

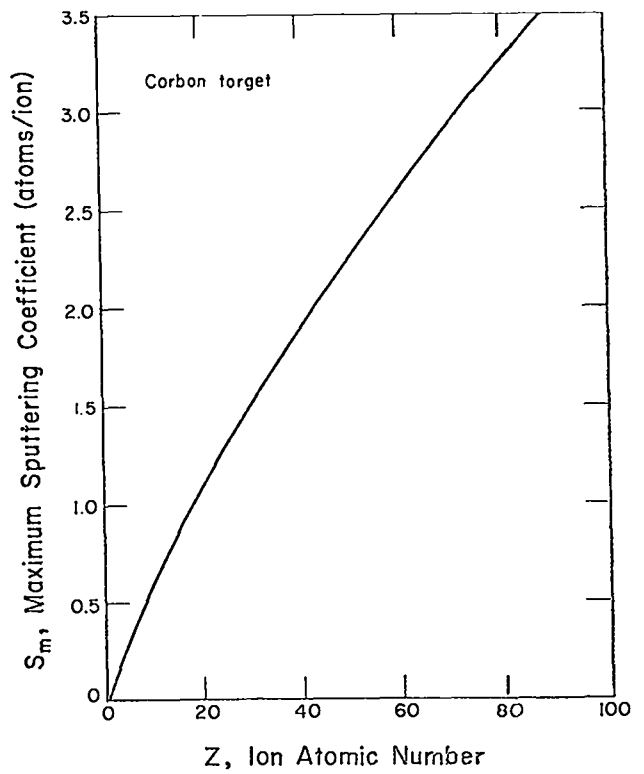


Fig. 87

Maximum sputtering coefficient for a carbon target.

Ion Fluence, N -- For the purpose of this parametric analysis, we assume that pellet composition can be characterized with adequate accuracy by an average atomic weight. Consequently, the number of plasma ions generated by a pellet microexplosion is

$$N = \frac{MA}{a}, \quad (4)$$

where A is Avogadro's number and M is pellet mass. If we assume further that the fusion energy is uniformly distributed over all ions, then the average energy per ion, E, is given by

$$E = \frac{fYa}{MA}, \quad (5)$$

where Y is the total microexplosion energy release in eV and f is the fraction of yield deposited in plasma debris.

Analysis and Results -- As stated in the introduction, the object of the present analysis is to calculate the total amount of material eroded from the wall, given by:

$$E_r = SH. \quad (6)$$

Toward this end the three ion energy regimes-- low, intermediate, and high--in which the sputtering coefficient, respectively increases, remains constant, and decreases, will be considered separately.

Low-Energy Regime, $E \leq E_m$ -- Plasma ions will be in the low-energy regime when the inequality $(fYa/MA) \leq E_m$ is satisfied; in general, this is true when the ratio of pellet yield to mass is low.

In this regime, the sputtering coefficient increases linearly with ion energy and is given by $S = (S_m/E_m)E$. By using this expression together with Eqs. (4) and (5) in Eq. (6), we obtain

$$E_r = \frac{S_m}{E_m} fY, \quad (7)$$

which, upon substitution for E_m and S_m expressions given by Eqs. (1) and (2), respectively, becomes:

$$E_r = \frac{C_1 + C_2 Z}{kZ^2} fY.$$

This result shows that in the low-energy regime (where the sputtering coefficient increases with ion energy) the total amount of material eroded is independent of pellet mass, is directly proportional to the total ion energy, and for a constant pellet yield will decrease as the atomic number Z of the pellet material is increased.

Intermediate-Energy Regime, $E_m < E \leq rE_m$ -- In this regime the ion energy satisfies the inequalities $E_m \leq (fYa)/(MA) \leq rE_m$ and the sputtering coefficient is constant with ion energy. Consequently, the amount of eroded material is given by

$$E_r = S_m \frac{MA}{a}. \quad (8)$$

Using Eqs. (2) and (3) to express E_r in terms of atomic number we obtain:

$$E_r = \frac{MA}{Z} \frac{C_1 + C_2 Z}{2 + \delta Z}.$$

This result shows that in the intermediate-energy regime (where the sputtering coefficient is independent of ion energy), the amount of eroded material does not depend directly on fuel-pellet yield, is proportional to pellet mass M , and for constant M decreases with increasing Z ; the decrease, however, may not be uniform for some combinations of values of C_1 , C_2 , and δ .

High-Energy Regime, $E > rE_m$ -- Plasma ions are in the high-energy regime when the inequality, $(fYa/MA) > rE_m$ is satisfied; in general, this inequality is satisfied when the ratio of pellet yield to mass is high.

Theoretical and experimental investigations indicate^{8,9} that in the high-energy regime the sputtering coefficient decreases with increasing energy as $\epsilon^{-1} \ln \epsilon$ (this function decreases

monotonically for $\epsilon > e$, hence the previous restriction on r); consequently we set:

$$S = \frac{r S_m}{\ln r} \frac{\ln \epsilon}{\epsilon},$$

where the multiplicative constant was determined from the continuity of S at $E = rE_m$.

Substituting the above expression for S together with Eqs. (4) and (5) into Eq. (6) yields

$$e_r = \frac{r(MA)^2}{fY \ln r} \frac{E_m S_m}{a^2} \ln \frac{fYa}{MAE_m}. \quad (9)$$

In this expression the product $E_m S_m$ increases as Z^3 [Eqs. (1) and (2)] and a^2 increases as Z^2 [Eq. (3)]; however, no convenient estimate exists that would reflect the variation of the logarithmic term with Z . The following considerations indicate the behavior of E_r . For low values of Z , E_m is relatively small making the argument of the logarithm large and the logarithm itself slowly varying with Z . Thus, the behaviour of E_r is determined predominantly by the factor $E_m S_m / a^2$ which increases with Z . For high values of Z the argument of the logarithm decreases as $(Z)^1$ and the logarithm itself diminishes more rapidly than the increasing factor $E_m S_m / a^2$. Thus, E_r eventually begins to decrease with increasing Z .

To verify the above deduced behavior and to obtain an indication of the value of Z at which E_r changes from an increasing to a decreasing function of Z , we have evaluated Eq. (9) numerically using for $E_m(Z)$ and $S_m(Z)$ exact expressions from Sigmund's theory⁹ and for Z exact values from the periodic table of elements. The calculation was carried out for $r = 2.80$, $f = 0.20$, $Y = 100$ MJ, and $M = 0.07$ g, chosen so that ions are in the high-energy regime for values of Z less than or equal to 48.

The result is plotted in Fig. 88; it shows that E_r behaves as predicted: it increases initially with Z , reaches a maximum (at $Z = 8$ for the particular set of parameter values used in this sample computation), and then decreases as Z increases; the curve is extended with dashes beyond

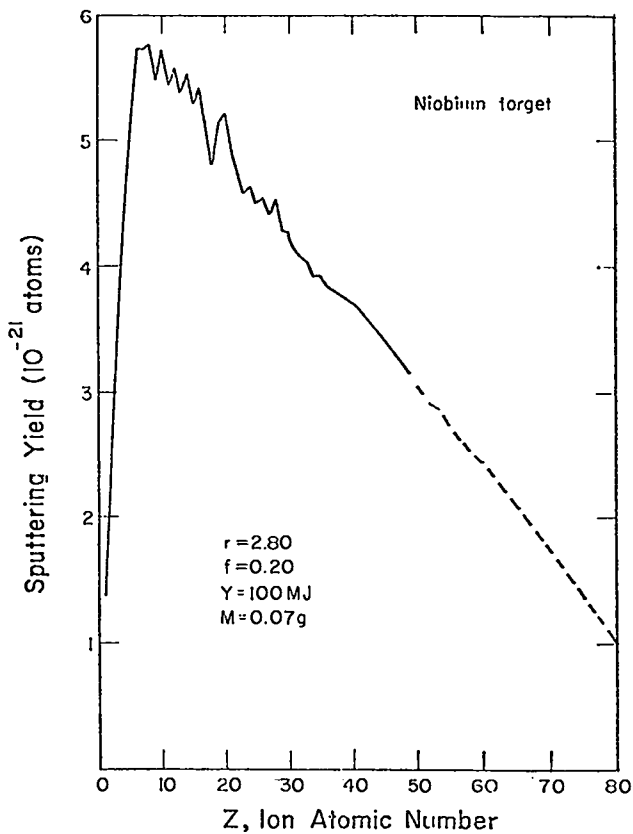


Fig. 88

Total sputtering erosion in the high ion-energy regime.

Z = 49 to illustrate the trend. The behavior, however, is not uniformly smooth but has small undulations superimposed on the general trend in the neighborhood of the maximum.

Conclusion -- Our analysis led to expressions that estimate the total amount of eroded wall material for different projectile ions in terms of ion atomic number and other parameters which characterize the ion fluence. The complementary problem of determining the amounts of different wall materials eroded by a given ion flux has been investigated extensively by Wehner and his collaborators;^{10, 11, 12} their findings are summarized in Sec. 7.4.2. of Ref. 8. Briefly, the sputtering yield follows closely, with minor exceptions, the state of electron concentrations in the d-shells of target material atoms and also crudely resembles the reciprocals of the heats of sublimation. Thus, the yield varies almost periodically with the atomic number of the target material. The results, presented graphically in

convenient form, may be found in Ref. 8 (pp. 315-316) and need not be reproduced here.

CAPITAL - A FORTRAN PROGRAM FOR ESTIMATION OF CAPITAL COSTS OF LASER AND LASER FUSION EXPERIMENTAL FACILITIES

(J. H. Pendergrass)

Introduction

As progress continues within the laser fusion research and development program, larger, more sophisticated experimental facilities will be required, and lasers as well as laser fusion outputs will be utilized in multipurpose engineering testing and weapons research facilities. As the required facilities increase in sophistication, size, and cost, and the science and technology involved matures, it becomes increasingly important to develop a methodology for early, detailed, and accurate assessment of the costs incurred in constructing and operating proposed laser fusion facilities. To satisfy this need for accurate and detailed cost estimates, we began the development of a computer program, CAPITAL, for estimation of capital costs for proposed laser fusion experimental facilities and conceptual generating stations.

In this rapidly developing area, the cost estimation made when an experimental facility is first proposed is typically relatively crude, but may provide an adequate basis for continued refinement. If crude preliminary cost estimates suggest that further examination of the merits of the proposed facility is warranted, more sophisticated and accurate cost estimates become possible and necessary as more detailed and definitive facility designs evolve. If a final design is approved, detailed and accurate cost estimates will be made to provide the basis for, e.g., funding requests and assessment of contractor bids. The design-evolution process for advanced-technology facilities of the types under consideration typically involves major changes in facility features throughout the process. Therefore, we decided to make CAPITAL as flexible and general as possible in the hope that the entire spectrum of facility design changes and levels of sophistication in cost estimation could be

accommodated with a single program. In addition, because cost estimation is usually performed with incomplete information, especially in a preliminary design stage when the technology is rapidly evolving, novel equipment is required, or economic conditions are fluctuating rapidly, we decided to provide CAPITAL with features that would facilitate the conduct of parametric studies. To promote portability, we also included as few local computer system-specific features in the first version of CAPITAL as possible.

Important Features of CAPITAL

Cost Estimation Methods -- Central characteristics of CAPITAL are methods used for capital cost estimation, cash flow, and interest cost during construction. The essential features of these methods are discussed below.

The first step in the cost-estimation process is specification of the components of a proposed facility. In our approach, we provide a master file in which we list all components that might appear in a laser fusion experimental facility. For a particular experimental facility, the particular components that appear in that facility are selected from the master file. The master file is constructed for easy modification.

In defining a particular proposed facility, accounts (referred to as base-level accounts) are selected from the master file through specification of account numbers. For each base-level account, input cost information must be supplied and capital costs, subdivided into materials, spares, engineering and design, inspection and testing, and craft labor costs, are computed as functions of time.

With regard to calculation of interest expense and cash flow, the principal assumptions for one of the methods of interest expense computation, provided as an example, are: (1) funds required during a construction period are drawn at the beginning of the construction period, (2) interest is compounded for each construction period, and (3) the interest rates applied to funds drawn for a particular construction period apply to those funds thereafter. With these assumptions, interest expense, cash flow, and cumulative interest expense

and cash flow for subsequent construction periods are calculated.

Among several options included to provide the flexibility that allows cost estimates of various degrees of sophistication mentioned previously are the following.

- Different interest rates can be specified for each construction period or a single interest rate can be specified for all construction periods; similarly, different lengths can be specified for each construction period or a single length can be specified for all construction periods; in addition, default values are provided.
- Different contingency factors can be specified for each base-level account and construction period, and similar flexibility with respect to escalation parameters and site factors is also provided.

Output of Computed Results -- Considerable flexibility in input-data listing and output of computed results is another feature of CAPITAL:

- Account numbers and descriptions of items included in the account as either base-level or non-base-level can be listed for all accounts in the master file if desired.
- Cash flow, cumulative cash flow, interest expense, and cumulative interest expense can be printed and print-plotted.
- For each base-level account and each construction period, materials, spares, engineering and design, and inspection and testing costs plus craft labor costs as a function of craft labor type, and corresponding contingency allowances, can be printed along with a description of items included in the base-level account.
- Capital-cost summaries can be printed which include descriptions of items contained in each arbitrarily designated summary account plus (1) the sum of expenditures for materials, spares, engineering and design, inspection and

testing, and corresponding contingency allowances; (2) the sum of craft labor costs and corresponding contingency allowances; and (3) the sum of items (1) and (2). A summary account can consist of either a base-level account or the summation of all contained lower ranking base-level accounts. As an option one can designate the set of all base-level accounts as a set of summary accounts. Grand totals for all accounts are also computed and printed.

Status of Development of CAPITAL

All features of current subroutines of program CAPITAL have been tested and shown to be free of error. The main program has been demonstrated to be free of FORTRAN error, but testing of some features of the main program continues.

Data Bases for CAPITAL

The current principal sources of data for the development and application of CAPITAL are the on-going design and cost estimation projects for HEGLF, the "Guide for Economic Evaluation of Nuclear Power Plants";¹³ the in-house program for estimation of cost of electrical power production in a laser fusion power plant, TROFAN, and CONCEPT.^{14,15} With respect to cost-information input for CAPITAL, provisions are included for calculating the cost parameters in subroutines to further automate the data-input process. Much of the cost information required for these subroutines will also be drawn from the sources listed above.

COMMERCIAL APPLICATION OF THERMIONIC CONVERSION USING A LASER FUSION-REACTOR ENERGY SOURCE

(T. G. Frank, E. A. Kern, L. A. Booth)

Introduction

Thermionic emission has been utilized in space-power research programs for the past two decades. This research led to the development of devices for converting heat to electricity generally referred to as thermionic converters. Emphasis in thermionic-conversion research by ERDA contractors is currently placed on the design of

systems to be used as topping cycles for electric generating stations. Thermionic conversion for this application is attractive because the heat-rejection temperatures are high enough to permit normal operation of conventional conversion cycles with the heat rejected from the thermionic converters.

Conceptual laser fusion reactors may offer significant advantages compared to fission reactors for utilizing thermionic-conversion topping cycles. These advantages stem from the performance characteristics of thermionic converters with increasing efficiency and output resulting from higher temperature operation and from the absence in laser fusion reactors of high-temperature limitations due to fuel-element distortion (or melting) and fission-product release. Temperatures in fusion reactors are limited, in principle, only by the properties of refractory metals.

The normal electric output of thermionic converters is low-voltage direct current. The reactor concepts investigated in this study would produce (1) low-voltage direct current from a thermionic topping cycle for electrochemical processing and (2) conventional commercial electric power with the reject heat from the topping cycle.

System Design

A high-temperature, refractory reactor blanket is required to gain maximum benefit from the thermionic topping cycle. The conceptual blanket studied includes a 0.5-m-thick graphite region enclosing the reactor cavity. The graphite, in turn, is enclosed by a 0.05-m-thick region consisting of boron carbide and graphite in which neutrons thermalized in the intervening graphite region are captured. The thermionic diodes are supported on the surface of the boron carbide-graphite region. We assumed that the thermionic-diode structures would completely enclose the radiating graphite surface and that 90% of the surface of these structures consists of thermionic emitters. Heat rejection from the thermionic-diode collectors is by conduction to an intermediate heat-transfer loop containing circulating sodium. The entire system is enclosed by a stainless steel structure.

Although a detailed reactor design study might result in the choice of cylindrical geometry, calculations for this study were done in spherical geometry, for convenience. A cross section of the spherical reactor model is shown in Fig. 89. Energy deposition in the graphite regions consists of deposition by neutron scattering, exoergic neutron reactions, and x and gamma radiation. We assumed that the energy of the pellet debris is recovered as heat directly from the cavity and is combined with the heat rejected by the thermionic diodes for conversion to electricity in a conventional steam turbine generating plant.

Results of Parametric Studies

The converter performance assumed is typified by units that have been tested in the laboratory and are being developed for power-plant application (so-called second-generation, near-term converters). The thermionic emitter and collector temperatures in the study ranged from 1400 to 1800 K and from 700 to 920 K, respectively. The diode power output per unit of emitter area was based on data given in Ref. 16 and is shown in Fig. 90. Based on data given in Refs. 16, 17, and 18, diode efficiency was estimated to be 53.5% of Carnot efficiency. This estimate does not include ohmic losses in the electrodes and losses in the conductors from the diodes to the load, which were taken to be 8 and 15%, respectively. Thus, the net thermionic conversion efficiency assumed is 42% of Carnot efficiency.

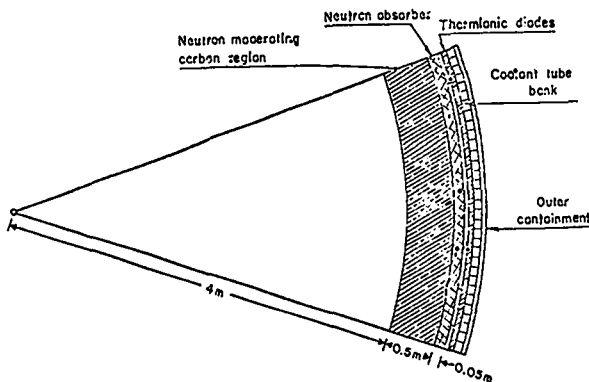


Fig. 89

Cross section of spherical laser fusion reactor model with thermionic topping cycle.

The diodes were assumed constructed from 0.127-cm-thick refractory metal plates with the properties of molybdenum. The necessary radiator surface temperatures and the radiating power level were determined from the thermionic-diode output and efficiency. Energy-deposition distributions in the reactor blanket were calculated with neutronics codes, and temperature distributions through the radiating blanket were calculated from these distributions and total power levels. The maximum temperature in the carbon blanket was well below the sublimation temperature (~4000 K) of carbon in all cases.

Conversion of the heat rejected by the thermionic diodes, ohmic losses in the conductors, and the energy of the pellet debris in a steam-turbine generating plant were evaluated with a temperature-dependent model used in LFR (Laser Fusion Reactor) parametric studies.

Capital costs of the reactors, of heat-transfer and steam generating equipment, and of the steam-turbine generating equipment were estimated in terms of 1973 dollars from data used in LFR systems studies. Capital costs of the thermionic systems were taken from estimates given in Refs. 16 and 17, which ranged from \$144/kWe to

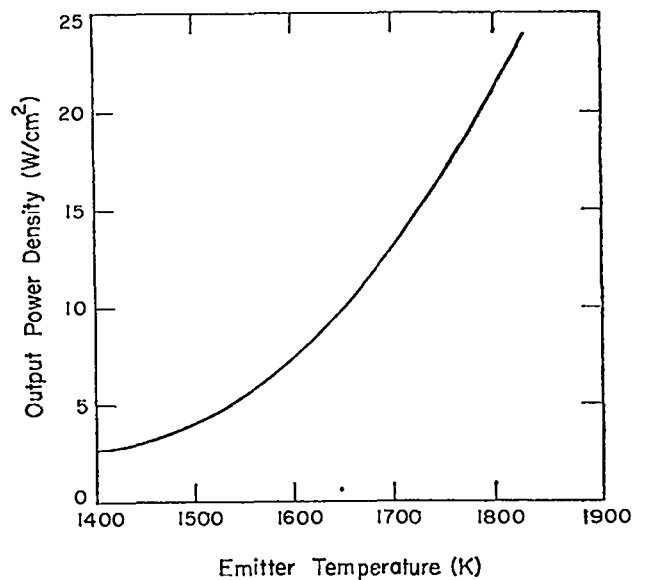


Fig. 90

Temperature dependence of thermionic-diode output power density.

\$160/kWe, based on 1972 dollars. A value of \$160/kWe was assumed for our study.

Energy deposition in the graphite blanket from 100-MJ fusion-pellet microexplosions was calculated to be 90 MJ per microexplosion. In addition, 23 MJ is recovered directly from the cavity from each microexplosion. Thus, exoergic nuclear reactions in the blanket result in an enhancement of the fusion yield by 13%.

Performance evaluations were based on a conceptual power plant containing 14 reactor cavities. The total thermionic power generated is, according to the model assumed, dependent only on emitter temperature and area and is given for the 14-reactor plant in Fig. 91.

The electric power generated by the steam cycle depends on the total reactor power level, on the efficiency of the topping cycle, and on the steam-turbine inlet temperature. These quantities are, in turn, dependent on the emitter and collector temperatures of the thermionic topping cycle. The net electric power produced by the

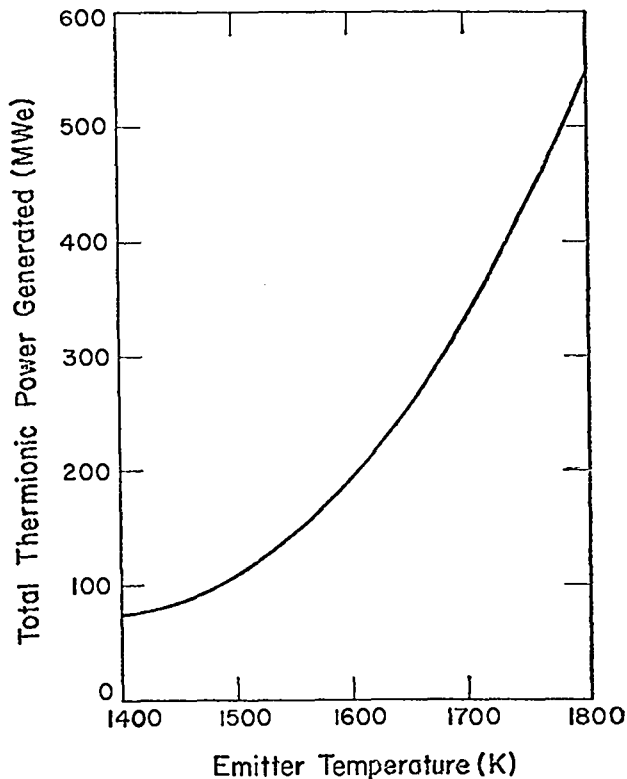


Fig. 91
Dependence on thermionic-emitter temperature of power generated by topping cycle.

steam cycle (after providing for recirculating power requirements) is shown in Fig. 92 as a function of diode collector temperature with emitter temperature as a parameter. The thermal-to-electric conversion efficiency for the combined cycles is shown in Fig. 93 as a function of diode collector temperature for the extremes of emitter temperature considered.

Economic analyses were made with a modified version of the laser fusion systems analysis computer program. We assumed that the direct-current output of the thermionic diodes would be used in an electrochemical process rather than being conditioned for distribution in a power grid; thus, the thermionic output was evaluated separately from the steam-turbine output. Because the reactor concept considered does not include a provision for tritium breeding, the fuel cost was increased to account for the purchase of tritium from another source.

No attempts were made to estimate component lifetimes or replacement schedules so that

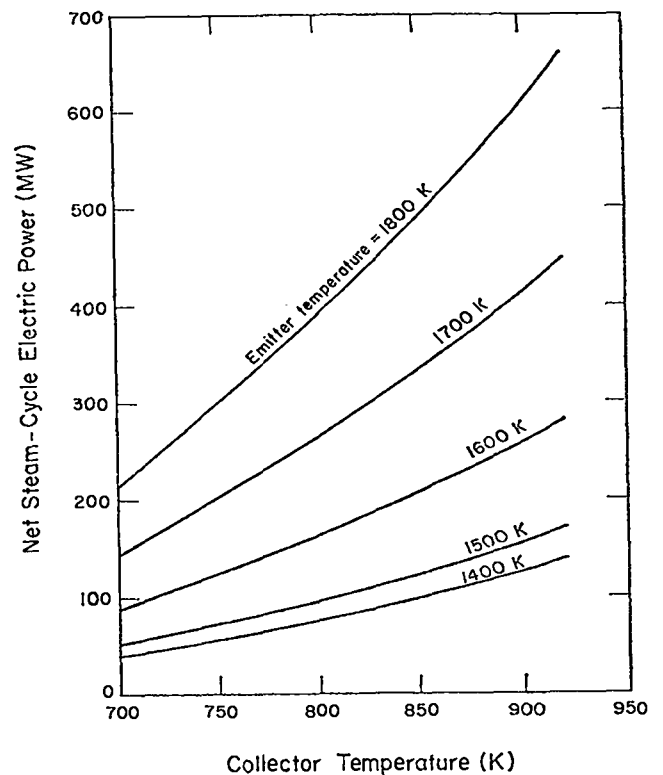


Fig. 92
Electric power generated by the steam cycle as function of thermionic-diode operating conditions.

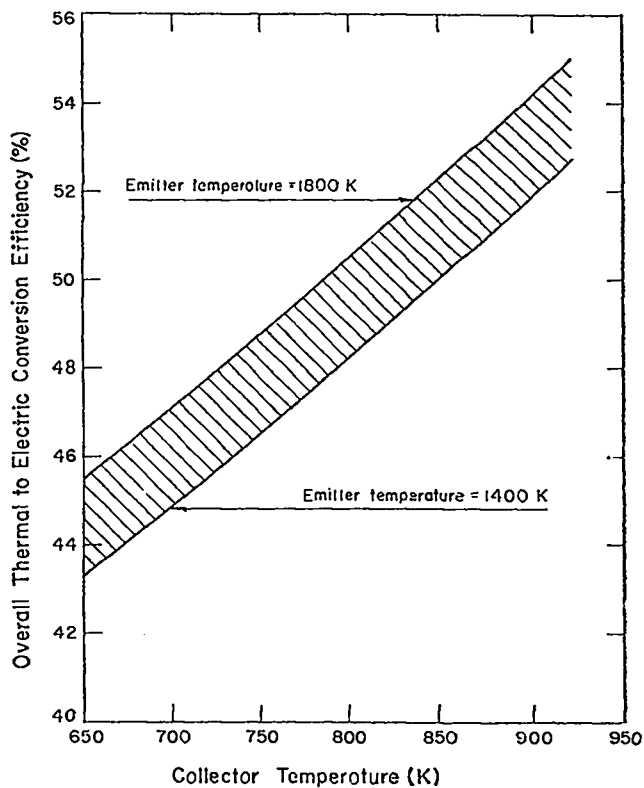


Fig. 93

Thermal-to-electric conversion efficiency of combined cycles as function of thermionic-diode operating conditions.

calculated power-production costs are too low by the amount of maintenance costs. A duty factor of 85% was assumed. Typical results of the economic analysis (in 1973 dollars) are given in Fig. 94, which consists of plots of production costs of thermionic power as functions of diode collector temperature, with the value of the power produced by the steam turbines as a parameter. The diode emitter temperature for these calculations was 1800 K. This method of evaluating production costs associated with the topping-cycle is based on treating the topping cycle output as a by-product which, in reality, it is not, because major changes in reactor design were incorporated to permit inclusion of the topping cycle.

Conclusions

The results of this preliminary scoping study of using thermionic conversion to create low-voltage direct current from fusion reactors for electrochemical processing are encouraging. Fusion

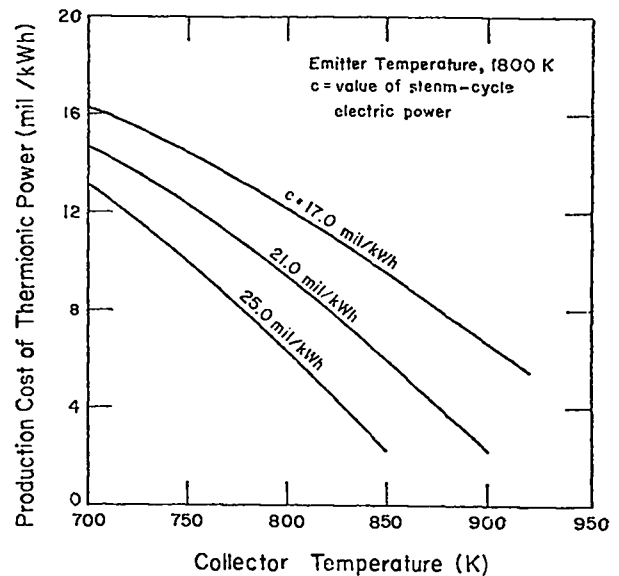


Fig. 94

Production costs of by-product thermionic power with the value of conventional electric power as a parameter.

reactors appear better suited to take advantage of thermionic topping cycles than fission or fossil-fuel generating stations, although optimization of thermionic topping cycles can only be achieved with major redesign of fusion-reactor blankets.

For the LFR example analyzed, net conversion efficiencies of combined thermionic and steam-turbine cycles in an electric generating station are very high, and the costs of producing direct current as a by-product are low. For example, if conventional electric power is sold at 21 mil/kWh and the thermionic-diode emitter and collector temperatures are 1800 and 875 K, respectively, the production cost of direct-current power is 4 mil/kWh. If this direct current were used to electrolyze water to produce hydrogen at 75% efficiency, the hydrogen production costs (neglecting additional capital amortization due to electrolysis equipment) would be 1.5\$/10⁶ Btu energy content of the product.

The reactor designs used in this study are only preliminary, and additional capital costs may result from analyses of more detailed systems. Plant maintenance cost should also be estimated and included in production costs. The thermionic performance data were taken from the open

literature and should be verified by investigators actively involved in thermionic research. A more detailed discussion of this study is given in Ref. 19.

REFERENCES

1. T. Frank, D. Freiwald, T. Merson, and J. Devaney, "A Laser Fusion Reactor Concept Utilizing Magnetic Fields for Cavity Wall Protection," presented at the First Topical Meeting on the Technology of Controlled Nuclear Fusion, ANS, (April 16-18, 1974).
2. J. J. Devaney, "Magnetically Protected First Wall for a Laser-Induced Thermonuclear Reaction," Los Alamos Scientific Laboratory report LA-5699-MS (August 1974).
3. D. A. Freiwald, D. O. Dickman, and J. C. Goldstein, "Computer Simulation of a DT Pellet Microexplosion in a Magnetically Protected Laser Fusion Reactor," Los Alamos Scientific Laboratory internal report, June 26, 1975.
4. D. A. Freiwald, D. O. Dickman, and J. C. Goldstein, Bull. Am. Phys. Soc. 20, 1238 (October 1975).
5. J. C. Goldstein and D. O. Dickman, 1976 CUBE Symposium, Albuquerque, New Mexico, October 26-28, 1976.
6. J. C. Goldstein, I. O. Bohachevsky, and D. O. Dickman, Bull. Am. Phys. Soc. 21, 1186 (October 1976).
7. I. O. Bohachevsky and J. F. Hafer, "Sputtering Erosion of Reactor Cavity Walls," Los Alamos Scientific Laboratory report LA-6633-MS (December 1976).
8. G. Carter and J. S. Colligon, "Ion Bombardment of Solids," American Elsevier (1968).
9. P. Sigmund, "Theory of Sputtering I. Sputtering Yield of Amorphous and Polycrystalline Targets," Phys. Rev. 184, (August 1969) p.363.
10. G. K. Wehner, "Sputtering Yields for Normally Incident Hg^+ -Ion Bombardment at Low Ion Energy," Phys. Rev. 108, (1957) p. 35.
11. N. Laegreid and G. K. Wehner, "Sputtering Yields of Metals for Ar^+ and Ne^+ Ions with Energies from 50 to 600 eV," J. Appl. Phys. (March 1961) p. 365.
12. N. Laegreid and S. D. Dahlgren, "Wall Sputtering and Wall Life," J. Appl. Phys. 44 (May 1973) p.2093.
13. "Guide for Economic Evaluation of Nuclear Plant Designs," NUS Corp. report NUS-531 (January 1969).
14. S. T. Brewer, H. I. Bowers, R. C. DeLozier, and R. J. Barnard, "CONCEPT, a Computer Code for Conceptual Cost Estimates of Steam-Electric Power Plants, Phase IV, User's Manual," ERDA-108 (June 1975).
15. H. I. Bowers, L. D. Reynolds, R. C. DeLozier, and B. E. Strite, "CONCEPT, Computerized Conceptual Cost Estimates for Steam-Electric Power Plants, Phase II, User's Manual," ORNL-4809 (April 1973).
16. E. J. Britt, G. O. Fitzpatrick, and N. S. Razor, "Thermionic Topping of Electric Power Plants," Record of 10th Intersociety Energy Conversion Engineering Conf., Newark, Delaware (August 18-22, 1975) p. 503.
17. F. N. Huffman, T. O. P. Speidel, and J. P. Davis, "Topping Cycle Applications of Thermionic Conversion," Record of 10th Intersociety Energy Conversion Engineering Conf., Newark, Delaware (August 18-22, 1975) p. 496.
18. J. G. Lundholm, "NASA Thermionic Converter Research and Technology Program," Record of 10th Intersociety Energy Conversion Engineering Conf., Newark, Delaware (August 18-22, 1975) p.356.
19. T. G. Frank, E. A. Kern, and L. A. Booth, "Commercial Application of Thermionic Conversion Using a Fusion Reactor Energy Source - A Preliminary Assessment," Los Alamos Scientific Laboratory report LA-6621-MS (January 1977).

VII. RESOURCES, FACILITIES, AND OPERATIONAL SAFETY

The design of HEGLF Facilities continued. Safety policies and procedures continued to be applied to successfully minimize hazards of operating high-energy lasers.

MANPOWER DISTRIBUTION

The distribution of employees assigned to the various categories of the ERDA-supported Laser Fusion Research Program is shown in Table XVI.

FACILITIES

High Energy Gas Laser Facility (HEGLF)

A review of the Architect-Engineer's design effort at the 30% point of Title II in early December 1976 disclosed that the design, in general, was progressing well on schedule. Only the design of electrical installations was lagging somewhat, and this effort is being increased.

In the interest of continuity, we have presented details in HEGLF building design and construction in Sec. I.

OPERATIONAL SAFETY

Historically, our laser fusion research activities have never caused biological damage to

any of our employees. This record has continued during this reporting period. One lost-time accident occurred, however, disrupting a perfect accident-free record (over 1 million man-hours): a technician injured his hand during a lathe operation in a machine shop.

A preliminary Safety Analysis Report (PSAR) for the High Energy Gas Laser Facility (HEGLF) has been prepared.

TABLE XVI

APPROXIMATE STAFFING LEVEL OF LASER PROGRAM
DECEMBER 31, 1976

<u>Program</u>	<u>Direct Employees</u>
Glass Laser Systems Development	1
CO ₂ Laser System Development	101
New Laser Systems R&D	18
Pellet Design and Fabrication	44
Laser Target Experiments	48
Diagnostics Development	23
Systems Studies and Applications	9
TOTAL	<u>244</u>

VIII. PATENTS, PRESENTATIONS, AND PUBLICATIONS

PATENTS ISSUED

U. S. Patent 3 994 796, issued November 30, 1976.
"Electrolytic Plating Apparatus for Discrete
Microsized Particles," inventor Anton Mayer.

Presentations

The following presentations were made at the 18th
Annual Meeting of the American Physical Society,
Plasma Physics Division, San Francisco, CA,
(November 15-19, 1976).

A. H. Williams, D. V. Giovanielli, and G. H.
McCall, "A Low-Mass Calorimeter for
Laser-Produced Plasmas."

D. R. Kohler, "Polarized-Stereo Photographs of
Second-Harmonic Light in a Plasma."

J. F. Kephart, "Measurements of the Angular
Distribution of Energetic Ions from Laser-
Produced Plasmas."

A. W. Ehler, "Electron Current from a
Laser-Produced Plasma."

A. G. Engelhardt and R. L. Carman,
"Multi-Wavelength Picosecond Interferometry of
a CO₂ Laser-Produced Plasma."

D. V. Giovanielli, "Wavelength Effects in
Laser Fusion."

D. V. Giovanielli and J. F. Kephart,
"Film-Streak Derived Spectra of Electrons
Emitted From Laser-Produced Plasmas."

J. R. Miller, "A New Method for Producing Cry-
ogenic Laser Fusion Targets."

E. H. Farnum and R. J. Fries, "Fabrication of
Multishell Laser Fusion Targets."

D. M. Stupin, E. H. Farnum, R. J. Fries, and
M. A. Winkler, "Quality Selection of Laser-
Fusion Target Microballoons."

V. Cottles, H. R. Maltrud, E. H. Farnum, and R.
J. Fries, "Nondestructive Assay of Fuel
Content in Laser Fusion Targets by Fluorescent
Photon Counting."

G. H. McCall, T. H. Tan, and A. H. Williams,
"Investigation of Vacuum Insulation Properties
of Laser-Produced Plasmas."

F. F. Benjamin, P. B. Lyons, and R. H. Day,
"X-Ray Calibration of RAR 2490 Film for
Application to Laser-Plasma Experiments."

A. J. Lieber, H. D. Sutphin, and C. B. Webb,
"Picosecond X-Ray Diagnostics Using a New
Proximity Focused X-Ray Streak Camera."

J. L. Shoet, D. B. vanHulsteyn, S. J.
Gitomer, J. F. Kephart, and R. P. Godwin,
"Anisotropy of Intensity and Polarization of
Free-Free X-Ray Bremsstrahlung From Flat
Targets."

K. B. Mitchell and R. P. Godwin, "Inner Shell
Excitation from 10 μ m Laser Produced Plasmas."

K. Lee, D. W. Forslund, J. M. Kindel, and E.
L. Lindman, "Stability and Heating in Steep
Laser-Produced Density Profiles."

D. W. Forslund, J. M. Kindel, and K. Lee,
"Wavelength Sensitivity of Laser Light
Absorption and Heating."

D. W. Forslund, J. M. Kindel, K. Lee, and E.
L. Lindman, "Stability and Absorption in Laser
Light Filaments."

J. M. Kindel, D. W. Forslund, S. J. Gitomer,
and E. L. Lindman, "Vacuum Insulation as a Way
to Stop Hot Electrons."

L. E. Thode, "The Role of Collisions and
Finite Boundary Conditions on the Beam-Plasma
Interaction."

W. R. Shanahan, "Instability of a Nonneutral
Electron Beam Propagating an Inhomogeneous
Magnetic Field."

J. C. Goldstein, I. Bohachevsky, and D. O.
Dickman, "Ion Motion in Laser Fusion Reactor
Vessel Studies."

B. Bezzerides, D. F. DuBois, and D. W.
Forslund, "Magnetic Fields Due to Absorption
of Laser Light."

B. B. Godfrey, "Collective Ion Acceleration in
Nonneutral Relativistic Electron Beams."

E. L. Lindman, R. J. Mason, and B. S.
Newberger, "Laser Pellets for Short Wavelength
Lasers."

R. J. Mason, D. Brockway, and E. L. Lindman,
"2-d Implosion of Structured Pellets for Laser
Fusion."

W. S. Hall, B. S. Newberger, D. M. Stupin, E.
H. Farnum, D. R. Kohler, and R. J. Fries,
"Interferometric Characterization of Laser
Fusion Microballoons."

W. P. Gula, "Behavior of Double Shelled
Electron Beam Fusion Pellets."

S. J. Gitomer, "Hydrodynamic Stability of Laser Driven Ablative Implosions: An Eigenvalue Approach."

M. A. Stroschio and D. B. Henderson, "Theoretical Results Relating Experimental X-Ray Spectra to the Number and Energy of Suprathermal Electrons in Laser-Heated Plasmas."

R. J. Faehl, R. B. Miller, and B. B. Godfrey, "Simulation of Virtual Cathode Formation During Vacuum Propagation."

The following presentations were made at the American Nuclear Society Meeting, Washington DC, (November 14-19, 1976).

L. S. Booth and T. G. Frank, "Potential for Economic Synthetic Fuel Production from Fusion."

I. D. Bohachevsky and J. F. Hafer, "Sputtering Erosion of Fusion Reactor Cavity Walls."

The following presentations were made at the American Physical Society Meeting, Stanford, CA, (December 20, 1976).

R. A. Fisher, "Observation of Coherent Resonance Fluorescence in Hot CO₂."

R. A. Fisher "Numerical Simulation of Self-Phase Modulation Near Electronic Resonances of a Crystal."

In addition, the following presentations were made at various institutions.

R. A. Fisher, "Resonant Transients: Free-Induction Decay and Pulse Reshaping in CO₂," Bell Telephone Laboratories, Murray Hill, New Jersey (November 10, 1976).

R. A. Fisher, "The Theory of Optical Nonlinearities in the Vicinity of Electronic Resonances in Solids," Solid State Theory Seminar, Physics Department, City College of New York, New York, New York (November 8, 1976).

R. A. Fisher "Optical Transients; Practical Applications for CO₂," Physics Department, New York University, New York, New York (November 5, 1976).

R. Ahrenkiel, "The Giant Magneto-Optic Effect in the Cobalt Spinel: Applications to Laser Fusion," Iowa State University (December 2-3, 1976).

R. Ahrenkiel, "Low Dark Current Photosensors," IEDM, Washington, D. C. (December 6,7, 1976).

J. M. Kindel, D. W. Forslund, E. L. Lindman, and K. Lee, "Theoretical Results on Stability, Absorption and Hot Electron Spectra in Steep Laser Produced Density Profiles," The European Conference on Laser Interaction with Matter, Ecole Polytechnique, Palaiseau, France (October 18-22, 1976).

D. W. Forslund, "Nonlinear Processes In Laser Light Absorption," Workshop in Plasma Physics, Ahmedabad, India (November 29-December 11, 1976).

K. Riepe and H. Jansen, "Pulsed Power Systems for the LASL High Energy Gas Laser Facility," presented at IEEE Internat. Pulsed Power Conf., Lubbock, Texas (November 9-11, 1976).

R. P. Godwin, "Wavelength Scaling of Laser Plasma Interactions," European Conf. on Laser Interaction with Matter, Palaiseau, France (October 18-22, 1976).

M. J. Nutter, "Computer-Assisted Data Collection, Retrieval and Control System for the LASL 2.5 kJ, 1ns CO₂ Laser System," presented at CUBE Symposium, Albuquerque, New Mexico (October 26-28, 1976).

S. Singer, "CO₂ Laser Systems for Fusion experiments," Workshop on Laser Interaction and Related Plasma Phenomena, Rensselaer Polytechnic Inst., Troy, New York (November 8-12, 1976).

D. C. Winburn, "Safety Aspects of Laser Fusion Research at the LASL," Internat. Conf. on Lasers and Electro-Optics Equipment, United States Trade Center, Tokyo, Japan (November 17, 1976).

PUBLICATIONS

The following abstracts appear in Plasma Science 1976, IEEE Conf. Record Abstracts (1976).

W. T. Leland, J. T. Ganley, and M. Kircher, "Calculation of Cathode Fall in Electron Beam Sustained Discharges," p.27.

J. T. Ganly, W. T. Leland, B. F. Bentley, and A. J. Thomas, "Measurement of Potential Distribution and Cathode Fall in Electron Beam Sustained Discharges," p.27.

S. Singer, J. V. Parker, M. J. Nutter, J. J. Hayden, J. P. Carpenter, and I. Liberman, "Gain Suppression in High Gain Carbon Dioxide Laser Amplifiers," p.15.

R. L. McCrory, C. W. Cranfill, and R. L. Morse, "Symmetry and Stability Studies of Thermally Generated Magnetic Field in Laser Produced Plasmas," p.98.

K. A. Taggart, R. L. Morse, R. L. McCrory, and R. N. Redmund, "Two Dimensional Studies of Turbulent Instabilities in High Aspect Ratio Laser Fusion Targets," p.37.

R. L. Morse, S. J. Gitomer, and B. S. Newberger, "Structure and Scaling Laws of Laser Driven Ablative Implosions," p.36.

T. H. Tan, D. V. Giovanielli, G. H. McCall, and A. H. Williams, "Wavelength Scaling Experiments using Carbon Dioxide and Glass Laser Produced Plasmas." p.97.

The following articles appear in other Publications.

G. S. Fraley, "Implosion Characteristics of Deuterium Tritium Pellets Surrounded by High Density Shells," Los Alamos Scientific Laboratory report, LA-6378-MS, (1976).

M. A. Stroschio, "Theoretical Results Relating Experimental X-Ray Spectra to the Number and Total Energy of Suprathermal Electrons in Laser Heated Plasmas," Los Alamos Scientific Laboratory report LA-6465-MS (1976).

W. T. Wallace and M. Kircher, "Gain Uniformity in Large Aperture Electron Beam Stabilized Carbon Dioxide Amplifiers," Los Alamos Scientific Laboratory report LA-6493-MS (1976).

G. S. Fraley, "Implosion Characteristics of Deuterium Tritium Pellets Surrounded by High Density Shells," Phys. Fluids 19 (1976) pp. 1495-1500.

R. A. Fisher, "Comment on: A Remark Concerning Ultra High Weakly Dispersive Pulse Propagation in Lossy Media," Am. J. Phys. 44 (1976) pp. 1002-5.

L. A. Booth, D. A. Friewald, T. G. Frank, and F. T. Finch, "Prospects of Generating Power with Laser-Driven Fusion," Proc. IEEE 64 (1976) pp. 1460-82.

R. W. Getzinger, K. D. Ware, J. P. Carpenter, "Generation and Amplification of Nanosecond - Duration Multiline Hf Laser Pulses," TIC (1976).

"Ultra High Power Lasers for Practicable Applications," (Proceedings) Seminar, Reston, VA., L. Wilson, Ed., S.P.I.E., (1976) pp. 39-43.

D. V. Giovanielli, J. F. Kephart, and H. Arthur, "Spectra and Angular Distributions of Electron Emitted from Laser Produced Plasmas," J. Appl. Phys. 47, pp. 2907-10.

C. J. Elliot and A. E. Greene, "Electron Energy Distributions in E-Beam Initiated Xenon and Argon Plasmas," J. Appl. Phys. 47 (1976) pp. 2946-53

B. J. Feldman and S. J. Gitomer, "Annular Lens Soft Aperture for High Power Laser Systems," Appl. Opt. 15, (1976) pp. 1379-80.

T. G. Frank, I. O. Bohachevsky, L. A. Booth, J. H. Pendergrass, "Heat Transfer Problems Associated with Laser Fusion," TIC (1976).

J. E. Brolley, Jr., R. B. Lazarus, and B. R. Suydam, "Maximum Entropy Restoration of Laser Fusion Target X-Ray Photographs," TIC (1976).

L. A. Booth and T. G. Frank, "Technology Assessment of Laser Fusion Power Production." (Abstract) Technology of Controlled Nuclear Fusion, 2nd Topical Meeting, Program of Summaries, Electric Power Research Institute (1976).

R. W. Getzinger, N. R. Greiner, K. D. Ware, J. P. Carpenter, and R. G. Menzel, "Controlled Energy Extraction and Sharp Nanosecond Pulses from an Hf Amplifier," IEEE J. Quantum Electron Qe12 (1976) pp. 556-8.

M. I. Buchwald, C. R. Jones, H. R. Fetterman, and H. R. Schlossberg, "Direct Optically Pumped Multiwavelength Carbon Dioxide Laser," Appl. Phys. Lett. 29 (1976) pp. 300-2.

C. D. Cantrell, III, and H. W. Galbraith, "Towards an Explanation of Collisionless Multiple Photon Laser Dissociation of Sulfur Hexafluoride," Opt. Commun. 18 (1976) pp. 513-6.

B. E. Newnam, D. H. Gill, J. H. Apfel, J. S. Matteucci, "Role of Electric Field Strength in Laser Damage of Dielectric Multilayers," TIC (1976).

A. Lieber, H. D. Sutphin, C. B. Clinton, and A. H. Williams, "Sub-Picosecond X-Ray Streak Camera Development for Laser Fusion Diagnostics," TIC (1976).

L. A. Booth, "Commercial Application of Laser Fusion," TIC (1976).

A. Lieber, H. D. Sutphin, and C. B. Webb, "Sub-Picosecond Proximity Focused Streak Camera for X-Ray and Visible Light," TIC (1976).

J. J. Hayden and I. Liberman, "Measurements at 10.6 Micrometers of Damage Threshold in Germanium, Copper, Sodium Chloride, and Other Optical Materials at Levels Up to 10/Sup 10/W/CM/Sup 2/," TIC (1976).

D. C. Winburn, "Safety Aspects of Laser Fusion Research at the Los Alamos Scientific Laboratory," Optics and Laser Technology (December 1976) p. 265.

D. C. Winburn, "Safety Considerations in the Laser Research Program at the Los Alamos Scientific Laboratory," Ann. N. Y. Acad. Sci. 267 (1976) pp. 135-151.